SANDIA REPORT

SAND97–2601 • UC–721
Unlimited Release
Printed January 1998

Crushed-Salt Constitutive Model Update

F. D. Hansen, G. D. Callahan, M. C. Loken, K. D. Mellegard

Prepared by
Sandia National Laboratories
Albuquerque, New Mexico 87185 and Livermore, California 94550

Sandia is a multiprogram laboratory operated by Sandia Corporation, a Lockheed Martin Company, for the United States Department of Energy under Contract DE-AC04-94AL85000.

Approved for public release; further dissemination unlimited.

Sandia National Laboratories

Issued by Sandia National Laboratories, operated for the United States Department of Energy by Sandia Corporation.

Available to DOE and DOE contractors from
Office of Scientific and Technical Information
P.O. Box 62
Oak Ridge, TN 37831

Prices available from (615) 576-8401, FTS 626-8401

Available to the public from
National Technical Information Service
U.S. Department of Commerce
5285 Port Royal Rd
Springfield, VA 22161

NTIS price codes
Printed copy: A08
Microfiche copy: A01

SAND97-2601
Unlimited Release
Printed January 1998

Distribution
Category UC-721

Crushed-Salt Constitutive Model Update

G.D. Callahan, M.C. Loken, K.D. Mellegard
RE/SPEC Inc.
Rapid City, SD 57709-0725

F.D. Hansen
WIPP Deputy Project Management and Technical Integration Department
Sandia National Laboratories
Albuquerque, NM 87185-5800

ABSTRACT

Modifications to the constitutive model used to describe the deformation of crushed salt are presented in this report. Two mechanisms—dislocation creep and grain boundary diffusional pressure solutioning—defined previously but used separately are combined to form the basis for the constitutive model governing the deformation of crushed salt. The constitutive model is generalized to represent three-dimensional states of stress. New creep consolidation tests are combined with an existing database that includes hydrostatic consolidation and shear consolidation tests conducted on Waste Isolation Pilot Plant and southeastern New Mexico salt to determine material parameters for the constitutive model. Nonlinear least-squares model fitting to data from the shear consolidation tests and a combination of the shear and hydrostatic consolidation tests produced two sets of material parameter values for the model. The change in material parameter values from test group to test group indicates the empirical nature of the model but demonstrates improvement over earlier work with the previous models. Key improvements are the ability to capture lateral strain reversal and better resolve parameter values. To demonstrate the predictive capability of the model, each parameter value set was used to predict each of the tests in the database. Based on the fitting statistics and the ability of the model to predict the test data, the model appears to capture the creep consolidation behavior of crushed salt quite well.

CONTENTS

CONTENTS (Continued)

Figures

Figures (Continued)

Figures (Continued)

Tables

1.0 INTRODUCTION

1.1 Background

Construction of the Waste Isolation Pilot Plant (WIPP) was initiated by the U. S. Department of Energy (DOE) in 1981 to develop the technology for the safe management, storage, and disposal of transuranic (TRU) radioactive wastes generated by DOE defense programs. The WIPP, located in southeastern New Mexico at a depth of approximately 655 meters in bedded halites, consists of a series of underground shafts, drifts, panels, and disposal rooms. The WIPP may eventually become a repository for TRU wastes, provided the facility is demonstrated to be in compliance with the Environmental Protection Agency's requirements. If the compliance requirements are satisfied, each disposal room will be filled with containers holding TRU wastes of various forms. Ultimately a seal system designed to prevent water from entering the repository and to prevent gases and brines from migrating out of the repository must be in place.

Crushed salt has been proposed as a viable material for permanent sealing of WIPP underground openings. Crushed salt's desirable characteristics include chemical compatibility, eventual mechanical similarity with the host salt formation, and availability from the site excavation. Laboratory tests have shown that crushed salt achieves desirable permeability characteristics as consolidation increases the material density. In addition, voids and fractures close and heal in salt in response to applied loads. Reconsolidated crushed salt becomes a long-term seal component. Thus an understanding of the consolidation processes in crushed salt is fundamental to the design and analysis of a credible seal system that will provide confidence and establish regulatory compliance.

To gain an understanding of the crushed-salt consolidation processes, knowledge of the overall repository isolation system is required along with the interactions of key components such as host geology, brine, waste forms, generated gases, and seal elements. Representative and defensible material, flow, and chemical models are needed that describe the behavior of these components in the isolation system. The objective of this report is to update the mechanical material model appropriate for describing crushed-salt deformation. The WIPP crushed-salt material model or constitutive model, which relates stress and strain, predicts deformations and stresses in the underground sealing system. The magnitude of the stresses and strains throughout the isolation system determines the location and extent of the disturbed rock zone and serviceability of the seal components. Because crushed salt is an important seal material, its constitutive model must satisfy the needs of performance assessment and regulatory compliance.

1.2 Earlier Work

Crushed salt has received international attention over the past 20 years, primarily within a repository setting. An earlier study (Callahan et al., 1995) searched the literature for constitutive models developed for crushed salt. Ten models, based to varying degrees on phenomenology, micromechanics, or empiricism, were found. Three of these models were selected for detailed examination. The three models are those attributable to Sjaardema-Krieg (1987), Zeuch and Holcomb (Zeuch, 1990), and Spiers and coworkers (Spiers and Brzesowsky, 1993). These constitutive models were developed to reproduce hydrostatic (isostatic) consolidation laboratory tests and include only the volumetric strain component. The Sjaardema and Krieg model is empirical and was retained for comparative purposes because it was used in the past for calculation of crushed-salt problems at the WIPP. The Zeuch and Holcomb model was constructed for nominally dry crushed salt and is based on the isostatic hot-pressing models combined with dislocation creep. The Spiers and coworkers model was formulated for wet crushed-salt aggregates and is based on grain boundary diffusional pressure solution processes. These three models were modified to include effects thought to be important for WIPP salt. A flow potential and associated three-dimensional generalization were developed for the models so that they could operate over a wide range of stress triaxialities (ratio of mean stress to effective or deviatoric stress) and be applicable to arbitrary states of stress. A database of applicable crushed-salt laboratory tests was constructed comprising 40 hydrostatic consolidation tests and 10 shear consolidation tests. The experimental data were fit to determine values for the material parameters associated with each of the models. The hydrostatic and shear consolidation tests and their combination were fit separately so that three different parameter value sets were obtained. If a constitutive model was representative and the data were unbiased, the change in parameter values among fits should have been minimal. However, in the earlier study, the change in the parameter values was significant. These three models performed about equally well, with the modified Spiers model exhibiting moderate superiority.

Following completion of the earlier study for the evaluation of potential constitutive models for crushed salt (Callahan et al., 1995), the constitutive model formulation was found to be inadequate at high fractional densities. In addition, because of the heavy bias in the database toward hydrostatic consolidation tests, along with the fact that none of the shear consolidation tests reached high enough fractional densities to exhibit positive lateral strains, the constants associated with the flow potential made it impossible for the simulated crushed salt to move toward a volume-preserving flow (as is exhibited by intact salt) as the fractional density approached one. Most of the test data in the crushed-salt laboratory database exhibit a positive lateral-to-axial strain rate ratio, whereas the lateral-to-axial strain rate ratio is negative for a triaxial test conducted on intact salt. However, as the crushed salt consolidates, at some density

level the lateral deformation must change direction (i.e., cease to move inward and begin to move outward as is observed for the intact salt tests). In addition to being a function of the density, this change in lateral strain direction is also, undoubtedly, a function of the state of stress. Having identified these shortcomings in the crushed-salt model, two additional shear consolidation tests were conducted to expand the database at higher fractional densities near 0.8 (RE/SPEC Inc., 1996). The functional form of the flow potential for the models was modified, and the models were refit to the database. This study, discussed in RE/SPEC Inc. (1996) and Callahan et al. (1996), resulted in satisfactory model predictions over a wide range of fractional densities and stress triaxialities. However, the governing deformation mechanisms for crushed salt with varying degrees of added moisture were contained independently in two separate models.

Thus a goal of the present study was to incorporate the governing mechanisms into a single model. In addition, four new laboratory shear consolidation experiments were conducted with fractional densities near the initial fractional density expected in the dynamically compacted crushed-salt seal (approximately 0.9). These tests allow the database to be expanded into fractional density ranges previously untested and provide information on the crushed-salt flow behavior as its density increases. These tests were added to the experimental database, which was fit to obtain material parameter values for the updated crushed-salt constitutive model. The sign convention used throughout this report is tension positive.

1.3 Report Organization

This report focuses on the mechanical constitutive behavior of crushed salt. Chapter 2 describes the constitutive model, provides the three-dimensional generalization of the model, and reduces the general model form to specific types of laboratory tests. Chapter 3 summarizes the crushed-salt experimental database along with recently completed tests used to fit the constitutive model and determine its material constants. Chapter 4 describes the nonlinear least-squares fitting procedure used to fit the constitutive model to the experimental database and presents the resulting parameter values. Chapter 5 compares the crushed model to other models for porous materials available in the literature. Chapter 6 discusses modifications to the moisture function and flow potential, which were subsequently not used in the final form of the crushed-salt model. The report is concluded with a summary and recommendations in Chapter 7, followed by a list of referenced material, a bibliography, and three appendices.

2.0 CRUSHED-SALT CONSTITUTIVE MODEL

This chapter presents the crushed-salt deformation mechanisms, the general form for the crushed-salt constitutive model, development of the three-dimensional generalization for the creep consolidation model, and reduction of the constitutive model to the form necessary to fit the laboratory data and evaluate the material model parameters.

2.1 Crushed-Salt Deformation Mechanisms

Multiple deformation mechanisms control the densification of crushed salt for the seal emplacement processes and range of conditions expected at the WIPP, where crushed salt is planned as a major sealing component in the shafts. During emplacement in the shafts, crushed salt will be dynamically compacted with small amounts of added moisture (less than 2 percent by weight) to a fractional density of about 0.9. During dynamic compaction, the densification of the crushed salt will occur through particle rearrangement, cataclasis, and plastic yield. These *instantaneous* processes provide a dense, locked-up aggregate. Further densification occurs over time through compactional loading on the crushed-salt column caused by creep of the host salt formation and inward movement of the shaft walls. As crushed salt is loaded, the principal densification mechanisms include dislocation creep and fluid-phase diffusional creep (grain boundary diffusional pressure solutioning). Without the added moisture during construction of the crushed-salt seal component, the importance of the diffusional creep mechanism would diminish. The model that defines the dislocation creep of intact salt is defined in terms of three dislocation mechanisms involving dislocation climb, an undefined (but experimentally and empirically well established) mechanism, and dislocation glide (Munson et al., 1989). The presence of the liquid phase leads to the additional deformational processes characterized by stress-induced dissolution, diffusion, and precipitation. The diffusional creep rate is controlled by the slowest of these serial processes. The grain boundary diffusional pressure solution mechanism dramatically enhances the densification rate in crushed salt (Spiers and Schutjens, 1990).

The idea of pressure solutioning as a deformation mechanism has been around for over 100 years but has only been studied in detail for application to geologic systems during the last 25 years. The fundamental process is characterized by a liquid phase occurring perhaps as a thin liquid film at grain interfaces. The diffusive mass transfer process has been called fluid-phase diffusional creep, solution-precipitation creep, pressure solution, and grain boundary diffusional pressure solution. The mechanism is analogous to diffusional creep (Coble creep) where matter is transported distances on the order of the grain size and controlled by diffusion of atoms

through the grain interfaces. In the solution-precipitation creep process, matter transport is characterized by diffusion through the fluid at the grain interfaces. A significant difference between the two creep processes is that solution-precipitation creep occurs at much lower temperatures than the classical diffusional creep.

The constitutive model developed for crushed salt discussed in the following sections incorporates the dislocation creep and pressure solutioning mechanisms.

2.2 General Form for the Crushed-Salt Constitutive Model

The total strain rate for the crushed-salt constitutive model is assumed to consist of two components. The components include nonlinear elastic $\left(\dot{\epsilon}_{ij}^{e} \right)$ and creep consolidation $\left(\dot{\epsilon}_{ij}^{c} \right)$ contributions, and the total strain rate is written as:

$$\dot{\epsilon}_{ij} = \dot{\epsilon}_{ij}^{e} + \dot{\epsilon}_{ij}^{c} \tag{2-1}$$

When the strains become finite, the expressions for strain rate should be interpreted as the rate of deformation. Both the nonlinear elastic and creep consolidation portions of the model describe the material behavior in bulk (volumetric) and in shear (deviatoric). However, as shown later, when the fractional density approaches unity, the creep consolidation portion of the model only describes deviatoric material behavior and is, in fact, the creep deformation model used for intact salt. The nonlinear elastic portion of the model presented by Callahan et al. (1995) has not changed and will not be presented again. The creep consolidation portion of the model is presented along with its evolution to the intact salt model.

2.3 Creep Consolidation Model

The creep consolidation model is of primary concern in this study, and thus this section is divided into subsections that address important issues regarding the creep consolidation portion of the crushed-salt consolidation model. Typically equations proposed to describe the behavior of a particular material are written in one-dimensional form or as scalar relationships. To be useful in numerical analyses and applicable to a variety of laboratory experiments with different load paths, any constitutive model must be generalized to include three-dimensional states of stress. The first subsection presents the generalization of the creep consolidation model. The next subsection collapses or reduces the generalized form of the creep consolidation equation to specific laboratory test conditions, which yields simplified forms that can be used in fitting the model to the experimental database. The third subsection presents the effective strain rate model

forms that represent the two mechanisms associated with the crushed-salt creep consolidation component of the constitutive model.

2.3.1 Creep Consolidation Model Generalization

To develop the creep consolidation constitutive equation for crushed salt, two operative deformation mechanisms are assumed: dislocation creep and grain boundary diffusional pressure solutioning. Dislocation creep is the governing mechanism for deformation of intact salt (e.g., Munson et al., 1989). The stress-induced dissolution and precipitation process or simply pressure solutioning is an operative mechanism when small quantities of water (brine) are contained in the aggregate (e.g., Spiers and Brzesowsky, 1993). As discussed by Stocker and Ashby (1973) and Helle et al. (1985), the creep and diffusional mechanisms are independent and additive. From the application of thermodynamic concepts, the three-dimensional generalization of kinetic equations is given by Fossum et al. (1988). Following this approach, the generalized average kinetic equation for the creep consolidation inelastic flow of crushed salt can be written as:

$$\dot{\epsilon}_{ij}^{c} = \left[\dot{\epsilon}_{eq}^{d}\left(\sigma_{eq}^{f}\right) + \dot{\epsilon}_{eq}^{w}\left(\sigma_{eq}^{f}\right) \right] \frac{\partial \sigma_{eq}}{\partial \sigma_{ij}} \tag{2-2}$$

where $\dot{\epsilon}_{ij}^{c}$ is the inelastic strain rate tensor and σ_{eq}^{f} is an equivalent stress measure. The equivalent inelastic strain rate measures for dislocation creep $\left(\dot{\epsilon}_{eq}^{d}\right)$ and pressure solutioning $\left(\dot{\epsilon}_{eq}^{w}\right)$ are written as functions of the equivalent stress measure. For use in the flow potential, another equivalent stress measure, σ_{eq}, is used to provide a nonassociative type of formulation that provides flexibility in governing the magnitude of the volumetric behavior.

Motivation for selection of the equivalent stress measures comes from laboratory experiments reported in previous work (Callahan et al., 1995; 1996). Tests on crushed-salt specimens exhibit a strong dependence on the pressure (mean stress) applied to the specimens. Shear consolidation experiments also exhibit differing behavior depending on the magnitude of applied stress difference. Thus the appropriate stress measure should include both mean and deviatoric stress dependencies. Laboratory tests on intact salt specimens show little dependence on moderate mean stress levels (< -2 MPa), and typically the deformation of intact salt is described as a volume-preserving process. Therefore one would expect the mean stress influence to decrease as the crushed salt approaches full consolidation. Perhaps most importantly, in a typical triaxial test, the effective stress measure describing the potential surface must provide a reversal in lateral strain rate as the fractional density approaches one. This condition is a natural consequence at low stress triaxialities (ratio of mean to deviatoric stress) because porous crushed salt decreases in volume but intact salt inelastic deformation is isochoric (volume preserving) unless damage is occurring.

Sofronis and McMeeking (1992) discuss the ratio of mean stress to deviatoric stress or stress triaxiality as considered by a number of researchers. They discuss investigations of stress triaxiality over ranges of fractional density, which are pertinent to the crushed-salt investigations. Crushed salt emplaced in the underground workings and shafts at the WIPP will experience moderate levels of stress triaxiality. Models for hot isostatic pressing (HIPing) of powders presented by Helle et al. (1985), which also provide the basis for Zeuch's (1990) crushed-salt model, have an infinite ratio of mean stress to shear stress. Therefore, Callahan et al. (1995) and RE/SPEC Inc. (1996) modified Zeuch's model for applicability in the moderate stress triaxiality ranges. Duva and Hutchinson (1984) developed a constitutive model for power-law creep of an incompressible matrix material containing a dilute concentration of spherical voids. Their model is thought to be valid for moderate stress triaxialities with fractional densities greater than 0.9. However, when the triaxiality is high, the model is only valid for porosities less than 1 percent. Duva (1986) modified the original model of Duva and Hutchinson (1984) so that the accuracy was improved at higher porosities for moderate triaxialities, but the model is still unsatisfactory for high triaxial stress states except when the porosity is low. Cocks (1989) states that the surface of constant energy dissipation rate (i.e., the creep potential surface) for a creeping solid is a function of stress and void volume fraction only, and independent of material parameters apart from a weak dependence on the creep stress exponent. Cocks' conclusion is based on a lower bound analysis for an isolated spherical void. Cocks' constitutive law for power-law creeping materials is not accurate for low porosities when the stress is predominantly hydrostatic, but performs better at higher void volume fractions. In contrast to the constitutive laws that contain a range of stress triaxialities, the models of Wilkinson and Ashby (1975), Arzt et al. (1983), and Helle et al. (1985) are valid only for states of pure hydrostatic stress; however, the models are probably more accurate over a larger range of fractional densities for these stress conditions. Sofronis and McMeeking (1992) developed a creep potential for power-law materials based on finite element calculations of spherical unit cells with a central spherical hole to represent the voids. They found that the dominant component, whether dilational or deviatoric, is always well represented. Comparisons with uniaxial compression experimental data from other sources showed that the ratio of the lateral-to-axial strain rates was predicted fairly accurately, although the strain rate magnitudes were not.

Crushed salt emplaced at the WIPP will experience broad ranges of fractional density and stress triaxiality over the life of the repository. As discussed for the earlier studies, little success has been achieved in a single constitutive model's ability to cover all these required conditions. Fortunately the crushed salt emplaced in the shaft will be dynamically compacted to an initial fractional density of about 0.9. This limits the accuracy required in the crushed-salt constitutive model to fractional densities between 0.9 and 1.0. However, much of the existing crushed-salt laboratory data have been generated for fractional densities less than 0.9. In our first study (Callahan et al., 1995), the most promising existing models for crushed salt were identified and generalized for arbitrary states of stress. However, the large number of hydrostatic consolidation test results in the database used to evaluate material parameters resulted in a model that was invalid at low stress triaxialities. The second study (RE/SPEC Inc., 1996; Callahan et al., 1996) corrected this problem by designing and adding two tests that expanded the experimental results

into a previously unrepresented region of material behavior, modifying the functional form of the flow potential, and independently fitting the flow potential to the strain rates to determine the parameter values. In the present study, the two identified operative mechanisms are combined in the constitutive model to characterize the consolidation of crushed salt.

With these considerations, the equivalent stress measures are homogeneous of degree one in terms of stress and are given by:

$$\sigma_{eq}^{f} = \left[\eta_0 \Omega_f^{\eta_1} \sigma_m^2 + \eta_2 \left(\frac{2 - D}{D} \right)^{\frac{2n_f}{n_f + 1}} (\sigma_1 - \sigma_3)^2 \right]^{1/2}$$

$$\sigma_{eq} = \left[\kappa_0 \Omega^{\kappa_1} \sigma_m^2 + \kappa_2 \left(\frac{2 - D}{D} \right)^{\frac{2n}{n + 1}} (\sigma_1 - \sigma_3)^2 \right]^{1/2} \qquad (2\text{-}3)$$

where:

$$\Omega_f = \left[\frac{(1 - D)\, n_f}{\left[1 - (1 - D)^{1/n_f} \right]^{n_f}} \right]^{\frac{2}{n_f + 1}} \qquad (2\text{-}4)$$

$$\Omega = \left[\frac{\left(1 - D_v\right) n}{\left[1 - \left(1 - D_v\right)^{1/n} \right]^{n}} \right]^{\frac{2}{n + 1}} \qquad (2\text{-}5)$$

$$D_v = \begin{cases} D_t & D \le D_t \\ D & D > D_t \end{cases} \qquad (2\text{-}6)$$

D = current fractional density

σ_m = mean stress = $\frac{\sigma_{kk}}{3}$

σ_3 = minimum principal stress

σ_1 = maximum principal stress

η_0, η_1, η_2, κ_0, κ_1, κ_2, n_f, n, and D_t = material parameters.

The fractional density relationships given in Equations 2-4 and 2-5 are similar to the densification relationship derived by Wilkinson and Ashby (1975) for an isolated spherical void

in a power-law creeping material when the fractional density is greater than 0.9. Their analytical solution to this problem showed that the macroscopic densification rate was proportional to the fractional density relationship written as:

$$\frac{\dot{D}}{D} \alpha \frac{(1 - D)}{\left[1 - (1 - D)^{1/n}\right]^n} \tag{2-7}$$

where n is the stress exponent for the power-law material. The functional form for the fractional density relationship is carried through in the models presented by Arzt et al. (1983), Helle et al. (1985), and Zeuch (1990). Sofronis and McMeeking (1992) adopted a similar form for their elliptic form of the potential function for power-law creep of a material containing spherical voids. Kwon and Kim (1996a; 1996b) used the potential functions derived by Kuhn and McMeeking (1992) and Sofronis and McMeeking (1992) to develop models for densification of alumina powder.

As crushed salt approaches full consolidation (i.e., D → 1), Ω_f and Ω approach zero and the dependence on mean stress diminishes, which is required for an incompressible material matrix. The fractional density functions multiplying the deviatoric terms in Equation 2-3 are taken from Sofronis and McMeeking (1992). They state that, under purely deviatoric situations, this term exceeds the lower bound developed by Ponte Casteneda and Willis (1988) for large fractional densities but provides a good approximation to the results of Duva and Hutchinson (1984). Thus, letting $D = 1$, Equation 2-3 becomes:

$$\begin{aligned} \sigma_{eq}^f &= \sqrt{\eta_2}\left(\sigma_1 - \sigma_3\right) \\ \sigma_{eq} &= \sqrt{\kappa_2}\left(\sigma_1 - \sigma_3\right) \end{aligned} \tag{2-8}$$

Twice the maximum shear stress or Tresca equivalent stress is used in the equivalent stress measures to describe the shear behavior, as is common for intact salt, and is given by:

$$\sigma_1 - \sigma_3 = 2\cos\psi\sqrt{J_2} \tag{2-9}$$

with the second and third invariants of the deviator stress (J_2 and J_3) defined by:

$$\begin{aligned} J_2 &= \frac{1}{2} s_{ij} s_{ji} \\ J_3 &= \frac{1}{3} s_{ij} s_{jk} s_{ki} \end{aligned} \tag{2-10}$$

where the Lode angle (ψ), which is a convenient alternative invariant to J_3, is given by:

$$\psi = \frac{1}{3}\sin^{-1}\left(\frac{-3\sqrt{3}J_3}{2J_2^{3/2}}\right), \left(-\frac{\pi}{6} \le \psi \le \frac{\pi}{6}\right) \tag{2-11}$$

The partial derivative given in Equation 2-2 may be determined using the chain rule as:

$$\frac{\partial \sigma_{eq}}{\partial \sigma_{ij}} = \frac{\partial \sigma_{eq}}{\partial \sigma_m}\frac{\partial \sigma_m}{\partial \sigma_{ij}} + \frac{\partial \sigma_{eq}}{\partial J_2}\frac{\partial J_2}{\partial \sigma_{ij}} + \frac{\partial \sigma_{eq}}{\partial \psi}\frac{\partial \psi}{\partial J_3}\frac{\partial J_3}{\partial \sigma_{ij}} \tag{2-12}$$

The derivatives of the invariants in Equation 2-12 are the same regardless of the invariant stress and strain measures selected. These derivatives are:

$$\begin{aligned}
\frac{\partial \sigma_m}{\partial \sigma_{ij}} &= \frac{\delta_{ij}}{3} \\
\frac{\partial J_2}{\partial \sigma_{ij}} &= s_{ij} \\
\frac{\partial \psi}{\partial J_3}\frac{\partial J_3}{\partial \sigma_{ij}} &= -\frac{\sqrt{3}}{2J_2^{3/2}\cos 3\psi}t_{ij}
\end{aligned} \tag{2-13}$$

where:

δ_{ij} = Kronecker delta

$$t_{ij} = s_{ip}s_{pj} - \frac{2}{3}J_2\delta_{ij}$$

Equation 2-12, defining the flow potential, also requires the partial derivatives of the equivalent stress measure (Equation 2-3) with respect to stress. Performing the required differentiation yields:

$$\frac{\partial \sigma_{eq}}{\partial \sigma_m} = \frac{\kappa_0 \Omega^{\kappa_1} \sigma_m}{\sigma_{eq}}$$

$$\frac{\partial \sigma_{eq}}{\partial J_2} = \frac{4 \kappa_2}{\sigma_{eq}} \left(\frac{2 - D}{D} \right)^{\frac{2n}{n+1}} \frac{\cos\psi \cos 2\psi}{\cos 3\psi} \tag{2-14}$$

$$\frac{\partial \sigma_{eq}}{\partial \psi} = -\frac{4 \kappa_2}{\sigma_{eq}} \left(\frac{2 - D}{D} \right)^{\frac{2n}{n+1}} \cos\psi \sin\psi J_2$$

Substituting Equations 2-12, 2-13, and 2-14 into Equation 2-2 provides the tensorial strain rate components for the creep consolidation portion of the crushed-salt model, which is given by:

$$\dot{\epsilon}_{ij}^{c} = \frac{\dot{\epsilon}_{eq}^{d} + \dot{\epsilon}_{eq}^{w}}{\sigma_{eq}} \left\{ \frac{\kappa_0 \Omega^{\kappa_1} \sigma_m}{3} \delta_{ij} + \kappa_2 \left(\frac{2 - D}{D} \right)^{\frac{2n}{n+1}} 2\sqrt{J_2} \cos\psi \right.$$

$$\left. \left(\left[\frac{\cos 2\psi}{\cos 3\psi} \right] \frac{s_{ij}}{\sqrt{J_2}} + \left[\frac{\sqrt{3} \sin\psi}{J_2 \cos 3\psi} \right] t_{ij} \right) \right\} \tag{2-15}$$

Equation 2-15 is seen to be undefined as the Lode angle approaches $\pm\pi/6$. In other words, the flow potential forms corners at $\psi = \pm\pi/6$, and the direction of straining is not unique. To eliminate this problem computationally, the flow potentials on either side of the corner are averaged, which produces an indeterminant form that is examined in the limit as $\psi \rightarrow \pm\pi/6$. Performing this limiting operation, Equation 2-15 becomes:

$$\dot{\epsilon}_{ij}^{c} = \frac{\dot{\epsilon}_{eq}^{d} + \dot{\epsilon}_{eq}^{w}}{\sigma_{eq}} \left\{ \frac{\kappa_0 \Omega^{\kappa_1} \sigma_m}{3} \delta_{ij} + \kappa_2 \left(\frac{2 - D}{D} \right)^{\frac{2n}{n+1}} \sqrt{3 J_2} \right.$$

$$\left. \left(\frac{s_{ij}}{\sqrt{3 J_2}} \mp \frac{t_{ij}}{2 J_2} \right) \right\} \tag{2-16}$$

The flow potential contains five material parameters (κ_0, κ_1, κ_2, D_i, and n) that need to be determined from laboratory experiments. To complete the crushed-salt creep consolidation

description, the kinetic equations describing dislocation creep and pressure solutioning in crushed salt need to be defined. In general, these kinetic equations could be a form of any specific model that captures the desired characteristics of the material deformation. Discussion of these specific forms is included in Sections 2.3.3 and 2.3.4 following presentation of other general considerations for the crushed-salt consolidation model.

2.3.2 Evaluation of Laboratory Test Equation Forms

To compare the crushed-salt constitutive equations to laboratory experiments, one needs to reduce the equations to the applicable test conditions. In particular, tests of interest are the hydrostatic compression, triaxial compression, and extension tests. To derive these forms, one simply needs to substitute the applicable test conditions into the constitutive equations and reduce them to their simplest forms. The hydrostatic compression test conditions can be easily obtained from the triaxial compression test conditions by letting the stress difference ($\Delta\sigma = \sqrt{3J_2}$) equal zero. The directions $\{zz, yy, xx\}$ are taken as $\{33, 22, 11\}$, and the $\{zz\}$ direction is taken to be the axial direction. For simplicity, the following variables are defined:

$$\alpha = \frac{\kappa_0 \Omega^{\kappa_1} \sigma_m}{3}$$
$$\beta = \kappa_2 \left[\frac{2 - D}{D}\right]^{\frac{2n}{n+1}} \sqrt{3 J_2} \qquad (2\text{-}17)$$

Fitting of the constitutive model can be conveniently separated into two separate stages. The first step includes fitting the ratio of the lateral strain rate to the axial strain rate defined as **R** and written as:

$$\mathbf{R} = \frac{\dot{\epsilon}_l^c}{\dot{\epsilon}_a^c} \qquad (2\text{-}18)$$

Fitting the strain rate ratio allows the parameter values associated with the flow potential (i.e., α and β in Equation 2-17) to be determined independently of the other material parameter values. Obviously the test data must contain experiments where the stress triaxiality conditions lie between zero and infinity for the fitting to be successful. This can be accomplished with the shear consolidation tests.

Reduction to Triaxial Compression Creep Test ($\psi = \pi/6$)

The triaxial compression creep test is prescribed by controlling a constant stress state defined by $\sigma_{zz} < \sigma_{xx} = \sigma_{yy}$. Under these stress conditions, the stress measures included in Equation 2-16 reduce to:

$$\sqrt{3J_2} = \Delta\sigma = \sigma_1 - \sigma_3$$

$$J_2 = \frac{\Delta\sigma^2}{3}$$

$$s_{zz} = \sigma_{zz} - \sigma_m = -\frac{2}{3}\Delta\sigma$$

$$s_{xx} = s_{yy} = \sigma_{xx} - \sigma_m = \frac{\Delta\sigma}{3} \qquad (2\text{-}19)$$

$$t_{zz} = s_{zz}^2 + s_{zx}^2 + s_{zy}^2 - \frac{2}{3}J_2 = \frac{2\Delta\sigma^2}{9}$$

$$t_{xx} = t_{yy} = s_{xx}^2 + s_{xy}^2 + s_{xz}^2 - \frac{2}{3}J_2 = -\frac{\Delta\sigma^2}{9}$$

$$\left(\frac{s_{zz}}{\sqrt{3J_2}} - \frac{t_{zz}}{2J_2}\right) = -1$$

$$\left(\frac{s_{xx}}{\sqrt{3J_2}} - \frac{t_{xx}}{2J_2}\right) = \frac{1}{2}$$

Therefore the axial (*a*), lateral (*l*), and volumetric (*v*) strain components and strain rate ratio for the creep consolidation portion of the model may be determined from Equations 2-16, 2-17, 2-18, and 2-19 as:

$$\dot{\epsilon}_a^c = [\alpha - \beta]\frac{\dot{\epsilon}_{eq}^d + \dot{\epsilon}_{eq}^w}{\sigma_{eq}}$$

$$\dot{\epsilon}_l^c = \left[\alpha + \frac{\beta}{2}\right]\frac{\dot{\epsilon}_{eq}^d + \dot{\epsilon}_{eq}^w}{\sigma_{eq}} \qquad (2\text{-}20)$$

$$\dot{\epsilon}_v^c = 3\alpha\,\frac{\dot{\epsilon}_{eq}^d + \dot{\epsilon}_{eq}^w}{\sigma_{eq}}$$

$$\mathbf{R} = \frac{\alpha + \frac{\beta}{2}}{\alpha - \beta}$$

Reduction to Triaxial Extension Test ($\psi = -\pi/6$)

The triaxial extension creep test is prescribed by controlling a constant stress state defined by $\sigma_{zz} > \sigma_{xx} = \sigma_{yy}$. Under these stress conditions, the stress measures in Equation 2-16 reduce to:

$$\sqrt{3J_2} = \Delta\sigma = \sigma_1 - \sigma_3$$

$$J_2 = \frac{\Delta\sigma^2}{3}$$

$$s_{zz} = \sigma_{zz} - \sigma_m = \frac{2}{3}\Delta\sigma \qquad (2\text{-}21)$$

$$s_{xx} = s_{yy} = \sigma_{xx} - \sigma_m = -\frac{\Delta\sigma}{3}$$

$$t_{zz} = s_{zz}^2 + s_{zx}^2 + s_{zy}^2 - \frac{2}{3}J_2 = \frac{2\Delta\sigma^2}{9}$$

$$t_{xx} = t_{yy} = s_{xx}^2 + s_{xy}^2 + s_{xz}^2 - \frac{2}{3}J_2 = -\frac{\Delta\sigma^2}{9}$$

$$\left(\frac{s_{zz}}{\sqrt{3J_2}} + \frac{t_{zz}}{2J_2}\right) = 1$$

$$\left(\frac{s_{xx}}{\sqrt{3J_2}} + \frac{t_{xx}}{2J_2}\right) = -\frac{1}{2}$$

Therefore the axial (a), lateral (l), and volumetric (v) strain components and strain rate ratio for the creep consolidation portion of the model may be determined from Equations 2-16, 2-17, 2-18, and 2-21 as:

$$\dot{\epsilon}_a^c = [\alpha + \beta] \frac{\dot{\epsilon}_{eq}^d + \dot{\epsilon}_{eq}^w}{\sigma_{eq}}$$

$$\dot{\epsilon}_l^c = \left[\alpha - \frac{\beta}{2}\right] \frac{\dot{\epsilon}_{eq}^d + \dot{\epsilon}_{eq}^w}{\sigma_{eq}} \qquad (2\text{-}22)$$

$$\dot{\epsilon}_v^c = 3\,\alpha \frac{\dot{\epsilon}_{eq}^d + \dot{\epsilon}_{eq}^w}{\sigma_{eq}}$$

$$\mathbf{R} = \frac{\alpha - \frac{\beta}{2}}{\alpha + \beta}$$

2.3.3 Equivalent Inelastic Strain Rate Form for Dislocation Creep

Dislocation creep of intact salt has been characterized by the Multimechanism Deformation (M-D) model (Munson, 1979; Munson and Dawson, 1979; Munson et al., 1989). Thus the equivalent inelastic strain rate measure for the dislocation creep portion of the crushed-salt model is taken to be the M-D material model. The model is written as:

$$\dot{\epsilon}_{eq}^d = F\,\dot{\epsilon}_s \qquad (2\text{-}23)$$

where $\dot{\epsilon}_{eq}^d$ is the kinetic equation and $\dot{\epsilon}_s$ is the steady-state strain rate. The transient function F consists of three branches — a work-hardening branch, an equilibrium branch, and a recovery branch — and is written in that order as:

$$F = \begin{cases} \exp\left[\Delta\left(1 - \dfrac{\zeta}{\epsilon_t^f}\right)^2\right] & \zeta < \epsilon_t^f \\ 1 & \zeta = \epsilon_t^f \\ \exp\left[-\delta\left(1 - \dfrac{\zeta}{\epsilon_t^f}\right)^2\right] & \zeta > \epsilon_t^f \end{cases} \qquad (2\text{-}24)$$

Δ and δ are the work-hardening and recovery parameters, respectively, and ϵ_t^f is the transient strain rate limit. The internal variable ζ is governed by the evolution equation:

$$\dot{\zeta} = (F - 1)\,\dot{\epsilon}_s \tag{2-27}$$

and the transient strain limit is given by:

$$\epsilon_t^f = K_0 e^{cT} \left(\frac{\sigma_{eq}^f}{\mu} \right)^m \tag{2-28}$$

where:

T = temperature

μ = shear modulus

K_0, c, and m = material parameters.

The work-hardening parameter is defined as a function of stress:

$$\Delta = \alpha + \beta \log \left(\frac{\sigma_{eq}^f}{\mu} \right) \tag{2-28}$$

where α and β are material parameters. Because of insufficient data, the recovery parameter (δ) is taken to be a constant. However, functional forms similar to Equation 2-27 are sometimes used for recovery, viz:

$$\delta = \alpha_r + \beta_r \log \left(\frac{\sigma_{eq}^f}{\mu} \right) \tag{2-28}$$

where α_r and β_r are material parameters.

The steady-state strain rate is the sum of the three individual strain rate mechanisms acting together:

$$\dot{\epsilon}_s = \sum_{i=1}^{3} \dot{\epsilon}_{s_i} \tag{2-29}$$

The three contributing mechanisms — dislocation climb, an undefined mechanism, and slip — are written respectively as:

$$\dot{\epsilon}_{s_1} = A_1 \left(\frac{\sigma_{eq}^f}{\mu} \right)^{n_1} \exp\left(-\frac{Q_1}{RT} \right) \tag{2-30}$$

$$\dot{\epsilon}_{s_2} = A_2 \left(\frac{\sigma_{eq}^f}{\mu} \right)^{n_2} \exp\left(-\frac{Q_2}{RT} \right) \tag{2-31}$$

$$\dot{\epsilon}_{s_3} = \left(B_1 e^{-Q_1/RT} + B_2 e^{-Q_2/RT} \right) \sinh\left[q \left(\frac{\sigma_{eq}^f - \sigma_0}{\mu} \right) \right] H\left(\sigma_{eq}^f - \sigma_0 \right) \tag{2-32}$$

where:

μ = shear modulus

q = activation volume

A_1, A_2, B_1, B_2, n_1, n_2, Q_1, Q_2, and σ_0 = experimental constants

R = universal gas constant

$H(.)$ = Heaviside step function.

2.3.4 Equivalent Inelastic Strain Rate Form for Pressure Solutioning

Spiers and Brzesowsky (1993) presented a grain boundary diffusional pressure solution model for wet crushed salt as:

$$\dot{\epsilon}_v^c = A V_m \frac{\exp\left(-\frac{Q_s}{RT}\right)}{T} \left(\frac{\sigma_m - P}{d^p}\right) \left(\frac{\left(1 + \epsilon_v\right)^{r_3}}{\left|\epsilon_v\right|^{r_4}}\right) \Gamma \tag{2-33}$$

where A, V_m, Q_s, r_3, and r_4 are material constants; T is absolute temperature; R is the universal gas constant; d is the grain size; and P is the pore pressure. The model consists of two functional forms, one for small strain and one for large strain, which are invoked depending on the prescribed value for Γ given as:

$$\Gamma = \begin{cases} 1 & \text{small strain } \left(\epsilon_v > -15\%\right) \\ \left[\dfrac{\epsilon_v + \phi_0}{\phi_0\left(\epsilon_v + 1\right)}\right]^{n_s} & \text{large strain } \left(\epsilon_v < -15\%\right) \end{cases} \tag{2-34}$$

where ϕ_0 is the initial porosity and n_s is a material parameter. Spiers and Brzesowsky (1993) developed the function Γ to account for increasing surface contact (increasing area and decreasing stress) as the strains become large. This geometrically interpreted variable serves to decrease the magnitude of the driving force.

The Spiers and Brzesowsky model is used to represent the equivalent inelastic strain rate form for pressure solutioning with modifications. The functional form given in Equation 2-33 is modified by changing the stress-dependent term (using the equivalent stress measure defined in Equation 2-3) and adding the effect of moisture (w is the moisture fraction by weight). The moisture function (simply w raised to a power, a) eliminates any strain rate contribution to the crushed-salt consolidation model when moisture content is zero. In addition, the pore pressure dependency (parameter P in Equation 2-33) has been dropped from the model because insufficient test data are available to include pore pressure as a state variable. With these modifications, the modified Spiers model used to define the kinetic equation becomes:

$$\dot{\epsilon}_{eq}^w = \frac{r_1 w^a}{d^p} \frac{e^{-\frac{Q_s}{RT}}}{T} \left(\frac{\left(1 + \epsilon_v\right)^{r_3}}{\left|\epsilon_v\right|^{r_4}}\right) \Gamma \sigma_{eq}^f \tag{2-35}$$

Notice that material constants A and V_m appearing in Equation 2-33 have been combined into one parameter, r_1, in Equation 2-35 and defined as:

$$r_1 = AV_m = \text{material constant} \left[\frac{\text{m}^p \cdot K}{\text{MPa} \cdot \text{s}}\right] \tag{2-36}$$

A problem is evident in the Spiers model at time zero. Equation 2-35 can be indeterminate because when $\sigma_{eq}^f = 0$ the initial volumetric strain is zero. To eliminate this problem during computations, some initial value must be assumed for the volumetric strain. Typically this initial strain value will be computed based on an original fractional density of 0.64 (random dense packing of spherical particles) and the fractional density at the beginning of creep consolidation. The modified Spiers model has seven material constants – a, p, Q_s, r_1, r_3, r_4, and n_s, excluding those that appear in the effective stress measure.

2.4 Summary of the Crushed-Salt Consolidation Model

The equation describing the combined crushed-salt constitutive model, which includes dislocation creep and pressure solutioning, is summarized in this section. The final equation for the total creep consolidation strain rate constitutive model for crushed salt is obtained by substituting Equations 2-23 and 2-35 into Equation 2-15:

$$\dot{\epsilon}_{ij}^c = \frac{1}{\sigma_{eq}}\left\{\frac{r_1 w^a}{d^p}\frac{e^{-\frac{Q_s}{RT}}}{T}\left(\frac{(1+\epsilon_v)^{r_3}}{|\epsilon_v|^{r_4}}\right)\Gamma\,\sigma_{eq}^f + F\,\dot{\epsilon}_s\right\}\times$$

$$\left\{\frac{\kappa_0\Omega^{\kappa_1}\sigma_m}{3}\delta_{ij} + \kappa_2\left(\frac{2-D}{D}\right)^{\frac{2n}{n+1}}\left(2\cos\psi\sqrt{J_2}\right)\left(\left[\frac{\cos 2\psi}{\cos 3\psi}\right]\frac{s_{ij}}{\sqrt{J_2}} + \left[\frac{\sqrt{3}\sin\psi}{J_2\cos 3\psi}\right]t_{ij}\right)\right\} \tag{2-37}$$

As the material approaches full consolidation, the fractional density approaches 1 and the M-D model creep component becomes the same as that for intact salt. Simultaneously the pressure solutioning portion of the model diminishes as the material approaches full consolidation. This decrease is implemented through the geometric Γ function, which becomes zero at full consolidation. Thus, at complete consolidation (i.e., $D = 1$), Equation 2-37 may be written as:

$$\dot{\epsilon}_{ij}^{c} = \sqrt{\kappa_2}\, F\, \dot{\epsilon}_s \left(\left[\frac{\cos 2\psi}{\cos 3\psi} \right] \frac{s_{ij}}{\sqrt{J_2}} + \left[\frac{\sqrt{3}\sin\psi}{J_2 \cos 3\psi} \right] t_{ij} \right) \tag{2-38}$$

which is identical to the M-D model for intact salt, provided $\kappa_2 = 1$. This condition is easily met by modifying κ_0 appropriately. Substitution of α and β given in Equation 2-17 into Equation 2-20 gives:

$$\mathbf{R} = \frac{\dfrac{\kappa_0 \Omega^{\kappa_1} \sigma_m}{3} + \dfrac{\kappa_2}{2} \left[\dfrac{2 - D}{D} \right]^{\frac{2n}{n+1}} \sqrt{3 J_2}}{\dfrac{\kappa_0 \Omega^{\kappa_1} \sigma_m}{3} - \kappa_2 \left[\dfrac{2 - D}{D} \right]^{\frac{2n}{n+1}} \sqrt{3 J_2}} \tag{2-39}$$

Dividing the numerator and denominator in Equation 2-39 by κ_2 gives:

$$\mathbf{R} = \frac{\dfrac{\kappa_0 \Omega^{\kappa_1} \sigma_m}{\kappa_2 3} + \dfrac{1}{2} \left[\dfrac{2 - D}{D} \right]^{\frac{2n}{n+1}} \sqrt{3 J_2}}{\dfrac{\kappa_0 \Omega^{\kappa_1} \sigma_m}{\kappa_2 3} - \left[\dfrac{2 - D}{D} \right]^{\frac{2n}{n+1}} \sqrt{3 J_2}} \tag{2-40}$$

Thus, if κ_0 is scaled by κ_2 and κ_2 is set equal to one, the appropriate strain rate ratio is maintained and the M-D model is produced exactly when $D = 1$. Therefore the described model provides a smooth transition from crushed salt to intact salt behavior.

3.0 EXPERIMENTAL DATABASE

A database of crushed-salt consolidation laboratory test results was assembled, analyzed, and reported in previous work (Callahan et al., 1995; 1996). This previous work started the process of formulating the functional form of a constitutive model for crushed salt and assembled existing test data into a database to obtain quantitative estimates for the material parameters appearing in the model. The assembled database consists of a collection of tests conducted for a variety of reasons. Thus the database contains biases and shortcomings when viewed strictly from the standpoint of developing constitutive models. The crushed-salt constitutive model has deviatoric and mean stress components that drive the strain response, and the database has shear and hydrostatic consolidation test results used for evaluating the parameters within those respective stress components. When circumstances allow, additional tests are conducted to fill gaps in the database. Two additional shear consolidation tests (RE/SPEC Inc. [1996] and Callahan et al. [1996]) were conducted and added to the database during our most recent work. These two tests represent the first tests with high initial fractional densities (near 0.8) that emulate intact salt behavior accompanied by volumetric consolidation. Associated with the current study, additional laboratory work was conducted to add test data to the shear consolidation portion of the extant database because that portion of the database was relatively sparse, particularly in the higher initial fractional density range expected at the WIPP. The remainder of this chapter is divided into two sections: the first summarizes the status of the database, and the second presents details on the four shear consolidation tests that were performed as part of the current effort.

3.1 Summary of Existing Test Data

The creation of the database being used for parameter estimation began with an extensive library search and compilation of potentially useful test results (Pfeifle, 1995). That compilation was reviewed to document those tests deemed inappropriate for parameter estimation, and the surviving tests formed the database for parameter estimation work (Callahan et al., 1995). Two subsequent shear consolidation tests were added to the database for recent parameter estimation work (Callahan et al., 1996). That database was constructed from two types of tests: hydrostatic consolidation and shear consolidation. The two parts of the database are shown separately here in Tables 3-1 and 3-2, which summarize the tests for the hydrostatic and shear consolidation groupings, respectively.

Table 3-1. Summary of Hydrostatic Test Conditions

Test I.D.	Test Type	Seq. No.	T (K)	σ_1 (MPa)	σ_3 (MPa)	Mean Grain Size (mm)	Added Water (%)	Test Duration (days)	ρ_0 (kg/m^3)	ρ_1 (kg/m^3)	ρ_f (kg/m^3)
CS1	1	1	298	-1.72	-172	2.30	0	4.0	1,430	1,490	1,548
CS2	1	2	298	-1.72	-1.72	1.36	0	4.3	1,480	1,570	1,720
CS3	1	3	298	-1.72	-1.72	0.77	0	4.0	1,410	1,480	1,552
CS4	1	4	298	-1.72	-1.72	0.42	0	4.0	1,290	1,400	1,485
CS5	1	5	298	-1.72	-1.72	2.30	4.44	3.8	1,360	1,440	1,697
CS6	1	6	298	-1.72	-1.72	1.36	4.28	4.0	1,440	1,500	1,775
CS7	1	7	298	-1.72	-1.72	0.77	4.57	4.3	1,420	1,470	1,572
CS8	1	8	298	-1.72	-1.72	0.42	4.61	4.0	1,400	1,430	1,822
CS9	1	9	298	-1.72	-1.72	2.30	0	37.0	1,480	1,530	1,759
CS10	1	10	298	-3.45	-3.45	2.30	0	34.2	1,470	1,570	1,648
HC1A	1	11	298	-1.72	-1.72	1.56	Sat	28.8	1,462	1,539	1,921
HC2A	1	12	298	-1.72	-1.72	1.56	Sat	98.7	1,388	1,574	2,026
HC3A	1	13	298	-3.45	-3.45	1.56	Sat	49.9	1,448	1,550	2,042
HC4A	1	14	298	-3.45	-3.45	1.56	Sat	110.8	1,409	1,610	2,065
HC5A	1	15	298	-6.90	-6.90	1.56	Sat	53.0	1,496	1,741	2,124
HC6A	1	16	298	-6.90	-6.90	1.56	Sat	77.9	1,395	1,721	2,125
27JUL82	1	1	294	-1.72	-1.72	2.5	0	2.7	1,273	1,390	1,440
04MAY82	1	2	313	-1.72	-1.72	2.5	0	2.8	1,396	1,563	1,621
30APR82	1	3	333	-1.72	-1.72	2.5	0	3.0	1,448	1,605	1,677
07MAY82	1	4	353	-1.72	-1.72	2.5	0	2.9	1,240	1,415	1,492
12MAY82	1	5	373	-1.72	-1.72	2.5	0	4.8	1,371	1,621	1,738
05FEB82	1	6	294	-3.44	-3.44	2.5	0	3.4	1,263	1,432	1,466
09APR82	1	7	313	-3.44	-3.44	2.5	0	3.0	1,330	1,495	1,561
26MAR82	1	8	333	-3.44	-3.44	2.5	0	3.9	1,242	1,393	1,451
02APR82	1	9	353	-3.44	-3.44	2.5	0	2.7	1,249	1,428	1,501
13APR82	1	10	373	-3.44	-3.44	2.5	0	2.8	1,240	1,424	1,522
29JAN82	1	11	294	-6.70	-6.70	2.5	0	3.2	1,279	1,506	1,557
26FEB82	1	12	294	-10.1	-10.1	2.5	0	3.1	1,256	1,538	1,601
27JU61	1	1	293	-0 69	-0.69	1.75	2.5	31.8	1,440	1,493	1,732
23JL51	1	2	293	-1.72	-1.72	1.75	0.5	19.7	1,498	1,593	1,827
14NV51	1	3	293	-1.72	-1.72	1.75	1.5	24.1	1,477	1,571	1,860
25FE61	1	4	293	-1.72	-1.72	1.75	2.0	36.6	1,455	1,548	1,853
10MY51	1	5	293	-1.72	-1.72	1.75	2.4	28.9	1,412	1,601	1,890
20AU51	1	6	293	-1.72	-1.72	1.75	3.0	20.0	1,348	1,516	1,821
16 JL51	1	7	293	-3.44	-3.44	1.75	0.5	20.6	1,391	1,608	1,920
18JU51	1	8	293	-3.44	-3.44	1.75	1.0	21.6	1,455	1,668	1,930
30OC51	1	9	293	-3.44	-3.44	1.75	1.5	13.8	1,477	1,648	1,930
16JA61	1	10	293	-3.44	-3.44	1.75	2.0	27.9	1,489	1,640	1,950
19DC44	1	11	293	-3.44	-3.44	1.75	2.4	52.1	1,434	1,566	1,899
13AU51	1	12	293	-3.44	-3.44	1.75	3.0	21.7	1,370	1,586	1,899

Table 3-2. Summary of Shear Consolidation Test Conditions

Test I.D.	Test Type	Seq. No.	T (K)	σ_1 (MPa)	σ_3 (MPa)	Mean Grain Size (mm)	Added Water (%)	Test Duration (days)	ρ_0 (kg/m^3)	ρ_1 (kg/m^3)	ρ_f (kg/m^3)
SC1B	2	1	298	-3.45	-4.14	1.56	2.34	62.9	1,449	1,574	2,009
SC2A	2	2	298	-3.45	-4.83	1.56	2.25	61.9	1,479	1,608	2,014
SC3A	2	3	298	-3.45	-5.52	1.56	2.21	61.7	1,448	1,575	2,005
SC4A	2	4	298	-6.90	-7.59	1.56	2.27	60.9	1,428	1,607	2,007
SC5A	2	5	298	-6.90	-8.97	1.56	2.52	61.4	1,522	1,764	2,135
SC6A	2	6	298	-6.90	-10.34	1.56	2.19	67.9	1,375	1,701	2,053
SC7A	2	7	298	-5.17	-6.55	1.56	2.33	66.0	1,455	1,665	2,091
SC8A	2	8	298	-5.17	-7.93	1.56	2.29	60.8	1,423	1,611	2,000
SC9B	2	9	298	-5.17	-9.31	1.56	2.33	60.9	1,415	1,683	2,080
SC10	2	10	298	-1.00	-6.00	1.56	0	28.1	1,531	1,808	1,819
SC11	2	11	298	-1.00	-6.00	1.56	0	17.0	1,483	1,688	1,724
120C891	2	1	293	-3.26	-3.70	2.00	2.40	33.8	1,284	1,516	1,805
RS/DCCS/1	2	1	298	-1.00	-5.00	0.5[a]	1.66	6.2	1,953	2,000	2,035
RS/DCCS/3	2	2	298	-2.00	-6.00	0.5[a]	1.63	37.1	1,954	1,964	2,087
RS/DCCS/4	2	3	298	-3.00	-7.00	0.5[a]	1.59	57.0	1,953	2,011	2,139
RS/DCCS/5	2	4	298	-4.00	-8.00	0.5[a]	1.55	59.1	1,939	1,953	2,093

(a) Grain size was assumed to be 0.5 because dynamic compacted reduces grain sizes.

Table 3-1 lists the 40 tests contained in the hydrostatic consolidation portion of the database. All the testing was performed in a drained condition; i.e., the pore pressure was zero. The database discussed by Callahan et al. (1995) contained 45 tests. Five of the hydrostatic consolidation tests were eliminated from the database as recommended by Callahan et al. (1995). These tests were performed under saturated conditions and were not very well drained, which resulted in the generation of pore pressures with reduced deformation. The maximum and minimum principal stresses are listed under the columns titled σ_1 and σ_3. The principal stresses are equal for the hydrostatic case, but the formatting of the table has been maintained for both types of tests. The initial dry density of the specimens, the density at the beginning of the consolidation stage, and the final density at the end of the test are given under the respective column headings titled ρ_o, ρ_i, and ρ_f.

Table 3-2 lists the shear consolidation tests in the database and is formatted like Table 3-1. The table contains the twelve tests that were used in previous work and another four tests that are part of the current work, which is reported in the next section. As with the hydrostatic consolidation tests, all the shear consolidation tests were performed in a drained condition.

The tests listed in Tables 3-1 and 3-2 comprise the entire database used for parameter estimation in Chapter 4. The original data files often contained thousands of data points and were of impractical size for regression analysis. Each data file was reduced in size to create representative data sets containing only 100 data points, with the first and last data points always being retained and the remaining data points uniformly sampled. This sampling technique is the same as was used in previous work.

3.2 Description of Recent Shear Consolidation Tests

Four shear consolidation creep tests were performed on dynamically compacted crushed-salt specimens that were fabricated with a laboratory scale device following a procedure similar to that used for dynamic compaction of large-scale samples (Hansen and Ahrens, 1996). This device served as a simulant of the compaction technique envisioned for the shaft sealing design. The laboratory scale device used two Proctor split compaction molds to receive the disaggregated salt. After compaction, the molds were removed and the ends of the cylindrical samples were machined to produce testable specimens with nominal dimensions of 100 millimeters in diameter and 200 millimeters in length. The starting material was wetted with a brine, so the specimen moisture content was nominally 1.6 percent by weight. The dry density of the specimens was about 1,985 kg/m^3, which is a fractional density of approximately 0.9 (assuming intact salt density of 2,160 kg/m^3). The energy input to create this density was approximately 2.6 times the modified Proctor energy. The specimens fabricated with the laboratory scale device were identified with the unique labels, RS/DCCS/*n*, where *n* took on values of 1, 2, 3, etc. to designate individual specimens.

The four shear consolidation tests were effectively standard triaxial compression creep tests ($\psi = \pi/6$), and typical test procedures have been described previously (Callahan et al., 1995; Brodsky, 1994). The specimens were initially loaded hydrostatically to the level of specified confining pressure (radial stress) and allowed to stabilize. The specified confining pressure levels for the four tests were –1, –2, –3, and –4 MPa, respectively. Data were collected during the hydrostatic loading phase. Following stabilization, the axial compressive stress for each test was increased by 4 MPa while holding the confining pressure constant so that each of the four specimens was subjected to a stress difference of $\Delta\sigma = 4$ MPa; only the confining pressure was different among tests. Data were also acquired when the axial stress difference was applied. After the axial stress difference was imposed, it was held constant at $\Delta\sigma = 4$ MPa while data were acquired during the shear consolidation creep phase. The test matrix for the shear consolidation creep tests is shown in Table 3-3, where the first column contains the specimen identification and the following three columns give the axial stress, lateral stress, and

temperature, respectively. All four tests were performed in a drained condition; i.e., the pore pressure was zero.

Table 3-3. Shear Consolidated Creep Test Matrix

Specimen Identification	Test Conditions		
	Axial Stress (MPa)	Lateral Stress (MPa)	Temperature (°C)
RS/DCCS/1	-5	-1	25
RS/DCCS/3	-6	-2	25
RS/DCCS/4	-7	-3	25
RS/DCCS/5	-8	-4	25

Analyses based on the constitutive model predicted that a stress state existed wherein the lateral strain rate would initially be negative (compaction) and then reverse direction and become positive as the specimen density increased. As seen in Table 3-3, the scheme for finding this stress state was to change the mean stress by testing at different confining pressures while holding the axial stress difference constant. The creep strain results from the four tests are compared in Figure 3-1, which plots axial and lateral creep strains as a function of time. A significant observation apparent in Figure 3-1 is the trend appearing in the lateral strain response; that is, the magnitude of the lateral strain rate decreases as the confining pressure (mean stress) increases. A very significant phenomenon was observed in the test performed at a confining pressure of –4 MPa. The lateral strain rate in that test was initially negative (specimen diameter decreasing); after some densification of the specimen, the lateral strain rate decreased and ultimately changed sign and became positive (specimen diameter increasing). This observation is important to the work presented in Chapter 4, where the parameters of the crushed-salt constitutive model are determined.

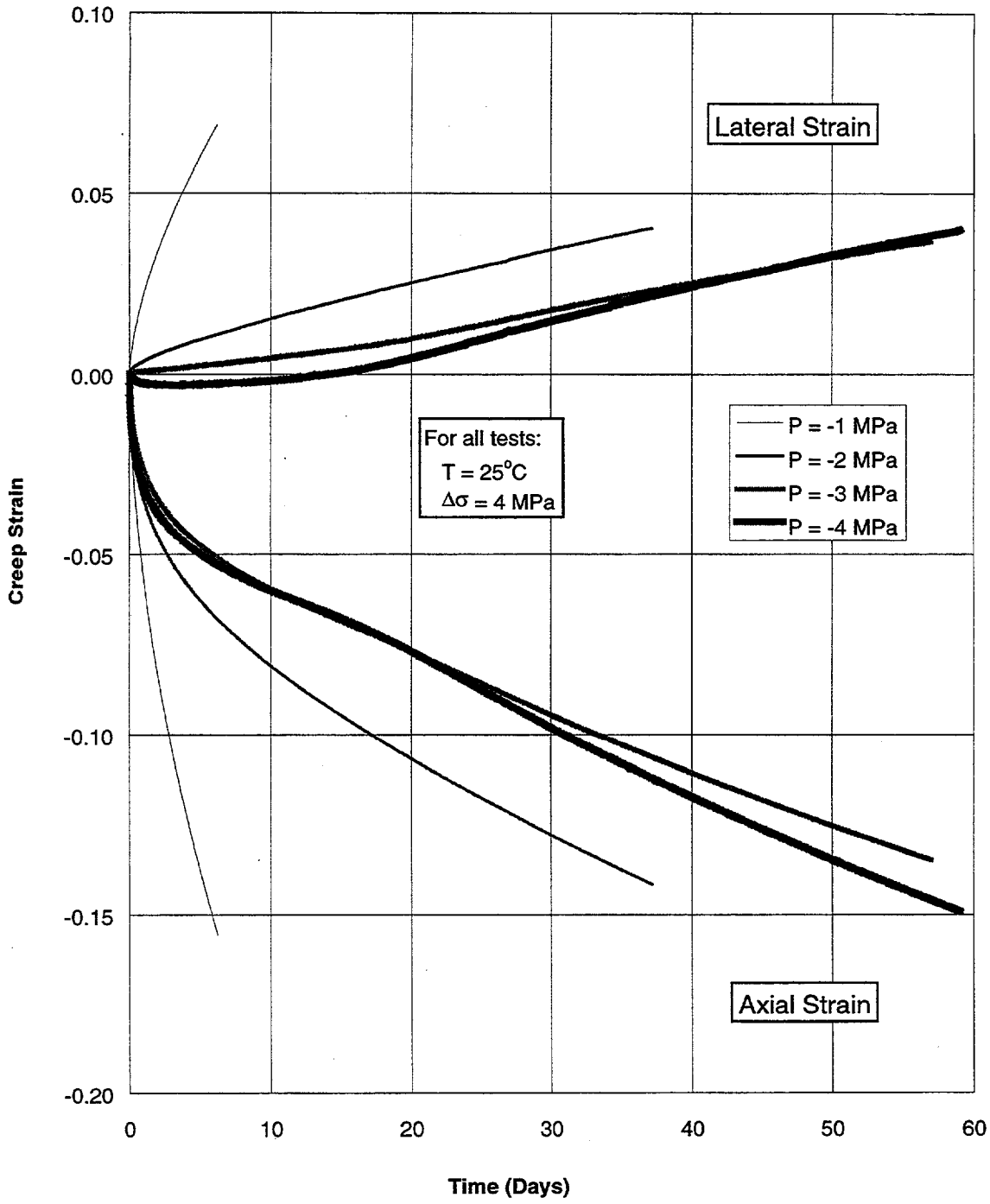

Figure 3-1. Axial and lateral strain as a function of time for four shear consolidation creep tests on dynamically compacted crushed salt.

4.0 MODEL FITTING

4.1 Introduction

The crushed-salt (C-S) constitutive model given in Equation 2-37 contains 33 material parameters. Seventeen of these parameters are contained in the dislocation creep (M-D) portion of the model. The M-D model parameters were fixed at the values provided by Munson et al. (1989) for clean salt. The remaining 16 material parameters consist of 5 flow potential material parameters and 11 creep consolidation parameters. These parameters were determined by fitting the equations that define the C-S constitutive model to the laboratory data such that the weighted squared difference between the measured and calculated response was minimized. First, the flow potential parameters (κ_0, κ_1, κ_2, n, and D_t) were determined by fitting Equation 2-20 (which defines the lateral-to-axial strain rate ratio) to the data measured in the 16 shear consolidation tests. Second, these flow rate parameters were fixed and the 11 creep consolidation parameters (η_0, η_1, η_2, n_f, a, p, n_s, r_1, r_3, r_4, and Q_s/R) were determined by fitting the rate equations that define the axial and lateral strains to the data measured in the 16 shear consolidation and 40 hydrostatic consolidation tests. These nonlinear regressions were performed using the personal-computer platform BioMedical Data Processing (BMDP, Version 7.01) statistical software package (Frane et al., 1985).

4.2 Modeling Procedure

The *object function* is the mathematical function that is to be minimized in the least-squares sense. For example, when performing a least-squares fit of some data to a straight line, the object function is the squared difference between the measured response (the data) and the predicted response from the equation for the straight line. The equation for the straight line when performing linear regression is called the *response model.*

The object function is evaluated at discrete points; these are the points where data have been taken or are available. Some of the measurements may be more important than others and should hold more importance or "weight" than other data points. Mathematically, the relative importance of the level of fit to each data point is accommodated through a *weighting function.*

Application of least squares results in an estimation of the parameters of the response model. In the example cited above, application of least squares will result in the estimation of the two parameters necessary to specify a straight line under the implicit assumption that the measurements will be distributed in the response model for fixed values of the (hopefully)

independent parameters. For complex nonlinear models, the independence of the parameters is not always obvious before fitting. The parameters from the least squares fit to a nonlinear model may not be appropriate if the parameters are highly correlated.

The response model will almost never reproduce all the measurements exactly. The difference between the measured data points and the predicted model response is termed the *residual*. When a weighting function is used in the model fitting, the weighted residual is also of interest. The weighted residual is the usual residual multiplied by the weighting function value for the specific observation or data point.

The object function reflects the relative importance attributed to individual data points and was developed under the following assumptions:

1. Within a given test, there are an equal number of measurement points (100). Each data point was assumed to have equal weight.
2. Within each test, the data are not uniformly distributed with respect to time; the data are denser early in time when the strain rates are highest. Thus the weight function that was used in the model fitting reflects the time step size relative to each data point in each test, such that higher weights are assigned to data points at the end of the test than are assigned to early-time data points.
3. Tests of longer duration were assumed to be more important than tests of shorter duration.
4. Residuals were normalized. They are represented as percent deviations from the measured data. Thus a 10 percent deviation from a very small strain results in the same error in the object function as a 10 percent deviation from a very large strain.

4.2.1 Response Functions

In the shear consolidation tests, there are two independent measurements (superscript m is used to indicate measurements): the volumetric strain $\left(\epsilon_v^m\right)$ and the axial strain $\left(\epsilon_a^m\right)$. The lateral strain $\left(\epsilon_l^m\right)$ was calculated as:

$$\epsilon_l^m = \frac{\epsilon_v^m - \epsilon_a^m}{2} \tag{4-1}$$

The axial strain rate $\left(\dot{\epsilon}_a^m\right)$ was calculated from the measurement of axial strain and elapsed time as follows. At every data point in the original test data file (some contained thousands of

data points), the axial strain rate was calculated as the linear least-square fit to a small interval of data (window) centered on the point in time. The window was then shifted by one data point to the next point in time and the linear fit was repeated. This process was repeated until a point was reached where the width of the window reached the end of the data file for each test. A 50-point window was used in this process. The lateral strain rate $\left(\dot{\epsilon}_l^m\right)$ was calculated in a similar fashion. The measured lateral-to-axial strain rate ratio ($\mathbf{R}^m$) is defined as:

$$\mathbf{R}^m = \frac{\dot{\epsilon}_l^m}{\dot{\epsilon}_a^m} \tag{4-2}$$

Following the development in Chapter 2, the response function used to determine the flow potential parameters is:

$$\mathbf{R}^p = \frac{\alpha + \frac{\beta}{2}}{\alpha - \beta} \tag{4-3}$$

where:

$\mathbf{R}^p$ = predicted lateral-to-axial strain rate ratio

$$\alpha = \frac{\kappa_0 \, \Omega^{\kappa_1} \, \sigma_m}{3}$$

$$\beta = \kappa_2 \left(\frac{2 - D}{D}\right)^{\frac{2n}{n+1}} \left(\sigma_1 - \sigma_3\right)$$

$$\Omega = \left\{\frac{\left(1 - D_v\right)n}{\left[1 - \left(1 - D_v\right)^{1/n}\right]^n}\right\}^{\frac{2}{n+1}}$$

$$D_v = \begin{cases} D_t & D \le D_t \\ D & D > D_t \end{cases}$$

D = current fractional density

σ_m = mean stress = $(\sigma_3 + 2\sigma_1)/3$

σ_3 = minimum principal stress

σ_1 = maximum principal stress

κ_0, κ_1, κ_2, n, and D_t = flow potential parameters.

Examination of Equation 4-3 reveals that two of the flow potential parameters (κ_0 and κ_2) are not independent of one another (cf., Equation 2-40). Therefore the parameter κ_2 was fixed at a value of 1.0 and the remaining four flow rate parameters were determined in the fit.

The response function (ρ) used to determine the creep consolidation parameters is:

$$\rho = 1 - \left\{\left[\left(1 - R_1\right)^2 + \left(1 - R_2\right)^2\right] wt\right\}^{1/2} \tag{4-4}$$

where:

$R_1 = \epsilon_a^p / \epsilon_a^m$

$R_2 = \epsilon_l^p / \epsilon_l^m$

$wt = \Delta t / \bar{t}$ = weighting function

Δt = time step size

$\bar{t}$ = normalizing time = 10^6(s)

ϵ_l^p = predicted lateral strain = $\int_0^t \dot{\epsilon}_l^p \, dt$

ϵ_a^p = predicted axial strain = $\int_0^t \dot{\epsilon}_a^p \, dt$

$\dot{\epsilon}_l^p$ = predicted lateral strain rate = $\left(\alpha + \beta/2\right) \dfrac{\dot{\epsilon}_{eq}}{\sigma_{eq}}$

$\dot{\epsilon}_a^p$ = predicted axial strain rate = $\left(\alpha - \beta\right) \dfrac{\dot{\epsilon}_{eq}}{\sigma_{eq}}$

$\dot{\epsilon}_{eq}$ = equivalent inelastic strain rate = $\dot{\epsilon}_{eq}^d + \dot{\epsilon}_{eq}^w$

σ_{eq} = equivalent stress measure = $\left[\kappa_0 \, \Omega^{\kappa_1} \, \sigma_m^2 + \kappa_2 \left(\dfrac{2 - D}{D}\right)^{\frac{2n}{n+1}} \left(\sigma_1 - \sigma_3\right)^2\right]^{1/2}$

$\dot{\epsilon}_{eq}^d$ = Munson-Dawson dislocation creep strain-rate model given in Equations 2-23 to 2-32

$\dot{\epsilon}_{eq}^w$ = Spiers pressure-solutioning inelastic strain-rate model given in Equations 2-34 and 2-35

η_0, η_1, η_2, n_f, a, p, n_s,
r_1, r_3, r_4, and Q_s/R = creep consolidation parameters.

The Munson-Dawson dislocation creep model has 17 parameters, which are given in Table 4-1 for clean WIPP salt.

Table 4-1. Munson-Dawson Model Parameter Values for Clean Salt (after Munson et al., 1989)

Parameter	Units	Clean Salt
A_1	yr^{-1} s^{-1}	2.645E+30 8.386E+22
A_2	yr^{-1} s^{-1}	3.050E+20 9.672E+12
Q_1/R Q_1	K cal/mol	12,581 25,000
Q_2/R Q_2	K cal/mol	5,033 10,000
n_1	—	5.5
n_2	—	5.0
B_1	yr^{-1} s^{-1}	1.919E+14 6.0856E+06
B_2	yr^{-1} s^{-1}	9.568E+05 3.034E-02
q	—	5,335
σ_0	MPa	20.57
m	—	3.0
K_0	—	6.275E+05
c	K^{-1}	9.198E-03
α	—	-17.37
β	—	-7.738
δ	—	0.58

4.2.2 Object Function

The object function is the sum-of-squared errors (SS_E). In determining the flow rate parameters, the sum-of-squared error is defined as:

$$SS_E = \sum_{i=1}^{N} \left(R_i^P - R_i^m\right)^2 \tag{4-5}$$

where:

R_i^P = predicted lateral to axial strain rate for the i^{th} data point (Equation 4-3)

R_i^m = measured lateral to axial strain rate for the i^{th} data point (Equation 4-2)

N = number of data points in test database.

In determining the creep consolidation parameters, the sum-of-squared error is defined as:

$$SS_E = \sum_{i=1}^{N} \left(1 - \rho_i\right)^2 \tag{4-6}$$

where:

ρ_i = response function defined in Equation 4-4 for the i^{th} data point.

4.3 Statistical Measures

One key aspect of the model-fitting effort is deciding if the model fit to one database is better than the fit to the other database. In this section, the statistical measures for evaluating and comparing fits to the candidate constitutive model are discussed.

4.3.1 Weighted Residual

In all types of regression, the residual squared times a weighting function is the function that is minimized, where the residual is defined as the difference between the observed and predicted functional values. The sum-of-squared error term defined in Equation 4-6 was used in evaluating the model fits to the two databases.

The specific weighting function associated with the sum-of-squared error is equal to the reciprocal of the measured axial strain squared $\left(\epsilon_a^m\right)^2$, the reciprocal of the measured lateral strain

squared $\left(\epsilon_l^m\right)^2$, the time increment (Δt), and the reciprocal of a normalizing time (10^6 *s*). Thus, if the response model (Equation 4-4) predicts zero axial strain and zero lateral strain over the duration of all tests in the database, the term SS_E in Equation 4-6 will have a value of twice the number of million seconds in the database. This is termed here the maximum value of the sum-of-squared error $\left(SS_E^{max}\right)$. The 40 hydrostatic consolidation tests constitute a total of 76.0(10^6) *s*. The 16 shear consolidation tests total 69.35(10^6) *s*. Therefore SS_E^{max} = 138.7 in the fit to the shear tests, and SS_E^{max} = 290.7 in the fit to the combined test database.

In a similar fashion, if the response model is a perfect predictor for all the tests in the database, the sum-of-squared error will be exactly zero. This is the minimum value of the sum-of-squared error.

For each model fit, the sum-of-squared error was normalized as follows:

$$0 \leq \overline{SS}_E \leq 1 \tag{4-7}$$

where:

$$\overline{SS}_E = SS_E / SS_E^{max}$$

The normalized sum-of-squared error was used in comparing the two model fits.

4.3.2 Parameter Multicollinearity

When fitting a mathematical relation to a set of laboratory-measured data, it is desirable to have enough information in the measured database to ensure that each of the parameters can be uniquely determined. Two possibilities can occur that will not allow for a unique determination of each parameter in a mathematical relation. First, the mathematical relation may inherently include parameters that are dependent on one another. For example, in the relation:

$$F = A + B \tag{4-8}$$

the parameters *A* and *B* cannot be determined uniquely.

Second, there may not be sufficient data in the database to uniquely determine the magnitude of certain model parameters. For example, there are minimal variations in grain size (*d*), moisture content (*w*), and temperature (*T*) in the shear consolidation tests ($\Delta\sigma \neq 0$). Thus, in fitting the candidate models to these tests, the parameters *p*, *a*, and Q_s/R in the term

$$\xi(d,w,T) = \frac{w^{a}}{d^{p}T} \exp\left(-Q_s/RT\right) \tag{4-9}$$

cannot be uniquely determined.

When either of the two aforementioned conditions exist, a condition of multicollinearity is said to exist (Montgomery and Peck, 1982). An examination of the parameter covariance matrix will determine the degree to which the material parameters are correlated to each other. The higher the parameter covariance, the higher the parameter collinearity. When a multicollinearity situation exists, one must (1) expand the database of measurements or (2) modify the functional form of the model.

The elements of the correlation matrix (C_{ij}) can be expressed as:

$$C_{ij} = \frac{q_{ij}}{\sqrt{q_{ii}\, q_{jj}}} \tag{4-10}$$

where:

$q_{ij} = \left[z_{ip}\, z_{pj}\right]^{-1}$

$z_{ij} = \dfrac{\partial\, \epsilon^{m}\left(x_j, \bar{p}\right)}{\partial p_i}$

$\bar{p}$ = set of parameters taken at their mean values

p_i = i^{th} parameter

x_j = j^{th} model variable

ϵ^{m} = measured response.

If the parameters are uncorrelated, then $C_{ij} = 0$. Conversely, the correlation coefficient is one if the parameters are totally correlated. The parameters are highly correlated if $C_{ij} \geq 0.90$, and a state of parameter multicollinearity may exist.

A scalar quantity, termed the parameter correlation measure (pcm), was used in this study as a global measure of the parameter correlations associated with each model's fit to each database. This measure is defined as:

$$\text{pcm} = \frac{\sum_{i=1}^{p-1}\sum_{j=p}^{i+1} C_{ij}^2}{\sum_{i=1}^{p-1} i} = \frac{2\sum_{i=1}^{p-1}\sum_{j=p}^{i+1} C_{ij}^2}{p^2 - p} \tag{4-11}$$

where p is the number of parameters in the model and $0 \leq \text{pcm} \leq 1$. The numerator in Equation 4-11 is the sum of the squares of the lower triangular components of the parameter correlation matrix (Equation 4-10), and the denominator simply normalizes the result by the number of components in the sum. Obviously, lower parameter correlations will reduce the magnitude of the parameter correlation measure. Finally, an average parameter correlation $(\bar{c})$ can be quantified as:

$$\bar{c} = \sqrt{\text{pcm}} \tag{4-12}$$

4.3.3 Parameter Variation Among Fits

The C-S constitutive model was fit to two databases: (1) the shear consolidation tests only and (2) the combination of shear and hydrostatic consolidation tests. If a specific model is truly a constitutive law in representing the consolidation of crushed salt, the material parameters in each of the different fits should be the same or nearly the same. To evaluate the parameter variation in each of the models, comparisons of the parameter values determined in the fits to the shear consolidation tests were made to the parameter values determined in the fit to the combined database. The ratio of the number of parameters that changed by more than one order of magnitude to the total number of model parameters was calculated for each of the fits to the hydrostatic and shear consolidation tests.

4.3.4 Predictive Capability

The aptness of each of the candidate models (predictive capability) can be demonstrated using the parameter values determined by fitting to the individual test databases. The material parameters determined in the fit to the shear consolidation tests were used to predict each of the hydrostatic consolidation tests. A quantitative measure of the predictive capability is simply the

sum-of-squared error (Equations 4-5 and 4-6). This measure was calculated using the BMDP Program AR (Section 4.4) by fixing the parameter values at those determined in the fit to the shear consolidation tests and fitting (predicting) the hydrostatic consolidation tests.

4.4 BMDP Statistical Software

This section describes in detail the BMDP nonlinear regression Programs 3R and AR used in the model fitting. BMDP is a statistical software package developed at the University of California at Berkeley, supported by grants from the Biotechnology Resources Branch of the National Institutes of Health and the National Science Foundation.

BMDP Program AR is a nonlinear regression program that estimates the parameters of a nonlinear function by least squares using a pseudo Gauss-Newton algorithm. The response model can be specified as a system of coupled rate equations. The response model derivatives are evaluated numerically based on the initial parameter estimates and are not updated during the regression. In addition to calculating the weighted sum-of-squared error (SS_E), the program calculates the coefficient of multiple determination (R_p^2), the residual mean-squared error (MS_E), and the coefficients of the parameter correlation matrix (C_{ij}). The various program features and supporting documentation of AR are provided in various BMDP technical reports, including Frane et al. (1985). Program AR was used in determining the creep consolidation parameters.

BMDP Program 3R is identical to AR with the following exceptions: (1) the model function cannot be expressed as a system of coupled rate equations and (2) the response model derivatives are updated continuously during the regression. Program 3R was used in determining the flow potential parameters.

The input files required to execute an AR or 3R analysis are described in detail by Dixon et al. (1985) and in the BMDP Users' Digest (Hill, 1984). Basically the input files can be thought of as a series of paragraphs that are further subdivided into sentences using keywords. Each paragraph is activated by a slash (/) followed immediately by a keyword. Each of these sentences are activated by keywords and ended with periods. All comment cards are noted using the pound symbol (#). The BMDP input files for the model fits are given in Appendix A.

The BMDP input files are composed of 12 paragraphs. The first paragraph (/INPUT) contains the title card, the database file name, the format to be used in reading the data, and the number of variables in the database. The second paragraph (/VARIABLES) names each of the 18 variables contained in the database file. The third paragraph (/TRANS) identifies the defined

variables (or functions of variables) that are specific to the response model. Specifically, MS and DS are the mean stress and stress difference, respectively. Similarly, D0 and DI are the emplaced and initial fractional density, respectively. The variable USE identifies which test database is to be used in the fit, and the variable WT is the weight function. The fourth paragraph (/REGRESS) identifies the dependent variable (DEPEND), the number of parameters in the model, the weight function variable (WEIGHT), the integration variable (ITIME) in the rate equations, the number of differential equations (NEQN), the number of iterations (ITER), the number of interval halvings for each iteration (HALVINGS), and the maximum number of integration steps (MAXC). The fifth paragraph (/PARAMETER) identifies the parameter names and the initial estimates, as well as the maximum and minimum values for each of the parameters. The sixth paragraph (/DIFIN) identifies the initial values for each of the dependent variables in the rate equations (Z(i),i=1,NEQN). The seventh paragraph (/DIFEQ) specifies the functional form of the rate equations (DZ(i), i=1,NEQN). The eighth paragraph (/FUN) identifies the dependent variable (response) function (F). The ninth through eleventh paragraphs (/SAVE, /PRINT, and /PLOT) specify output options for the program. The last paragraph (/END) identifies the end of the input file.

4.5 Results

In this section the results of the model fits are presented and discussed in terms of the model parameters and the statistical measures defined in Section 4.3.

The C-S constitutive model contains a total of 16 parameters. Five of these parameters are termed the flow potential parameters (κ_0, κ_1, κ_2, n, and D_t). These parameters were determined by fitting the C-S constitutive model to the lateral-to-axial strain rate ratios measured in the 16 shear consolidation tests. The remaining 11 parameters in the C-S constitutive model are termed the creep consolidation parameters (η_0, η_1, η_2, n_f, a_1, p, n_s, r_1, r_3, r_4, and Q_s/R). Two sets of creep consolidation parameters were determined: one set each resulting from fits to a database composed of 16 shear consolidation tests and to a combined database composed of the 16 shear and 40 hydrostatic consolidation tests. The parameters were determined by fitting the C-S constitutive model to the axial and lateral strains measured in each of the tests. The parameters η_0, η_1, η_2, and n_f define the stress measure σ_{eq}^{f}. Moisture dependence, grain-size dependence, and temperature dependence are defined by the parameters a, p, and Q_s/R, respectively. The remaining parameters (r_1, r_3, and r_4) are for the Spiers pressure-solutioning model (Equation 2-35). In both fits, the parameter η_2 was fixed at unity, ensuring that the C-S constitutive model smoothly transitions into the M-D dislocation creep model at a fractional density of 1.0, according to Equation 2-8.

4.5.1 Flow Potential Parameters

The flow potential parameters are given in Table 4-2. Plots of the predicted and measured lateral-to-axial strain rate ratios as a function of density for each of the 16 shear consolidation tests are given in Appendix B.

Table 4-2. Flow Potential Parameters

Parameter	Magnitude	Units
K_0	0.095	—
K_1	1.412	—
K_2	1.000	—
n	7.578	—
D_t	0.891	—

4.5.2 Creep Consolidation Parameters

The creep consolidation parameters for each of the two model fits are given in Table 4-3. Plots of the predicted and measured lateral and axial strains for each of the 16 shear consolidation tests and 40 hydrostatic consolidation tests are given in Appendix C.

4.6 Statistical Measures

4.6.1 Sum-of-Squared Error

The sum-of-squared error (SS_E) was calculated using Equation 4-5 for each of the model fits to the shear test database and the combined test database. Using these results and Equation 4-7, the normalized sum-of-squared error $\left(\overline{SS}_E\right)$ was calculated for each of the model fits. The results are given in Table 4-4.

Table 4-3. Creep Consolidation Parameters

Parameter	Units	Shear Tests	Combined Tests
η_0	—	0.1319	$2.581(10^{-2})$
η_1	—	3.9387	2.587
η_2	—	1.000	1.00
n_f	—	3.5122	4.792
a	—	0.3179	0.0230
p	—	1.6366	1.099
n_s	—	0.1209	0.0
r_1	m^p•k(MPa•s)	$3.58(10^{-4})$	$5.53(10^{-4})$
r_3	—	6.7325	11.12
r_4	—	0.0	0.6003
Q_s/R	K	1074.5	811.28

Table 4-4. Sum-of-Squared Error, SS_E

Test Database	SS_E	$\overline{SS}_E$
Shear	10.41	0.075
Combined	37.9	0.130

These results indicate that the model fit to the shear test database is qualitatively better than the fit to the combined tests (i.e., 7 percent relative error in comparison to 13 percent relative error).

4.6.2 Parameter Multicollinearity

The parameter correlation coefficient matrices for each of the two model fits are given in Tables 4-5 and 4-6. High parameter correlations (>0.90) are indicative of possible parameter multicollinearity. As noted in Section 4.3.2, high parameter correlations are indicative of either (1) deficiencies in the functional form of the C-S constitutive model or (2) deficiencies (or gaps) in the test database.

Table 4-5. Parameter Correlation Coefficient Matrix—Model Fit to Shear Consolidation Tests

	n_t	η_0	η_1	a	p	n_s	r_1	r_s	r_4	Q_s/R
n_t	1.0									
η_0	0	1.0								
η_1	-1.0	0	1.0							
a	0	0.1161	0	1.0						
p	0	0.2081	0	0.8733	1.0					
n_s	0	-0.0359	0	-0.3507	-0.3923	1.0				
r_1	0	-0.1910	0	-0.9088	-0.9716	0.3375	1.0			
r_3	0	-0.0165	0	0.1381	0.3908	-0.6131	-0.3347	1.0		
r_4	0	-0.1392	0	-0.9858	-0.8583	0.4379	0.8655	-0.1531	1.0	
Q_s/R	0	0.0143	0	-0.1111	-0.3849	0.5813	0.3144	0.9955	0.1276	1.0

Table 4-6. Parameter Correlation Coefficient Matrix—Model Fit to Combined Test Database

	n_t	η_0	η_1	a	p	n_s	r_1	r_s	r_4	Q_s/R
n_t	1.0									
η_0	-0.6128	1.0								
η_1	-0.9603	0.4052	1.0							
a	0.1552	-0.2347	-0.1098	1.0						
p	0.1547	0.0350	-0.1722	0.0654	1.0					
n_s	-0.0363	0.1291	0.0016	0.5740	0.4327	1.0				
r_1	-0.2663	0.1258	0.2754	0.1462	-0.3891	0.0097	1.0			
r_3	0.2624	-0.1480	-0.2551	-0.0825	0.4067	0.0097	0.0881	1.0		
r_4	0.0305	0.0281	-0.0443	-0.2723	0.1707	-0.0894	-0.9394	-0.2828	1.0	
Q_s/R	-0.2654	0.1436	0.2590	0.0747	-0.4851	-0.0878	-0.1369	-0.9816	0.3348	1.0

In general, most of the parameter correlations are low (<0.90) for both fits. However, four sets of parameters in the fit to the shear test database ($n_f - \eta_1$, $a_1 - r_4$, $p - r_1$, and $r_3 - Q_s/R$) and three sets of parameters in the fit to the combined test database ($n_f - \eta_1$, $r_1 - r_4$, and $r_3 - Q_s/R$) have correlation coefficients greater than 0.90.

The parameter correlation measure (pcm) and the average correlation coefficient $(\bar{c})$ were evaluated using Equations 4-11 and 4-12, respectively. The results are given in Table 4-7 for each of the model fits.

Table 4-7. Parameter Correlation Measure

Test Database	pcm	$\bar{c}$
Shear	0.200	0.447
Combined	0.120	0.346

The results in Table 4-7 indicate that the parameters are slightly less correlated in the fit to the combined test database. However, the average correlation coefficient is less than 0.5 in both fits, which indicates that the possibility of parameter multicollinearity is low.

4.6.3 Parameter Variation Among Fits

A quantitative measure of the parameter variation between the C-S constitutive model fits to the two databases was defined in Section 4.3.5. The measure simply indicates the percentage change in each of the parameter values in the fit to the combined test database as compared to the parameter value determined in the model fit to the shear consolidation tests. The variation in parameter values in the fit to the combined test database is given in Table 4-8. As can be seen in this table, no parameters varied by more than one order of magnitude (i.e., parameter variation >10). Qualitatively the parameters did not change appreciably overall in the two model fits.

4.6.4 Predictive Capability

The predictive capability of the C-S constitutive model is measured qualitatively by how successfully the model fits to the shear consolidation tests predict the hydrostatic consolidation tests. Figures showing the C-S constitutive model fits to the hydrostatic consolidation tests are given in Appendix C, specifically Figures C-1 through C-40. The sum-of-squared error in predicting the hydrostatic consolidation tests was calculated using Equation 4-6. These results are given in Table 4-9.

Visual examination of Figures C-17 to C-28 reveals that the model fit to the shear test database does not predict the hydrostatic tests that are dry ($w = 0$), particularly as the mean stress increases. Therefore the shear database model parameters were used to predict the wet hydrostatic consolidation tests. As seen in Table 4-9, the sum-of-squared error in predicting these tests (22.84) is nearly identical to that determined in the model fit to the combined tests (22.00).

Table 4-8. Parameter Variation

Parameter	Variation (%)
η_0	19
η_1	66
n_f	136
a_1	7
p	67
n_s	0
r_1	149
r_3	165
r_4	0
Q_s/R	75

Table 4-9. Sum-of-Squared Error in Hydrostatic Consolidation Tests

Database Fit	Database Predicted	
	Hydrostatic	Wet Hydrostatic
Shear	$>10^{22}$	22.84
Combined	23.61	22.00

These results suggest that the crushed-salt constitutive model (with parameter values determined from the shear consolidation tests) has excellent predictive quality. As shown in Table 4-9, this form of the model *predicts* the wet hydrostatic tests nearly as well as the model *fits* to the same tests. As further evidenced in the figures in Appendix C, visual comparison of the two fits shows qualitative sameness, even though the parameter values themselves might appear to be quite different (Table 4-3). For some tests (e.g., CS3 and CS9) the shear-determined parameters predict the laboratory data even better than the fit. Furthermore the model contains both a volumetric (hydrostatic) component and a deviatoric (shear) component, both of which are

captured in the shear consolidation tests. This provides a good sense of compatibility between theory (the model) and reality (the data). Thus the model not only characterizes (fits) the shear data well; it can also reproduce (predict) simpler conditions nearly as well. This provides strong evidence that the model has the potential for predicting the consolidation of crushed salt in other, more complex conditions, including the behavior of the shaft seal.

5.0 MODEL COMPARISONS

Over the past 20 years the behavior of particles has received growing interest in an effort to optimize manufacturing processes for forming parts from metallic powders and ceramics. On the surface, the task of predicting the behavior of a well-characterized material changed only by the introduction of voids would seem to be a straightforward process. However, the task is much more formidable because of the idealized, continually changing geometry and potential changes in the micromechanisms themselves over a wide range of porosity. Much of the research conducted to date is derived from cell models (i.e., a single void surrounded by the matrix material) analyzed to develop microscopic models that are homogenized to produce a macroscopic model of a void-filled material. Naturally the single cell models do not behave exactly like aggregates with random void distributions, nor do they account for interaction of the voids. Thus bounding solutions are typically derived that provide estimates for the random aggregate assemblage. Cell model analysis methods have mainly included analytical solutions and finite element analyses. Analytical solutions are usually derived for the simpler void geometries, which are typically spherical or cylindrical with preferred orientations. Then macroscopic solutions are derived that bound the microscopic cell solutions. Finite element analyses have been applied to problems similar to the analytical solution cell geometries, but they also provide flexibility in void shape and orientation. Hypothesized macroscopic constitutive models are matched to the cell behavior resulting from the finite element analyses. In this chapter, the effective stress measure for the crushed-salt flow potential is compared to each of these model types. The analytical model was developed by Gurson (1977) and later modified by Tvergaard (1981), and the finite element unit cell calculation-assisted model was developed by Sofronis and McMeeking (1992). Gurson's and Tvergaard's models are classic models for voided material that are cited by numerous researchers. Thus the crushed-salt model is compared with their models to enhance our understanding of the crushed-salt model predictive ability over a wide range of fractional densities and stress triaxialities. The Sofronis and McMeeking model forms the basis for the crushed-salt model. Comparison with this model shows the effect of modifications aimed at making the model more representative of crushed salt. Comparisons to these models are discussed separately in the remainder of this chapter.

5.1 Gurson and Tvergaard Models Comparison

Gurson (1977) developed approximate yield criteria and flow rules for porous ductile materials. Previous plastic models relied on the deviatoric response of the material matrix predicting incompressibility and could not predict the dilational aspects evident in porous inelastic materials. Gurson used simple cell models to develop upper bound yield loci to provide an approximate picture of the role of the hydrostatic stress in the yield and flow of porous, ductile

materials. Gurson considered long, circular, cylindrical voids and spherical voids as the void geometries. Later, Tvergaard (1981) recommended a modification to Gurson's model based on his numerical calculations to account for void interaction.

Comparison of the crushed-salt flow potential function (described in Chapter 2) to Gurson's and Tvergaard's models may help bring a physical basis to the crushed-salt model. However, at the outset we must recognize a significant difference between these earlier plastic models and the crushed-salt model. The plastic models are concerned with void nucleation and growth causing bulk dilatancy, which commonly accompanies large plastic flow. Thus the plastic models attempt to capture the increase in volume, whereas the crushed-salt model attempts to capture the decrease in volume. However, for the most part, consistency of the dilatancy terms is accomplished by the accompanying change in sign of the mean stress from tension to compression.

The yield or plastic potential function (F) developed by Gurson and modified by Tvergaard can be written as:

$$F = \left(\frac{\sigma_e}{\sigma_0}\right)^2 + 2q_1(1 - D)\cosh\left(\frac{3\alpha q_2 \hat{\sigma}}{2\sigma_0}\right) - \left[1 + q_3(1 - D)^2\right] \tag{5-1}$$

where:

$$\sigma_e = \left(\frac{3}{2}s_{ij}s_{ij}\right)^{1/2} = \sqrt{3J_2}, \text{ von Mises effective stress}$$

$$s_{ij} = \sigma_{ij} - \sigma_m\delta_{ij}, \text{ deviatoric stress}$$

$$\hat{\sigma} = \begin{cases} \sigma_p, \text{ in-plane mean stress (cylindrical voids)} \\ \sigma_m = \dfrac{\sigma_{kk}}{3}, \text{ mean stress (spherical voids)} \end{cases}$$

$$\alpha = \begin{cases} \sqrt{3}, & \text{cylindrical voids} \\ 1, & \text{spherical voids} \end{cases}$$

$$q_1, q_2, q_3 = \begin{cases} q_1 = q_2 = q_3 = 1, & \text{Gurson model} \\ q_1 = 1.5,\ q_2 = 1,\ q_3 = q_1^2, & \text{Tvergaard model} \end{cases}$$

D = fractional density

σ_0 = material equivalent yield stress.

The variable σ_p is the partial trace of the stress tensor in the plane orthogonal to the axis of the void for the cylindrical void model and the mean stress for the spherical void model. Equation 5-1 describes the level or magnitude of stress required to yield a porous, plastic material as described by Gurson and Tvergaard. The direction of flow is described by the normal to the yield surface and defined as the derivative of the yield function with respect to stress for associative flow. For comparative purposes, the effective stress measure used to describe the crushed-salt flow potential is used, which is given in Equation 2-3 and repeated here for convenience.

$$\sigma_{eq} = \left[\kappa_0 \Omega^{\kappa_1} \sigma_m^2 + \kappa_2 \left(\frac{2 - D}{D} \right)^{\frac{2n}{n+1}} (\sigma_1 - \sigma_3)^2 \right]^{\frac{1}{2}} \tag{5-2}$$

To aid in comparing the crushed-salt equivalent stress with Gurson's and Tvergaard's models, Equation 5-2 is rewritten as a similar type of yield function (F_{cs}) as:

$$F_{cs} = \left[\kappa_0 \Omega^{\kappa_1} \sigma_m^2 + \kappa_2 \left(\frac{2 - D}{D} \right)^{\frac{2n}{n+1}} (\sigma_1 - \sigma_3)^2 \right]^{\frac{1}{2}} - \left[1 + (1 - D)^2 \right]^{\frac{1}{2}} \tag{5-3}$$

The added term in Equation 5-3 makes the magnitudes of the effective stress similar to the magnitudes predicted by Gurson's and Tvergaard's yield functions. However, the flow direction is unaffected by the additional term because the derivative of Equation 5-3 with respect to stress remains the same as that for Equation 5-2. In this comparison, the shapes of the resulting curves are most important because Equation 5-2 governs the direction of flow for the crushed-salt model.

To aid in a numerical comparison of the models, consider a triaxial compression test where:

$$\begin{aligned} &\sigma_3 < \sigma_1 = \sigma_2 \\ &\sigma_e = \sqrt{3 J_2} = \sigma_1 - \sigma_3 = \Delta\sigma \end{aligned} \tag{5-4}$$

Substituting Equation 5-4 into Equations 5-1 and 5-3 and solving for $\Delta\sigma$ at yield ($F = F_{cs} = 0$) gives:

$$\Delta\sigma = \left[-2q_1(1 - D)\sigma_0^2 \cosh\left(\frac{3\alpha q_2 \sigma_m}{2\sigma_0} \right) + \left(1 + q_3[1 - D]^2\right)\sigma_0^2 \right]^{1/2} \quad (5\text{-}5)$$

for Gurson's and Tvergaard's model and

$$\Delta\sigma_{cs} = \left[\frac{1}{\kappa_2} \left(\frac{2 - D}{D} \right)^{\frac{-2n}{n+1}} \left(-\kappa_0 \Omega^{\kappa_1} \sigma_m^2 + 1 + [1 - D]^2 \right) \right]^{1/2} \quad (5\text{-}6)$$

for the crushed-salt model. Substitution of mean stress values produces effective stress (stress difference) values that form data pairs for plotting in stress space.

To compare Equations 5-5 and 5-6, fractional density values of 0.9, 0.8, and 0.7 or porosity values ($\phi = 1 - D$) of 0.1, 0.2, and 0.3 are assumed. The crushed-salt model parameter values given in Chapter 4 (Table 4-2) are used in the comparison. For Gurson's and Tvergaard's models, σ_0 is taken to equal one. Figures 5-1 and 5-2 are compressive stress space plots that compare the crushed-salt model to Gurson's and Tvergaard's models for spherical voids and long, circular, cylindrical voids, respectively. As shown in Figure 5-1, the crushed-salt model shape is most similar to Gurson's and Tvergaard's model shapes at the lowest fractional density. In addition, the crushed-salt model appears to be less sensitive to changes in fractional density. Comparison to the cylindrical void form of Gurson's and Tvergaard's models given in Figure 5-2 is academic because the cylindrical void model includes the partial trace of the stress tensor normal to the axis of the void, whereas the crushed-salt model includes the mean stress. Thus the abscissa is different for the models as labeled in Figure 5-2. However, it is still interesting that the crushed-salt model appears to compare most closely with Gurson's and Tvergaard's cylindrical void model at the higher fractional densities, which is the opposite of what was observed in Figure 5-1 for the spherical void model.

5.2 Sofronis and McMeeking Model Comparison

Sofronis and McMeeking (1992) conducted finite element calculations for a unit spherical cell containing a concentric spherical hole to characterize a power-law creep material containing voids. Calculations were carried out for isostatic and nonisostatic cases. Based on the results of

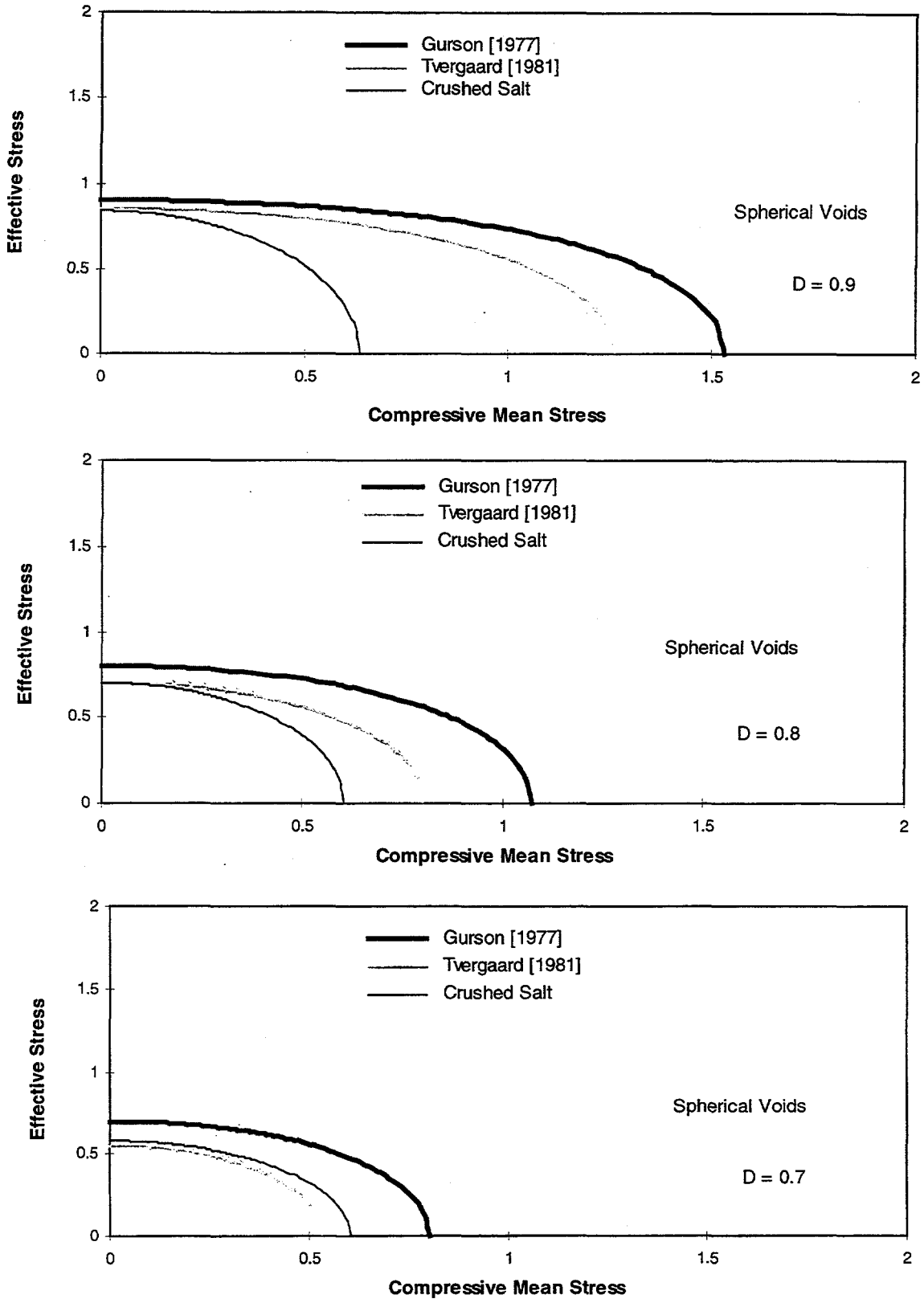

Figure 5-1. Comparison of the crushed-salt model to Gurson's and Tvergaard's models, assuming spherical voids.

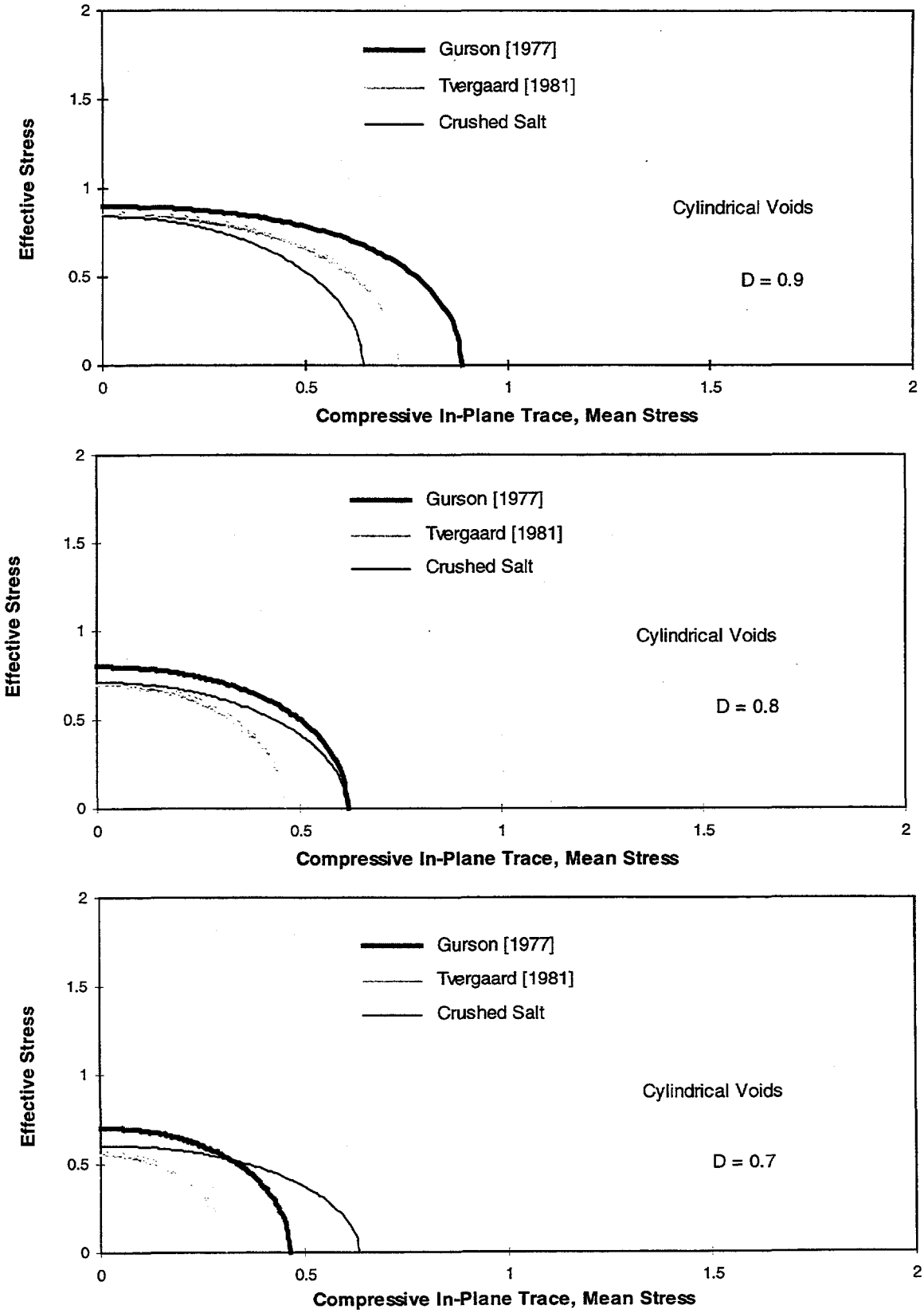

Figure 5-2. Comparison of the crushed-salt model to Gurson's and Tvergaard's models, assuming long, circular, cylindrical voids.

the calculations and equation forms suggested by others, they formulated an elliptic potential function to describe the porous material, which may be written as:

$$F_{sm} = \left[\left(\frac{(1 - D)m}{\left(1 - (1 - D)^{1/m}\right)^m} \right)^{\frac{2}{m+1}} \left(\frac{3\sigma_m}{2m} \right)^2 + \left(\frac{2 - D}{D} \right)^{\frac{2m}{m+1}} (3J_2) \right]^{1/2} \tag{5-7}$$

where m is the effective stress exponent for the creep power law. To compare Equations 5-2 and 5-7, contours are computed where the potential functions are equal to one. As for the comparison to the Gurson and Tvergaard models, a triaxial compression test is assumed and the stress differences are computed for values of mean stress. Thus Equations 5-2 and 5-7 are rewritten as:

$$\Delta\sigma_{cs} = \left[\frac{1}{\kappa_2} \left(\frac{2 - D}{D} \right)^{\frac{-2n}{n+1}} \left(-\kappa_0 \, \Omega^{\kappa_1} \sigma_m^2 + 1 \right) \right]^{1/2}$$

$$\Delta\sigma_{sm} = \left\{ \left(\frac{2 - D}{D} \right)^{\frac{-2m}{m+1}} \left[- \left(\frac{(1 - D)m}{\left[1 - (1 - D)^{1/m}\right]^m} \right)^{\frac{2}{m+1}} \left(\frac{3\sigma_m}{2m} \right)^2 + 1 \right] \right\}^{1/2} \tag{5-8}$$

The crushed-salt model parameters given in Chapter 4 are used for the crushed-salt model, and the exponent m in Sofronis and McMeeking's model was assumed to be equal to n. Figure 5-3 contains compressive stress space plots that compare the crushed-salt potential to the one presented by Sofronis and McMeeking (1992). Despite the subtle differences between the crushed salt and Sofronis and McMeeking potential functions, Figure 5-3 shows significant differences in their contours. Comparison of Figure 5-3 to Figure 5-1 shows that Sofronis and McMeeking's model compares closely with Gurson's spherical void model.

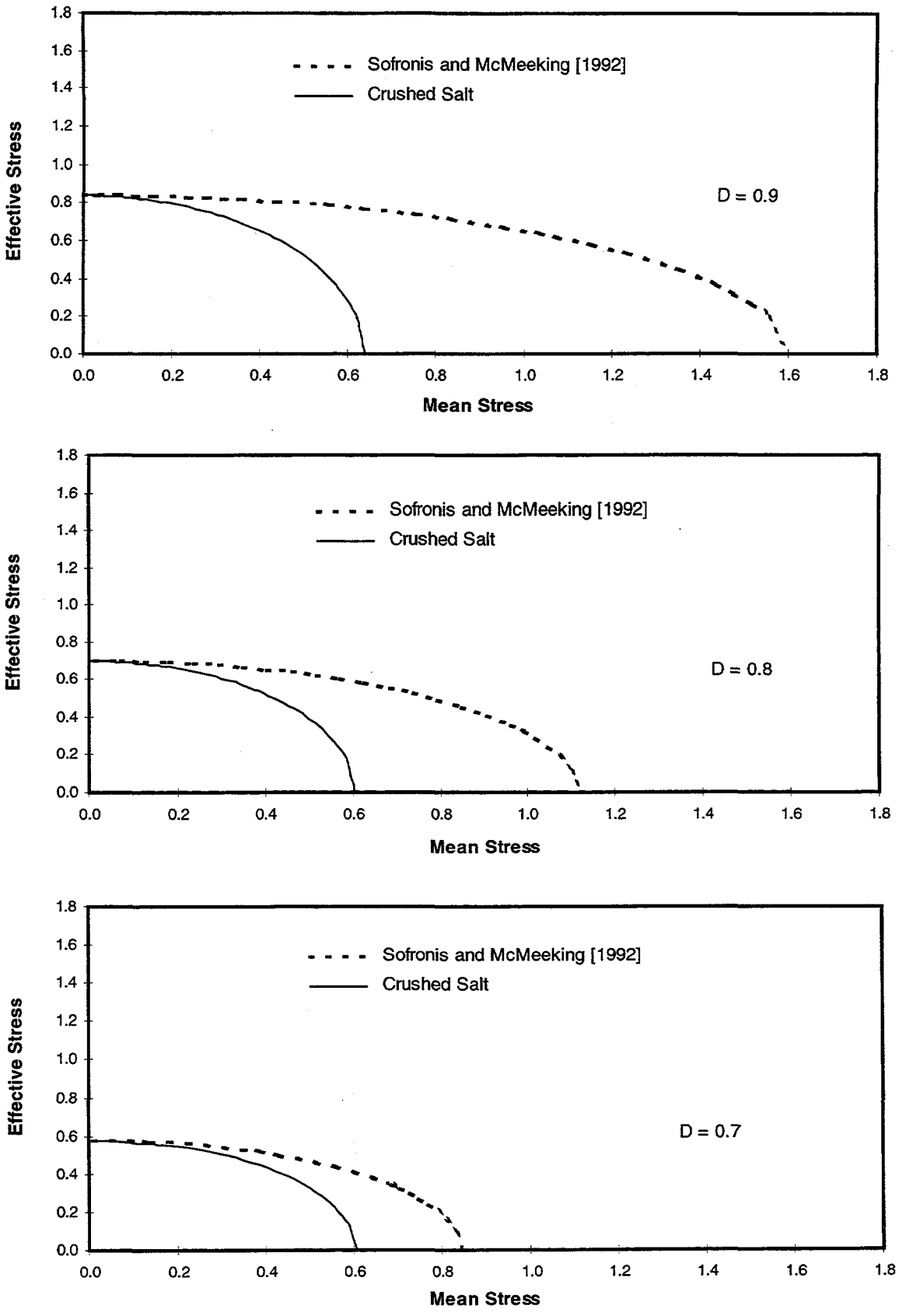

Figure 5-3. Comparison of the crushed-salt model to Sofronis and McMeeking's model.

6.0 OTHER MODEL CONSIDERATIONS

During the course of this study, various functional forms addressing specific parts of the constitutive model were developed in an effort to improve the constitutive model. Model improvement was judged by fitting the experimental database and observing changes in the goodness of fit. These investigations mainly involved the moisture function and the flow potential, which are discussed in the remainder of this chapter.

6.1 Moisture Function

Many researchers (e.g., Pfeifle and Senseny [1985], Holcomb and Shields [1987], Yost and Aronson [1987], Fordham [1988], Spiers et al. [1989], Zeuch and Holcomb [1991], Zeuch et al. [1991], and Wang et al. [1992]) have found that the addition of a small amount of moisture significantly increases the consolidation rate of crushed salt. In addition, there appears to be a quantity of moisture above which further increases in the consolidation rate are not noticeable. However, the amount of moisture producing the largest consolidation rate may vary depending on temperature and pressure. When a significant amount of moisture is available, a retardation in the consolidation rate could occur if the interconnected porosity disappears and the moisture is trapped, leading to the generation of pore pressures. In Chapter 2, the Spiers and Brzesowsky (1993) grain boundary diffusional pressure solutioning model was adapted to represent the increased creep consolidation caused by added moisture. However, during their model development, Spiers and Brzesowsky assumed that the aggregate was flooded with brine. Since an essentially unlimited supply of saturated solution phase was assumed, moisture or brine content does not appear explicitly in their model as a state variable. Therefore, moisture functions were assumed as direct multipliers of the Spiers and Brzesowsky model's predicted effective strain rate to account for varying moisture content. The first functional relationship for moisture effects (M) was taken from Callahan et al. (1995) and is written as:

$$M = 1 - e^{-aw} \tag{6-1}$$

where:

w = moisture fraction by weight

a = material parameter.

Equation 6-1 has a value of zero when the moisture content is zero and asymptotically approaches a value of one as the moisture content increases without bound. The rate at which M approaches the asymptote is governed by parameter a. Equation 6-1 served as a direct multiplier on the equivalent consolidation strain rate contributed by the pressure solutioning portion of the crushed-salt constitutive model. Thus, when the moisture content was zero, only the dislocation creep mechanism contributed to the strain rate, and when the moisture content was nonzero, both the dislocation creep and pressure solutioning mechanisms contributed to the strain rate. When the creep consolidation model was fit to the experimental data, the fitting algorithm produced a large value for parameter a. Thus the function included in Equation 6-1 acted like a Heaviside function, turning the pressure solutioning portion of the model on and off, depending on whether or not a particular specimen was wet or dry. No improvement in the goodness of fit could be achieved by accounting for the moisture variation once moisture was present. In other words, the significant difference between wet and dry specimen deformation is accounted for by the binary nature of the function, but once moisture is present the variation for different moisture contents is not significant. Four potential explanations exist to help understand this behavior:

1. The specimen-to-specimen variability is as great as changes caused by moisture content differences.

2. Moisture content effects are correlated to other test conditions or combinations of test conditions that mask the moisture effects.

3. The test conditions (i.e., the database) are inadequate.

4. The effect of moisture is nearly constant for our range of grain sizes.

The tests included in the database with added moisture are shown in Table 6-1. Thirty-six of the 56 tests in the database were conducted with added moisture. Review of the figures presented in Appendix C shows that specimen-to-specimen variability can be significant. For example, test conditions for Tests CS7 and CS8 (Figures C-7 and C-8) are nearly the same, yet their strain rates and deformation are quite different.

Table 3-2 showed the mean grain size for each of the tests in the database. As noted in the table footnote, the grain size was estimated for four tests. For the remaining tests, the grain size was measured using standard sieve analysis. Also of significance is the fact that six of the tests were performed on dynamically compacted crushed-salt specimens. Tests SC10 and SC11 were performed on field samples from the large-scale dynamic compaction tests. Tests RS/DCCS/1, RS/DCCS/3, RS/DCCS/4, and RS/DCCS/5 were performed on laboratory samples from the small-scale dynamic compaction tests. The remaining tests were performed on mine-run salt, with the loads applied quasi-statically.

Table 6-1. Hydrostatic and Shear Consolidation Tests Conducted with Added Moisture

Test ID	% Moisture by Weight	Average Grain Size (mm)	Mean Stress (MPa)	Stress Difference (MPa)
27JU61	2.50	1.75	–0.69	0.0
23JL51	0.50	1.75	–1.72	0.0
14NV51	1.50	1.75	–1.72	0.0
25FE61	2.00	1.75	–1.72	0.0
10MY51	2.40	1.75	–1.72	0.0
20AU51	3.00	1.75	–1.72	0.0
CS6	4.28	1.36	–1.72	0.0
CS5	4.44	2.30	–1.72	0.0
CS7	4.57	0.77	–1.72	0.0
CS8	4.61	0.42	–1.72	0.0
HC2A[a]	15.19	1.56	–1.72	0.0
HC1A[a]	16.47	1.56	–1.72	0.0
16JL51	0.50	1.75	–3.44	0.0
18JU51	1.00	1.75	–3.44	0.0
30OC51	1.50	1.75	–3.44	0.0
16JA61	2.00	1.75	–3.44	0.0
19DC44	2.40	1.75	–3.44	0.0
13AU51	3.00	1.75	–3.44	0.0
HC4A[a]	13.96	1.56	–3.45	0.0
HC3A[a]	16.08	1.56	–3.45	0.0
HC5A[a]	9.84	1.56	–6.90	0.0
HC6A[a]	10.41	1.56	–6.90	0.0
DCCS/1[b]	1.66	0.50	–2.33	4.00
DCCS/3[b]	1.63	0.50	–3.33	4.00
12OC891	2.40	2.00	–3.41	0.44
SC1B	2.34	1.56	–3.68	0.69
SC2A	2.25	1.56	–3.91	1.38
SC3A	2.21	1.56	–4.14	2.07
DCCS/4[b]	1.59	0.50	–4.33	4.00
DCCS/5[b]	1.55	0.50	–5.33	4.00
SC7A	2.33	1.56	–5.63	1.38
SC8A	2.29	1.56	–6.09	2.76
SC9B	2.33	1.56	–6.55	4.14
SC4A	2.27	1.56	–7.13	0.69
SC5A	2.52	1.56	–7.59	2.07
SC6A	2.19	1.56	–8.05	3.44

(a) Saturated tests moisture content computed from initial void ratio.

(b) Grain size for the dynamically compacted specimens is an estimate.

In the model fitting performed in this study, the consolidation rate was not assumed to be dependent on the type of loading used to preconsolidate the crushed salt. However, recent microscopic analysis has suggested that the consolidation rate is greatly enhanced in the dynamic compaction process. Furthermore this analysis has revealed that the deformation is localized to zones where the grain size is much smaller in comparison to the mean grain size reported: i.e., approximately 2–5 microns for the large-scale compaction test and 20 microns for the small-scale compaction tests. These zones are located along the "lift planes" where the material has been pulverized because of the localized dynamic effort used to compact the crushed salt. The conclusion of this microscopy is that the global functional form that defines the grain-size dependence used in the current model fit may not be appropriate because the deformation is localized. However, this information was not available at the time this study was initiated.

Figures 6-1, 6-2, and 6-3 plot moisture content versus average grain size, compressive mean stress, and stress difference. The saturated tests were not plotted on these figures so that the individual tests could be seen in the range up to 5 percent moisture by weight. These figures illustrate holes in the database but also illustrate that moisture content is not directly correlated to these other variables.

Spiers and Brzesowsky (1993) present data that illustrate the effect of grain size on strain rate in wet aggregates. However, their experiments were conducted on grain sizes about an order of magnitude smaller (0.098 to 0.41 millimeter) than those in the database discussed in Chapter 3. Information presented by Callahan et al. (1995) shows that the strain rates in these larger grain-size tests are quite similar despite the different moisture contents (e.g., see Callahan et al. [1995], Figure 4-9). Based on this information, it appears that moisture content variation in these larger grain sizes is not as important as the smaller grain sizes. However, insufficient data are available to judge where the transition occurs.

Because information could not be collected using Equation 6-1, a different functional form for moisture content was adopted. This form is written as:

$$M = w^{a} \tag{6-2}$$

As in Equation 6-1, Equation 6-2 has a value of zero when the moisture content is zero, but grows as the moisture content increases. The rate at which M increases is governed by parameter a. Equation 6-2 served as a direct multiplier on the equivalent consolidation strain rate contributed by the pressure solutioning portion of the crushed-salt constitutive model. Thus when the moisture content was zero only the dislocation creep mechanism contributed to the strain rate, and when the moisture content was nonzero both the dislocation creep and pressure solutioning mechanisms contributed to the strain rate. Equation 6-2 is the form used in the constitutive model presented in Chapter 2.

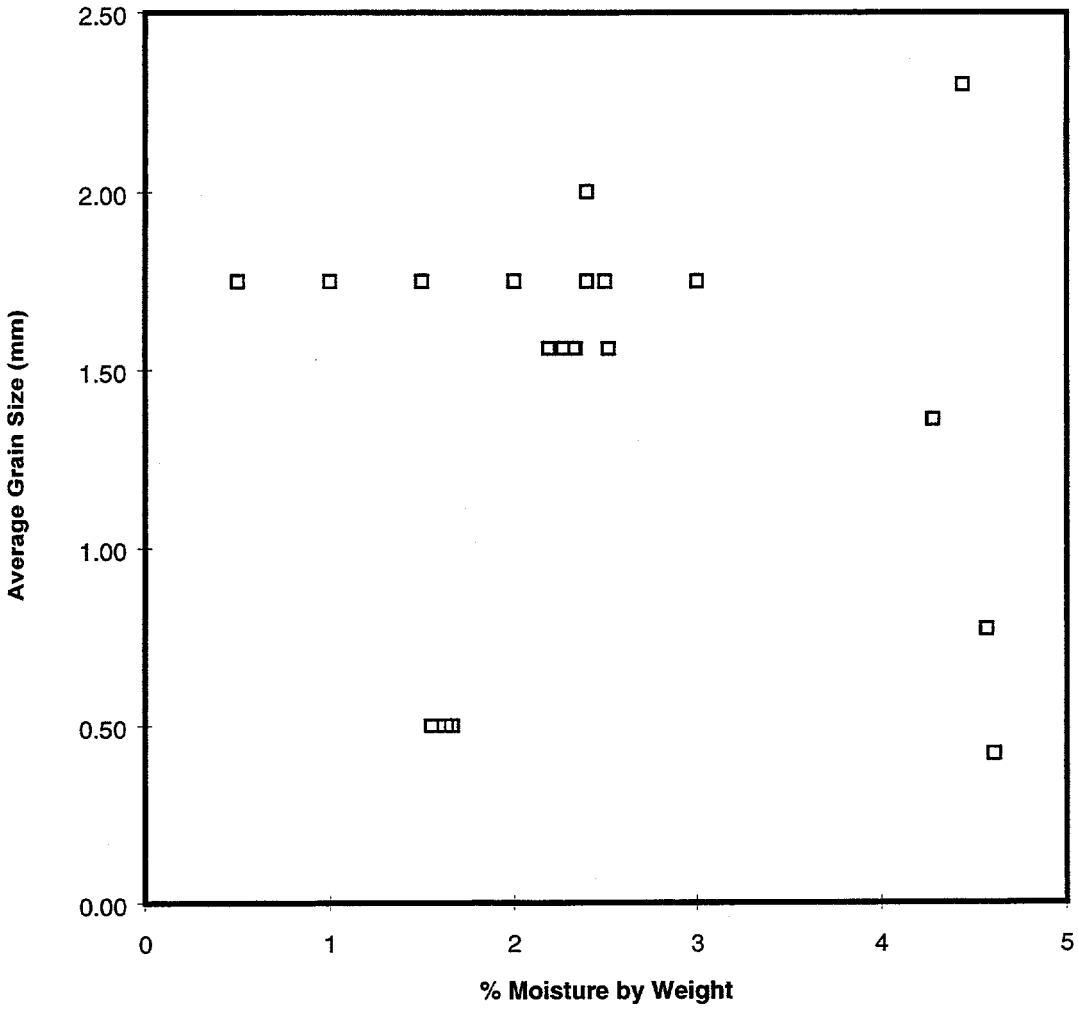

Figure 6-1. Plot of shear and hydrostatic consolidation tests as a function of moisture content and grain size.

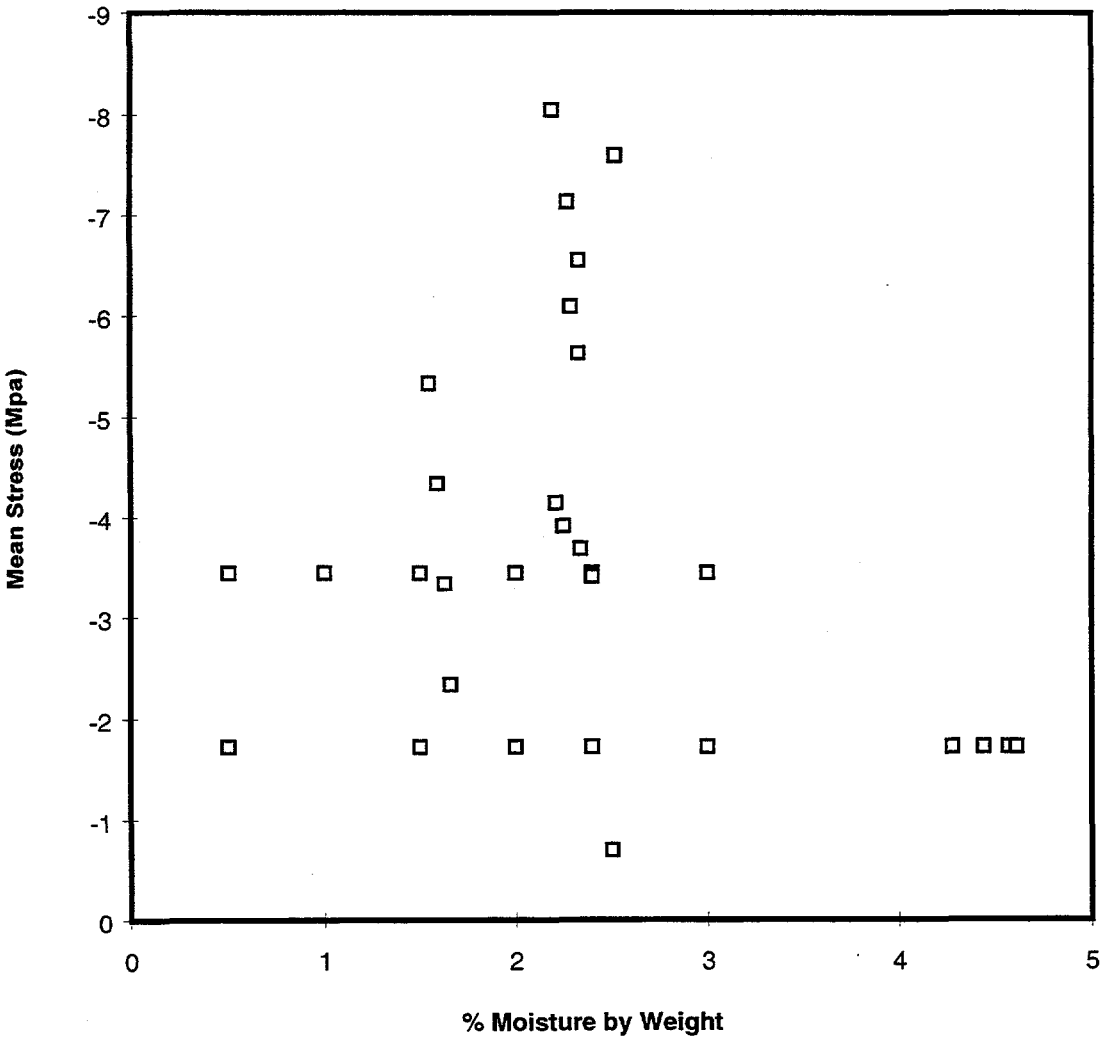

Figure 6-2. Plot of shear and hydrostatic consolidation tests as a function of moisture content and mean stress.

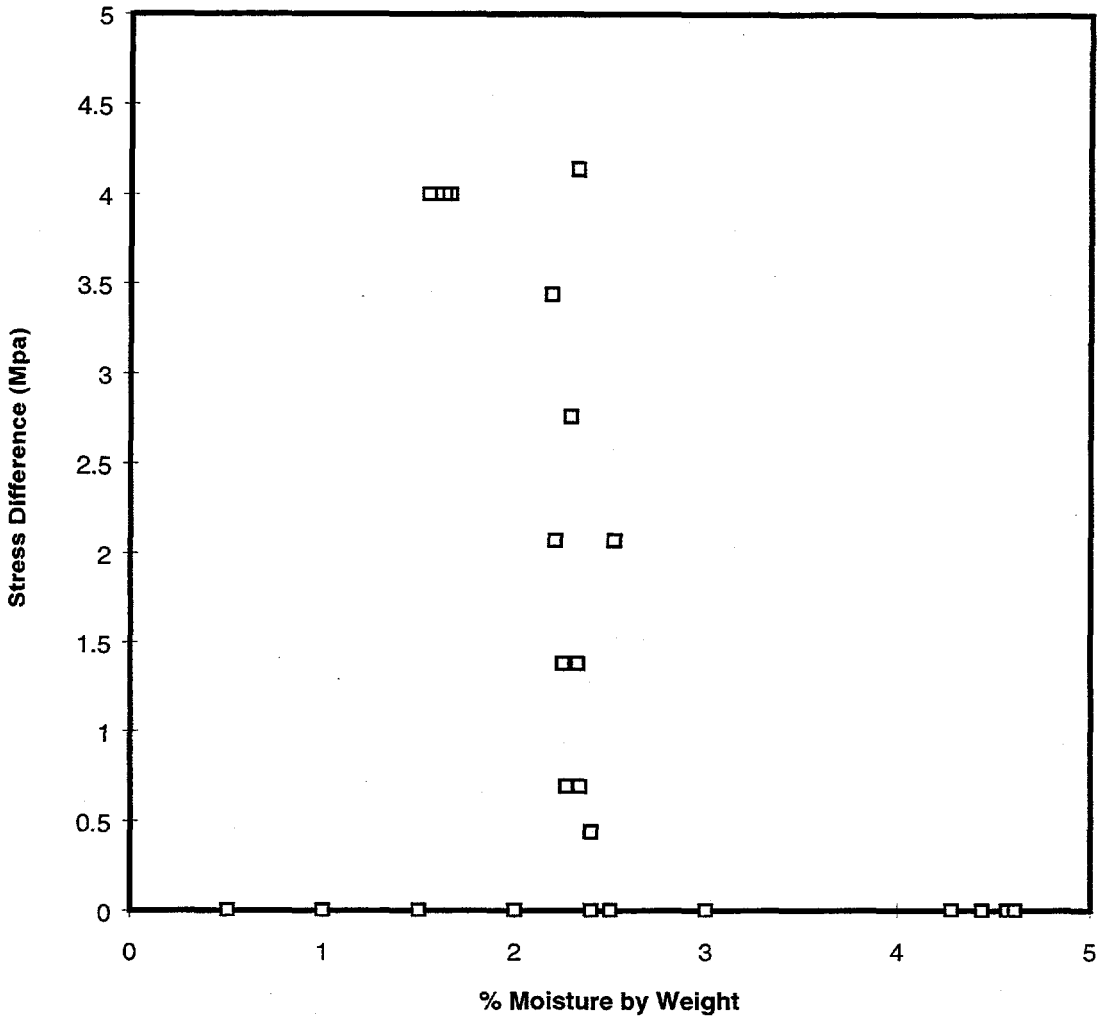

Figure 6-3. Plot of shear and hydrostatic consolidation tests as a function of moisture content and stress difference.

6.2 Flow Potential

Two different attempts were made to improve the goodness of fit for the flow potential. The first attempt involved a change in Ω given in Equation 2-5, which was successful. The second attempt consisted of the consideration of different stages in the densification process, which was not successful. These two modifications to the flow potential are described in the remainder of this section.

The fractional density function, Ω, was originally written as:

$$\Omega = \left[\frac{(1 - D)\, n}{\left[1 - (1 - D)^{1/n}\right]^n} \right]^{\frac{2}{n+1}} \tag{6-3}$$

Comparing Equation 6-3 to Equation 2-5 shows that Equation 2-5 incorporates a transition defined by parameter D_v, whereas Equation 6-3 does not. For fractional density values less than D_v, Equation 2-5 produces a constant value for Ω. The goodness of fit to the lateral-to-axial strain rate ratios (Appendix B) was improved when Equation 2-5 was used; thus this functional form was adopted.

Many researchers consider different stages in the densification process (e.g., Helle et al. [1985]). Usually a fractional density (D) of 0.9 is assumed to be a demarcation between an initial stage and a final stage in the process. The initial stage ($D < 0.9$) is characterized by distinguishable particles densifying by neck growth at the increasing number of contact points. The final stage ($0.9 < D < 1$) is characterized by an array of spherical holes that decrease in size as densification progresses. With these distinctive regions identified and apparently used successfully by others, an attempt was made to improve the flow potential by considering multiple stages in the consolidation process. This was accomplished by considering an initial stage, a transitional stage, and a final stage defined as follows:

$$\begin{aligned} \text{Initial Stage} &= D_0 \le D \le D_s \\ \text{Transitional Stage} &= D_s \le D \le D_t \\ \text{Final Stage} &= D_t \le D \le 1 \end{aligned} \tag{6-4}$$

D_s and D_t are assumed to be parameter values. The transitional zone is included so that a smooth transition occurs between the discontinuous initial and final stages. The effective stress measure for the final stage is assumed to be the same as the effective stress measure given in Equation 2-3. The effective stress measure for the initial stage is assumed to be:

$$\sigma_{eq_1} = \zeta_0 \frac{\sigma_0}{m+1}\left[\Omega_1\left(\frac{|\sigma_m|}{\sigma_0}\right)^{\frac{m+1}{m}} + \left(\frac{2-D}{D}\right)^{\frac{2m}{m+1}}\left(\frac{\sigma_1-\sigma_3}{\sigma_0}\right)^{\frac{m+1}{m}}\right]^m \quad (6\text{-}5)$$

where:

$$\Omega_1 = \left(\frac{D_0}{D}\right)^{1/3}\left(\frac{D-D_0}{1-D_0}\right)^{1/2}\left(\frac{1-D}{D^2(D-D_0)}\right)^m \quad (6\text{-}6)$$

D_0 = initial fractional density (0.64)

D = current fractional density

σ_m = mean stress = $\frac{\sigma_{kk}}{3}$

σ_3 = minimum principal stress

σ_1 = maximum principal stress

ζ_0, σ_0, and m = material parameters.

Motivation for use of the functional form described by Equation 6-6 comes from Helle et al. (1985). This is the geometrical relationship they used for initial stage densification. This form was also used by Zeuch (1990) for WIPP salt, since he adopted the hot isostatic pressing equations of Helle et al.

In the transition region, the effective stress is:

$$\sigma_{eq}^t = \frac{D_t - D}{D_t - D_s}\sigma_{eq_1} + \frac{D - D_s}{D_t - D_s}\sigma_{eq} \quad (6\text{-}7)$$

The flow potential is described by the derivative of the effective stress measure. The derivative in the initial stage is:

$$\frac{\partial \sigma_{eq_1}}{\partial \sigma_{ij}} = \zeta\left\{\alpha_1 \delta_{ij} + \beta_1\left(\left[\frac{\cos 2\psi}{\cos 3\psi}\right]\frac{s_{ij}}{\sqrt{J_2}} + \left[\frac{\sqrt{3}\sin\psi}{J_2\cos 3\psi}\right] t_{ij}\right)\right\} \quad (6\text{-}8)$$

where:

$$\zeta = (\zeta_0)^{1/m}\left(\frac{\sigma_0}{m+1}\right)^{\frac{1-m}{m}}\left(\sigma_{eq_1}\right)^{\frac{m-1}{m}}$$

$$\alpha_1 = \frac{\Omega_1 \operatorname{sgn}(\sigma_m)}{3}\left|\frac{\sigma_m}{\sigma_0}\right|^{1/m} \tag{6-9}$$

$$\beta_1 = \left[\frac{2-D}{D}\right]^{\frac{2m}{m+1}}\left(\frac{2\sqrt{J_2}\cos\psi}{\sigma_0}\right)^{1/m}$$

Equation 6-8 is seen to be undefined as the Lode angle approaches $\pm\pi/6$. In other words, the flow potential forms corners at $\psi = \pm\pi/6$, and the direction of straining is not unique. To eliminate this problem computationally, the flow potentials on either side of the corner are averaged, which produces an indeterminant form that is examined in the limit as $\psi \rightarrow \pm\pi/6$. Performing this limiting operation, Equation 6-8 becomes:

$$\frac{\partial \sigma_{eq_1}}{\partial \sigma_{ij}} = \zeta\left\{\alpha_1 \delta_{ij} + \beta_1\left(\frac{s_{ij}}{\sqrt{3J_2}} \mp \frac{t_{ij}}{2J_2}\right)\right\} \tag{6-10}$$

Following the procedure used to compute the lateral-to-axial strain rate ratio outlined in Chapter 2, Equation 6-10 may be used to express the initial stage strain rate ratio for a triaxial compression test as:

$$\mathbf{R}_1 = \frac{\alpha_1 + \frac{\beta_1}{2}}{\alpha_1 - \beta_1} \tag{6-11}$$

In the transition zone, the flow potential is written as:

$$\frac{\partial \sigma^t_{eq_1}}{\partial \sigma_{ij}} = \frac{(D_t - D)}{(D_t - D_s)}\frac{\partial \sigma_{eq_1}}{\partial \sigma_{ij}} + \frac{(D - D_s)}{(D_t - D_s)}\frac{\partial \sigma_{eq}}{\partial \sigma_{ij}} \tag{6-12}$$

Substitution of Equations 6-5 and 2-5 into Equation 6-12 yields:

$$\frac{\partial \sigma^{t}_{eq_1}}{\partial \sigma_{ij}} = \frac{(D_t - D)}{(D_t - D_s)} \zeta \left\{ \alpha_1 \delta_{ij} + \beta_1 \left(\left[\frac{\cos 2\psi}{\cos 3\psi} \right] \frac{s_{ij}}{\sqrt{J_2}} + \left[\frac{\sqrt{3} \sin \psi}{J_2 \cos 3\psi} \right] t_{ij} \right) \right\}$$
$$+ \frac{(D - D_s)}{(D_t - D_s)} \frac{1}{\sigma_{eq}} \left\{ \alpha \delta_{ij} + \beta \left(\left[\frac{\cos 2\psi}{\cos 3\psi} \right] \frac{s_{ij}}{\sqrt{J_2}} + \left[\frac{\sqrt{3} \sin \psi}{J_2 \cos 3\psi} \right] t_{ij} \right) \right\} \tag{6-13}$$

Then, as was done for Equation 6-8 to create Equation 6-10 at the corners, Equation 6-13 becomes:

$$\frac{\partial \sigma^{t}_{eq_1}}{\partial \sigma_{ij}} = \frac{(D_t - D)}{(D_t - D_s)} \zeta \left[\alpha_1 \delta_{ij} + \beta_1 \left(\frac{s_{ij}}{\sqrt{3J_2}} \mp \frac{t_{ij}}{2J_2} \right) \right]$$
$$+ \frac{(D - D_s)}{(D_t - D_s)} \frac{1}{\sigma_{eq}} \left[\alpha \delta_{ij} + \beta \left(\frac{s_{ij}}{\sqrt{3J_2}} \mp \frac{t_{ij}}{2J_2} \right) \right] \tag{6-14}$$

Again, following the procedure used to compute the lateral-to-axial strain rate ratio outlined in Chapter 2, Equation 6-14 may be used to express the transitional stage strain rate ratio for a triaxial compression test as:

$$\mathbf{R}_t = \frac{(D_t - D)\zeta \left(\alpha_1 + \frac{\beta_1}{2} \right) + (D - D_s) \frac{1}{\sigma_{eq}} \left(\alpha + \frac{\beta}{2} \right)}{(D_t - D)\zeta (\alpha_1 - \beta_1) + (D - D_s) \frac{1}{\sigma_{eq}} (\alpha - \beta)} \tag{6-15}$$

Thus Equations 2-20, 6-11, and 6-15 form the equations fitted to the laboratory test data for densification stages described in Equation 6-4. Use of the densification stages did not improve the goodness of fit for the flow potential. Thus the equations as stated in Chapter 2 were retained.

7.0 SUMMARY AND CONCLUSIONS

Crushed salt is planned to be a major long-term component of the shaft seal system at the WIPP. The crushed-salt seal gradually becomes effective as it consolidates over time because of the creep of the surrounding intact salt, which produces shaft closure and loading of the crushed salt. The ability to predict creep consolidation of crushed salt is important to the design and compliance evaluation of WIPP seals. The work reported here represents a continuation of earlier studies devoted to constitutive models for crushed-salt reconsolidation. Understanding the creep consolidation of WIPP crushed salt and our ability to predict its mechanical behavior have been greatly improved as a result of these studies. Crushed-salt consolidation is important in two specific areas:

1. Crushed salt consolidates with time as the intact salt surrounding the shaft creeps inward. This consolidation process resists movement of the surrounding intact salt and produces a load on the shaft surface, which promotes healing of the disturbed rock zone (DRZ) in the salt immediately surrounding the shaft. This healing greatly reduces the DRZ's flow characteristics and helps eliminate this potential pathway.

2. The consolidation of crushed salt reduces the permeability and porosity of the crushed salt itself, greatly enhancing the crushed salt as an effective seal material.

The present study is a continuation of two earlier studies (Callahan et al. [1995], RE/SPEC Inc. [1996], Callahan et al. [1996]). The objectives of the current study were to incorporate the governing deformation mechanisms into a single model and to enhance the database with shear consolidation tests applicable to the operating conditions expected for the dynamically compacted crushed-salt seal material. Before these studies were initiated, the only model used to characterize creep consolidation of WIPP crushed salt was the model proposed by Sjaardema and Krieg (1987).

The first study (Callahan et al. [1995]) identified ten models developed to characterize the deformation of crushed salt. Three of these models were selected for further evaluation. The models were modified to include effects of potentially important parameters such as deviatoric stress, temperature, moisture content, and particle size. The models were generalized to be applicable to three-dimensional states of stress and fit to an assembled database of hydrostatic and shear consolidation tests applicable to the WIPP. The study identified two primary operative mechanisms that contribute to crushed-salt deformation: dislocation creep and grain boundary diffusional pressure solutioning. The first mechanism dominates in dry granular aggregates, whereas the second mechanism is only operative in wet granular aggregates. These mechanisms are included separately in two of the constitutive models evaluated in the first study.

The second study (RE/SPEC Inc. [1996], Callahan et al. [1996]) was conducted to correct deficiencies discovered in the three models. Basically the models were unable to predict a

reversal in the lateral strain rate in a triaxial test. The ability to predict this behavior is a necessary condition for the transition to intact salt behavior as the crushed-salt fractional density approaches one. Unfortunately all tests in the crushed-salt laboratory database assembled in the first study exhibit primarily a positive lateral-to-axial strain rate ratio. Thus the database was biased toward conditions unrepresentative of the anticipated dynamically compacted crushed salt with initial fractional densities near 0.9. Therefore two additional shear consolidation tests with initial fractional densities near 0.8 were conducted and added to the database. The functional form of the flow potential was modified, and the shear consolidation tests were fit to determine material constants for the three crushed-salt consolidation models. The refined model characterizations were found to provide appropriate behavior under uniaxial states of stress, enable a sign reversal of the lateral strain rate, and provide a natural transition to intact salt at complete consolidation. However, predictions of the hydrostatic tests with the models were found to be quite poor.

In this study the creep consolidation model for crushed salt was updated to combine dislocation creep and grain boundary diffusional pressure solutioning into a single constitutive model. The dislocation creep model was adapted from the multimechanism deformation constitutive model (Munson et al. [1989]) used to describe creep deformation of intact salt. The pressure solutioning model was adapted from the densification model for wet salt aggregates presented by Spiers and Brzesowsky (1993). The strain rates from the two contributing mechanisms are additive, with the contribution from the pressure solutioning portion of the model disappearing as the moisture content goes to zero. When the fractional density of the crushed salt reaches one, the model produces intact salt behavior predicted by the multi-mechanism deformation model. Four new laboratory shear consolidation experiments were conducted with fractional densities near the initial fractional density expected in the dynamically compacted crushed-salt seal (approximately 0.9). These tests expand the database into fractional density ranges previously untested and provide information on the crushed-salt flow behavior as its density increases. One test clearly demonstrates the reversal in lateral deformation as the density increases. These tests were added to the experimental database, which was fit to obtain material parameter values for the updated crushed-salt constitutive model. The results of the model fitting produced material parameter values representative of the entire database. Two separate fits were performed. The first fit used only the shear consolidation tests in the database, and the second fit used both the shear and hydrostatic consolidation tests. In our previous studies, dramatic changes in the parameter values were observed when the different tests were fit. In the present study, these separate fits produced similar parameter values, which indicates that the constitutive model is more representative of the physics of the creep consolidation of crushed salt than were the previous models.

As a result of this study, a constitutive model for crushed salt is available that contains the observed mechanisms for crushed-salt consolidation. When consolidation is complete, the model predicts intact salt behavior. The model characterizes the experimental data quite well over a wide range of porosities and stress triaxialities.

8.0 REFERENCES

Arzt, E., M.F. Ashby, and K.E. Easterling. 1983. "Practical Applications of Hot-Isostatic Pressing Diagrams: Four Case Studies," *Metallurgical Transactions A.* Vol. 14A, no. 2, 211-221.

Brodsky, N.S. 1994. *Hydrostatic and Shear Consolidation Tests with Permeability Measurements on Waste Isolation Pilot Plant Crushed Salt.* SAND93-7058. Albuquerque, NM: Sandia National Laboratories.

Callahan, G.D., M.C. Loken, L.L. Van Sambeek, R. Chen, T.W. Pfeifle, J.D. Nieland, and F.D. Hansen. 1995. *Evaluation of Potential Crushed-Salt Constitutive Models.* SAND95-2143. Prepared by RE/SPEC Inc., Rapid City, SD. Albuquerque, NM: Sandia National Laboratories.

Callahan, G.D., M.C. Loken, L.D. Hurtado, and F.D. Hansen. 1996. "Evaluation of Constitutive Models for Crushed Salt," *4th International Conference on the Mechanical Behavior of Salt, École Polytechnique de Montréal, Mineral Engineering Department, Québec, Canada, June 17-18, 1996.* SAND96-0791C.

Cocks, A.C.F. 1989. "Inelastic Deformation of Porous Materials," *Journal of the Mechanics and Physics of Solids.* Vol. 37, no. 6, 693-715.

Dixon, W.J., M.B. Brown, L. Engelman, J.W. Frane, M.A. Hill, R.I. Jennrich, and J.D. Toporek. 1985. *BMDP Statistical Software.* 1985 printing. Berkeley, CA: University of California Press. (ISBN: 0-520-04408-8).

Duva, J.M. 1986. "A Constitutive Description of Nonlinear Materials Containing Voids," *Mechanics of Materials.* Vol. 5, no. 2, 137-144.

Duva, J.M., and J.W. Hutchinson. 1984. "Constitutive Potentials for Dilutely Voided Nonlinear Materials," *Mechanics of Materials.* Vol. 3, no. 1, 41-54.

Fordham, C.J. 1988. "Behavior of Granular Halite for Use as a Backfill in Potash Mines." Ph.D. dissertation. Waterloo, Ontario, Canada: University of Waterloo. (Not available from UMI, University Microfilms International, Ann Arbor, MI. Available at University of Waterloo Library, Waterloo, Ontario as: CA2ONUW 42088B25.)

Fossum, A.F., G.D. Callahan, L.L. Van Sambeek, and P.E. Senseny. 1988. "How Should One-Dimensional Laboratory Equations be Cast Into Three-Dimensional Form?," *Key Questions in Rock Mechanics, Proceedings of the 29th U.S. Symposium on Rock Mechanics, University of Minnesota, Minneapolis, MN, June 13-15, 1988.* Eds. P.A. Cundall, R.L. Sterling, and A.M. Starfield. Brookfield, VT: A.A. Balkema. 35-41.

Frane, J.W., L. Engelman, and J. Toporek. 1985. *BMDP Programmer's Guide and Subroutine Writeups: Documentation of the FORTRAN Source. Part I. Programmer's Guide. Part II. Subroutine and Common Block Writeups.* BMDP Technical Report No. 55. Los Angeles, CA: BMDP Statistical Software, Department of Biomathematics, University of California.

Gurson, A.L. 1977. "Continuum Theory of Ductile Rupture by Void Nucleation and Growth. I. Yield Criteria and Flow Rules for Porous Ductile Media," *Transactions of the ASME. Series H, Journal of Engineering Materials and Technology.* Vol. 99, no. 1, 2-15.

Hansen, F.D., and E.H. Ahrens. 1996. "Large-Scale Dynamic Compaction of Natural Salt," *4th International Conference on the Mechanical Behavior of Salt, École Polytechnique de Montréal, Mineral Engineering Department, Québec, Canada, June 17-18, 1996.* SAND96-0792C.

Helle, A.S., K.E. Easterling, and M.F. Ashby. 1985. "Hot-Isostatic Pressing Diagrams: New Developments," *Acta Metallurgica.* Vol. 33, no. 12, 2163-2174.

Hill, M.A. 1984. *BMDP User's Digest: A Condensed Guide to the BMDP Computer Program.* 3rd ed. Los Angeles, CA: BMDP Statistical Software, Inc. (Copy on file in the Sandia WIPP Central Files, Sandia National Laboratories, Albuquerque, NM as WPO#48077.)

Holcomb, D.J., and M. Shields. 1987. *Hydrostatic Creep Consolidation of Crushed Salt with Added Water.* SAND87-1990. Albuquerque, NM: Sandia National Laboratories.

Kuhn, L.T., and R.M. McMeeking. 1992. "Power-Law Creep of Powder Bonded by Isolated Contacts," *International Journal of Mechanical Sciences.* Vol. 34, no. 7, 563-573.

Kwon, Y.S., and K.T. Kim. 1996a. "High Temperature Densification Forming of Alumina Powder—Constitutive Model and Experiments," *Transactions of the ASME. Journal of Engineering Materials and Technology.* Vol. 118, no. 4, 448-455.

Kwon, Y.S., and K.T. Kim. 1996b. "Densification Forming of Alumina Powder—Effects of Power Law Creep and Friction," *Transactions of the ASME. Journal of Engineering Materials and Technology.* Vol. 118, no. 4, 471-477.

Montgomery, D.C., and E.A. Peck. 1982. *Introduction to Linear Regression Analysis.* New York, NY: John Wiley & Sons.

Munson, D.E. 1979. *Preliminary Deformation-Mechanism Map for Salt (with Application to WIPP).* SAND79-0076. Albuquerque, NM: Sandia National Laboratories.

Munson, D.E., and P.R. Dawson. 1979. *Constitutive Model for the Low Temperature Creep of Salt (with Application to WIPP).* SAND79-1853. Albuquerque, NM: Sandia National Laboratories.

Munson, D.E., A.F. Fossum, and P.E. Senseny. 1989. *Advances in Resolution of Discrepancies Between Predicted and Measured In Situ WIPP Room Closures*. SAND88-2948. Albuquerque, NM: Sandia National Laboratories.

Pfeifle, T.W. 1995. "WIPP Crushed Salt Database for Constitutive Model Evaluations." Calculation File 325/04/03. Prepared for Sandia National Laboratories, Albuquerque, NM. Rapid City, SD: RE/SPEC Inc. (Copy on file in the Sandia WIPP Central Files, Sandia National Laboratories, Albuquerque, NM as WPO#36823.)

Pfeifle, T.W., and P.E. Senseny. 1985. "Permeability and Consolidation of Crushed Salt from the WIPP Site." Topical Report RSI-0278. Prepared for Sandia National Laboratories, Albuquerque, NM. Rapid City, SD: RE/SPEC Inc. (Copy on file in the Sandia WIPP Central Files, Sandia National Laboratories, Albuquerque, NM as WPO#36824.)

Ponte Castaneda, P., and J.R. Willis. 1988. "On the Overall Properties of Nonlinearly Viscous Composites," *Proceedings of the Royal Society of London, Series A*. Vol. 416, no. 1850, 217-244.

RE/SPEC Inc. 1996. "Crushed-Salt Constitutive Model Refinement." Calculation No. 325/04/05. Prepared for Sandia National Laboratories, Albuquerque, NM. Rapid City, SD: RE/SPEC Inc. (Copy on file in the Sandia WIPP Central Files, Sandia National Laboratories, Albuquerque, NM as WPO#48071.)

Sjaardema, G.D., and R.D. Krieg. 1987. *A Constitutive Model for the Consolidation of WIPP Crushed Salt and Its Use in Analyses of Backfilled Shaft and Drift Configurations*. SAND87-1977. Albuquerque, NM: Sandia National Laboratories.

Sofronis, P., and R.M. McMeeking. 1992. "Creep of Power-Law Material Containing Spherical Voids," *Transactions of the ASME, Journal of Applied Mechanics*. Vol. 59, no. 2, pt. 2, S88-S95.

Spiers, C.J., and R.H. Brzesowsky. 1993. "Densification Behaviour of Wet Granular Salt: Theory Versus Experiments," *Seventh Symposium on Salt, Kyoto, Japan, April 6-9, 1992*. Eds. H. Kakihana, H.R. Hardy, Jr., T. Hoshi, and K. Toyokura. Amsterdam; New York: Elsevier. Vol. 1, 83-92. (Copy on file in the Sandia WIPP Central Files, Sandia National Laboratories, Albuquerque, NM as WPO#39215.)

Spiers, C.J., and P.M.T.M. Schutjens. 1990. "Densification of Crystalline Aggregates by Fluid-Phase Diffusional Creep," *Deformation Processes in Minerals, Ceramics and Rocks, London, England, April 1987*. Eds. D.J. Barber and P.G. Meredith. Mineralogical Series 1. London; Boston: Unwin Hyman. 334-353.

Spiers, C.J., C.J. Peach, R.H. Brzesowsky, P.M.T.M. Schutjens, J.L. Liezenberg, and H.J. Zwart. 1989. *Long-Term Rheological and Transport Properties of Dry and Wet Salt Rocks. Final Report.* Nuclear Science and Technology Series. EUR 11848 EN. Luxembourg: Office for Official Publications of the European Communities. (Copy on file in the Sandia WIPP Central Files, Sandia National Laboratories, Albuquerque, NM as WPO#48013.)

Stocker, R.L., and M.F. Ashby. 1973. "On the Rheology of the Upper Mantle," *Reviews of Geophysics and Space Physics.* Vol. 11, no. 2, 391-426.

Tvergaard, V. 1981. "Influence of Voids on Shear Band Instabilities Under Plane Strain Conditions," *International Journal of Fracture.* Vol. 17, no. 4, 389-407.

Wang, M.L., S.K. Miao, A.K. Maji, and C.L. Hwang. 1992. "Effect of Water on the Consolidation of Crushed Rock Salt," *Proceedings of the 9th Conference on Engineering Mechanics, College Station, TX, May 24-27, 1992.* New York, NY: American Society of Civil Engineers. 531-534.

Wilkinson, D.S., and M.F. Ashby. 1975. "Pressure Sintering by Power Law Creep," *Acta Metallurgica.* Vol. 23, no. 11, 1277-1285.

Yost, F.G., and E.A. Aronson. 1987. *Crushed Salt Consolidation Kinetics.* SAND87-0264. Albuquerque, NM: Sandia National Laboratories.

Zeuch, D.H. 1990. "Isostatic Hot-Pressing Mechanism Maps for Pure and Natural Sodium Chloride: Applications to Nuclear Waste Isolation in Bedded and Domal Salt Formations," *International Journal of Rock Mechanics and Mining Sciences & Geomechanics Abstracts.* SAND88-2207J. Vol. 27, no. 6, 505-524.

Zeuch, D.H., and D.J. Holcomb. 1991. *Experimental and Modeling Results for Reconsolidation of Crushed Natural Rock Salt Under Varying Physical Conditions.* SAND90-2509. Albuquerque, NM: Sandia National Laboratories.

Zeuch, D.H., D.J. Zimmerer, and M.E. Shields. 1991. *Interim Report on the Effects of Brine-Saturation and Shear Stress on Consolidation of Crushed, Natural Rock Salt from the Waste Isolation Pilot Plant (WIPP).* SAND91-0105. Albuquerque, NM: Sandia National Laboratories.

APPENDIX A

Input Files to BMDP, Nonlinear Regression Programs 3R and AR

This appendix contains three input files. The first file (FLOW.INP) was the input file to the Program 3R and was used to determine the flow rate parameters. The second and third files (MDSP2.INP and MDSP3.INP) were the input files to the Program AR. The files were used to determine two sets of the creep consolidation parameters fit to the shear consolidation database (MDSP2.INP) and the combined shear and hydrostatic consolidation database (MDSP3.INP).

```
#    file = e:\325\md\flow.inp
#
#          fit to shear consolidation tests only (itype = 2)
#
# ================================================================
#
#    This code uses the BMDP routine AR to fit the differential
#    equations that describe the axial and lateral strain rates
#    as functions of the following test conditions:
#       1.  mean stress                              (MS)
#       2.  stress difference                        (DS)
#       3.  emplaced fractional density              (D0)
#       4.  initial fractional density               (DI)
#       5.  grain size                               (DD)
#       6.  absolute temperature                     (T)
#       7.  moisture content                         (W)
#
# ================================================================
#
# ------  INPUT PARAGRAPH
#
/INPUT
    TITLE = 'SPIERS MODEL FIT TO SHEAR CONSOLIDATION TESTS -- sp.INP'.
    FILE = 'E:\325\MD\flow.dat'.                    # Data file name
    FORMAT = '(2I3,3F10.0,F6.1,2F9.4,4F9.5,F9.3,F9.6,
              2F9.3,F5.2,F7.2,3e10.3)'.
    VARIABLES = 21.
#
# ------  VARIABLES PARAGRAPH  ------
#
/VARIABLE
  NAMES=ICASE,ITEST,TIME,DT,TF,TEMP,AS,LS,EVT,EVC,EAT,EAC,RHO,D,
        RHO0,RHOI,DD,W,EVR,EAR,ELR.
#
# ------  TRANSFORMATION PARAGRAPH ------
#
/TRANS
     MS = (2.0*LS+AS)/3.0.      # mean stress, as=axial stress, ls=conf. pres.
     DS = LS - AS.              # stress difference
    ELC = (EVC - EAC)/2.        # lateral strain, evt=vol. strain, eat=ax.strain
     D0 = 1382.4/2160.          # emplaced fractional density
     DI = RHOI/2160.            # initial fractional density
    RAT = ELR/EAR.              # regression function

#    FLOW PARAMETERS

     KAP0 = .0952.
      KAP1 = 1.412.
      KAP2 = 1.001.
       DDT = .89098.
        NK = 7.578.

    USE = TIME NE 0.          # use shear consolidation tests
     WT = 1.           # uniform weight function
#
# ------  REGRESS PARAGRAPH  ------
#
/REGRESS
      DEPEND = RAT.             # Dependent variable
      PARAMETERS=1.            # Number of regression parameters
      WEIGHT = WT.              # WEIGHT VARIABLE
      ITER = 1.                 # NUMBER OF ITERATIONS
      HALVINGS = 2.             # NUMBER OF INTERVAL HALVINGS
#
# ------  PARAMETERS PARAGRAPH  ------
#
#    Specify the names, initial estimates, and the range of the sixteen
# regression parameters, where R1 is the over all leading parameter; R3, R4,
# and N are strain dependent parameters; KAPPA0, KAPPA1, KAPPA2, M2 determine
# the equivalent stress measure for the flow-rule; ETA0, ETA1, ETA2, and M1
# determine the equivalent stress measure in strain rate measure; A1 and A2
# are water-content dependent parameters; P defines grain size dependence;
# and QCR defines temperature effect.
#
/PARAMETER
     NAMES =     DUM.

   INITIAL =   1.0.
```

```
MINIMUM =       0.0.
MAXIMUM =       50.0.
#
# ------  SPECIFY FUNCTION  ------
#
/FUN
     IF(D LE DDT) THEN VAR = DDT.
     IF(D GT DDT) THEN VAR = D.
     NUM = (1 - VAR)*NK.
     DEN = (1 -(1-VAR)**(1/NK) ) ** NK.
     OMEGAK = (NUM/DEN) ** (2/(NK+1)).
     KAP = KAP0 * OMEGAK**KAP1.
    TERMK = ( (2-D)/D )**( 2*NK/(NK+1) ).

  ALPHA2 = KAP * MS/3.
   BETA2 = KAP2 * TERMK * DS.

     F2A = (ALPHA2 -     BETA2).
     F2L = (ALPHA2 + 0.5*BETA2).
       F = F2L/F2A.
#
# ------  SPECIFY VARIOUS PRINTING AND PLOTTING OPTIONS  ------
#
/SAVE
      FILE = 'E:\325\MD\flow.SAV'.
      NEW.
      KEEP = rho,RAT.
      FORMAT = '(f10.3,5E12.3)'.
/PRINT
          FORMAT = E.
/PLOT
          RESIDUAL.
/END
```

```
#    file = e:\dynamic\MDsp2.inp
#
#          fit to shear consolidation tests only (itype = 2)
#
# ================================================================
#
#    This code uses the BMDP routine AR to fit the differential
#    equations that describe the axial and lateral strain rates
#    as functions of the following test conditions:
#       1.  mean stress                                  (MS)
#       2.  stress difference                            (DS)
#       3.  emplaced fractional density                  (D0)
#       4.  initial fractional density                   (DI)
#       5.  grain size                                   (DD)
#       6.  absolute temperature                         (T)
#       7.  moisture content                             (W)
#
# ================================================================
#
# ------  INPUT PARAGRAPH
#
/INPUT
    TITLE = 'MD-SPIERS MODEL FIT TO shear CONSOLIDATION TESTS -- MDsp2.INP'.
    FILE = 'e:\325\md\ALL.CSV'.                    # Data file name
    FORMAT = '(2I3,3F10.0,F6.1,2F9.4,4F9.5,F9.3,F9.6,2F9.3,F5.2,F7.2)'.
    VARIABLES = 18.
#
# ------  VARIABLES PARAGRAPH  ------
#
/VARIABLE
  NAMES=ICASE,ITEST,TIME,DT,TF,TEMP,AS,LS,EVT,EVC,EAT,EAC,RHO,D,RHO0,RHOI,DD,W.
#
# ------  TRANSFORMATION PARAGRAPH ------
#
/TRANS
     MS = (2.0*LS+AS)/3.0.       # mean stress, as=axial stress, ls=conf. pres.
     DS = LS - AS.               # stress difference
    ELC = (EVC - EAC)/2.         # lateral strain, evt=vol. strain, eat=ax.strain
#    ELT = (EVT - EAT)/2.
#     DIFL = ELT-ELC.
#     DIFA = EAT-EAC.
     D0 = 1382.4/2160.           # emplaced fractional density
#     D02 = RHO0/2160.
     DI = RHOI/2160.             # initial fractional density
    ONE = 1.0.                   # regression function

#   17 MUNSON-DAWSON CREEP PARAMETERS FOR CLEAN SALT (FIXED)

     A1 = 8.386E+22.
     A2 = 9.672E+12.
    Q1R = 12581.
    Q2R = 5033.
     N1 = 5.5.
     N2 = 5.0.
     B1 = 6.0856E+6.
     B2 = 3.034E-2.
      Q = 5335.
     S0 = 20.57.
      M = 3.
     K0 = 6.275E+5.
      C = 9.198E-3.
  ALPHA = -17.37.
   BETA = -7.738.
  DELTA = 0.58.
     MU = 12400.                 # SHEAR MODULUS

#    USE SHEAR CONSOLIDATION TESTS

   USE = ICASE EQ 2.

#    ELIMINATE SNL SATURATED HYDROSTATIC TESTS

     IF(KASE GE 4001 AND KASE LE 4500) THEN USE = 0.

#    WEIGHT FUNCTIONS

     WT1 = DT/1.E+6.
     WT = 1.0.                   # uniform weight function
```

```
#    ESTIMATE GRAIN SIZE FOR DCCS TESTS

     DC = DD.
     IF(KASE GT 5700) THEN DC = 0.5.
#
# ------  REGRESS PARAGRAPH  ------
#
/REGRESS
      DEPEND = ONE.              # Dependent variable
      PARAMETERS=17.             # Number of regression parameters
      WEIGHT = WT.               # WEIGHT VARIABLE
      ITIME = 3.                 # INTEGRATION VARIABLE NUMBER
      NEQN = 3.                  # Number of differential equations
      ITER = 1.                 # NUMBER OF ITERATIONS
      HALVINGS = 3.              # NUMBER OF INTERVAL HALVINGS
      MAXC = 300000.             # MAXIMUM NUMBER OF TIMES 'DIFEQ' IS USED
#
# ------  PARAMETERS PARAGRAPH  ------
#
#    Specify the names, initial estimates, and the range of the sixteen
# regression parameters, where R1 is the over all leading parameter; R3, R4,
# and N are strain dependent parameters; KAPPA0, KAPPA1, KAPPA2, M2 determine
# the equivalent stress measure for the flow-rule; ETA0, ETA1, ETA2, and M1
# determine the equivalent stress measure in strain rate measure; A1 and A2
# are water-content dependent parameters; P defines grain size dependence;
# and QCR defines temperature effect.
#
/PARAMETER
     NAMES =     KAP0,          KAP1,      KAP2, DUM,
                   NK,           DDT,        NA,

                 ETA0,          ETA1,      ETA2,
                  AA1,            PP,       NSP,
                   R1,            R3,        R4, QSR.

   INITIAL =  0.0952,         1.41202,    1.001, 1.00,
              7.5776,         0.89098,    3.735,

             .1424,        3.254,      3.424,
              0.2269,          1.1248,      .1038,
             2.68e-4,          7.26,      .1440,  1028.5.

MINIMUM =       16 * -10.0.
MAXIMUM =       16 * 5000.0.
#DELTA   =       6*.1,
#                6*.05,
#                1E-3,       1, .05.
  FIXED = KAP0, KAP1, KAP2,
            NK,  DDT,  na,
          eta0, eta1, eta2,
           aa1,   pp,  nsp,
            r1,   r3,   r4,     qsr.

# ------  INITIAL VALUES FOR DIFERENTIAL EQUATIONS  ------
#
/DIFIN
      Z1 = EAC.
      Z2 = ELC.
      Z3 = 0.
#
# ------  SPECIFY THE DIFFERENTIAL EQUATION  ------
#
/DIFEQ
     IF(TIME NE 0) THEN (

     VOL = Z1 + 2*Z2.
     VOLT = VOL + LN(0.64/DI).
     DEN = DI / EXP(VOL).

  IF(DEN GE 1.0) THEN (
        MD = 0.
        SP = 0. ).

  IF(DEN LT 1.0) THEN (

     IF(DEN LE DDT) THEN VAR = DDT.
     IF(DEN GT DDT) THEN VAR = DEN.
```

```
     OMEGAA = ((1.-DEN)*NA / (1-(1-DEN)**(1/NA))**NA)**(2/(NA+1)).
     OMEGAK = ((1.-VAR)*NK / (1-(1-VAR)**(1/NK))**NK)**(2/(NK+1)).
     ETA = ETA0 * OMEGAA**ETA1.
     KAP = KAP0 * OMEGAK**KAP1.
    TERMA = ((2-DEN)/DEN)**(2*NA/(NA+1)).
    TERMK = ((2-DEN)/DEN)**(2*NK/(NK+1)).
    SEQF = SQRT(ETA * MS**2 + ETA2 * TERMA * DS**2).
    SEQ  = SQRT(KAP * MS**2 + KAP2 * TERMK * DS**2).

  ALPHA2 = KAP * MS/3.
   BETA2 = KAP2 * TERMK * DS.

     F2A = (ALPHA2 -     BETA2) / SEQ.
     F2L = (ALPHA2 + 0.5*BETA2) / SEQ.

      ES1 = A1*(SEQF/MU)**N1 * EXP (-Q1R / TEMP).
      ES2 = A2*(SEQF/MU)**N2 * EXP (-Q2R / TEMP).
      ES3 = 0.

      IF(SEQF GT S0) THEN (
        ARG = Q * (SEQF-S0)/MU.
        ES3 = 0.5*( B1*EXP(-Q1R/TEMP) + B2*EXP(-Q2R/TEMP) )
            * ( EXP(ARG) - EXP(-ARG) ) .).

      ESS = ES1 + ES2 + ES3.

      EFT = K0*EXP(C*TEMP)*(SEQF/MU)**M.
      BIGD = ALPHA + BETA * LOG(SEQF/MU).

      IF(Z3 LT EFT) THEN F = EXP(  BIGD*(1-Z3/EFT)**2).
      IF(Z3 EQ EFT) THEN F = 1.
      IF(Z3 GT EFT) THEN F = EXP(-DELTA*(1-Z3/EFT)**2).

      MD = F * ESS.

      CR = ABS(EXP(VOLT)-1).

      IF(CR LE 0.15) THEN GAMMA = 1.0.
      IF(CR GT 0.15) THEN
         GAMMA = (ABS((D0-EXP(VOLT))/((1-D0)*EXP(VOLT))))**NSP.

      X3 = EXP((R3-1)*VOLT)/(ABS(1-EXP(VOLT)))**R4.

      IF(W EQ 0) THEN M2 = 0.
      IF(W GT 0) THEN M2 = W**AA1.
      G2 = 1/DC**PP.
      T2 = EXP(-QSR/TEMP)/TEMP.

      SP = R1*M2*G2*T2*X3*GAMMA*SEQF.).

     DZ1 = (MD + SP) * F2A.
     DZ2 = (MD + SP) * F2L.
     DZ3 = (F-1) * ESS.    ).

     IF(TIME EQ 0) THEN (

     DZ1 = 0.
     DZ2 = 0.
     DZ3 = 0.    ).
#
#  ------  SPECIFY THE DEPENDENT VARIABLE FUNCTION
#
/FUN
  IF(TIME NE 0.) THEN (
      AA = Z1/EAC.
      BB = Z2/ELC.
       F = 1.0 - SQRT(((1.0-AA)**2 + (1.0-BB)**2)*WT1).  ).
  IF(TIME EQ 0.) THEN (
     NEW = 0.
      Z1 = EAC.
      Z2 = ELC.
      Z3 = 0.
       F = 1.0 ).
#
#  ------  SPECIFY VARIOUS PRINTING AND PLOTTING OPTIONS  ------
#
/SAVE
      FILE = 'e:\325\md\MDSP2.SAV'.
```

```
#    file = e:\dynamic\MDsp3.inp
#
#          fit to hydrostatic and shear consolidation tests only (itype = 1 and 2)
#
# ================================================================
#
#    This code uses the BMDP routine AR to fit the differential
#    equations that describe the axial and lateral strain rates
#    as functions of the following test conditions:
#       1.  mean stress                                  (MS)
#       2.  stress difference                            (DS)
#       3.  emplaced fractional density                  (D0)
#       4.  initial fractional density                   (DI)
#       5.  grain size                                   (DD)
#       6.  absolute temperature                         (T)
#       7.  moisture content                             (W)
#
# ================================================================
#
# ------   INPUT PARAGRAPH
#
/INPUT
    TITLE = 'MD-SPIERS MODEL FIT TO ALL CONSOLIDATION TESTS -- MDsp3.INP'.
    FILE = 'e:\325\md\ALL.CSV'.                    # Data file name
    FORMAT = '(2I3,3F10.0,F6.1,2F9.4,4F9.5,F9.3,F9.6,2F9.3,F5.2,F7.2)'.
    VARIABLES = 18.
#
# ------   VARIABLES PARAGRAPH  ------
#
/VARIABLE
  NAMES=ICASE,ITEST,TIME,DT,TF,TEMP,AS,LS,EVT,EVC,EAT,EAC,RHO,D,RHO0,RHOI,DD,W.
#
# ------   TRANSFORMATION PARAGRAPH ------
#
/TRANS
     MS = (2.0*LS+AS)/3.0.       # mean stress, as=axial stress, ls=conf. pres.
     DS = LS - AS.               # stress difference
    ELC = (EVC - EAC)/2.         # lateral strain, evt=vol. strain, eat=ax.strain
#    ELT = (EVT - EAT)/2.
#     DIFL = ELT-ELC.
#     DIFA = EAT-EAC.
     D0 = 1382.4/2160.           # emplaced fractional density
#     D02 = RHO0/2160.
     DI = RHOI/2160.             # initial fractional density
    ONE = 1.0.                   # regression function

#   17 MUNSON-DAWSON CREEP PARAMETERS FOR CLEAN SALT (FIXED)

     A1 = 8.386E+22.
     A2 = 9.672E+12.
    Q1R = 12581.
    Q2R = 5033.
     N1 = 5.5.
     N2 = 5.0.
     B1 = 6.0856E+6.
     B2 = 3.034E-2.
      Q = 5335.
     S0 = 20.57.
      M = 3.
     K0 = 6.275E+5.
      C = 9.198E-3.
  ALPHA = -17.37.
   BETA = -7.738.
  DELTA = 0.58.
     MU = 12400.                 # SHEAR MODULUS

#    USE SHEAR CONSOLIDATION TESTS

#    USE = ICASE EQ 2.

#    ELIMINATE SNL SATURATED HYDROSTATIC TESTS

     IF(KASE GE 4001 AND KASE LE 4500) THEN USE = 0.

#    WEIGHT FUNCTIONS

     WT1 = DT/1.E+6.
     WT = 1.0.                   # uniform weight function
```

```
#    ESTIMATE GRAIN SIZE FOR DCCS TESTS

     DC = DD.
     IF(KASE GT 5700) THEN DC = 0.5.
#
# ------  REGRESS PARAGRAPH  ------
#
/REGRESS
      DEPEND = ONE.              # Dependent variable
      PARAMETERS=17.             # Number of regression parameters
      WEIGHT = WT.               # WEIGHT VARIABLE
      ITIME = 3.                 # INTEGRATION VARIABLE NUMBER
      NEQN = 3.                  # Number of differential equations
      ITER = 1.                 # NUMBER OF ITERATIONS
      HALVINGS = 3.              # NUMBER OF INTERVAL HALVINGS
      MAXC = 300000.             # MAXIMUM NUMBER OF TIMES 'DIFEQ' IS USED
#
# ------  PARAMETERS PARAGRAPH  ------
#
#    Specify the names, initial estimates, and the range of the sixteen
# regression parameters, where R1 is the over all leading parameter; R3, R4,
# and N are strain dependent parameters; KAPPA0, KAPPA1, KAPPA2, M2 determine
# the equivalent stress measure for the flow-rule; ETA0, ETA1, ETA2, and M1
# determine the equivalent stress measure in strain rate measure; A1 and A2
# are water-content dependent parameters; P defines grain size dependence;
# and QCR defines temperature effect.
#
/PARAMETER
     NAMES =     KAP0,          KAP1,     KAP2, DUM,
                   NK,           DDT,       NA,

                 ETA0,          ETA1,     ETA2,
                  AA1,            PP,      NSP,
                   R1,            R3,       R4, QSR.

   INITIAL =  0.0952,         1.41202,    1.001, 1.00,
               7.5776,        0.89098,    4.792,

              2.736e-2,        2.587,     4.21,
                0.0230,          .649,    -2.277e-2,
              3.834e-4,         11.12,     .6003,  811.28.

MINIMUM =       16 * -10.0.
MAXIMUM =       16 * 5000.0.
#DELTA   =       6*.1,
#               6*.05,
#               1E-3,       1, .05.
  FIXED = KAP0, KAP1, KAP2,
            NK,  DDT,   na,
          eta0, eta1, eta2,
           aa1,   pp,  nsp,
            r1,   r3,   r4,   qsr.

# ------  INITIAL VALUES FOR DIFERENTIAL EQUATIONS  ------
#
/DIFIN
      Z1 = EAC.
      Z2 = ELC.
      Z3 = 0.
#
# ------  SPECIFY THE DIFFERENTIAL EQUATION  ------
#
/DIFEQ
     IF(TIME NE 0) THEN (

     VOL = Z1 + 2*Z2.
     VOLT = VOL + LN(0.64/DI).
     DEN = DI / EXP(VOL).

 IF(DEN GE 1.0) THEN (
       MD = 0.
       SP = 0. ).

 IF(DEN LT 1.0) THEN (

     IF(DEN LE DDT) THEN VAR = DDT.
     IF(DEN GT DDT) THEN VAR = DEN.
```

```
     OMEGAA = ((1.-DEN)*NA / (1-(1-DEN)**(1/NA))**NA)**(2/(NA+1)).
     OMEGAK = ((1.-VAR)*NK / (1-(1-VAR)**(1/NK))**NK)**(2/(NK+1)).
      ETA = ETA0 * OMEGAA**ETA1.
      KAP = KAP0 * OMEGAK**KAP1.
     TERMA = ((2-DEN)/DEN)**(2*NA/(NA+1)).
     TERMK = ((2-DEN)/DEN)**(2*NK/(NK+1)).
     SEQF = SQRT(ETA * MS**2 + ETA2 * TERMA * DS**2).
     SEQ  = SQRT(KAP * MS**2 + KAP2 * TERMK * DS**2).

  ALPHA2 = KAP * MS/3.
   BETA2 = KAP2 * TERMK * DS.

      F2A = (ALPHA2 -     BETA2) / SEQ.
      F2L = (ALPHA2 + 0.5*BETA2) / SEQ.

       ES1 = A1*(SEQF/MU)**N1 * EXP (-Q1R / TEMP).
       ES2 = A2*(SEQF/MU)**N2 * EXP (-Q2R / TEMP).
       ES3 = 0.

       IF(SEQF GT S0) THEN (
         ARG = Q * (SEQF-S0)/MU.
         ES3 = 0.5*( B1*EXP(-Q1R/TEMP) + B2*EXP(-Q2R/TEMP) )
             * ( EXP(ARG) - EXP(-ARG) ) .).

       ESS = ES1 + ES2 + ES3.

       EFT = K0*EXP(C*TEMP)*(SEQF/MU)**M.
       BIGD = ALPHA + BETA * LOG(SEQF/MU).

       IF(Z3 LT EFT) THEN F = EXP(  BIGD*(1-Z3/EFT)**2).
       IF(Z3 EQ EFT) THEN F = 1.
       IF(Z3 GT EFT) THEN F = EXP(-DELTA*(1-Z3/EFT)**2).

       MD = F * ESS.

       CR = ABS(EXP(VOLT)-1).

       IF(CR LE 0.15) THEN GAMMA = 1.0.
       IF(CR GT 0.15) THEN
          GAMMA = (ABS((D0-EXP(VOLT))/((1-D0)*EXP(VOLT))))**NSP.

       X3 = EXP((R3-1)*VOLT)/(ABS(1-EXP(VOLT)))**R4.

       IF(W EQ 0) THEN M2 = 0.
       IF(W GT 0) THEN M2 = W**AA1.
       G2 = 1/DC**PP.
       T2 = EXP(-QSR/TEMP)/TEMP.

       SP = R1*M2*G2*T2*X3*GAMMA*SEQF.).

      DZ1 = (MD + SP) * F2A.
      DZ2 = (MD + SP) * F2L.
      DZ3 = (F-1) * ESS.     ).

      IF(TIME EQ 0) THEN (

      DZ1 = 0.
      DZ2 = 0.
      DZ3 = 0.     ).
#
#  ------  SPECIFY THE DEPENDENT VARIABLE FUNCTION
#
/FUN
  IF(TIME NE 0.) THEN (
      AA = Z1/EAC.
      BB = Z2/ELC.
       F = 1.0 - SQRT(((1.0-AA)**2 + (1.0-BB)**2)*WT1).  ).
  IF(TIME EQ 0.) THEN (
     NEW = 0.
      Z1 = EAC.
      Z2 = ELC.
      Z3 = 0.
       F = 1.0 ).
#
# ------  SPECIFY VARIOUS PRINTING AND PLOTTING OPTIONS  ------
#
/SAVE
      FILE = 'e:\325\md\MDSP3.SAV'.
```

```
      NEW.
      KEEP = TIME,EAC,ELC.
      FORMAT = '(5E12.3)'.
/PRINT
          FORMAT = E.
/PLOT
          RESIDUAL.
/END
```

APPENDIX B

Lateral-to-Axial Strain Rate Ratio Model Fits to the Shear Consolidation Tests

This appendix contains the plots of the model fits to the 16 shear consolidation tests used in determining the flow potential parameters. Each plot shows the measured and predicted lateral-to-axial strain rates ratios as a function of density for each of the 16 tests.

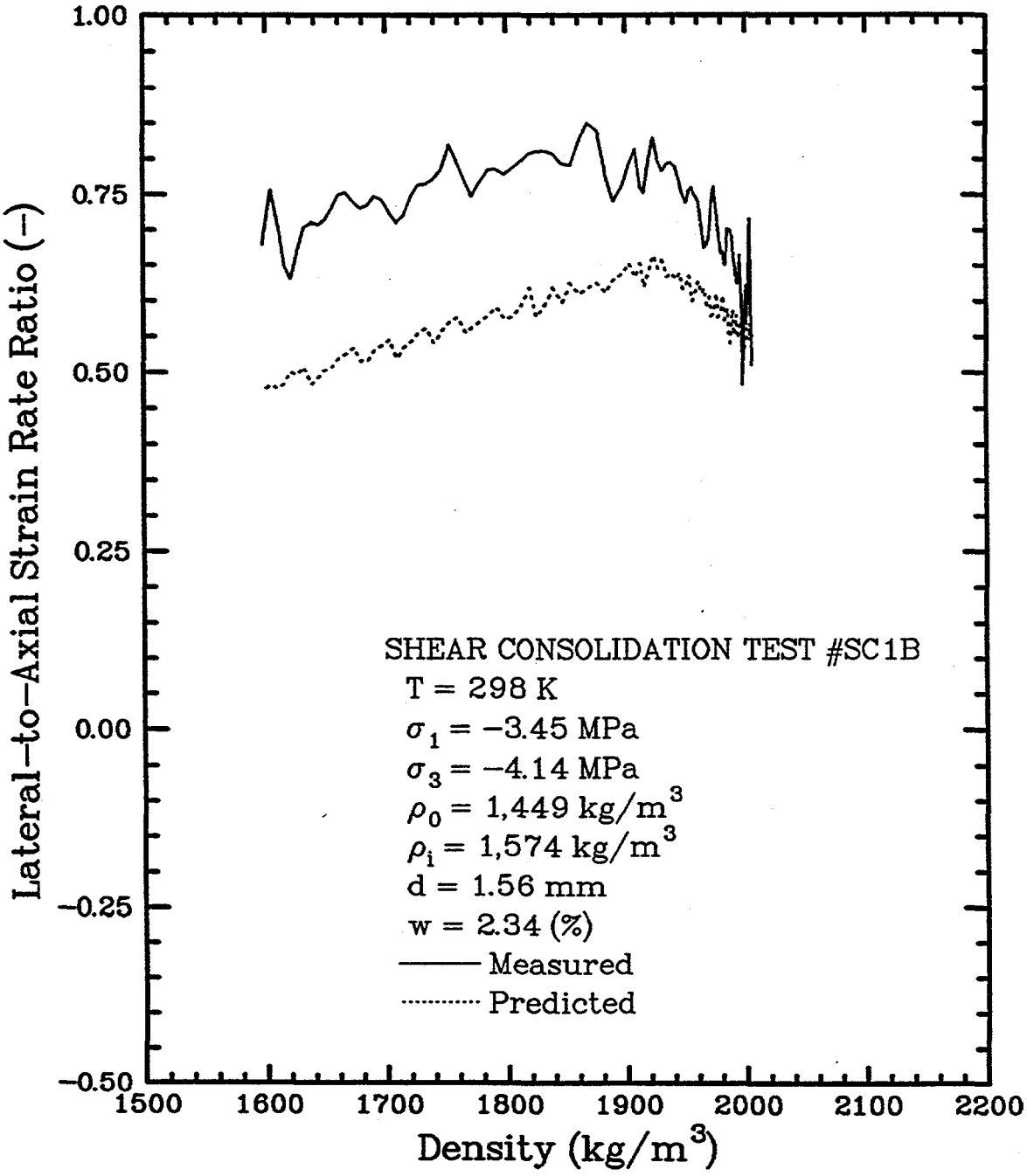

Figure B-1. Lateral-to-Axial Strain Rate Ratio as a Function of Density for Shear Consolidation Test SC1B.

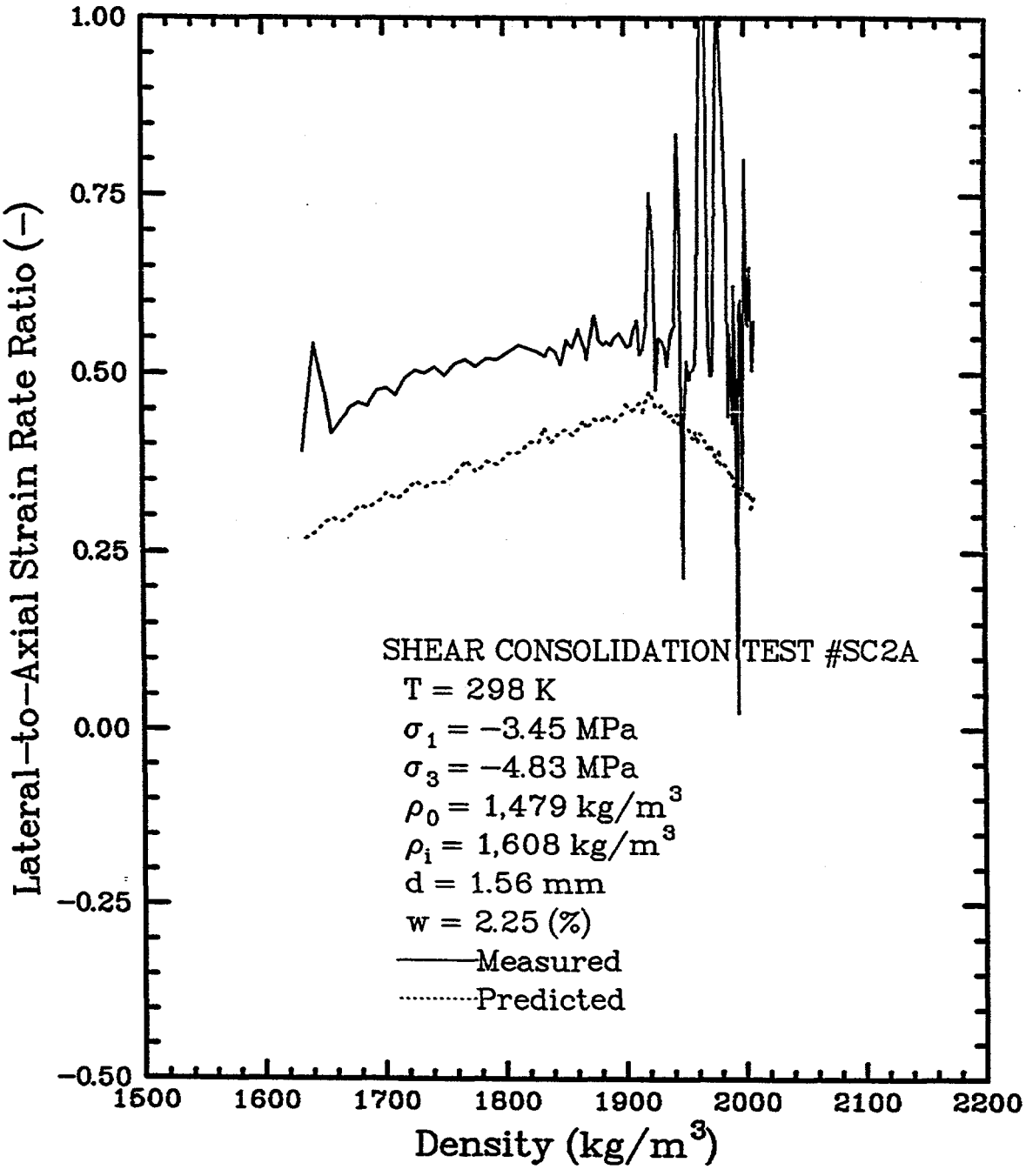

Figure B-2. Lateral-to-Axial Strain Rate Ratio as a Function of Density for Shear Consolidation Test SC2A.

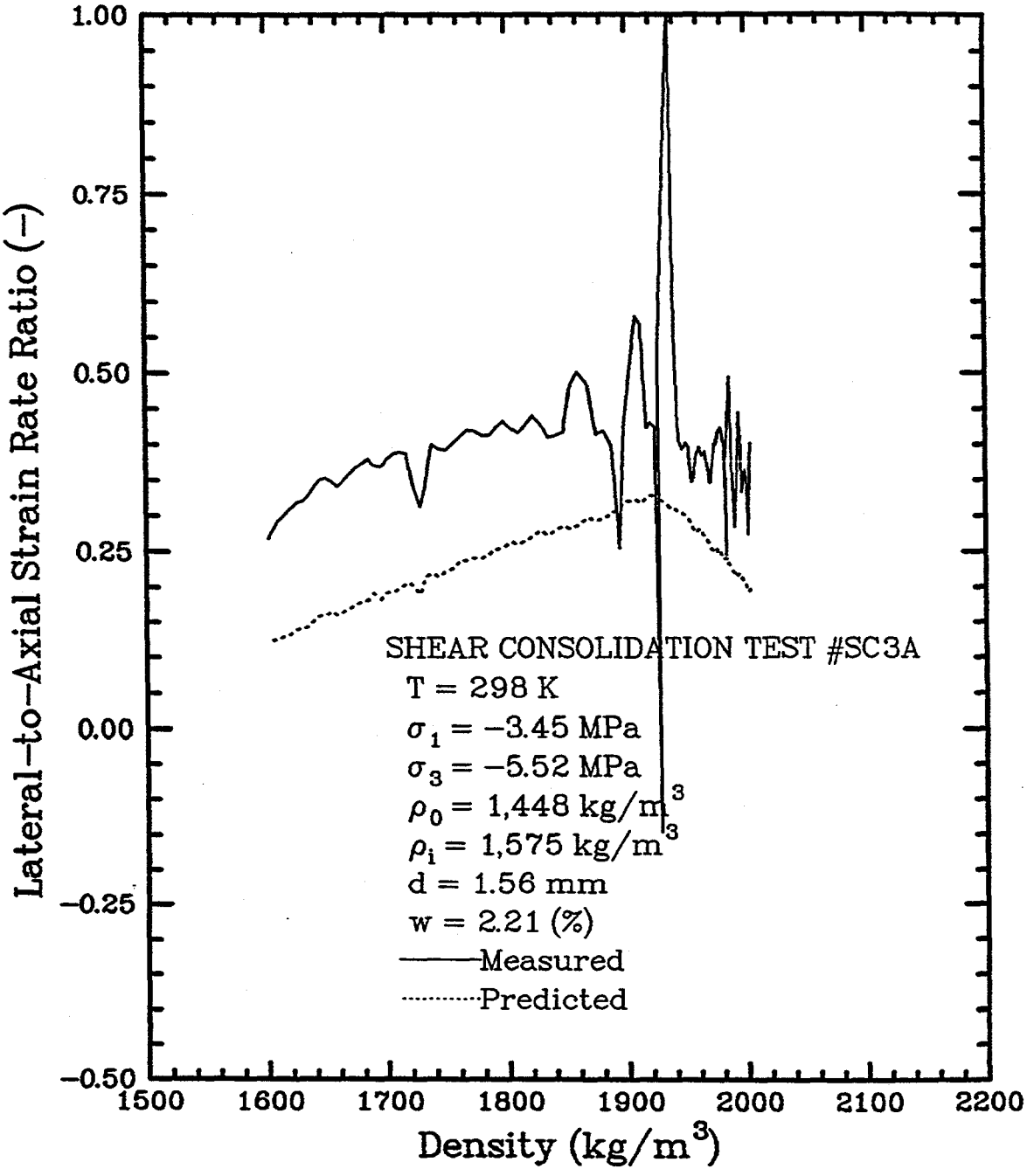

Figure B-3. Lateral-to-Axial Strain Rate Ratio as a Function of Density for Shear Consolidation Test SC3A.

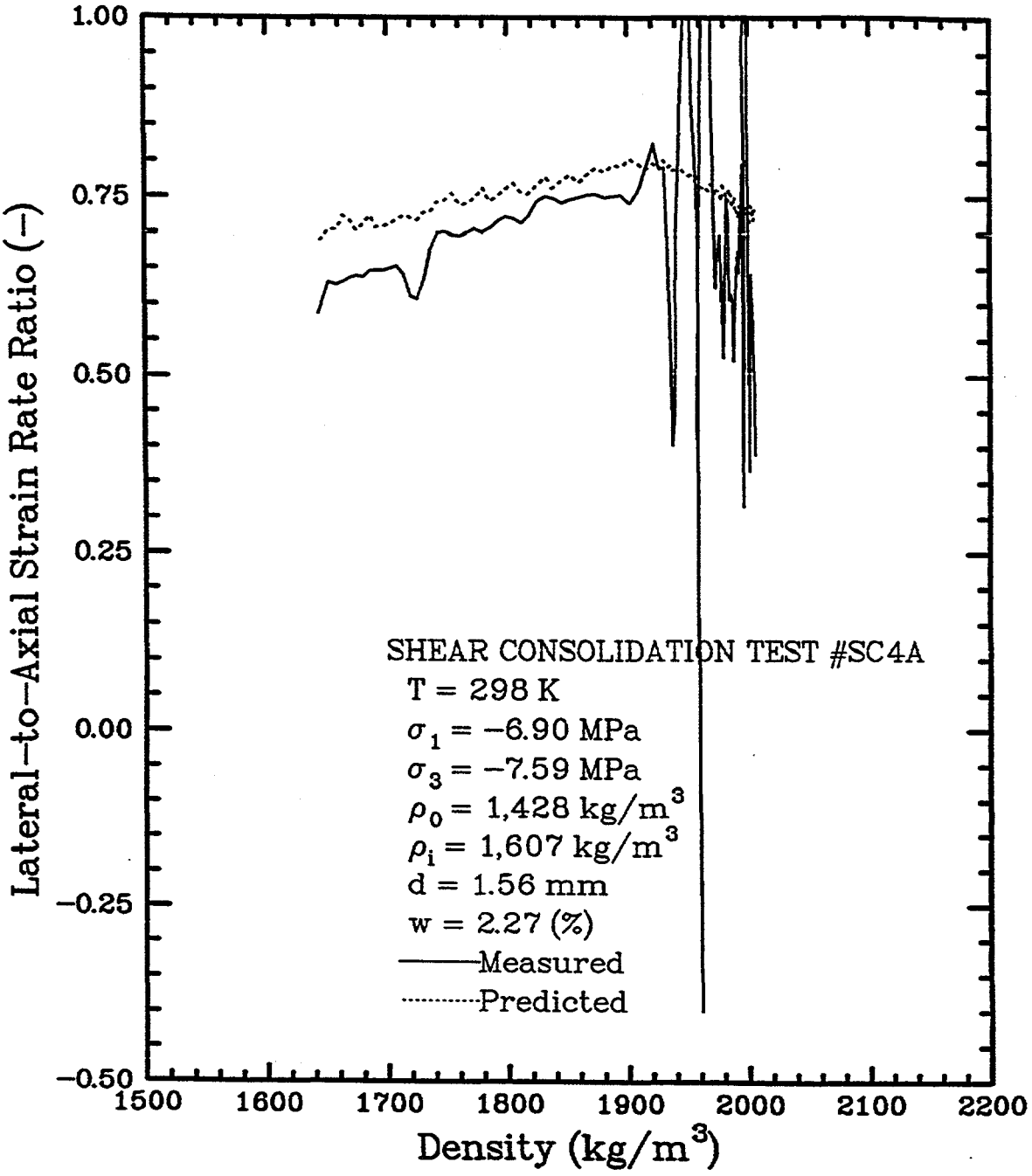

Figure B-4. Lateral-to-Axial Strain Rate Ratio as a Function of Density for Shear Consolidation Test SC4A.

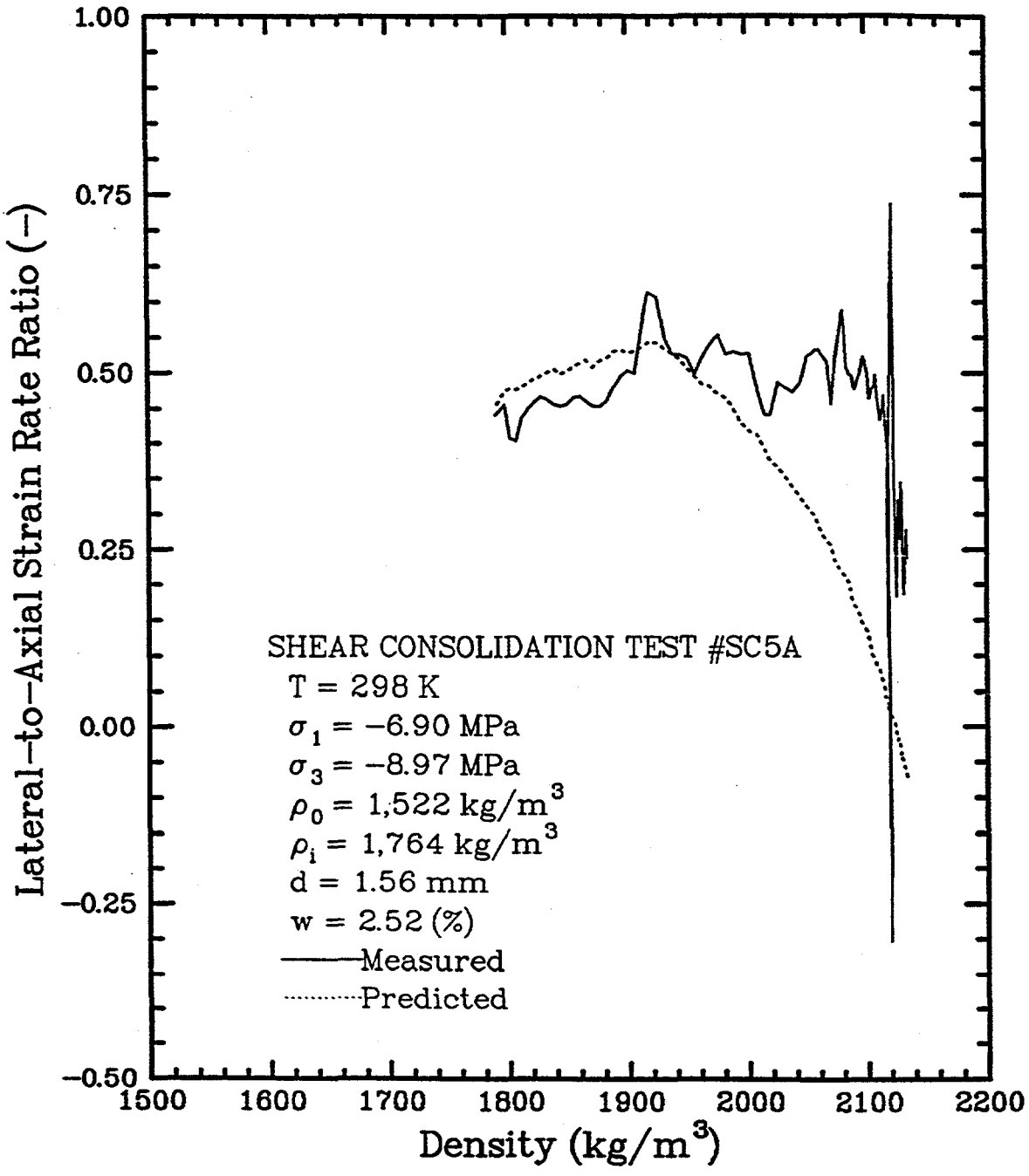

Figure B-5. Lateral-to-Axial Strain Rate Ratio as a Function of Density for Shear Consolidation Test SC5A.

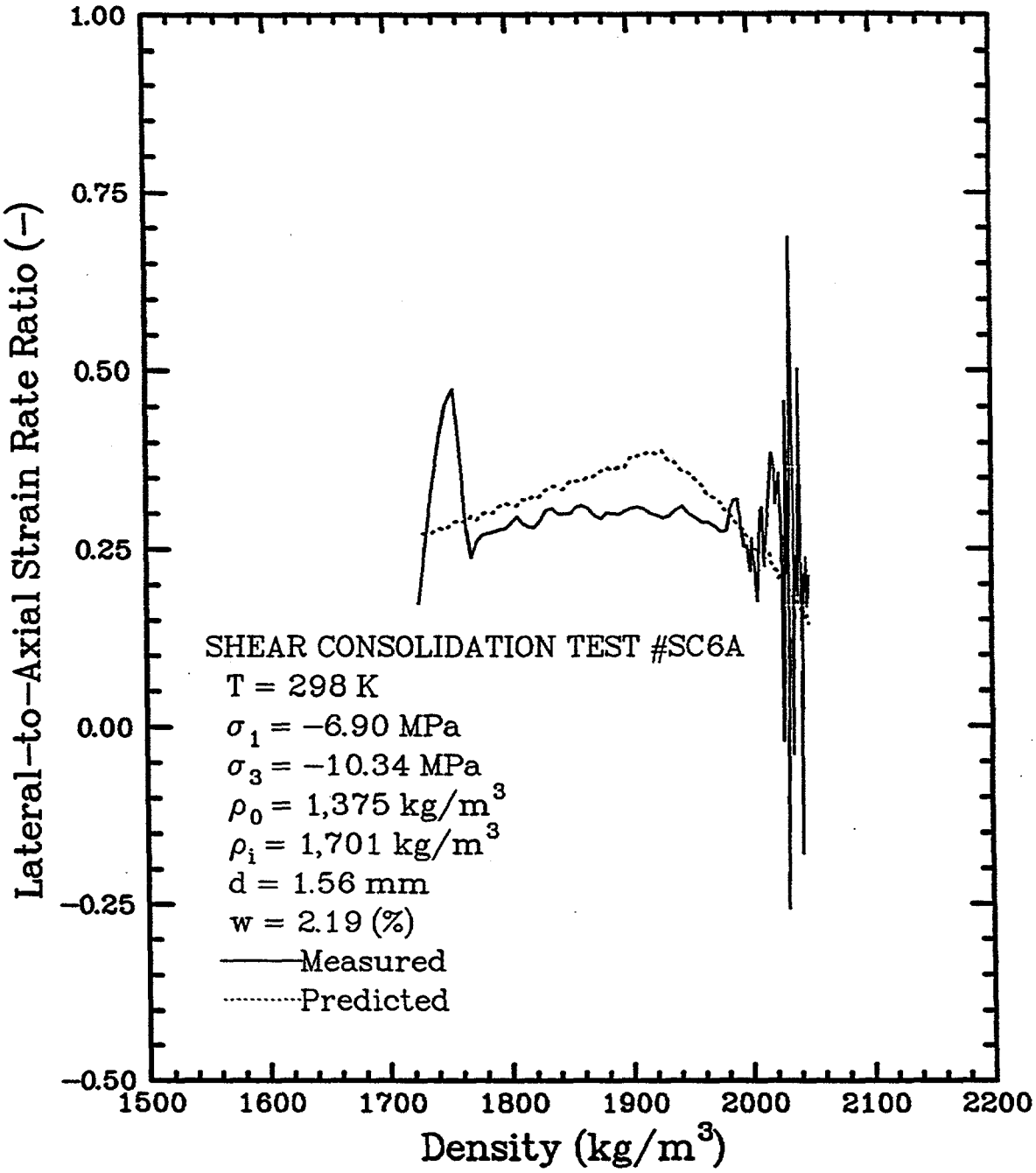

Figure B-6. Lateral-to-Axial Strain Rate Ratio as a Function of Density for Shear Consolidation Test SC6A.

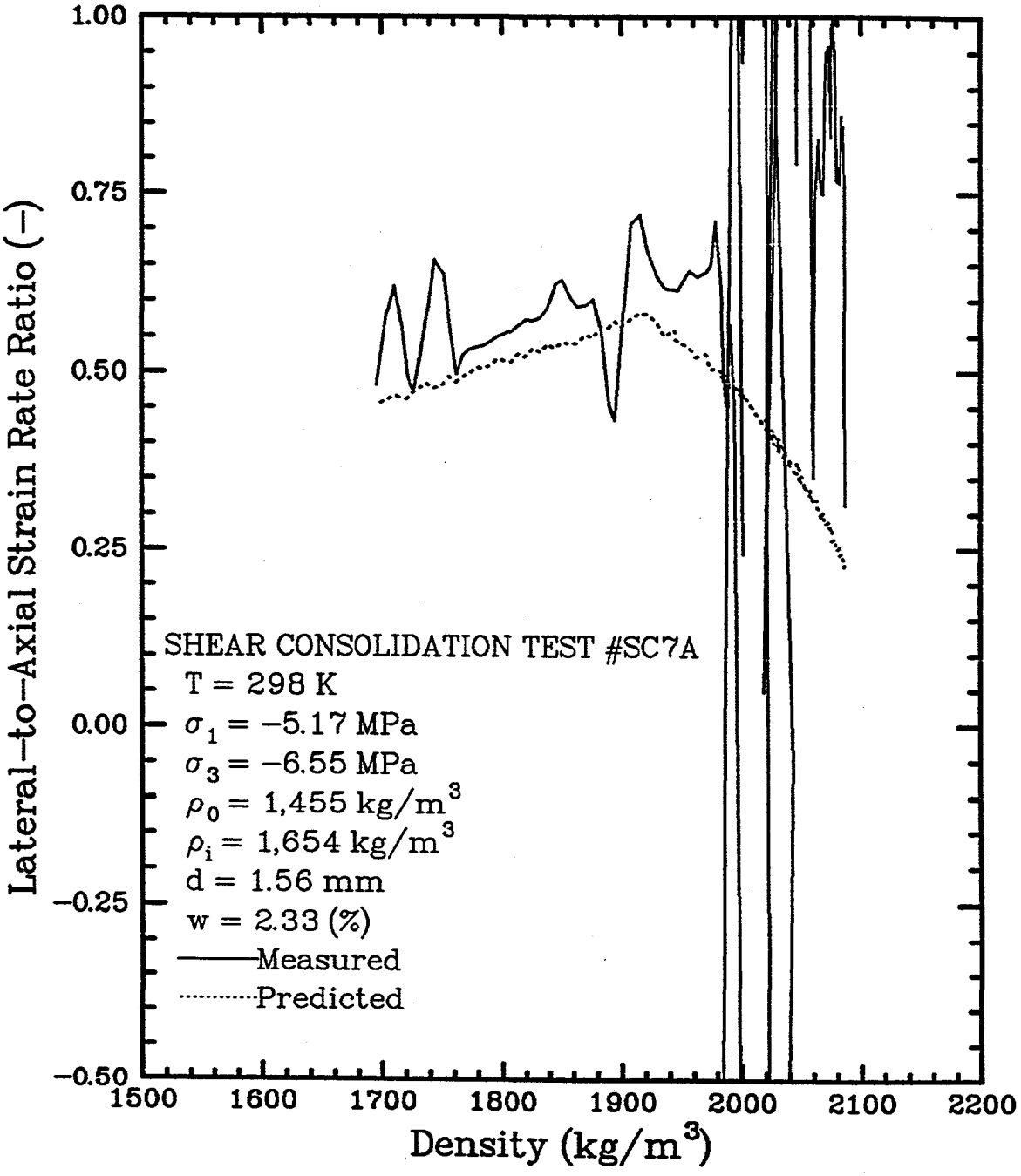

Figure B-7. Lateral-to-Axial Strain Rate Ratio as a Function of Density for Shear Consolidation Test SC7A.

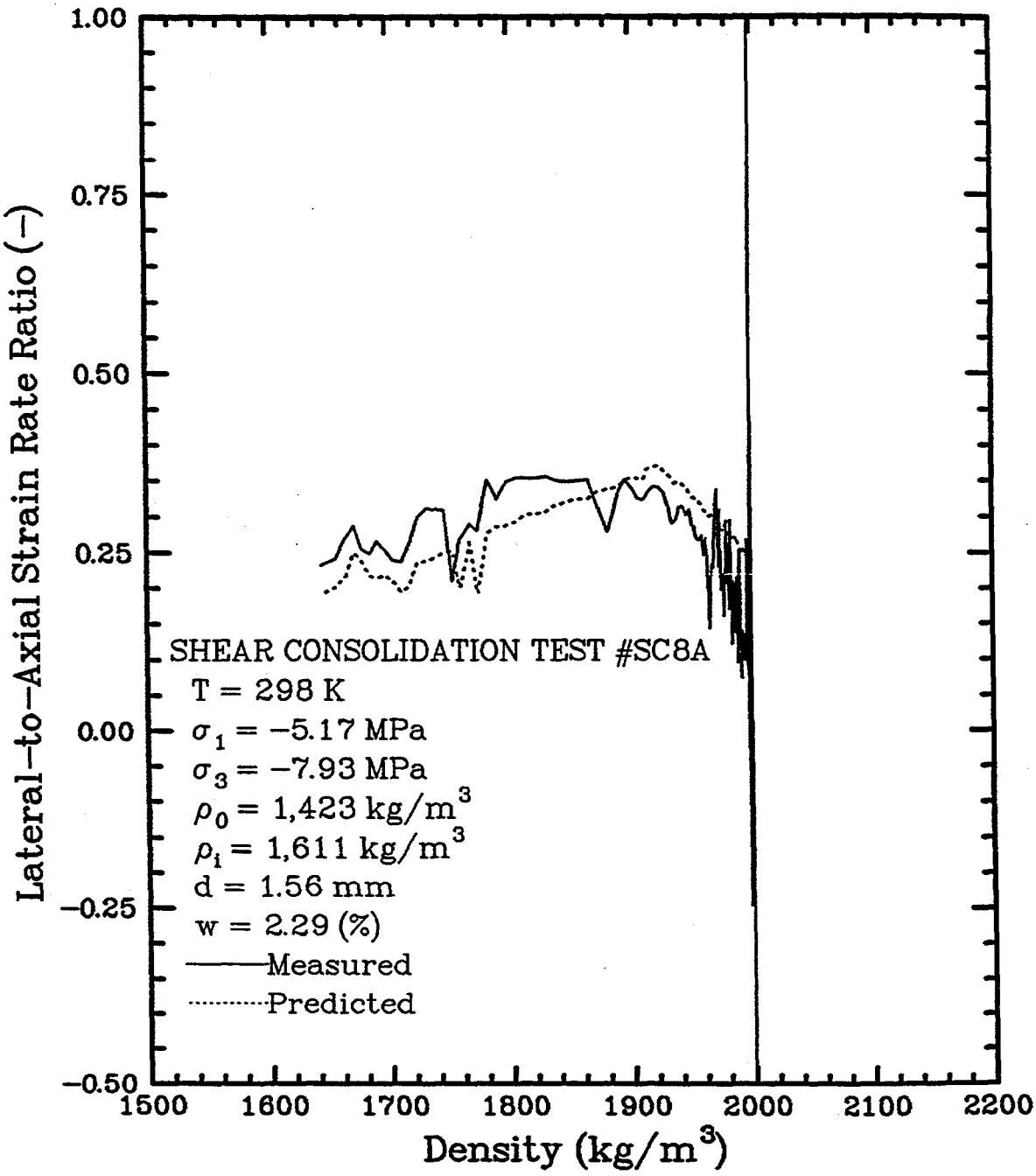

Figure B-8. Lateral-to-Axial Strain Rate Ratio as a Function of Density for Shear Consolidation Test SC8A.

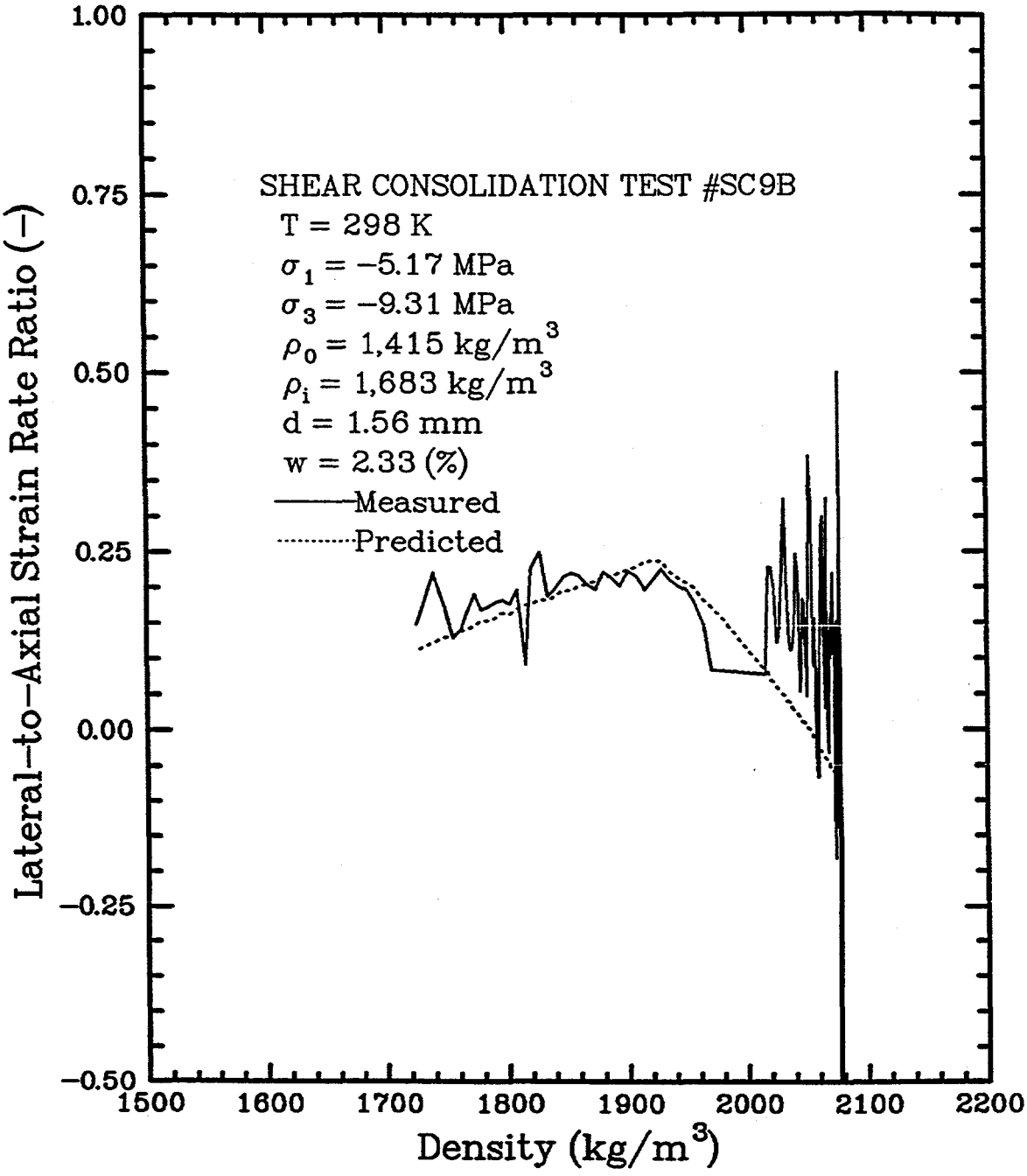

Figure B-9. Lateral-to-Axial Strain Rate Ratio as a Function of Density for Shear Consolidation Test SC9B.

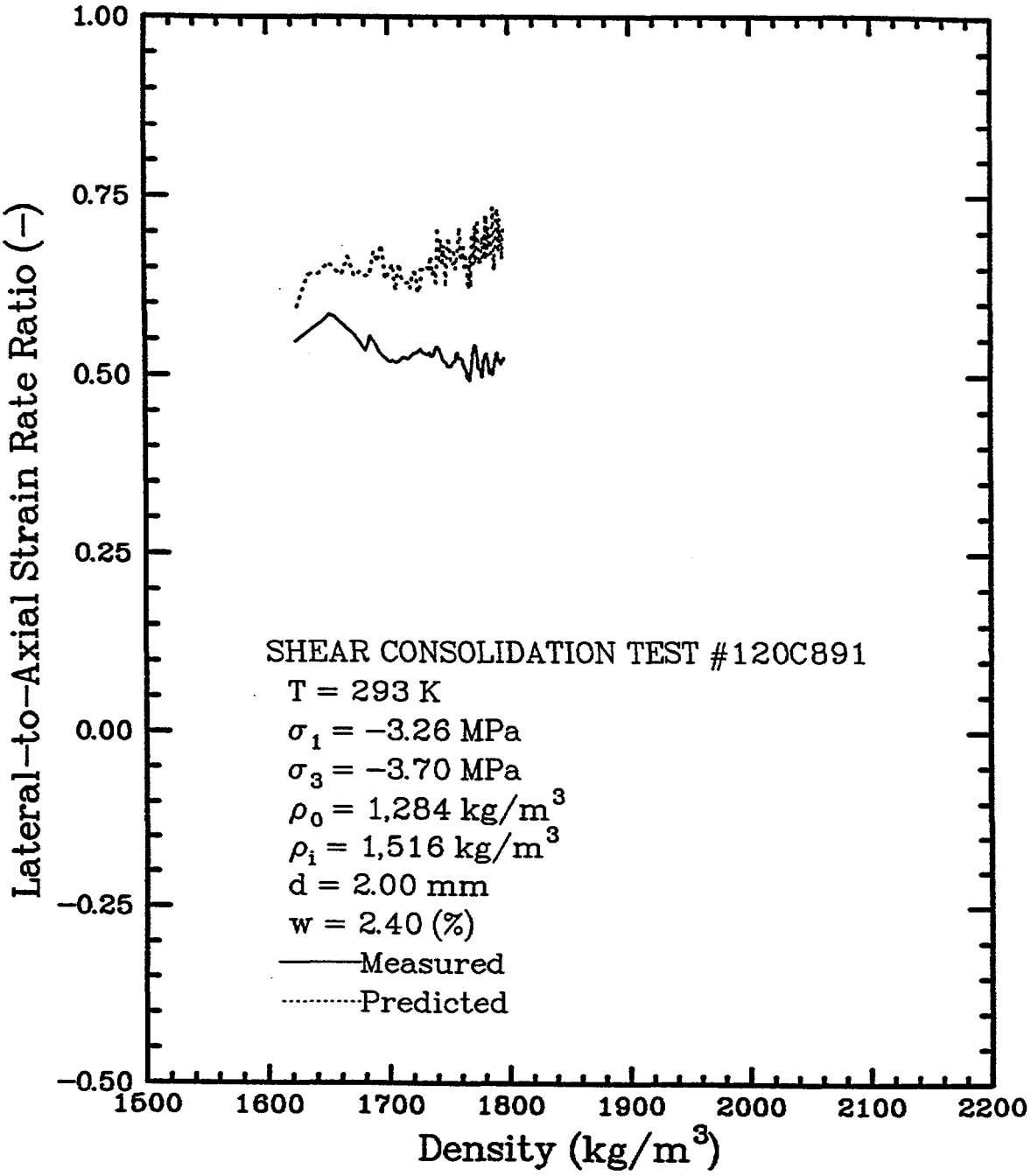

Figure B-10. Lateral-to-Axial Strain Rate Ratio as a Function of Density for Shear Consolidation Test 120C891.

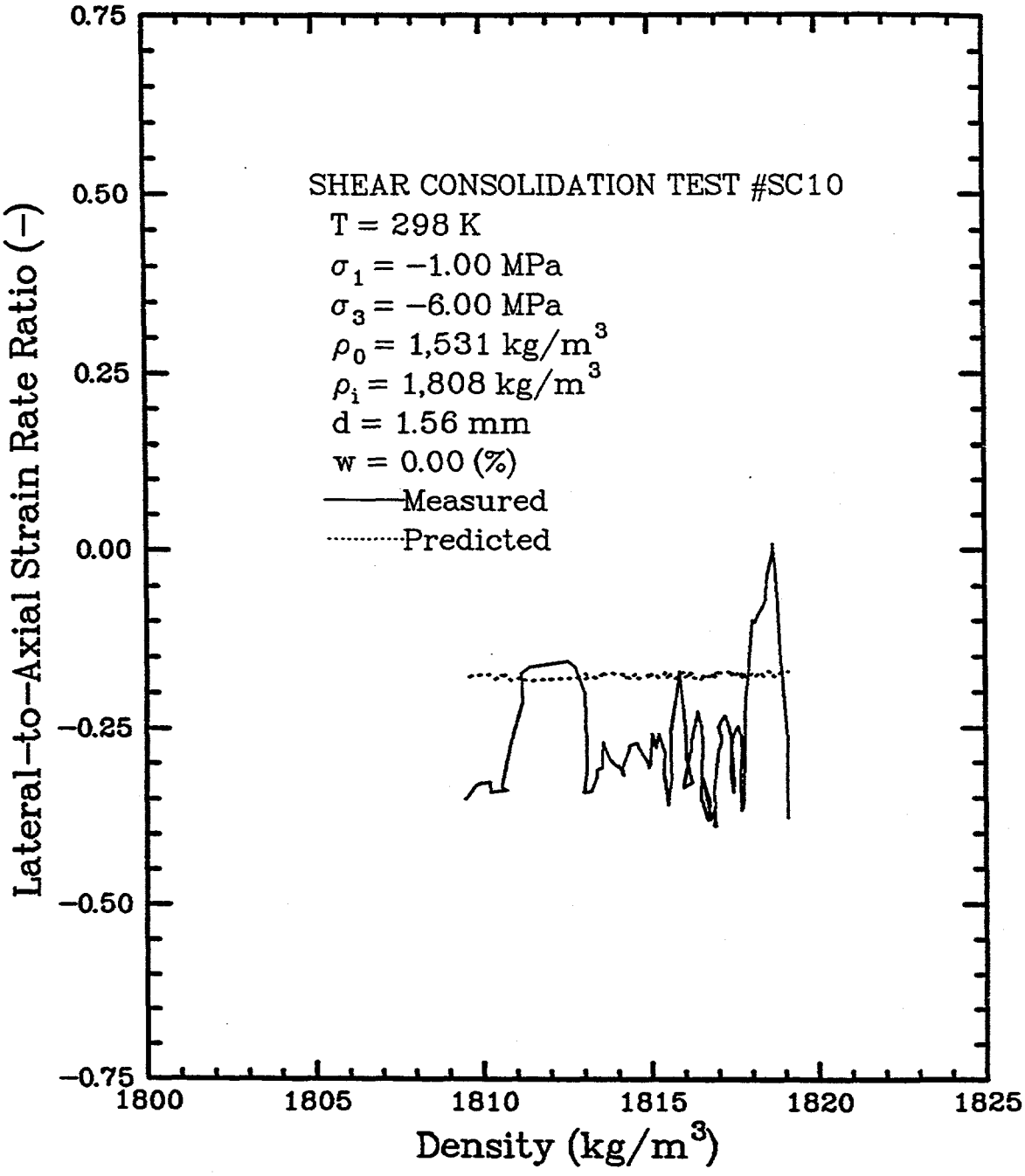

Figure B-11. Lateral-to-Axial Strain Rate Ratio as a Function of Density for Shear Consolidation Test SC10.

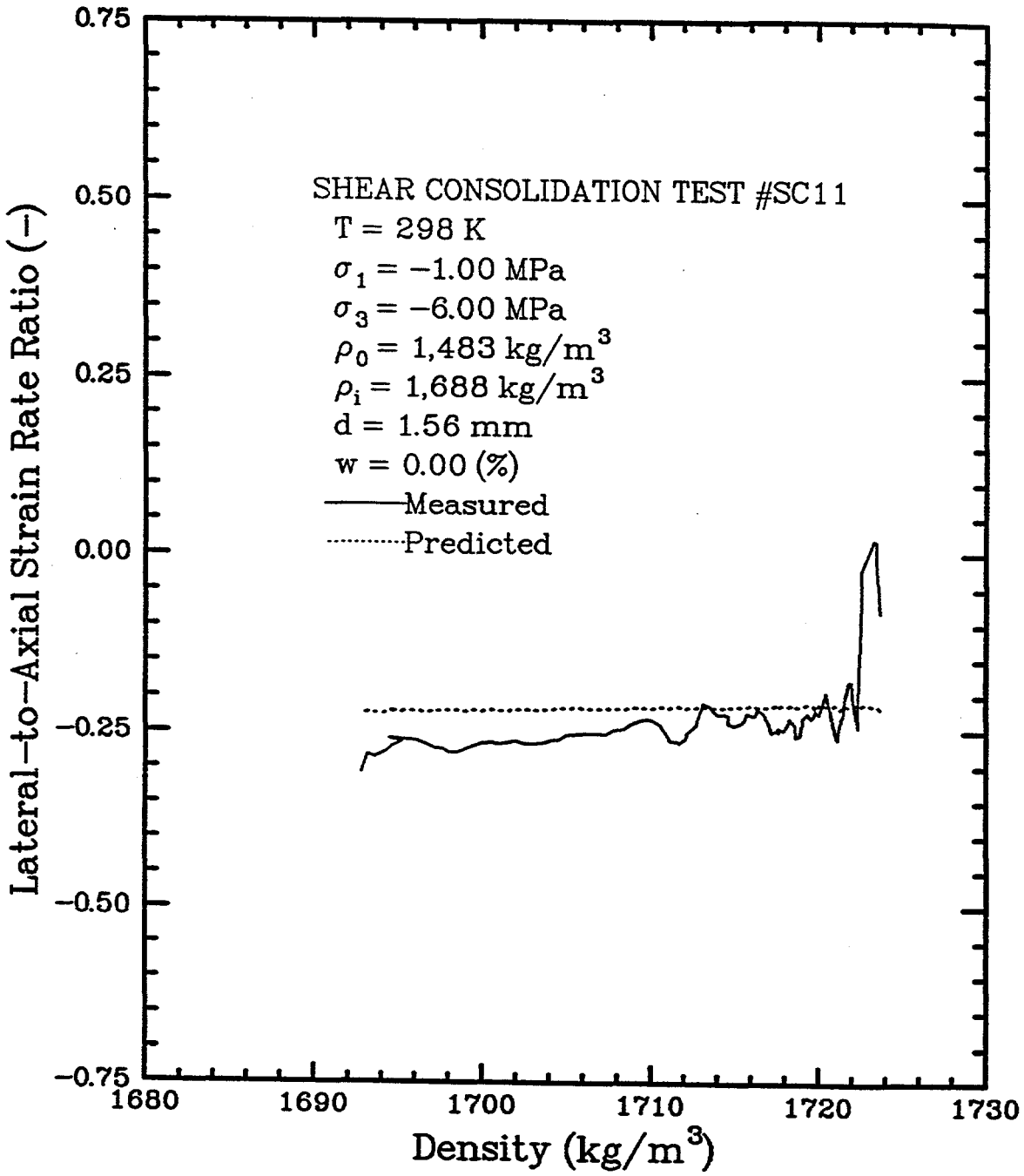

Figure B-12. Lateral-to-Axial Strain Rate Ratio as a Function of Density for Shear Consolidation Test SC11.

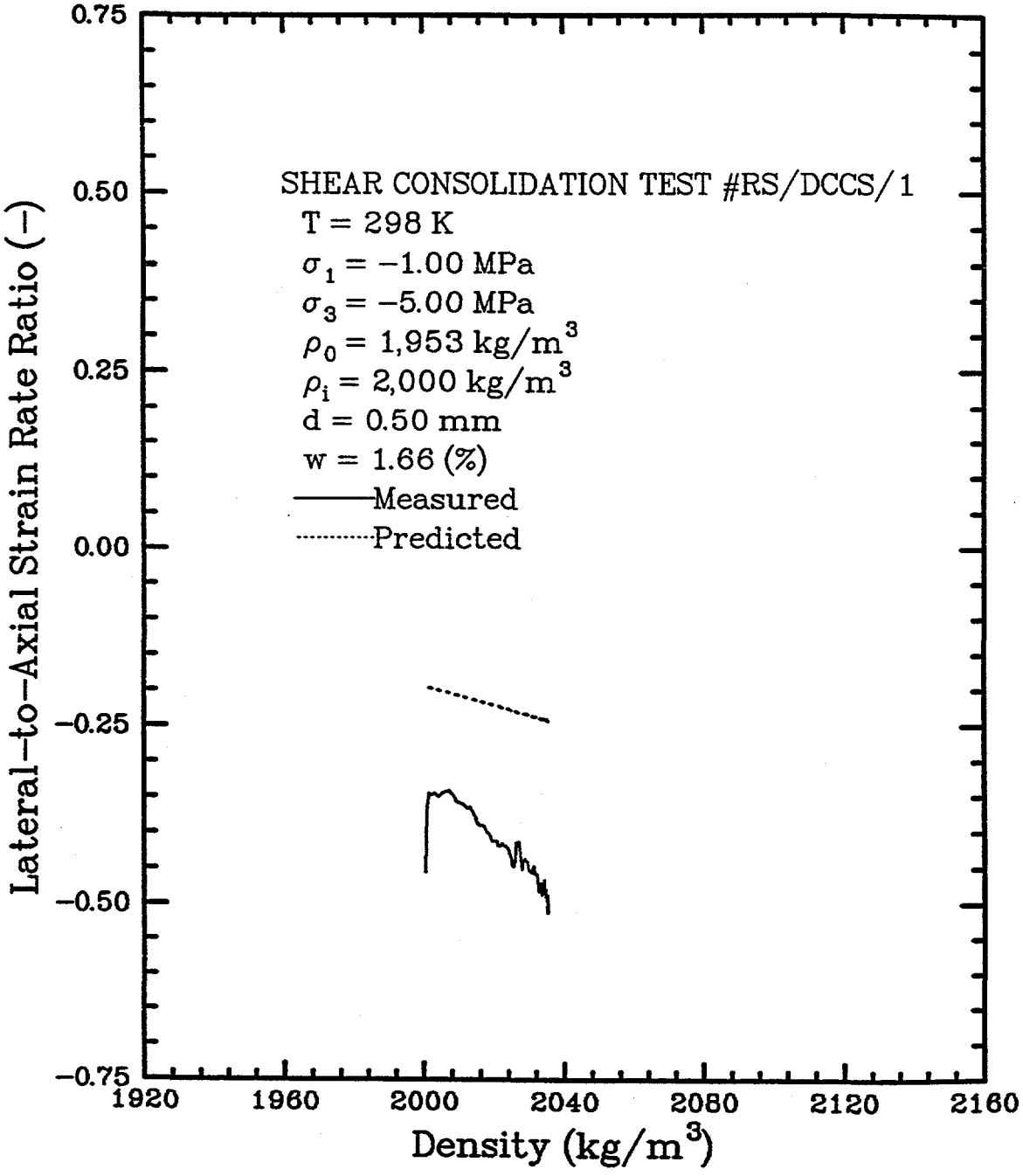

Figure B-13. Lateral-to-Axial Strain Rate Ratio as a Function of Density for Shear Consolidation Test RS/DCCS/1.

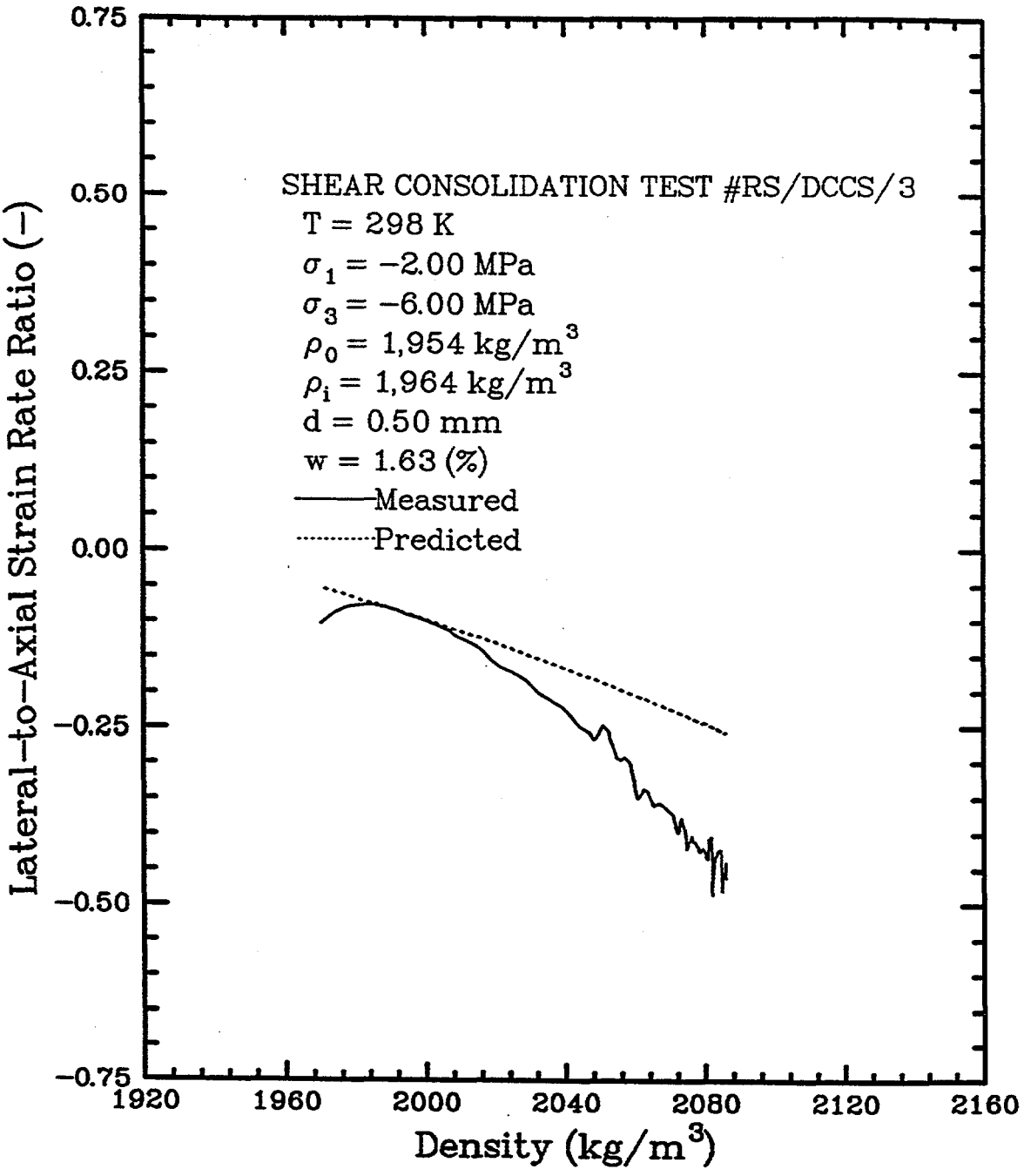

Figure B-14. Lateral-to-Axial Strain Rate Ratio as a Function of Density for Shear Consolidation Test RS/DCCS/3.

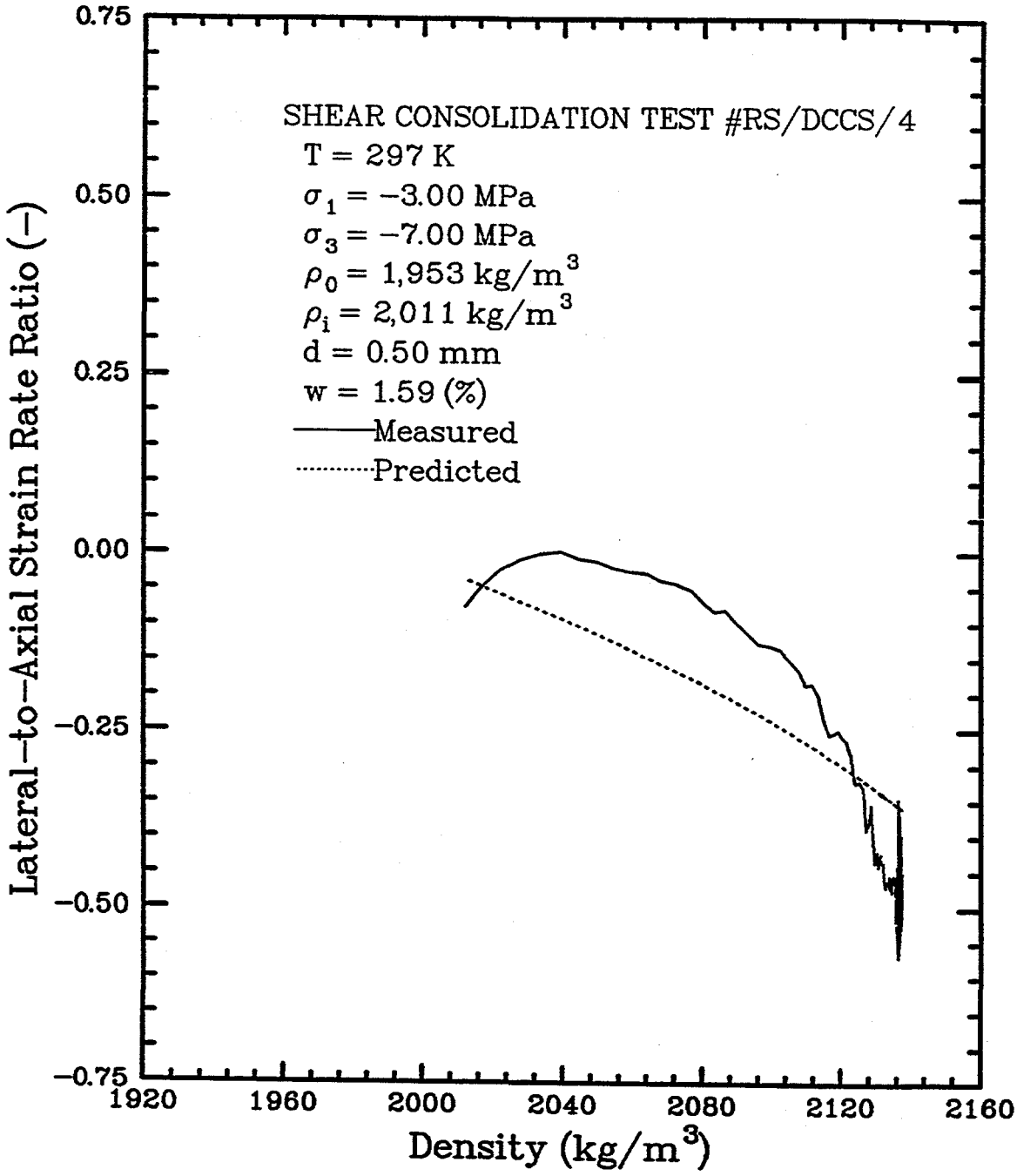

Figure B-15. Lateral-to-Axial Strain Rate Ratio as a Function of Density for Shear Consolidation Test RS/DCCS/4.

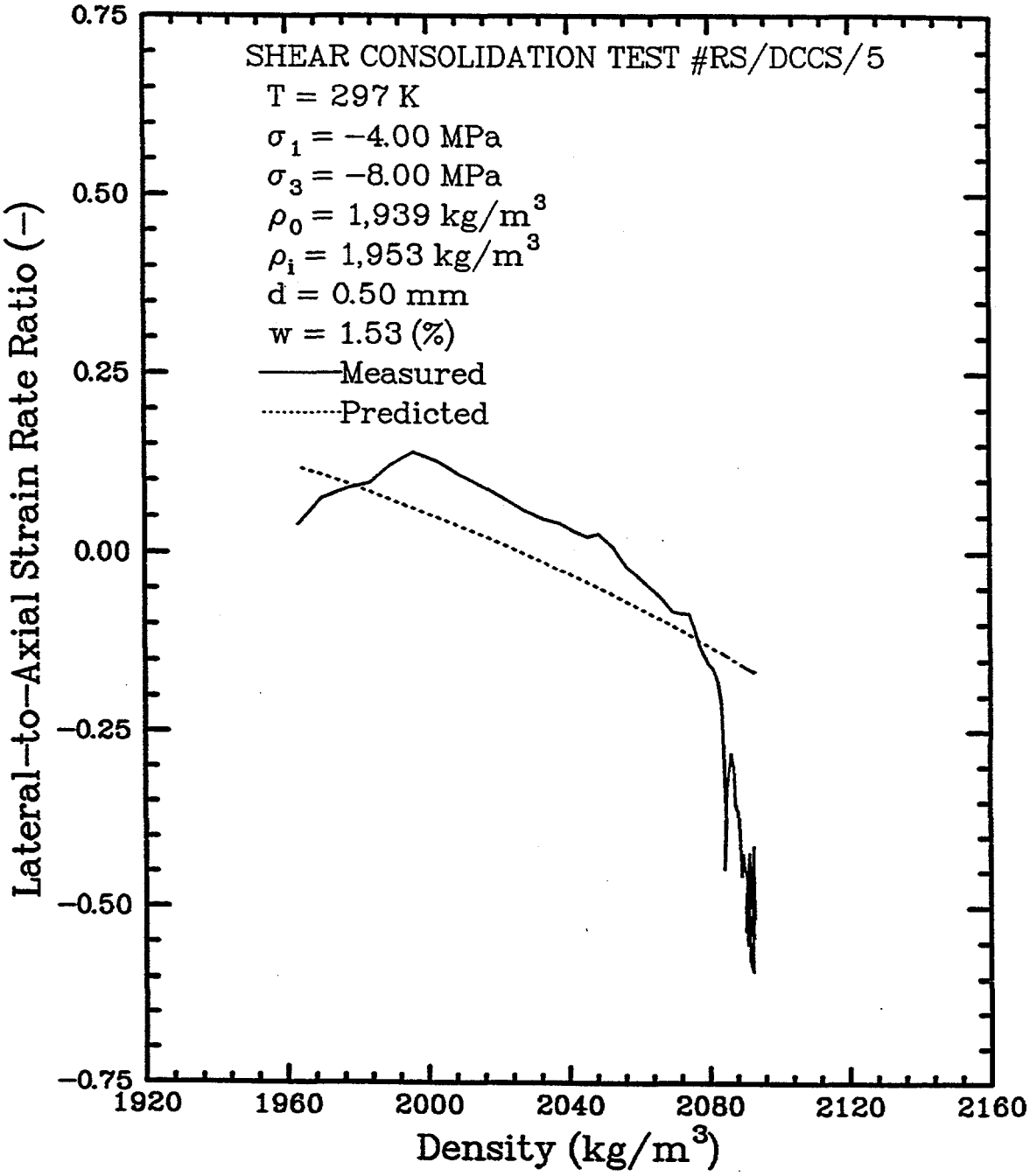

Figure B-16. Lateral-to-Axial Strain Rate Ratio as a Function of Density for Shear Consolidation Test RS/DCCS/5.

APPENDIX C

C-S Constitutive Model Fits to the Hydrostatic and Shear Consolidation Tests

This appendix contains the plots of the C-S constitutive model fits to the 40 hydrostatic consolidation tests and the 16 shear consolidation tests. The two C-S constitutive model fits are fits to two test databases; namely, (1) a database containing the 16 shear consolidation tests only and (2) a database containing the combined 56 shear and hydrostatic consolidation tests.

The appendix contains 56 figures. Each figure shows the two model fits to each particular laboratory test; either a hydrostatic consolidation test (Figure C-1 through C-40) or a shear consolidation test (Figures C-41 through C-56). The plots labeled "Shear Database" represent the C-S constitutive model fit to the shear test database, and the plots labeled "Combined Database" represent the C-S constitutive model fit to the combined test database.

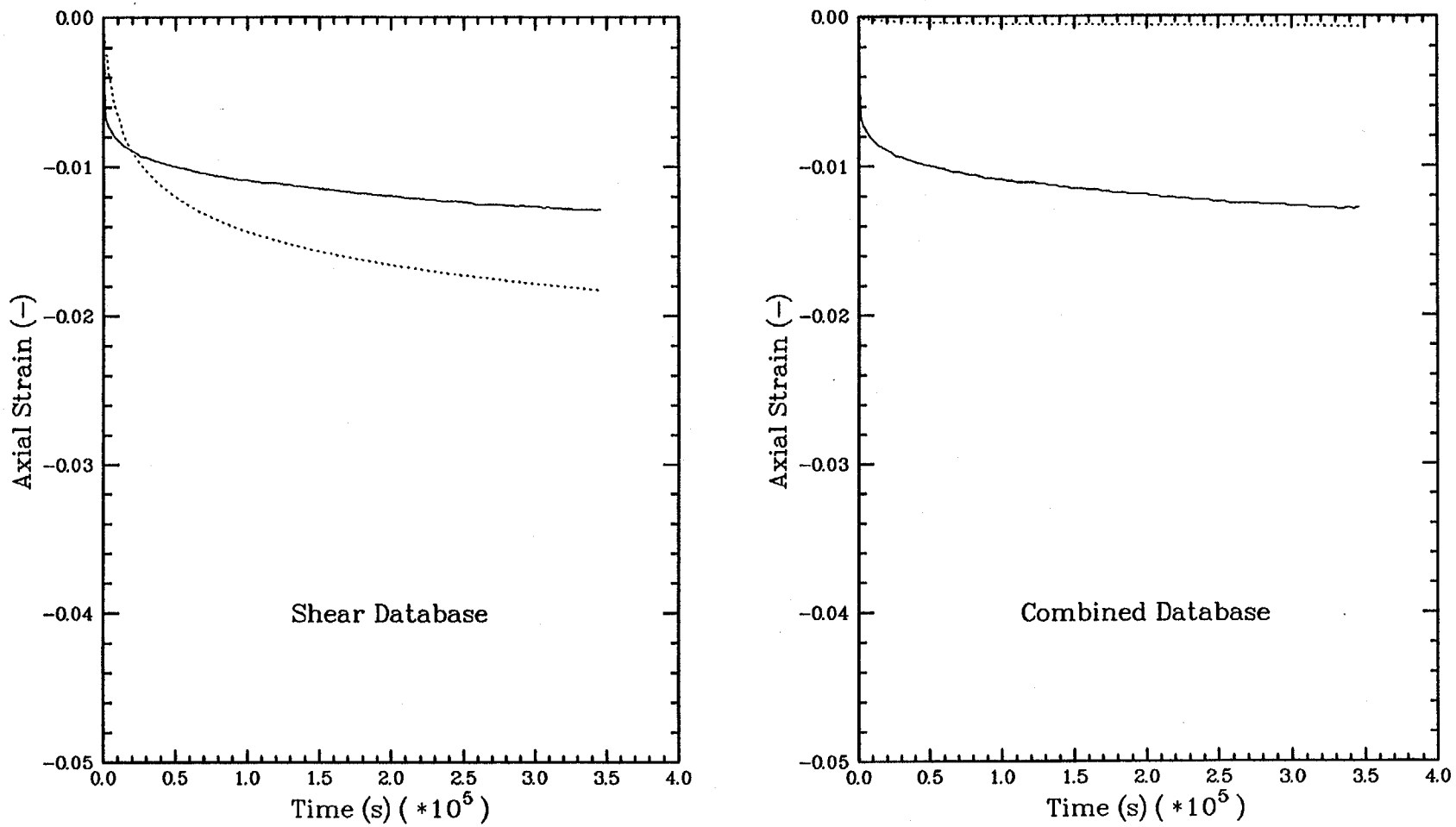

Figure C-1. Hydrostatic Consolidation Test CS1

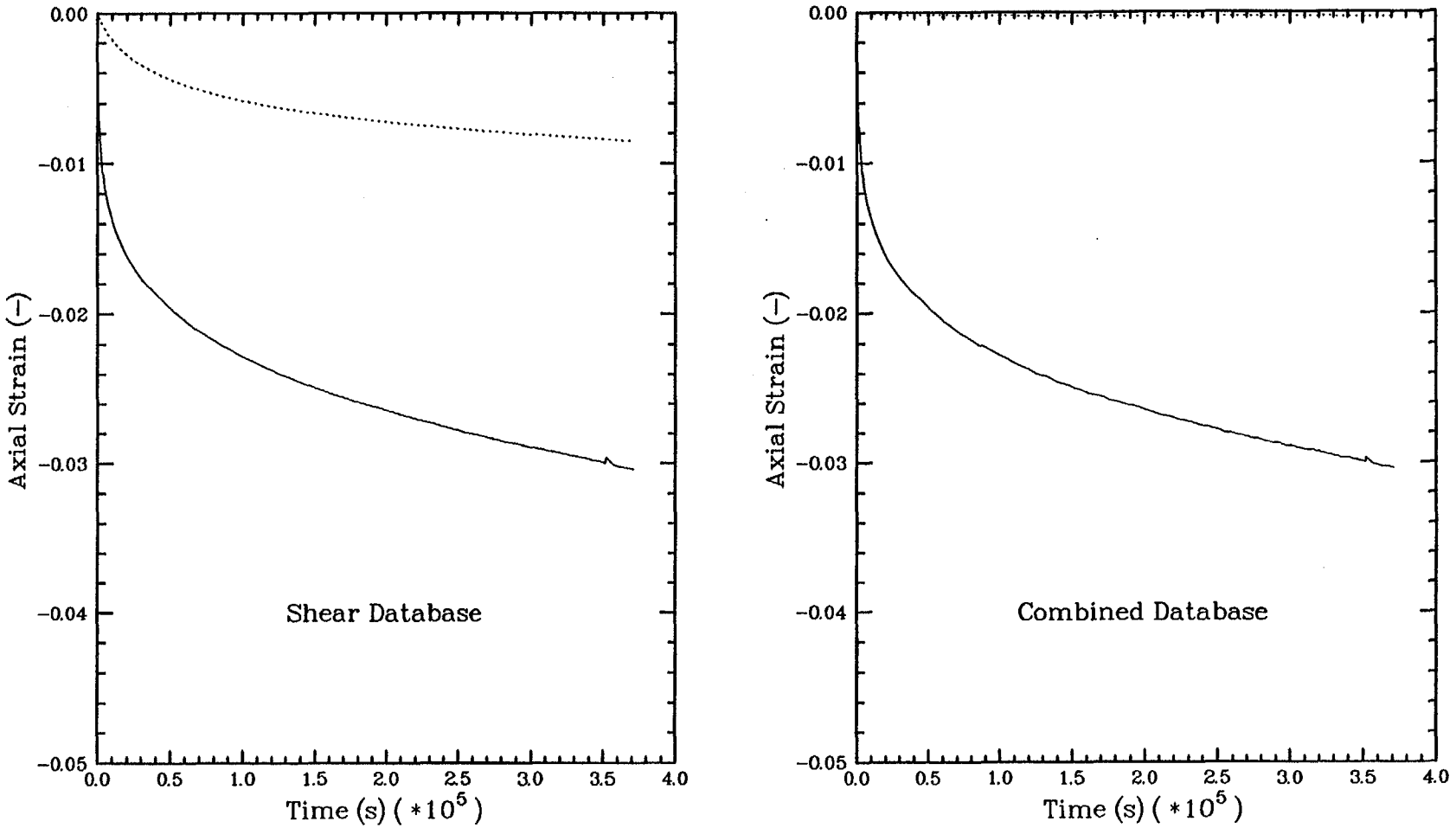

Figure C–2. Hydrostatic Consolidation Test CS2

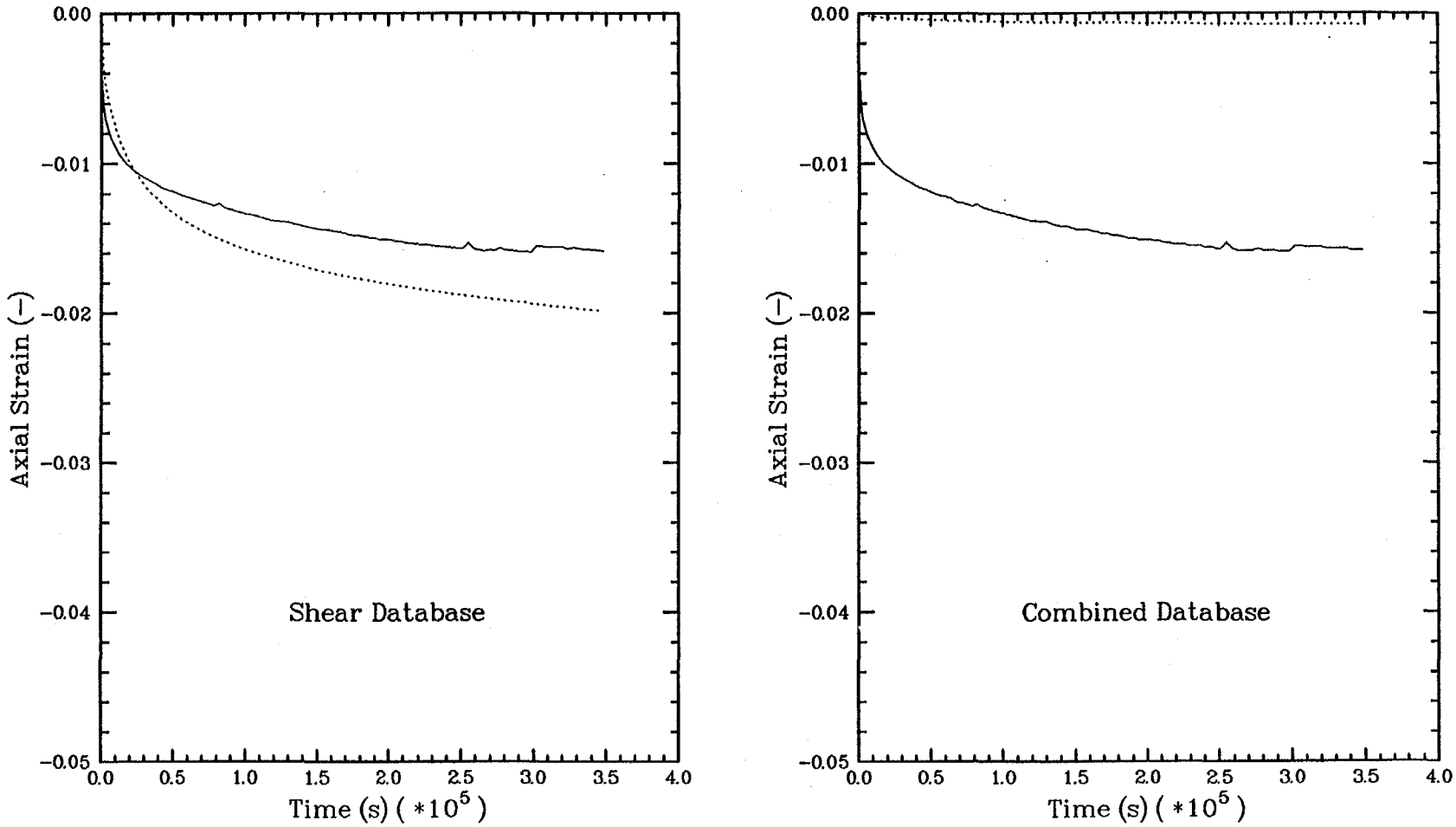

Figure C-3. Hydrostatic Consolidation Test CS3

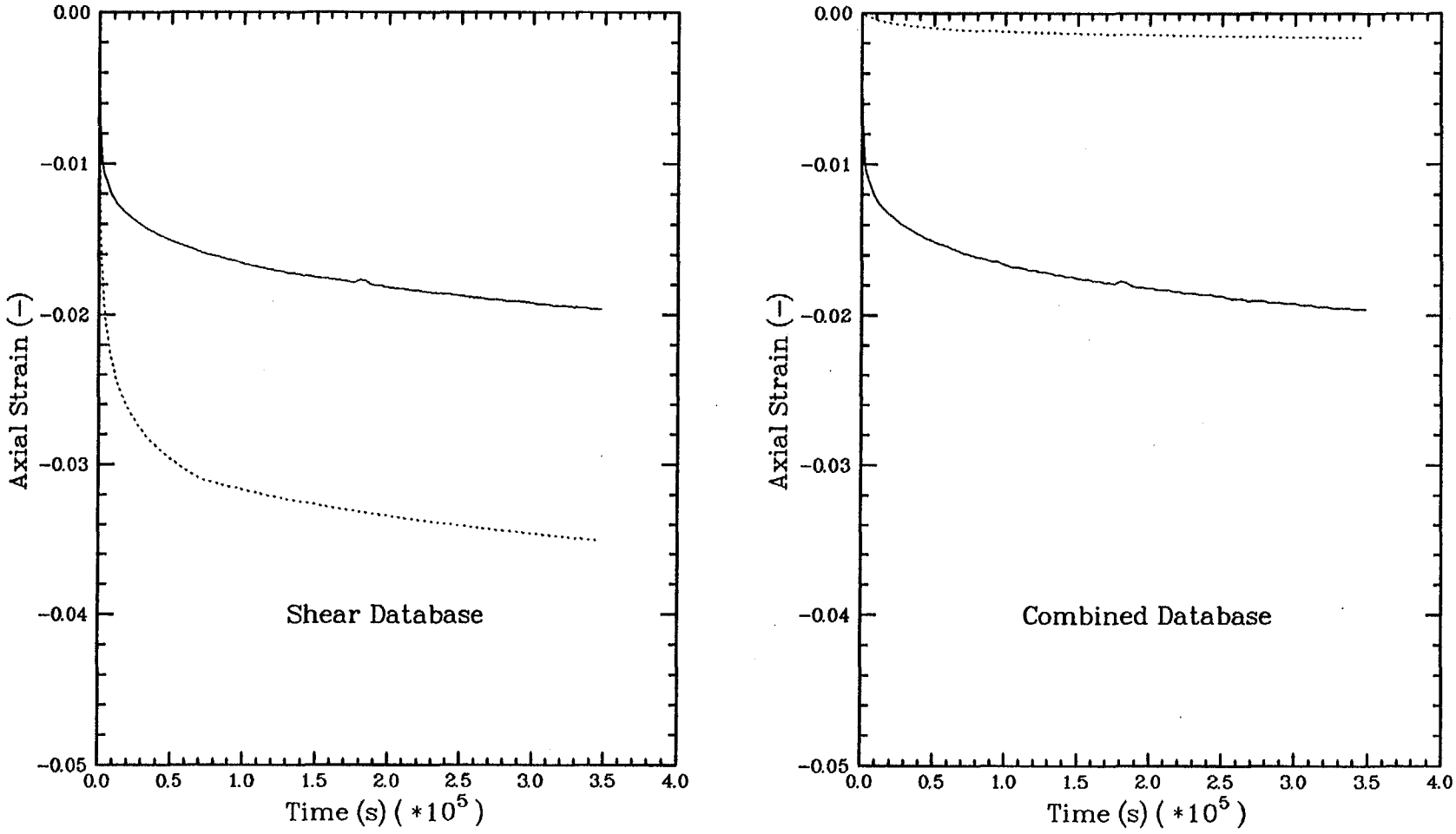

Figure C-4. Hydrostatic Consolidation Test CS4

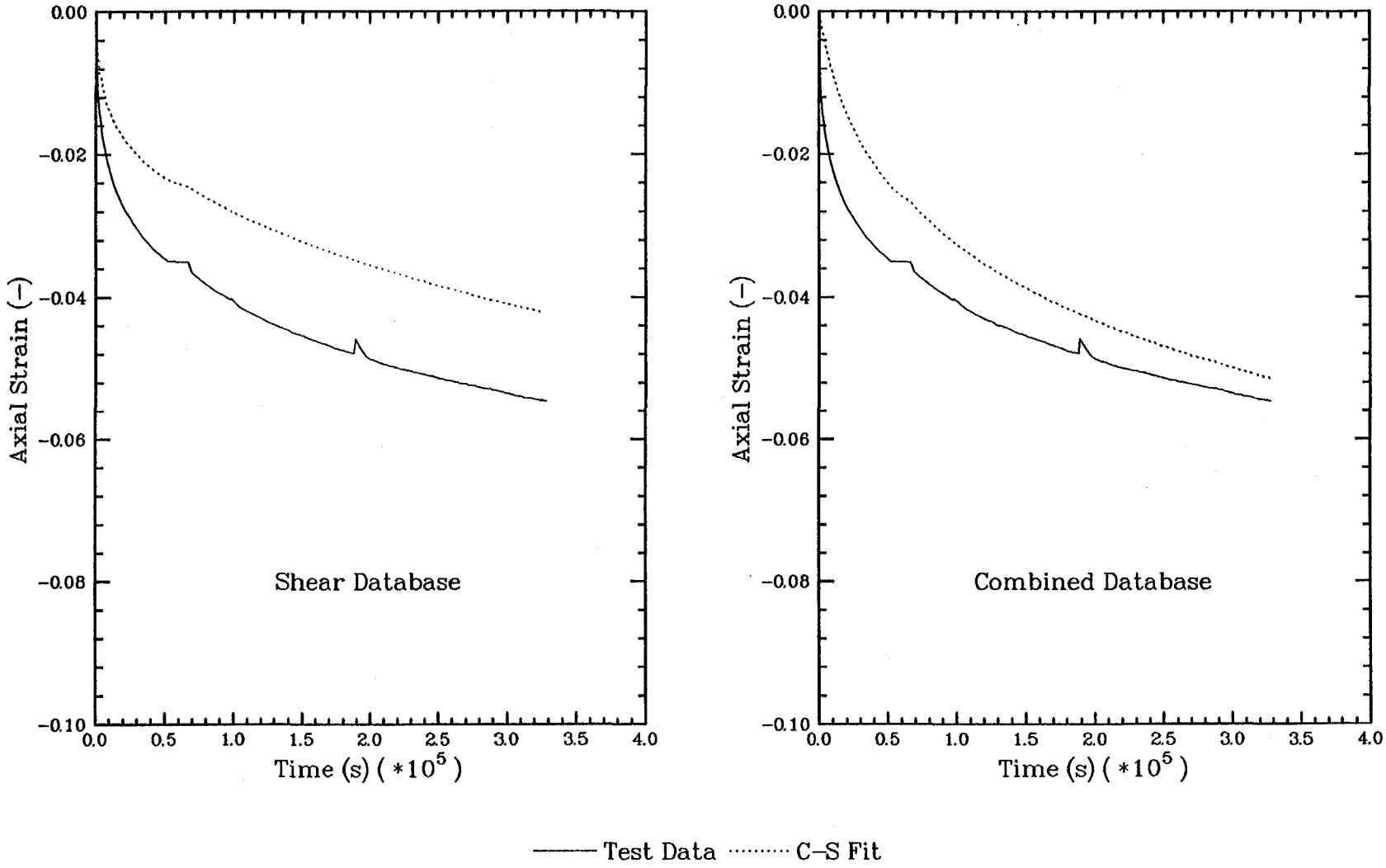

Figure C-5. Hydrostatic Consolidation Test CS5

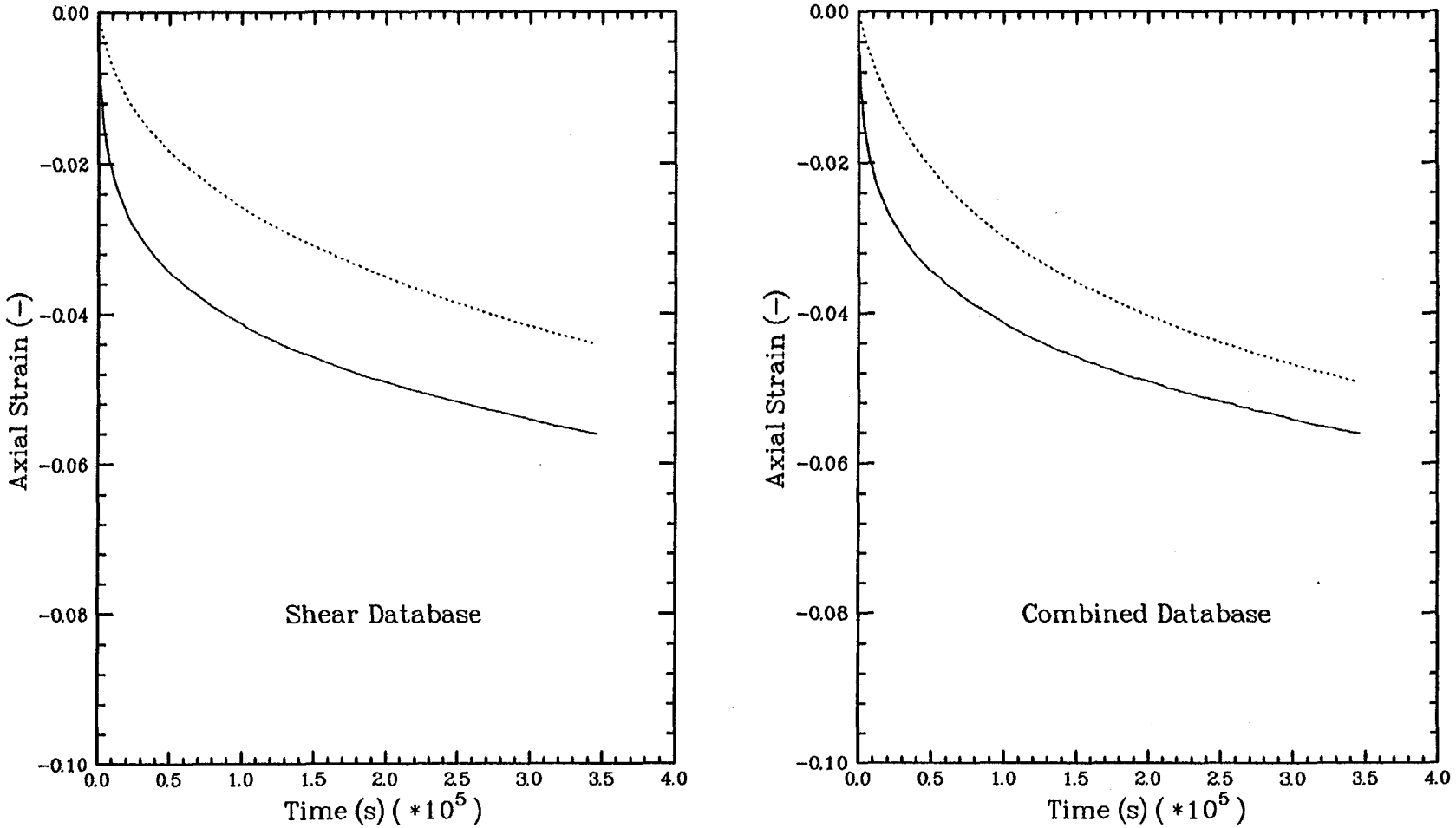

Figure C-6. Hydrostatic Consolidation Test CS6

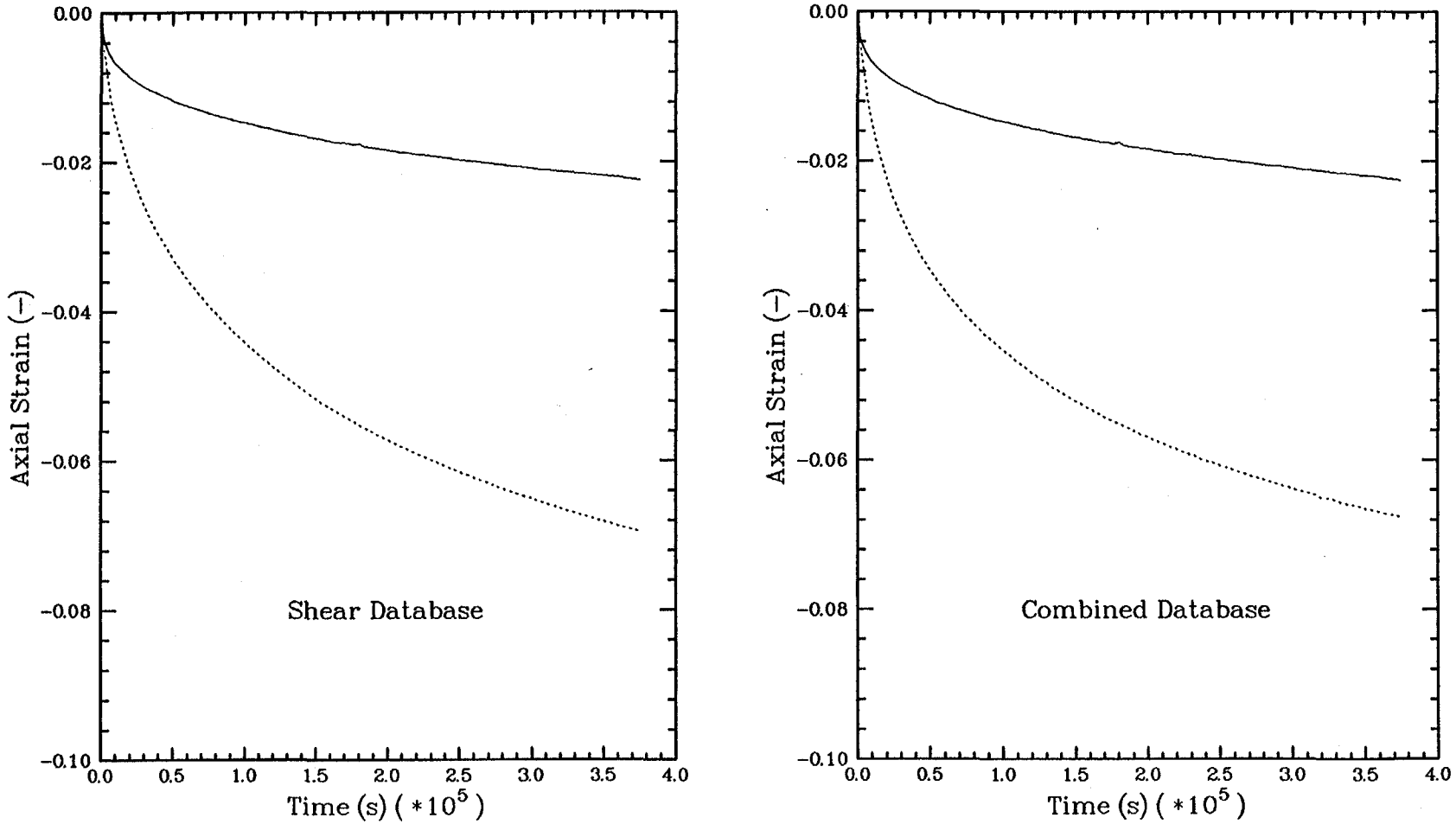

Figure C-7. Hydrostatic Consolidation Test CS7

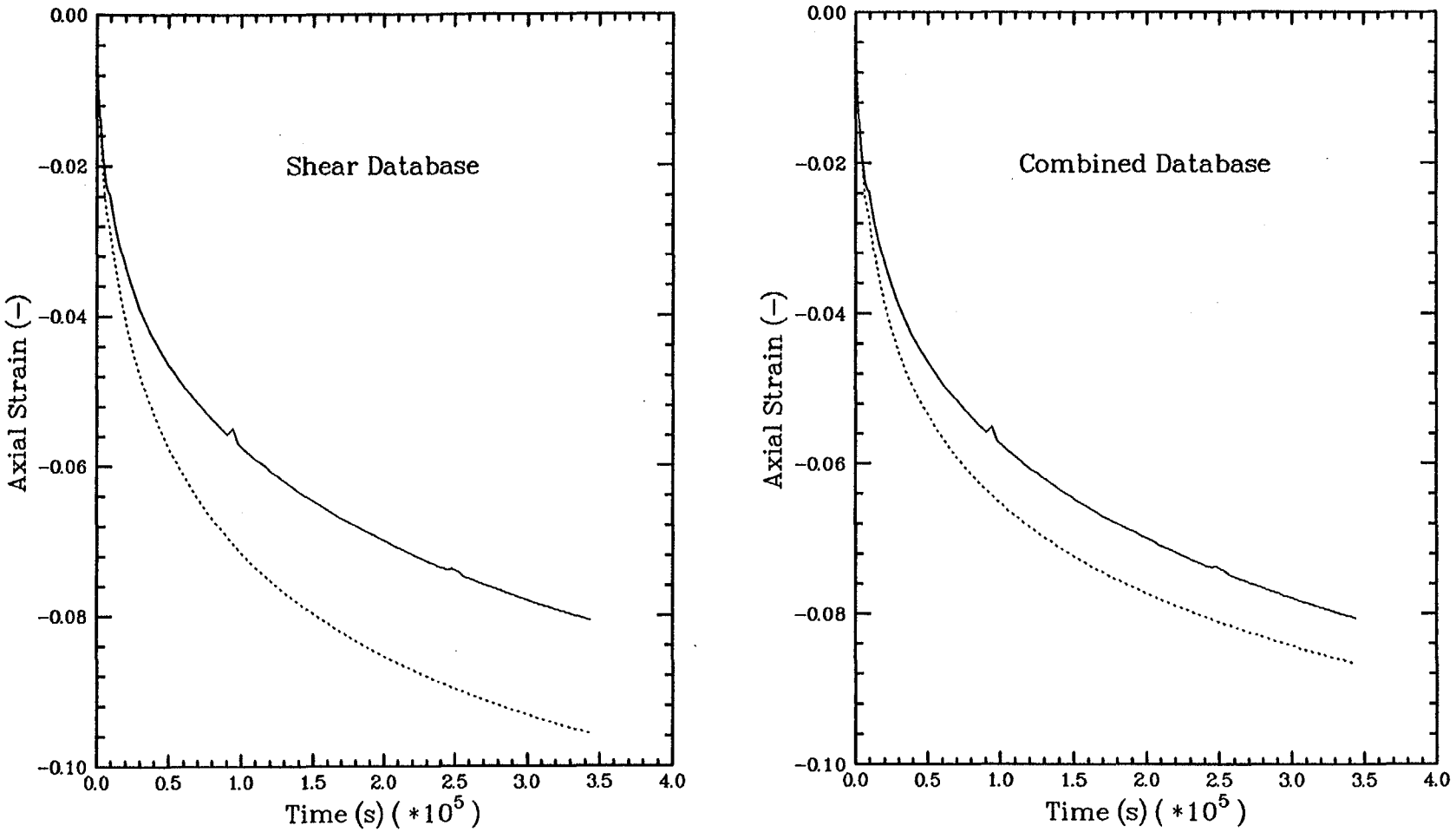

Figure C–8. Hydrostatic Consolidation Test CS8

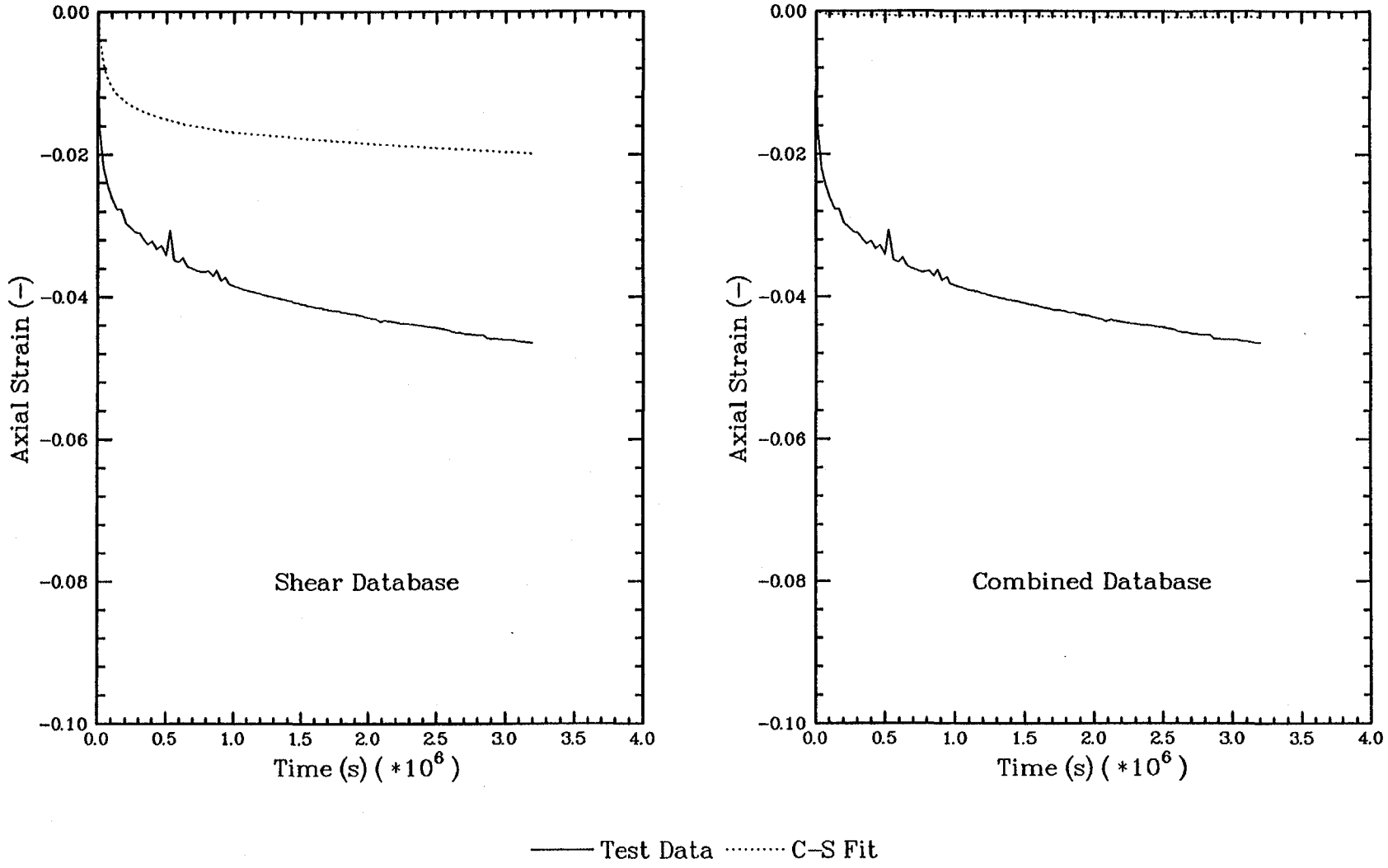

Figure C-9. Hydrostatic Consolidation Test CS9

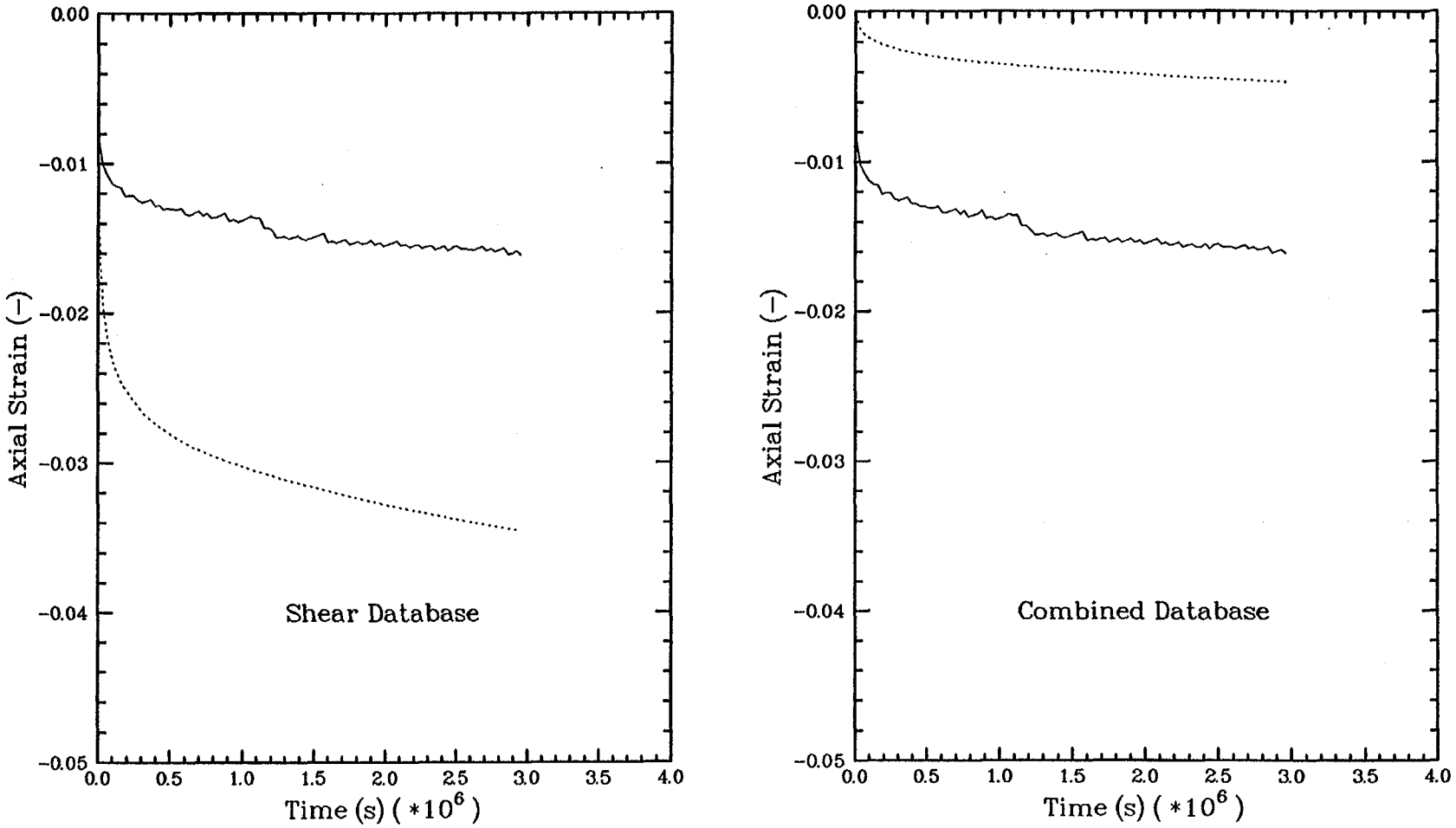

Figure C-10. Hydrostatic Consolidation Test CS10

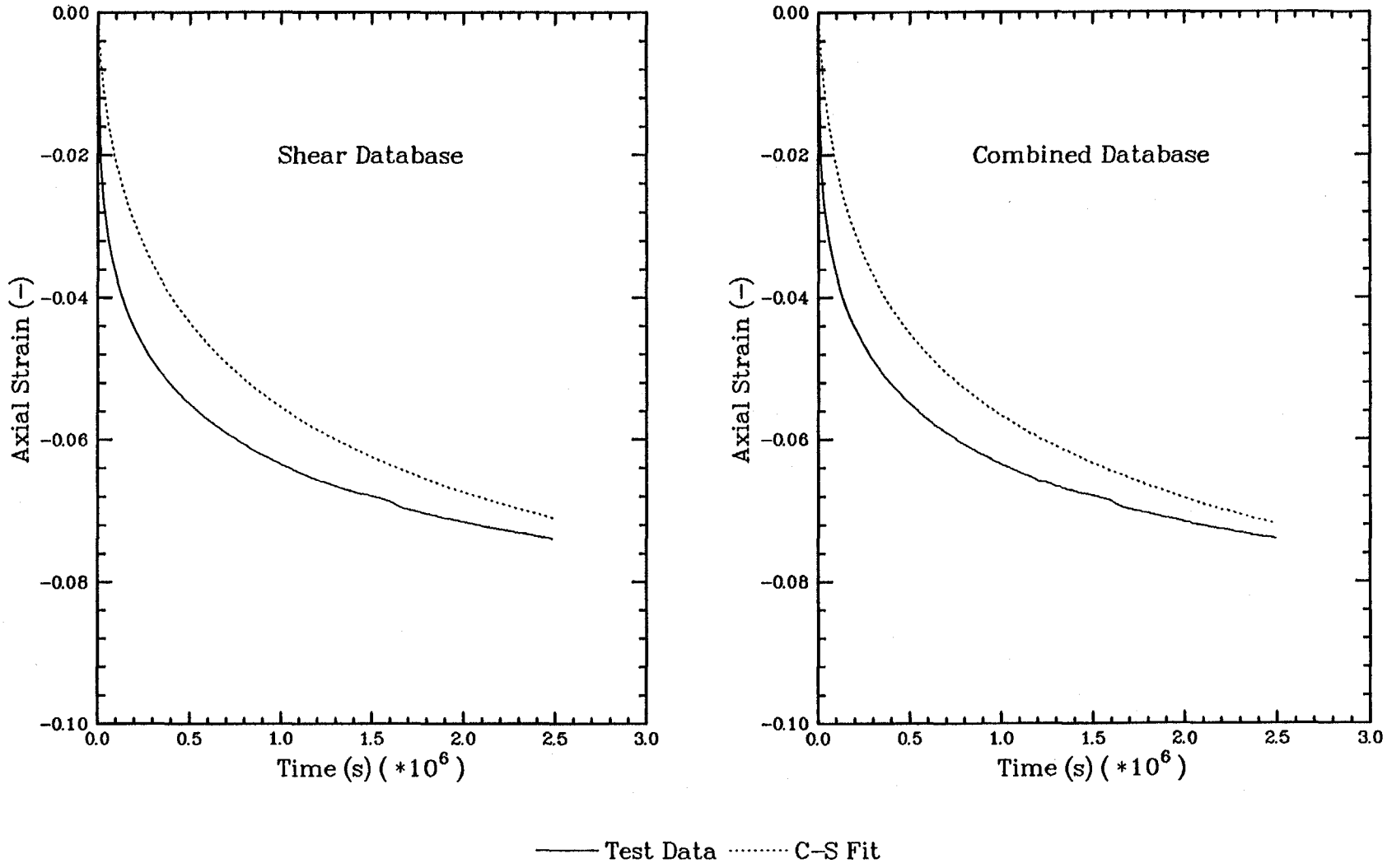

Figure C-11. Hydrostatic Consolidation Test HC1A

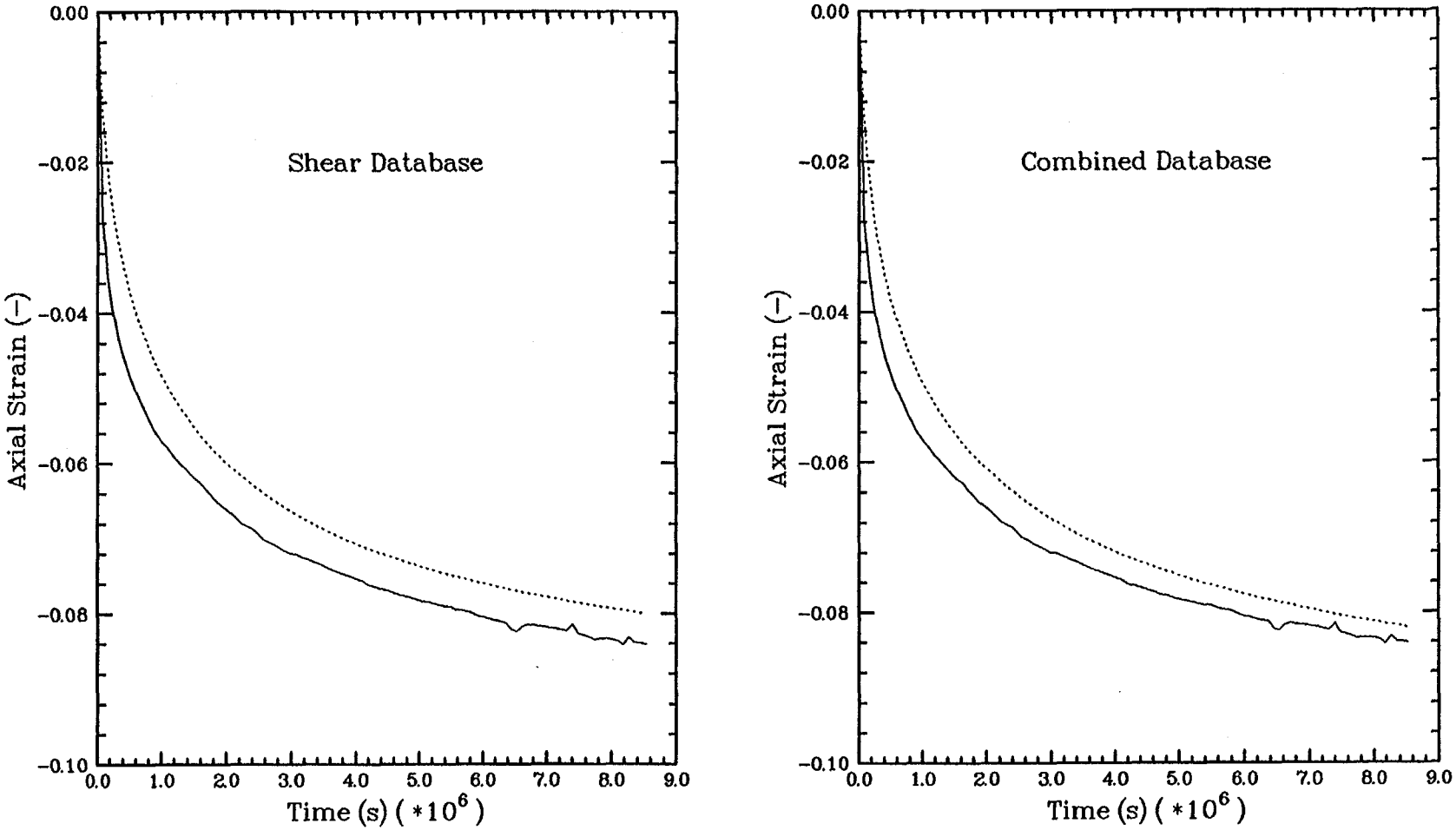

Figure C-12. Hydrostatic Consolidation Test HC2A

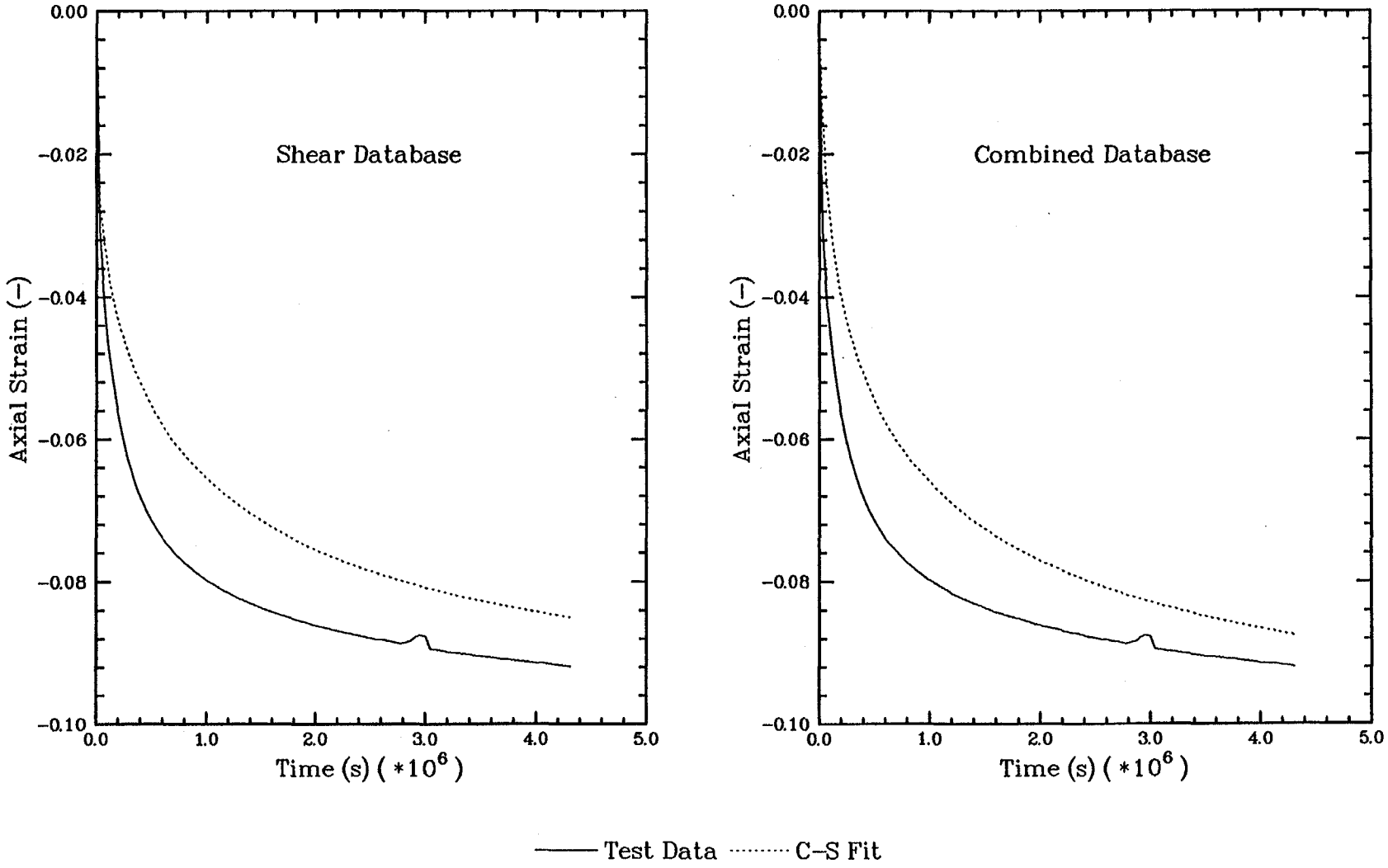

Figure C–13. Hydrostatic Consolidation Test HC3A

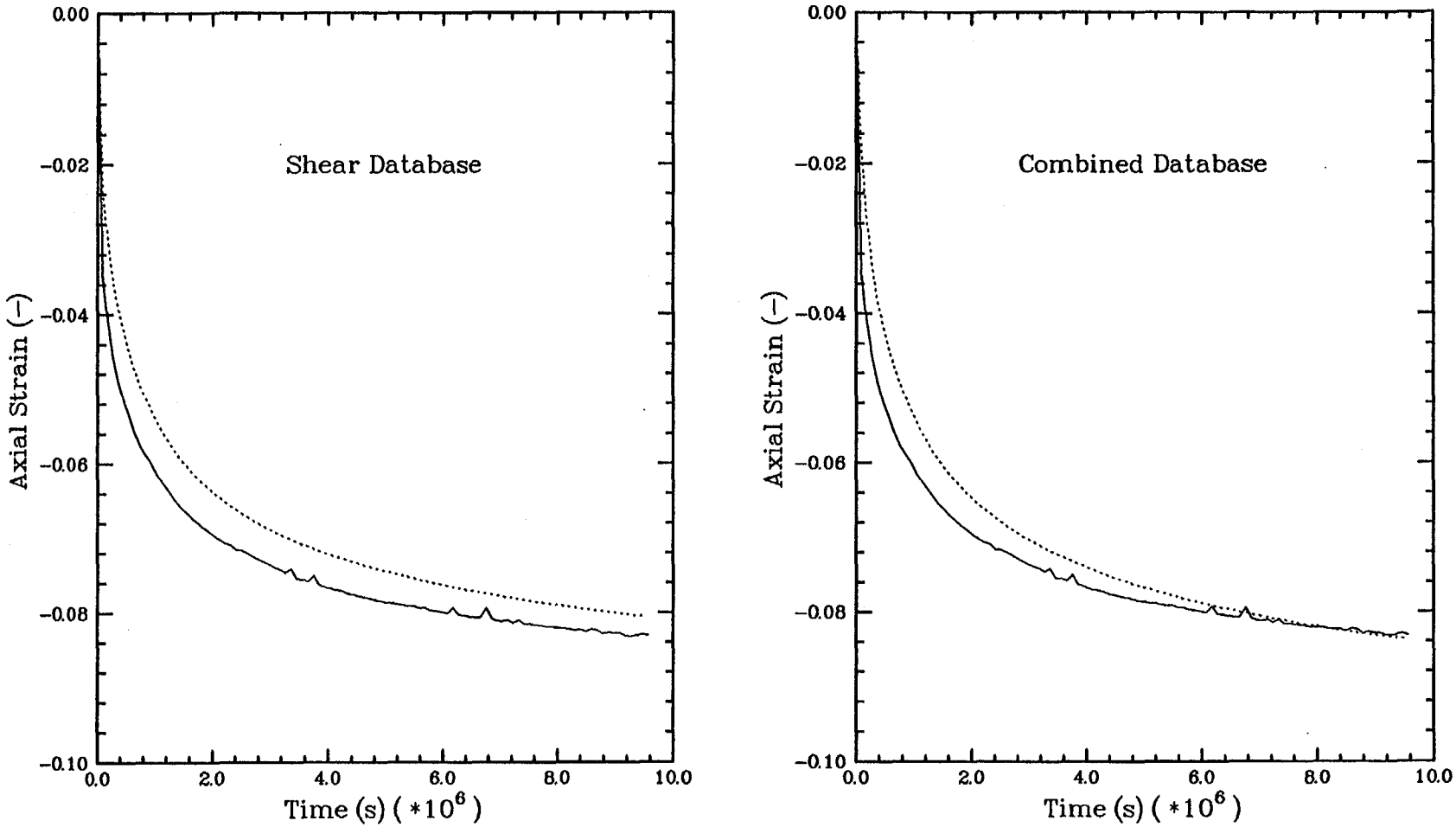

Figure C-14. Hydrostatic Consolidation Test HC4A

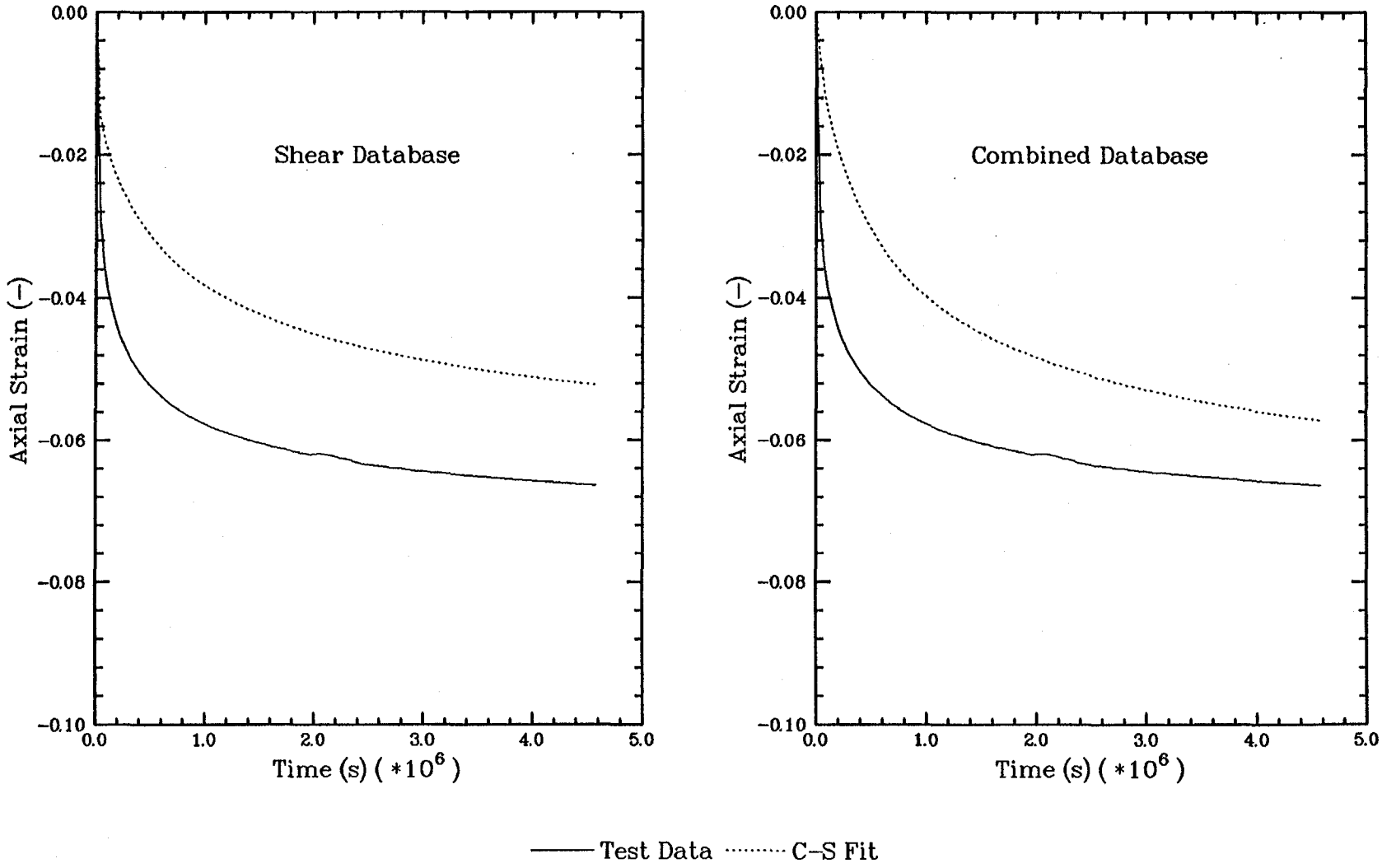

Figure C–15. Hydrostatic Consolidation Test HC5A

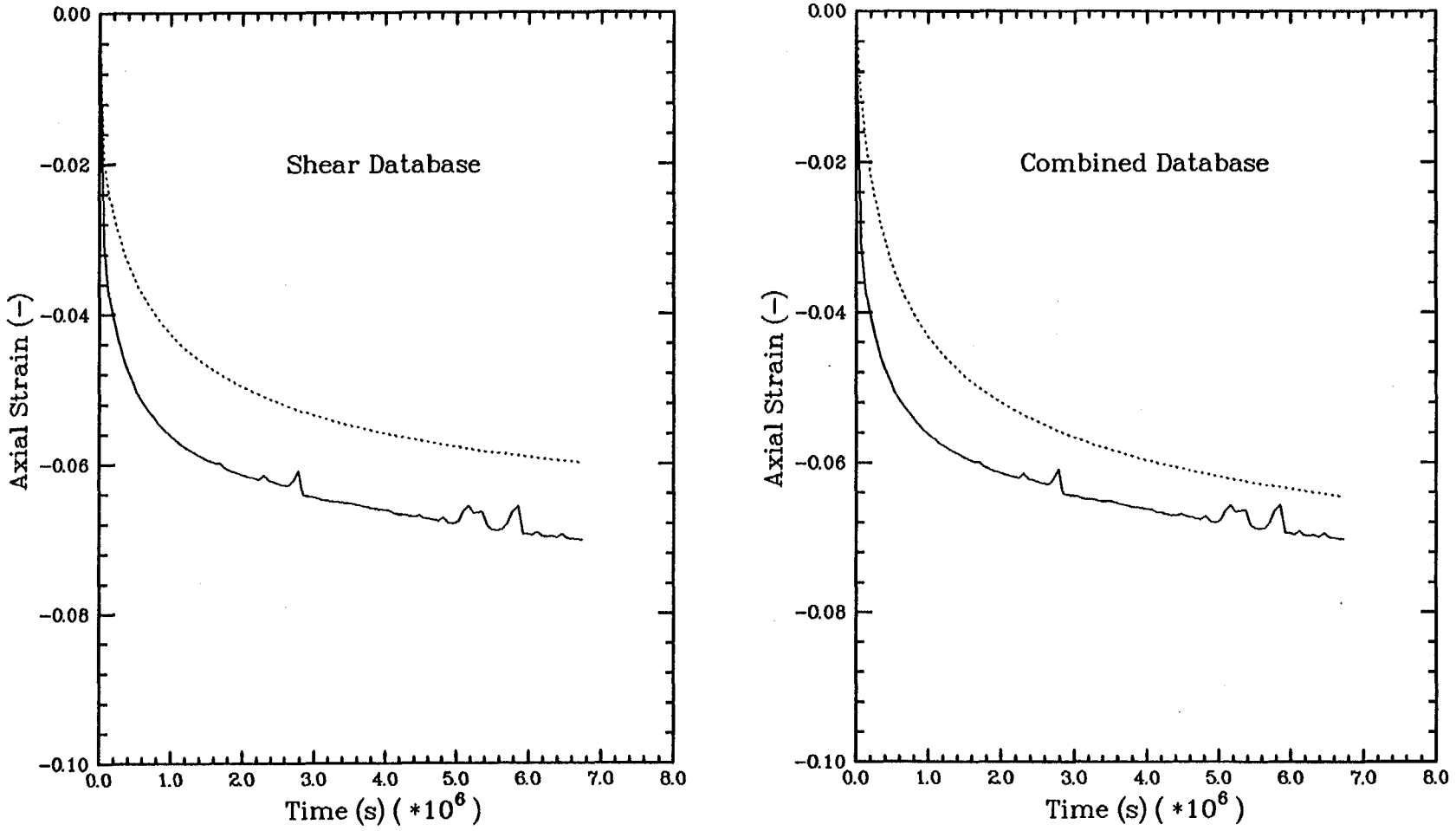

Figure C-16. Hydrostatic Consolidation Test HC6A

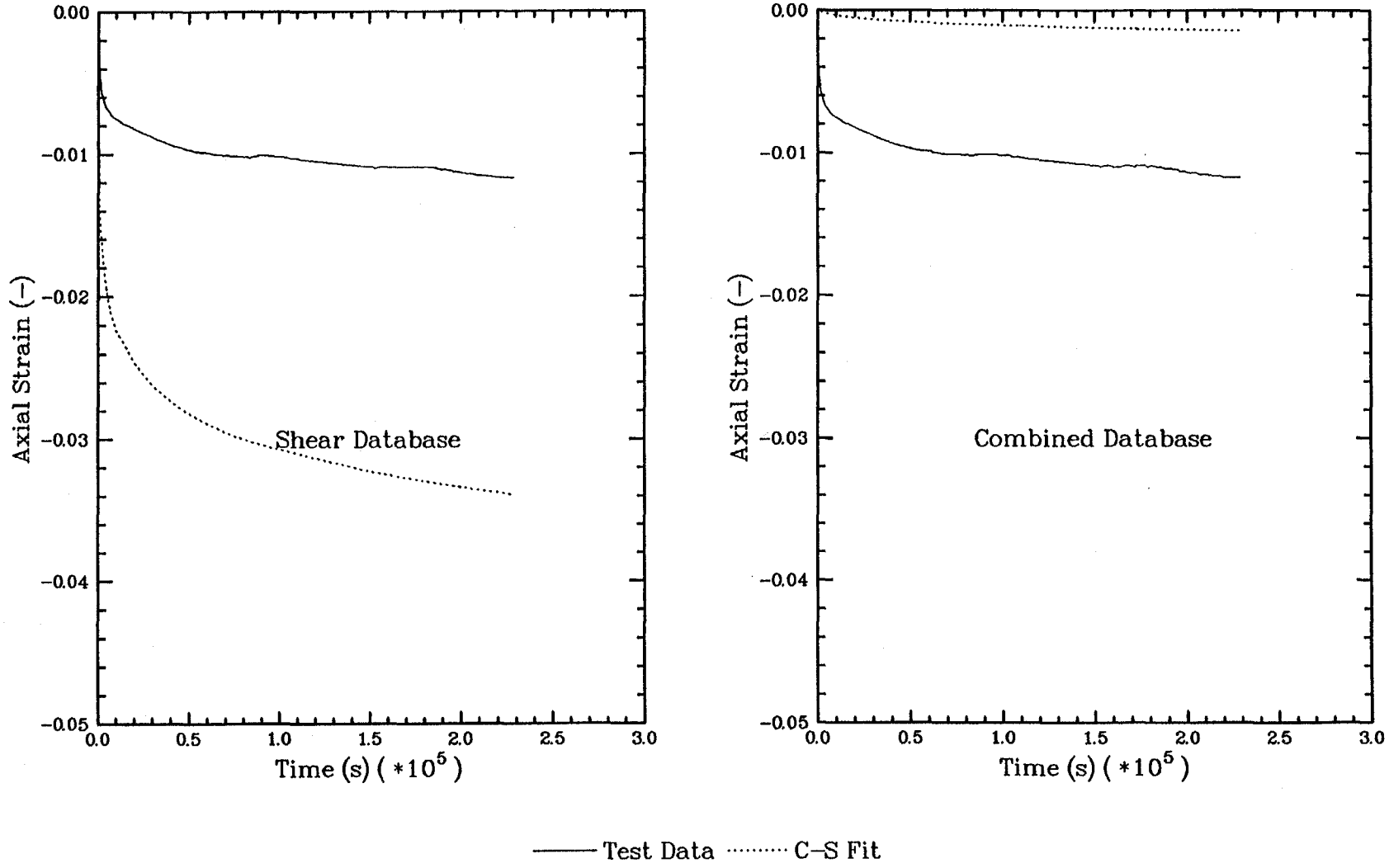

Figure C-17. Hydrostatic Consolidation Test 27JUL82

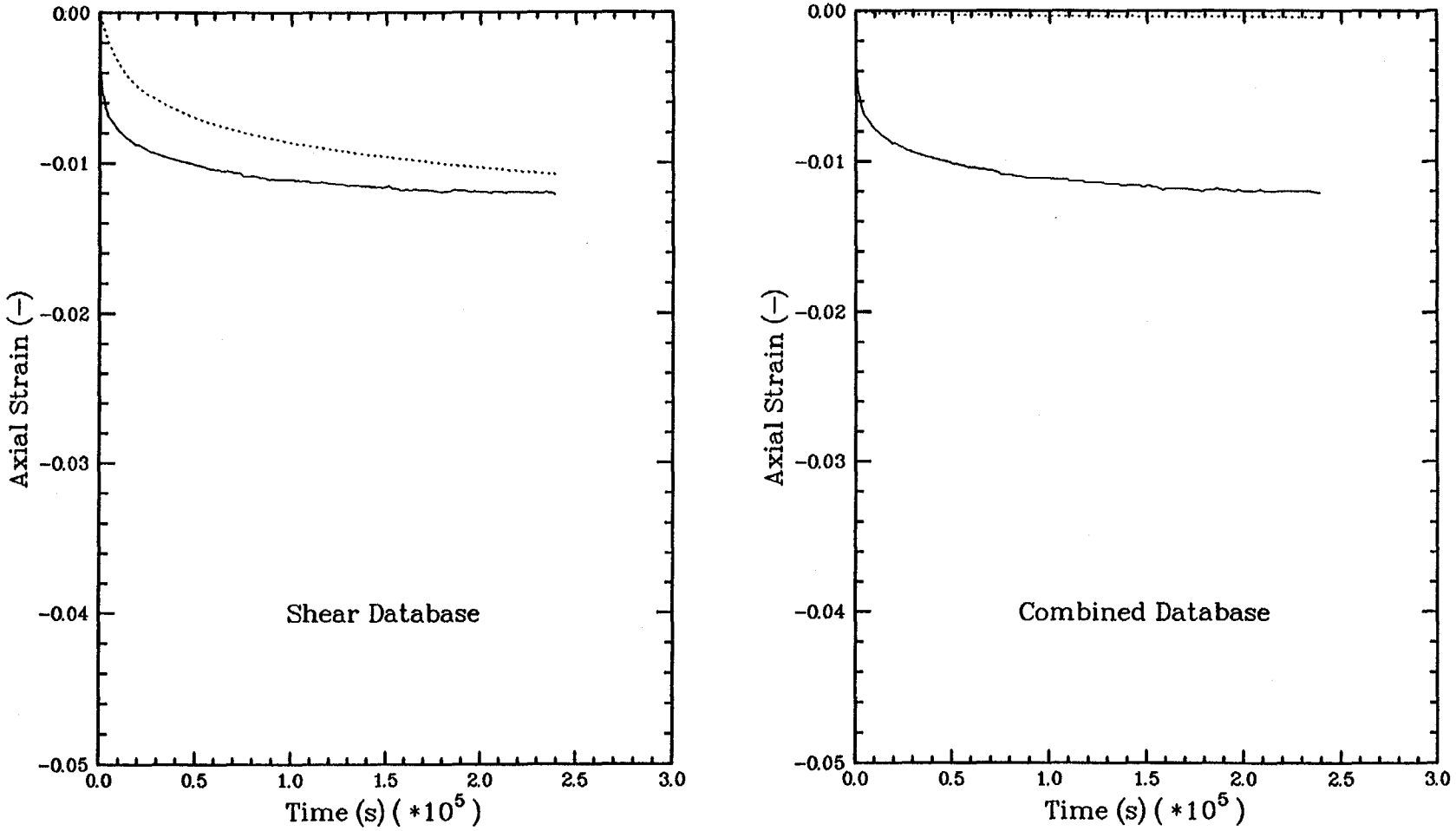

Figure C-18. Hydrostatic Consolidation Test 04MAY82

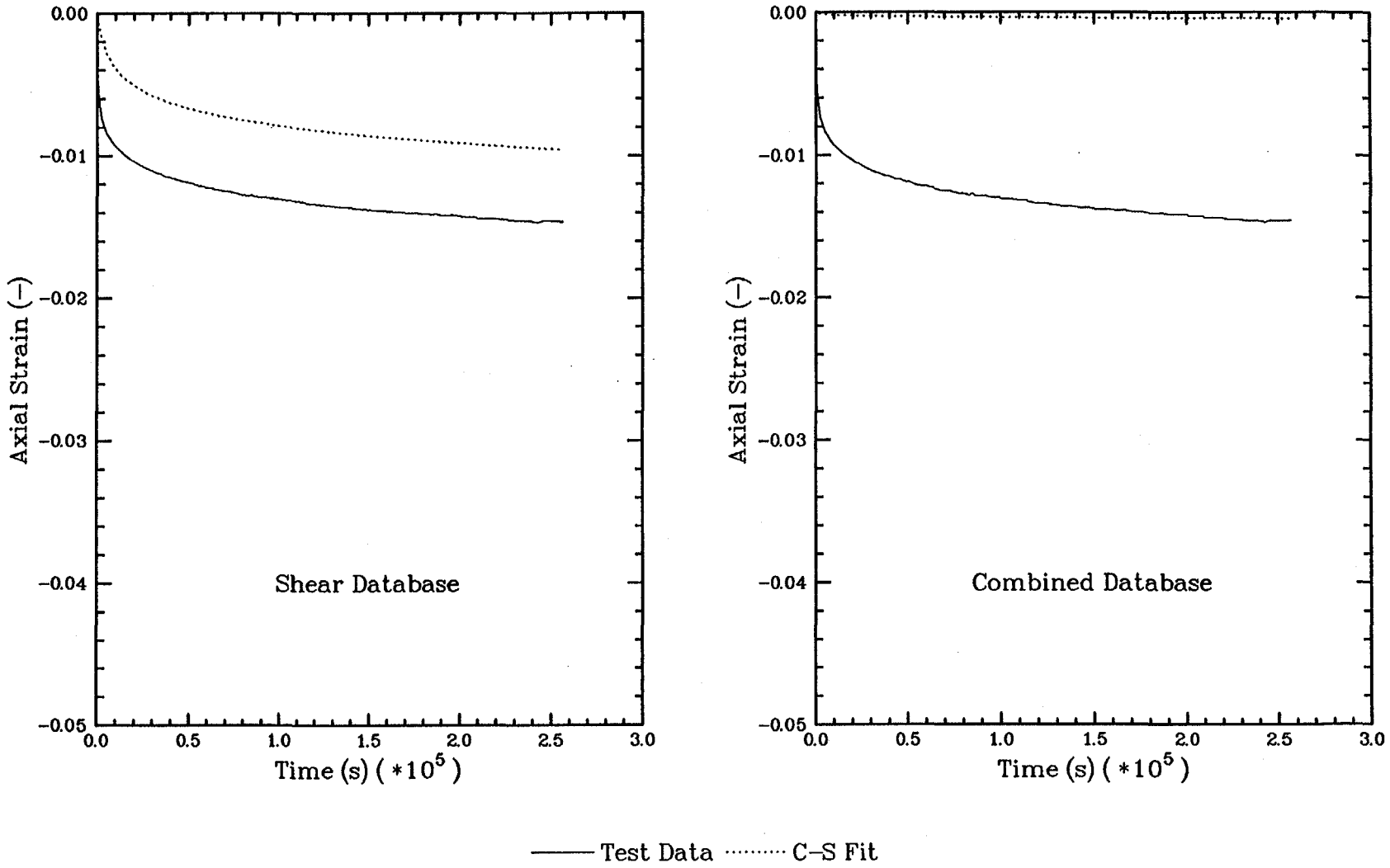

Figure C-19. Hydrostatic Consolidation Test 30APR82

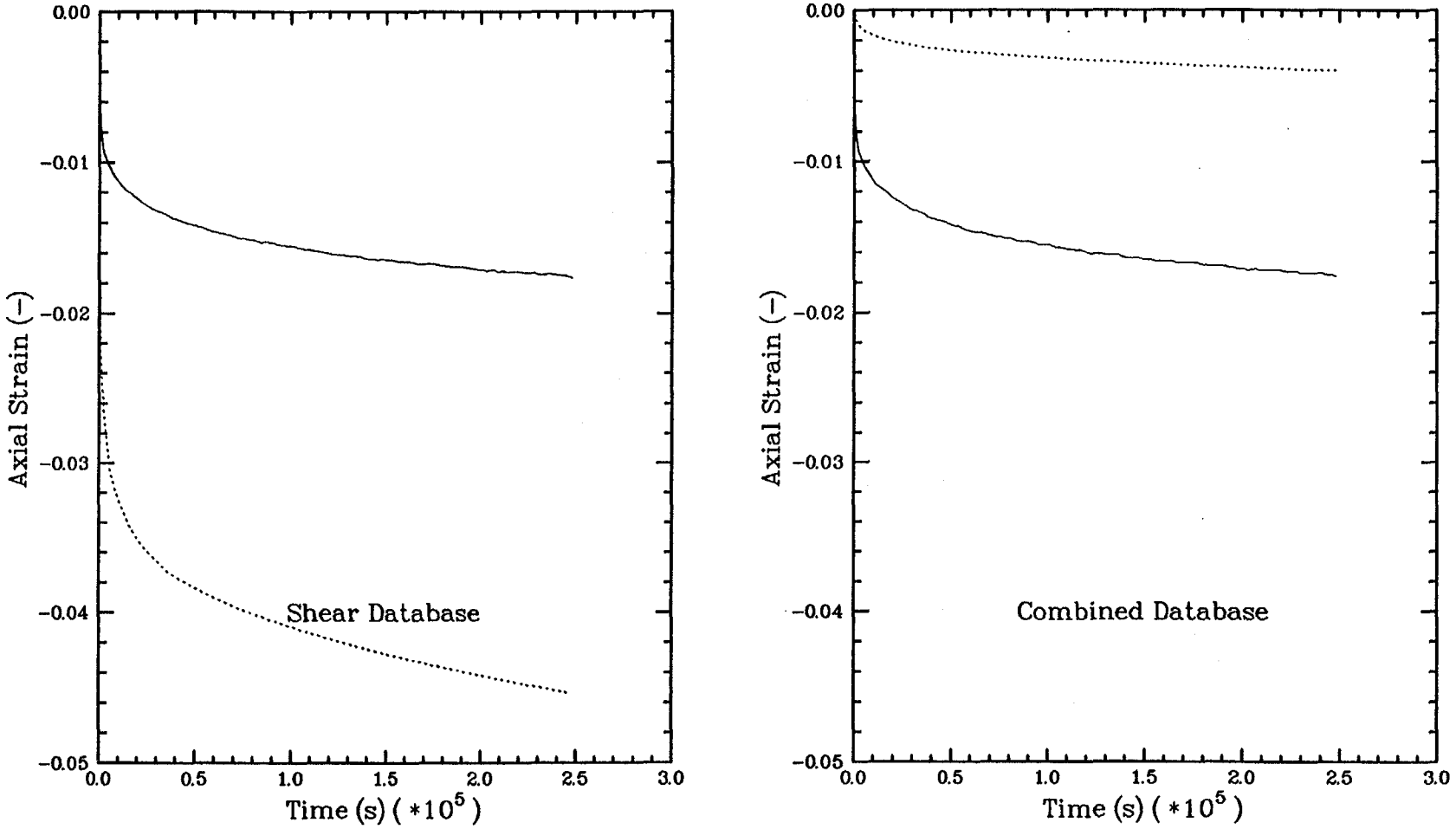

Figure C-20. Hydrostatic Consolidation Test 07MAY82

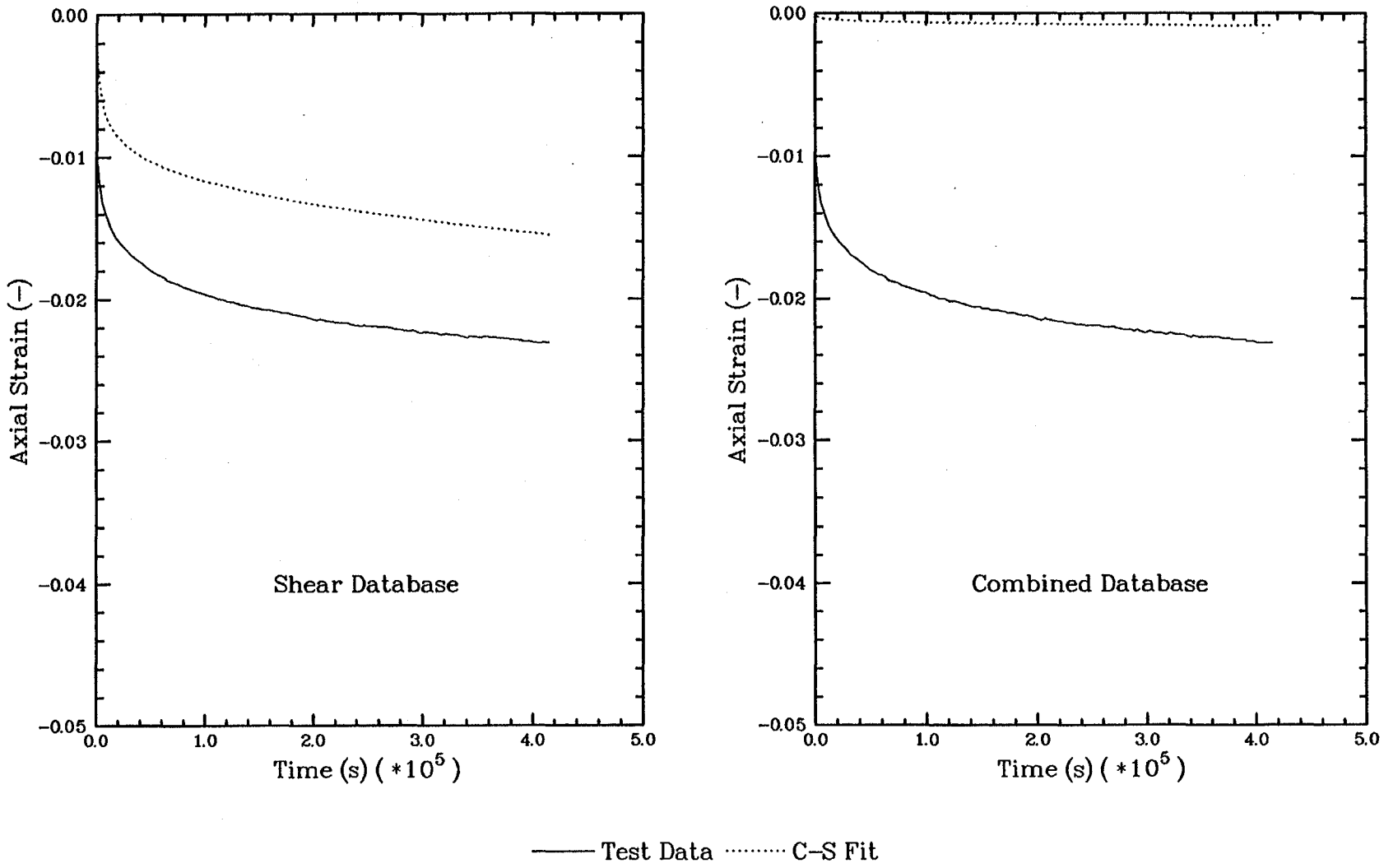

Figure C-21. Hydrostatic Consolidation Test 12MAY82

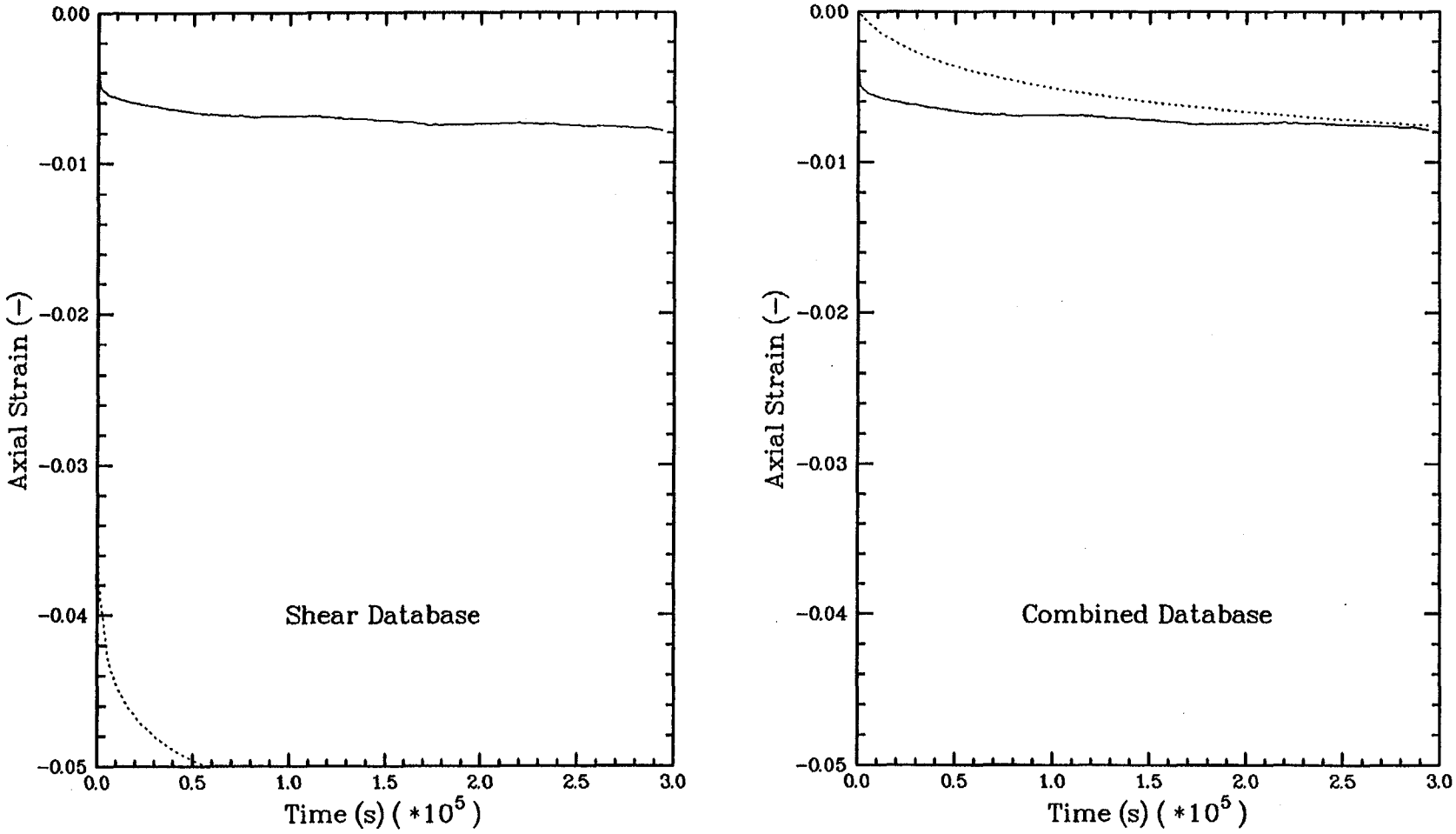

Figure C-22. Hydrostatic Consolidation Test 05FEB82

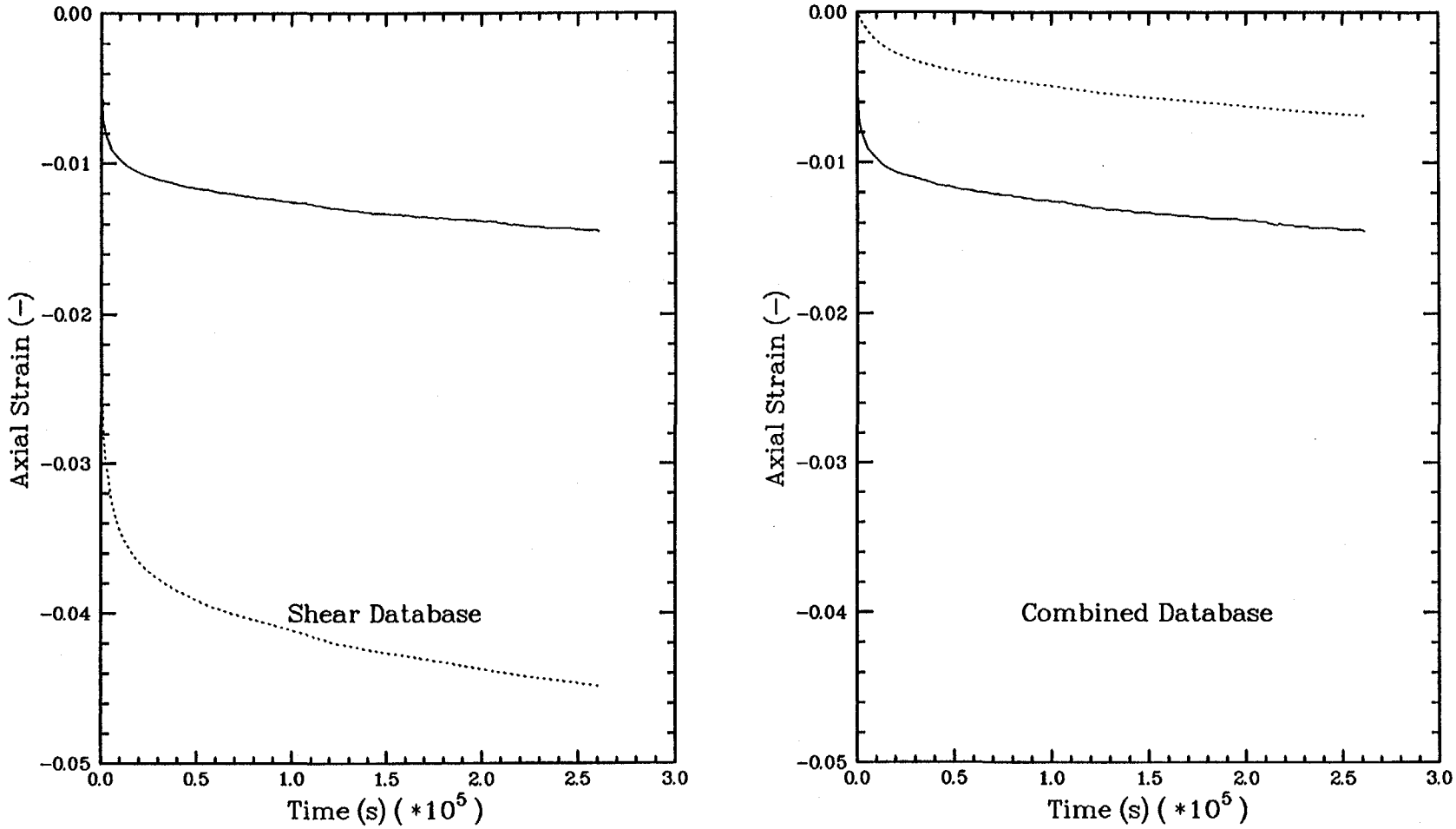

Figure C-23. Hydrostatic Consolidation Test 09APR82

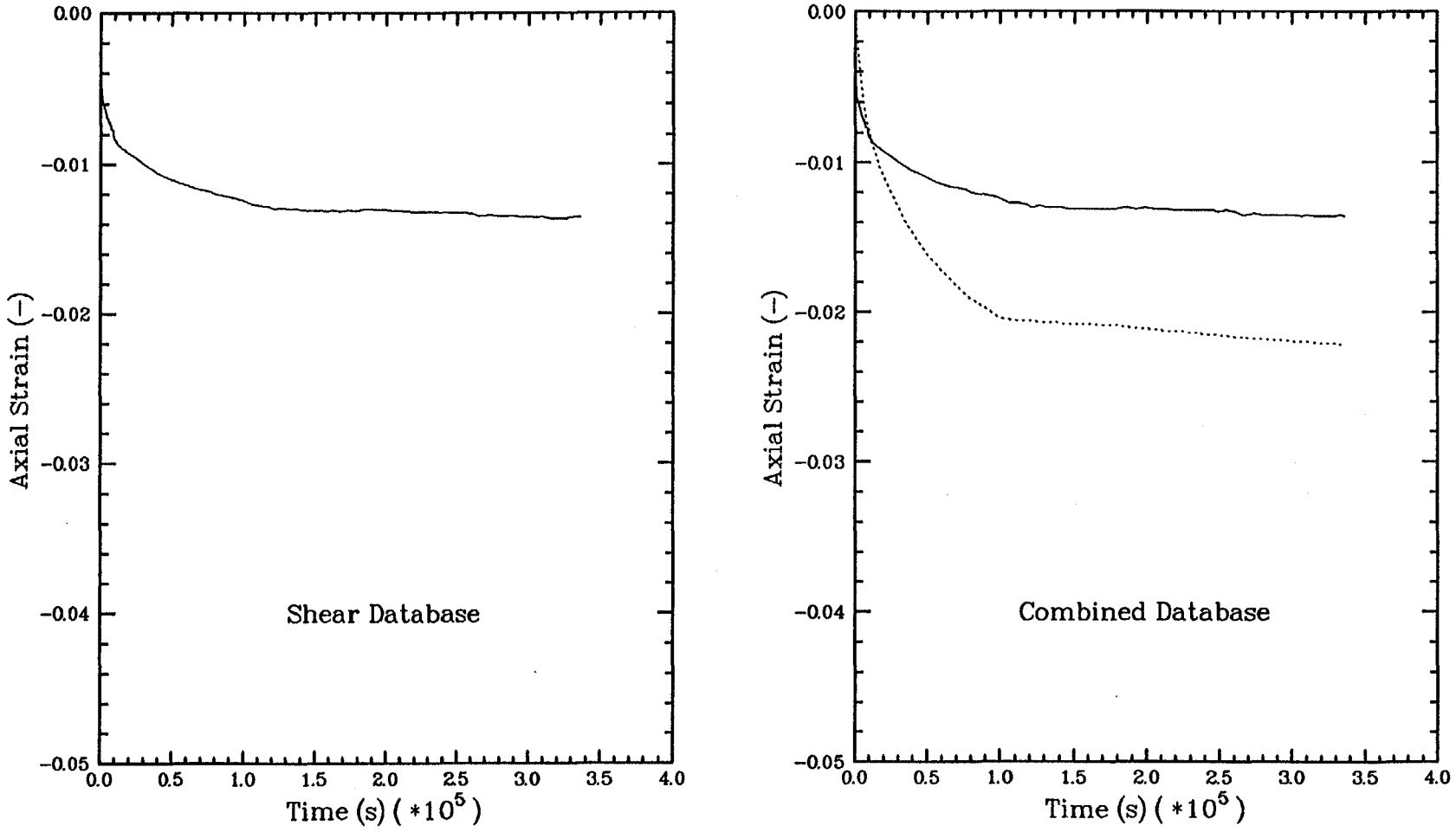

Figure C-24. Hydrostatic Consolidation Test 26MAR82

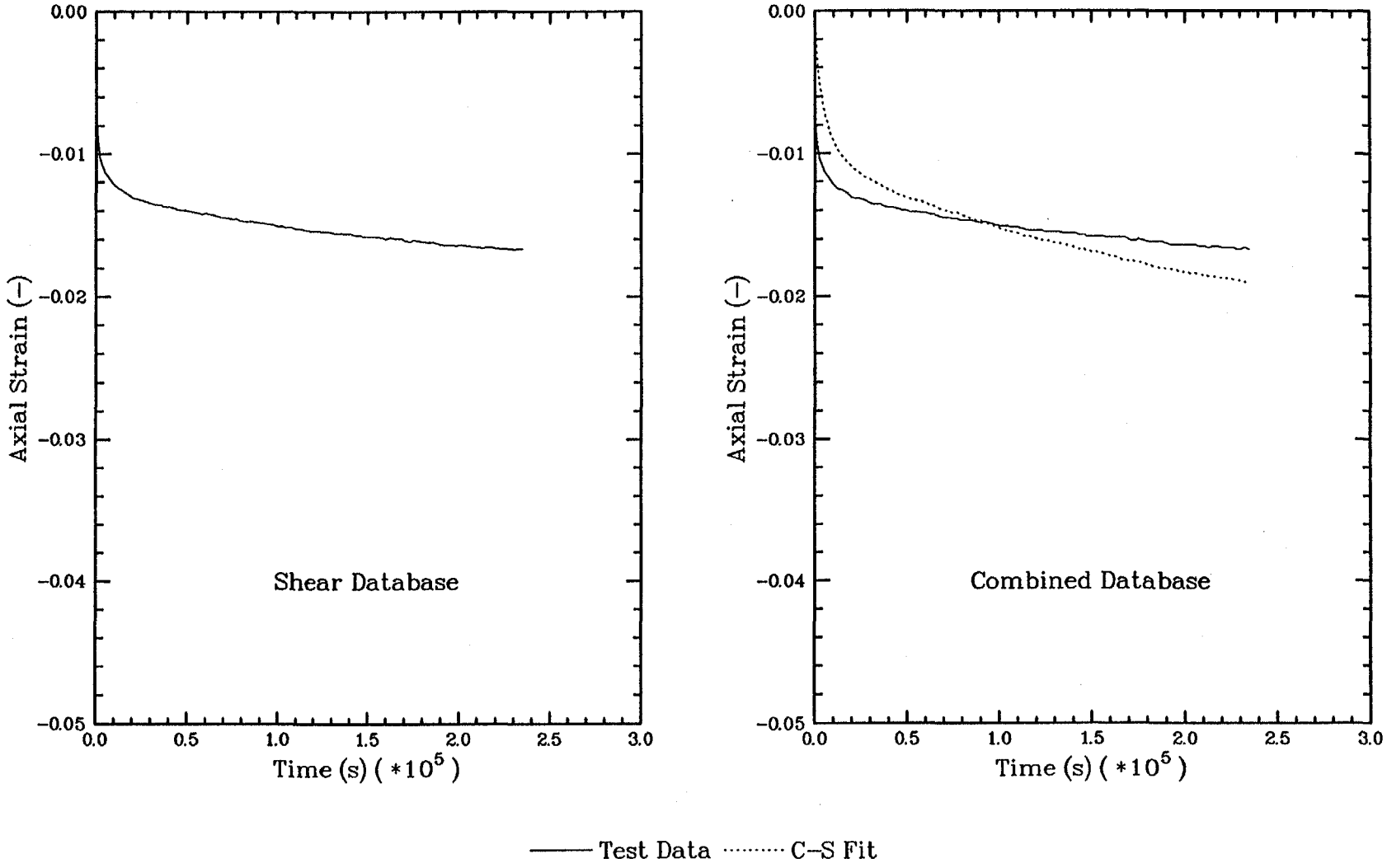

Figure C-25. Hydrostatic Consolidation Test 02APR82

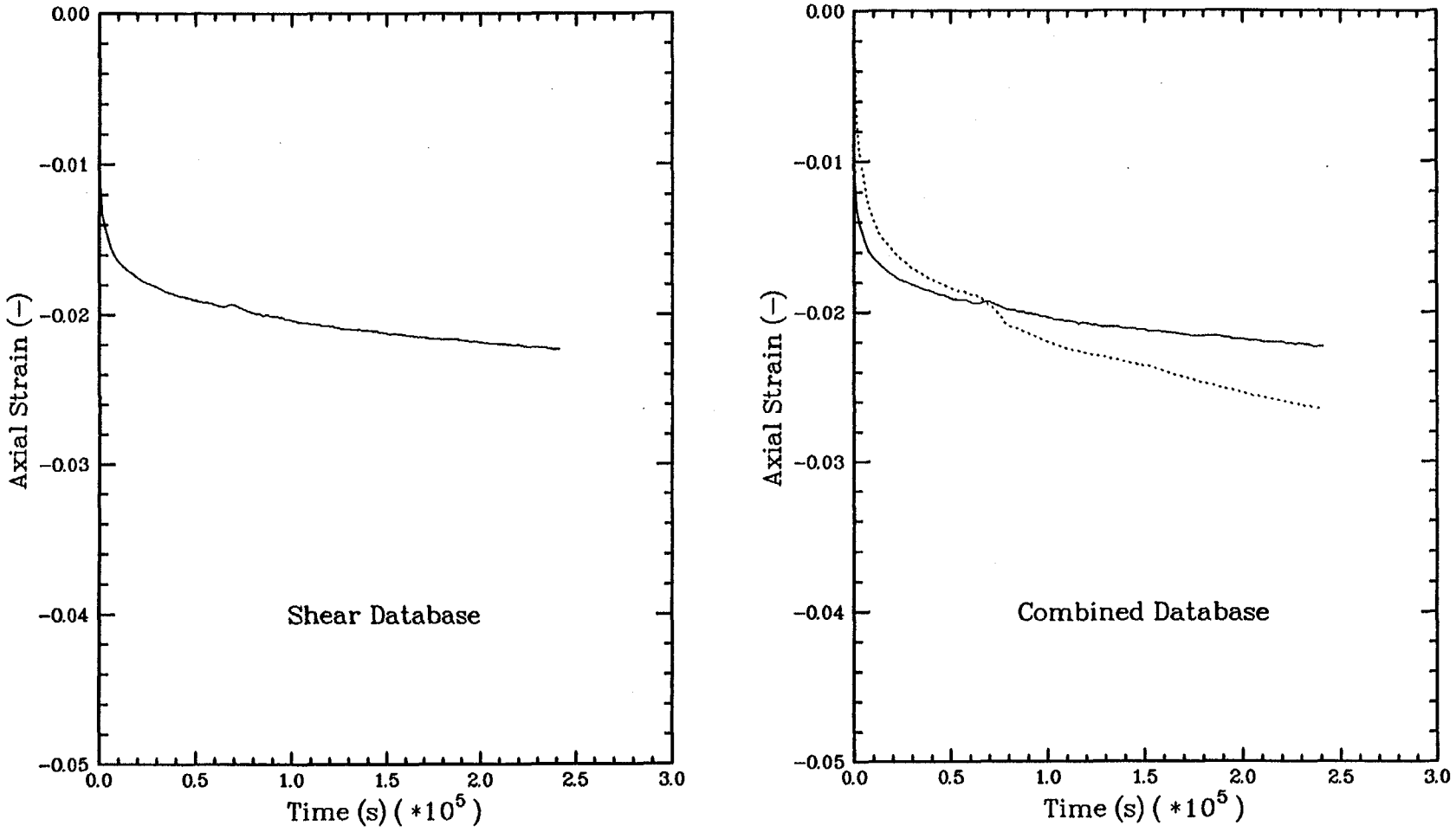

Figure C-26. Hydrostatic Consolidation Test 13APR82

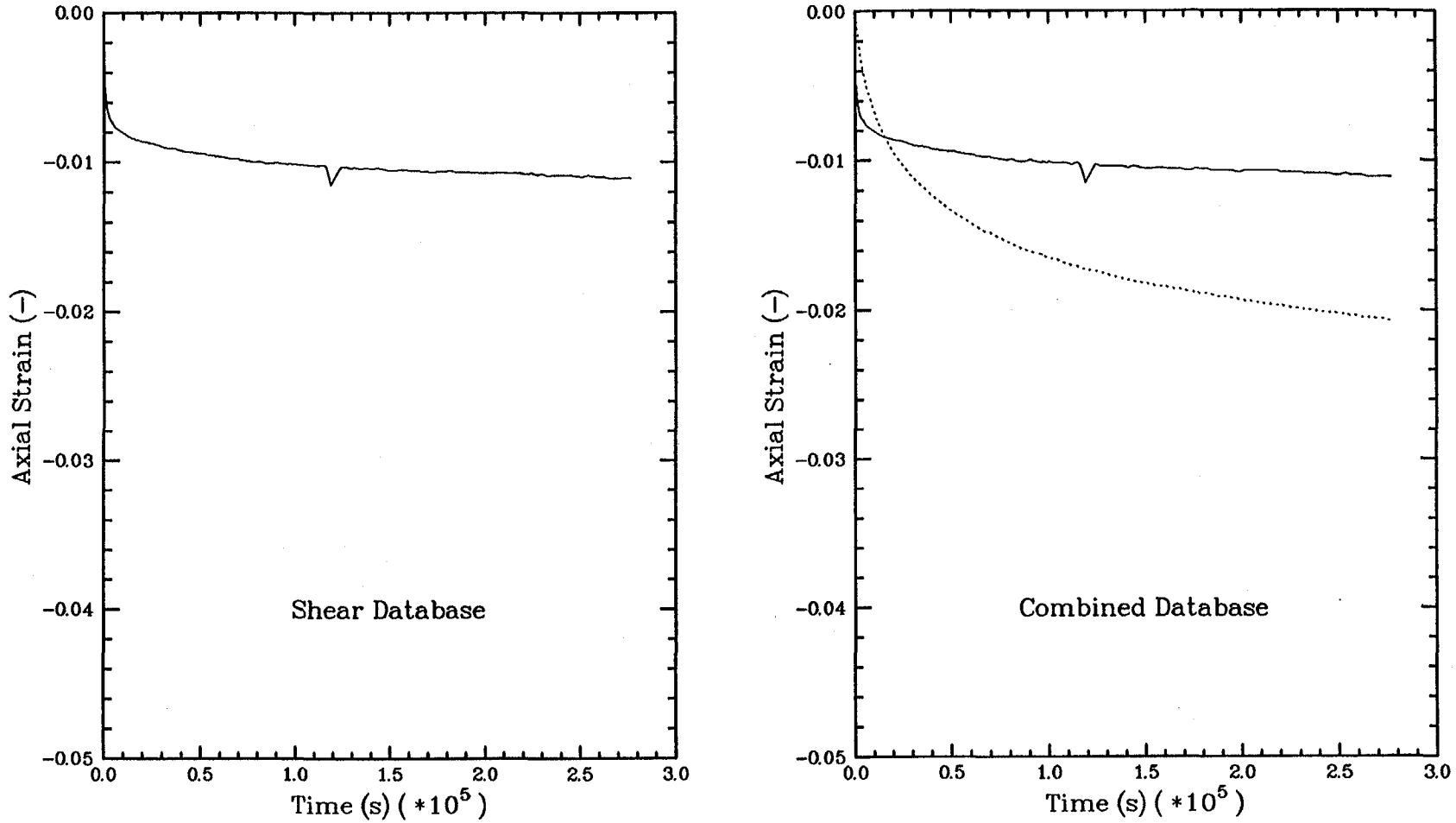

Figure C-27. Hydrostatic Consolidation Test 29JAN82

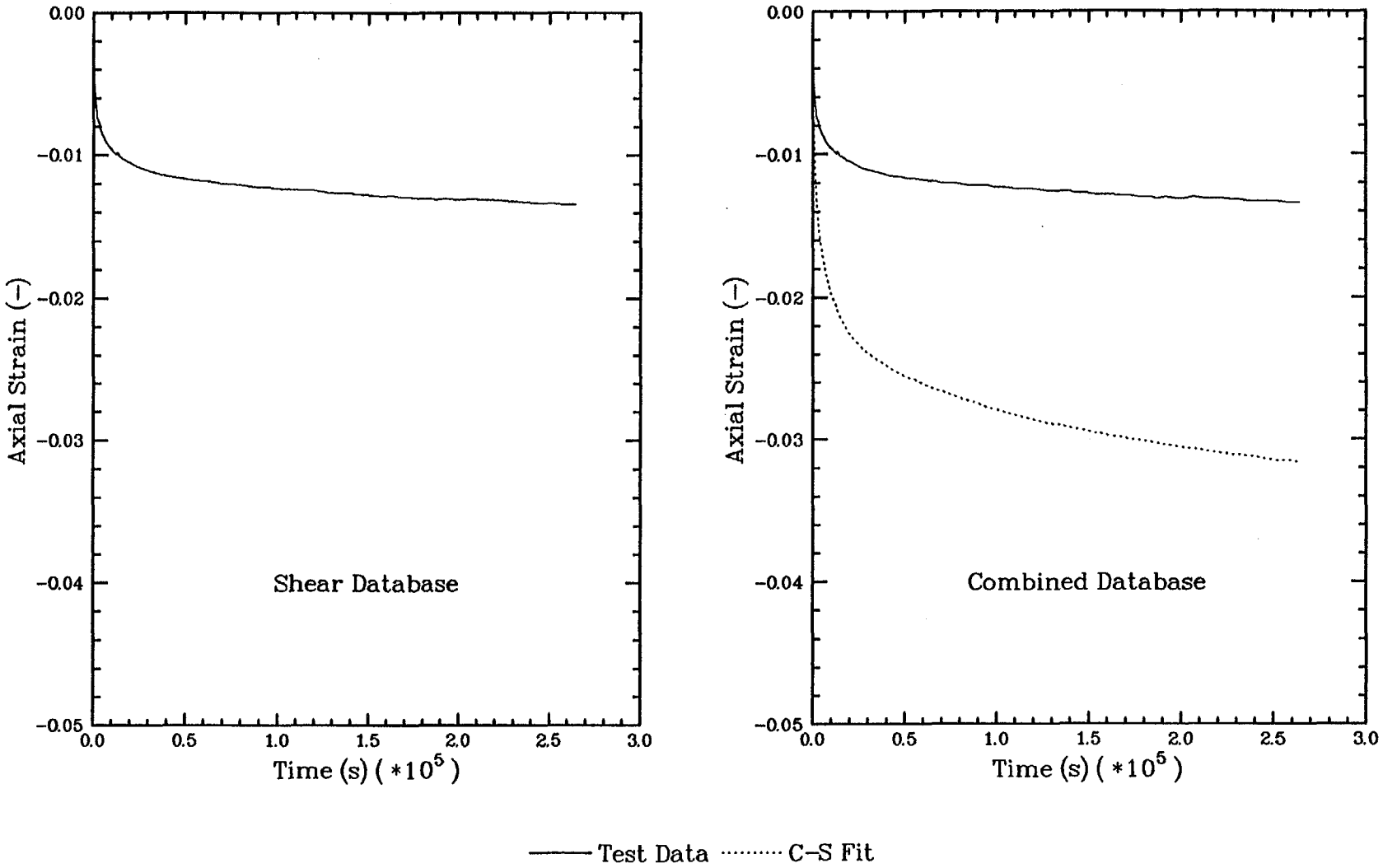

Figure C-28. Hydrostatic Consolidation Test 26FEB82

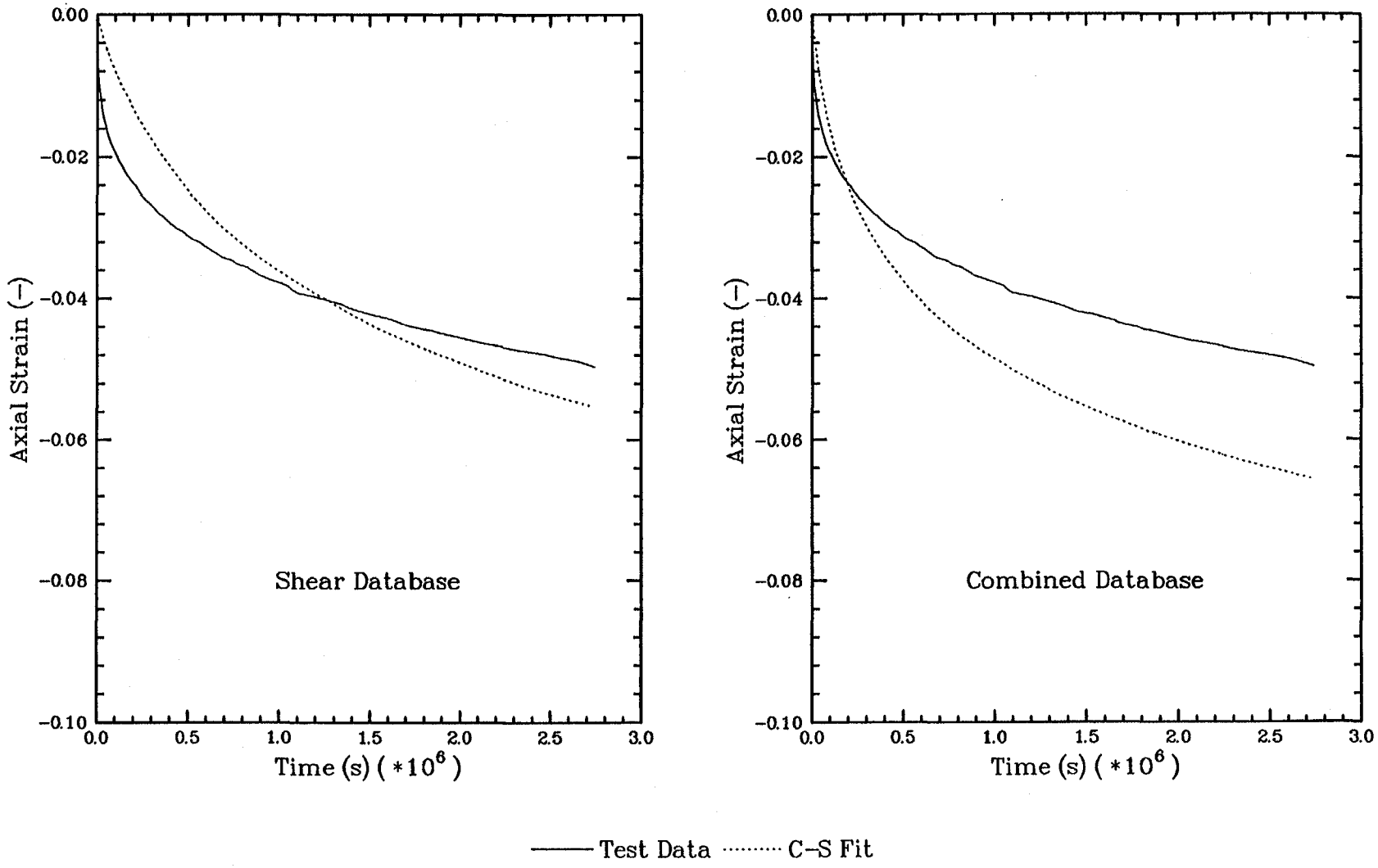

Figure C-29. Hydrostatic Consolidation Test 27JU61

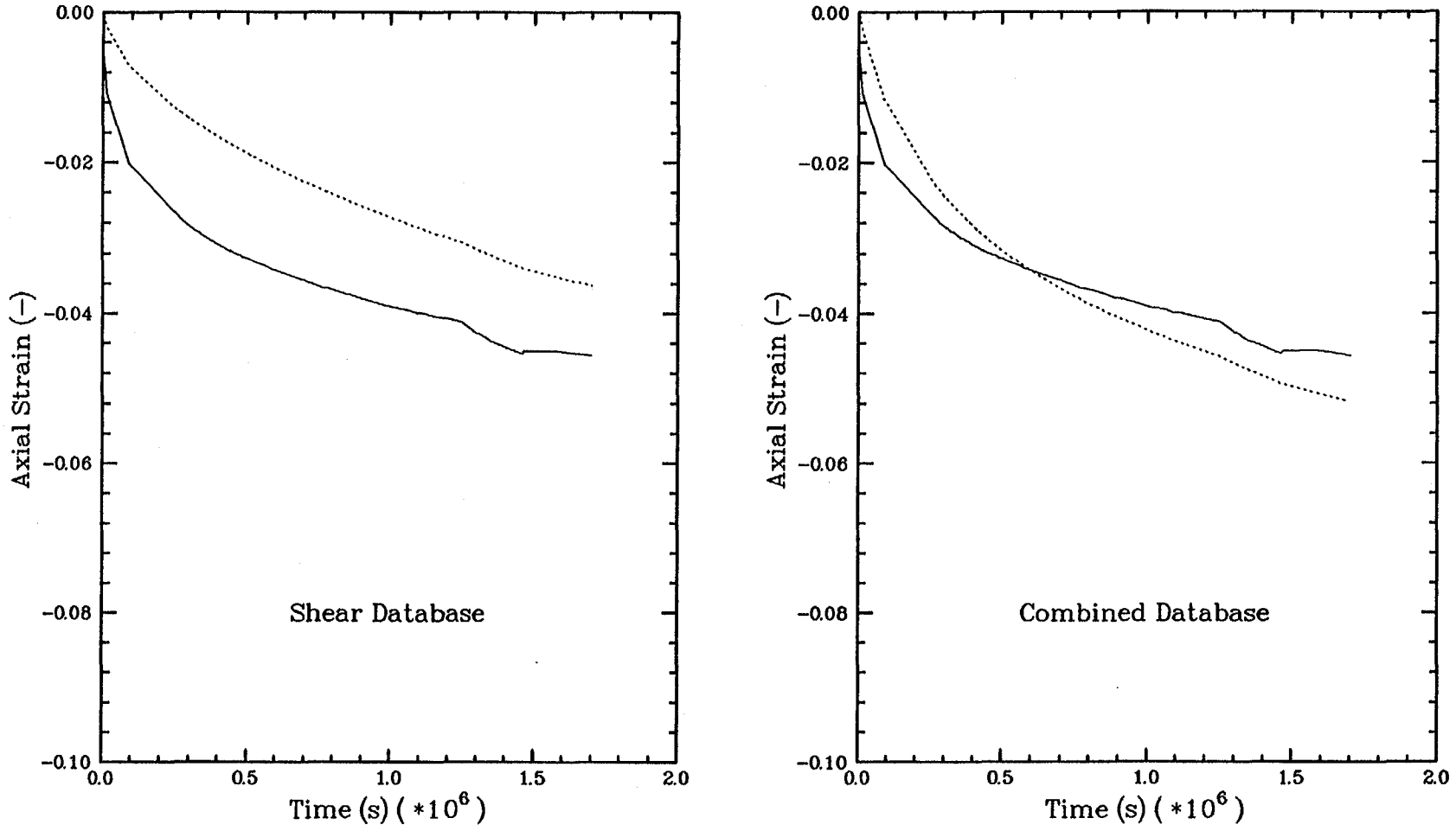

Figure C-30. Hydrostatic Consolidation Test 23JL51

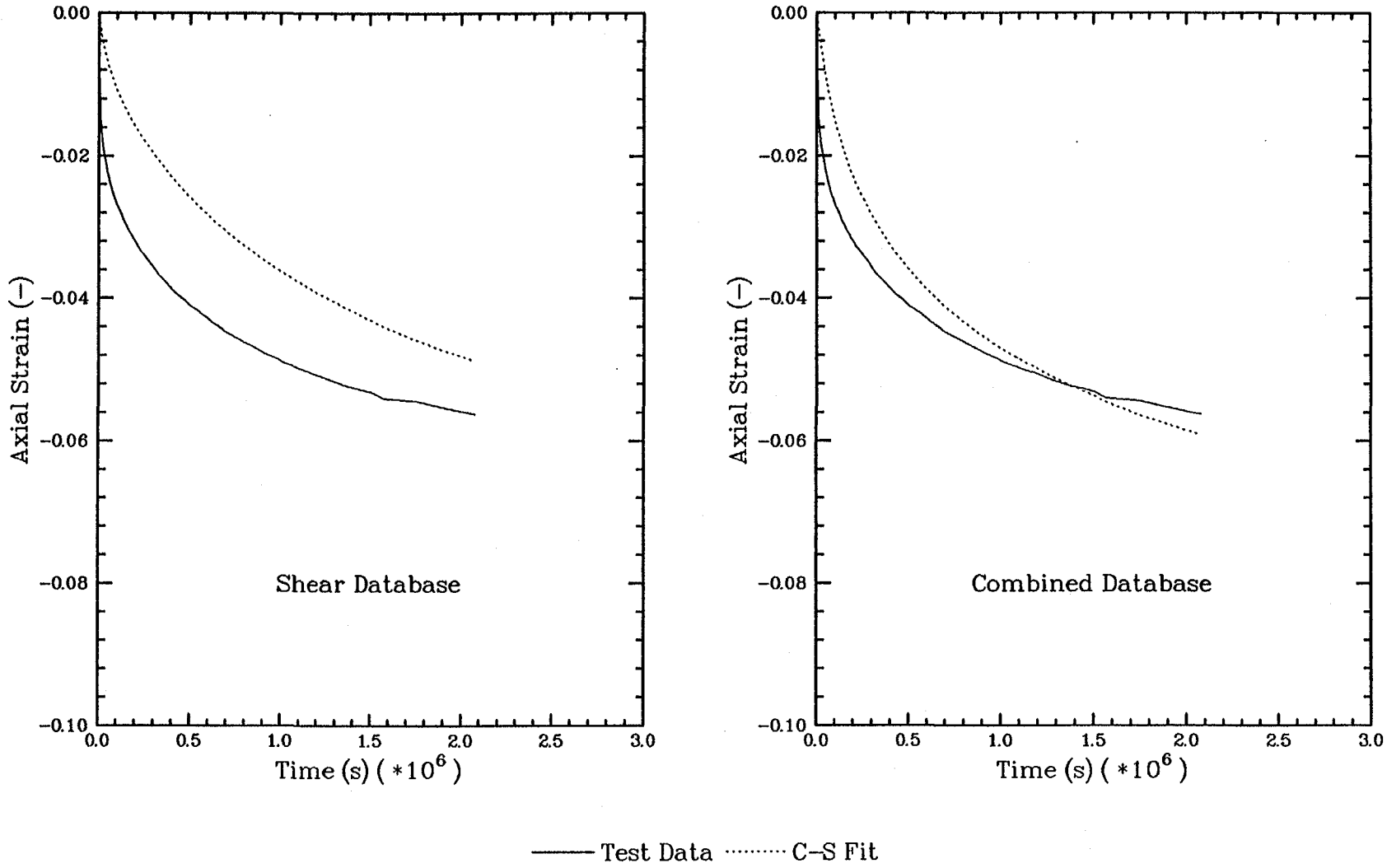

Figure C-31. Hydrostatic Consolidation Test 14NV51

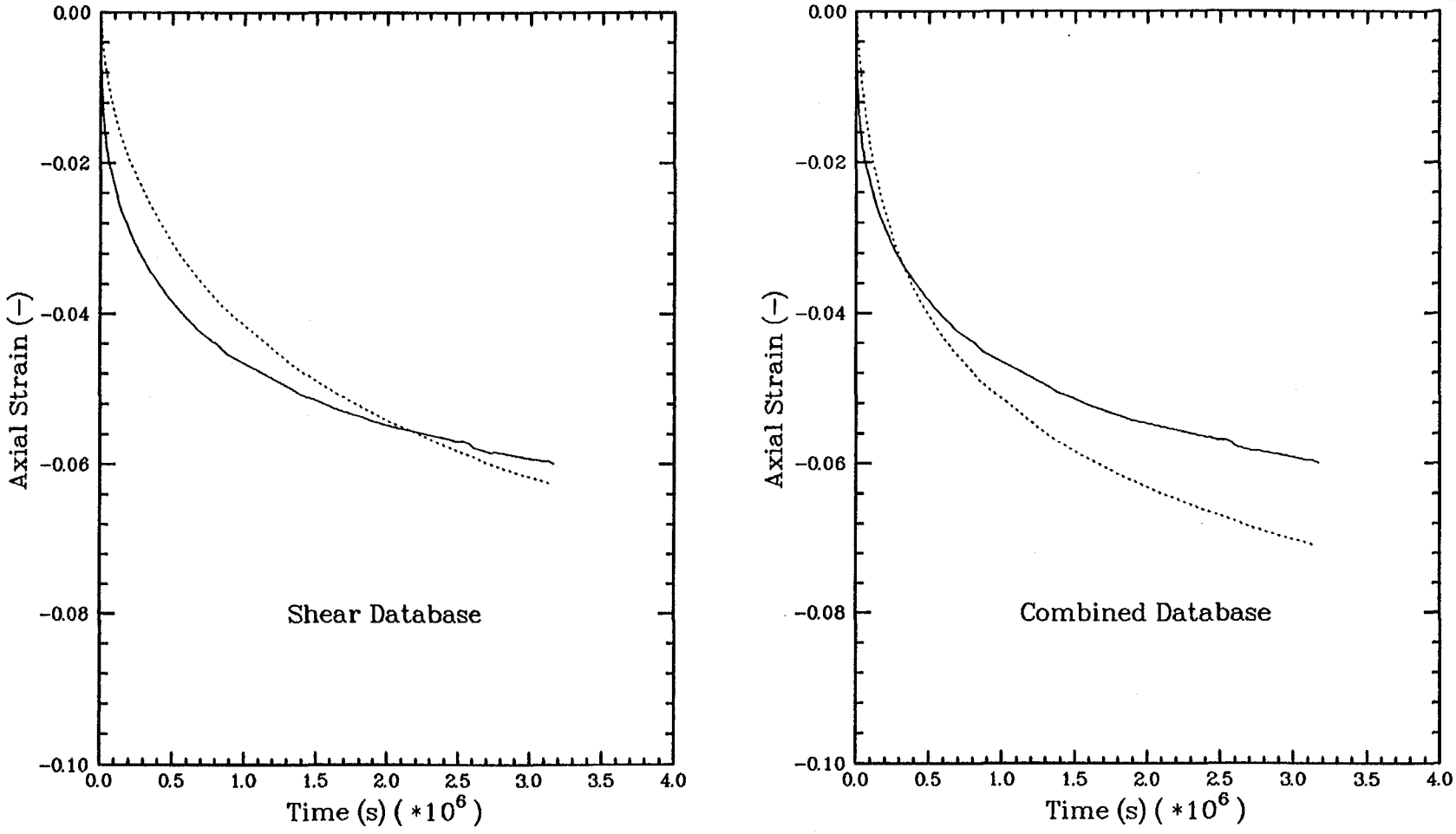

Figure C-32. Hydrostatic Consolidation Test 25FEB61

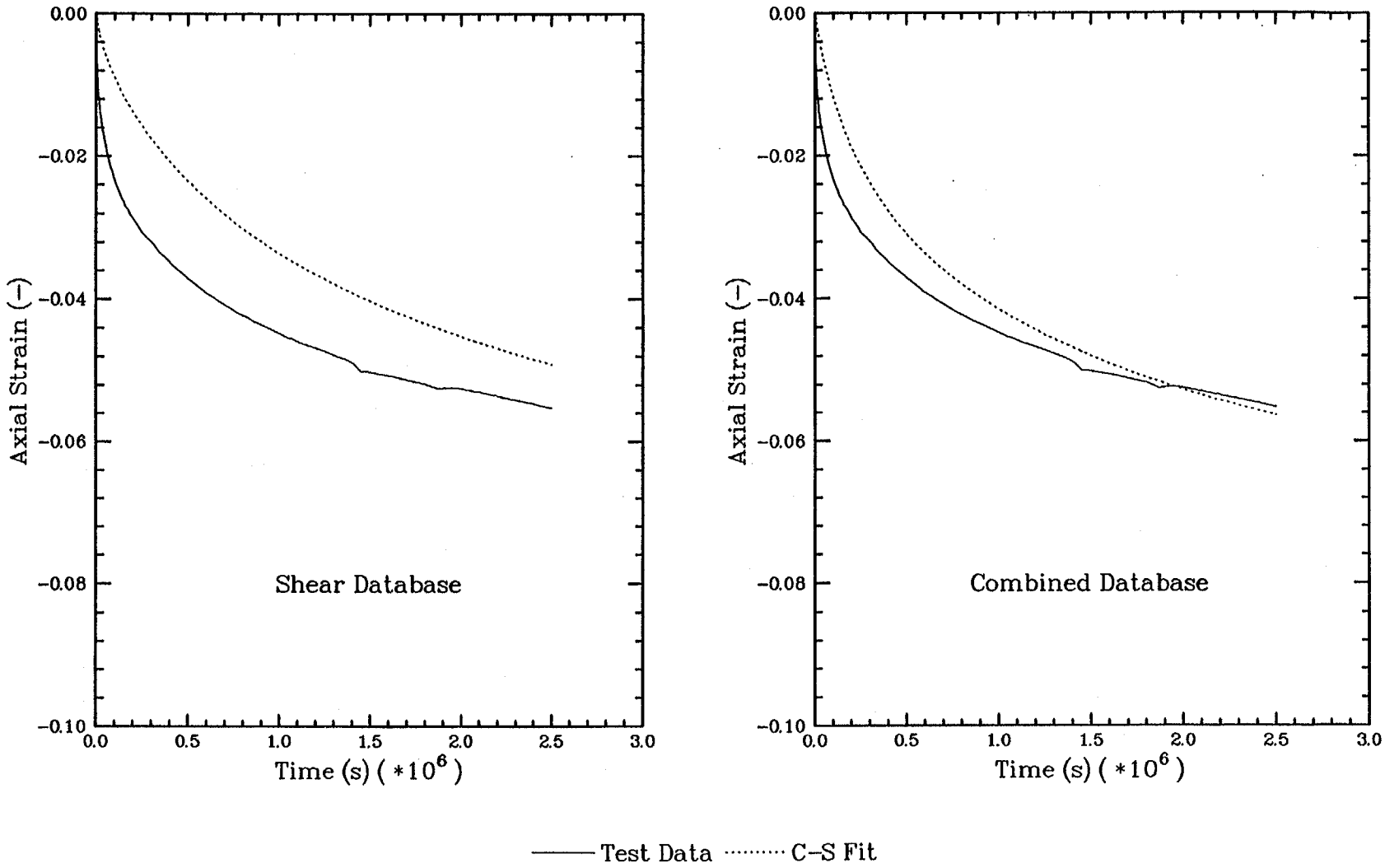

Figure C-33. Hydrostatic Consolidation Test 10MY51

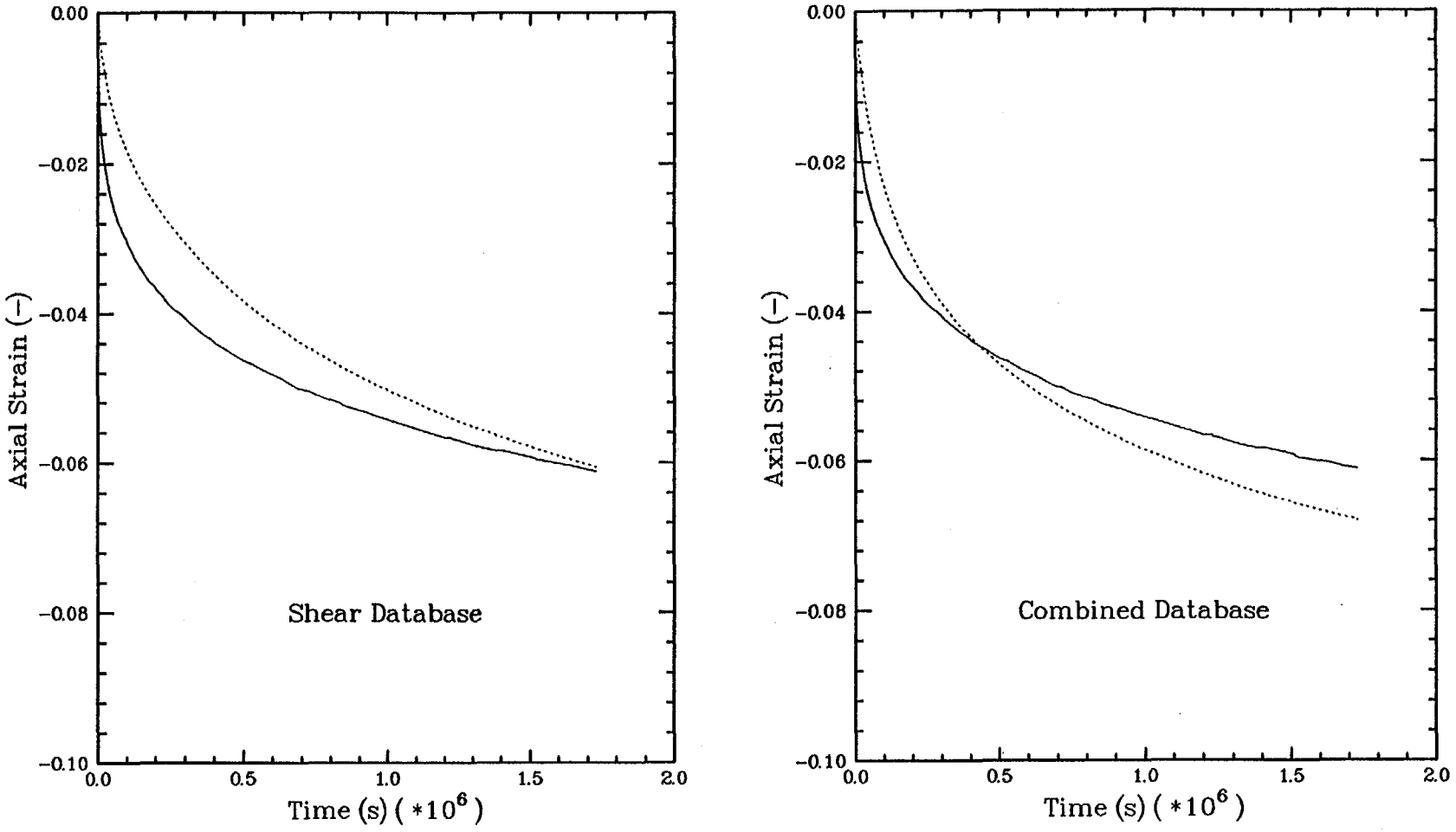

Figure C-34. Hydrostatic Consolidation Test 20AU51

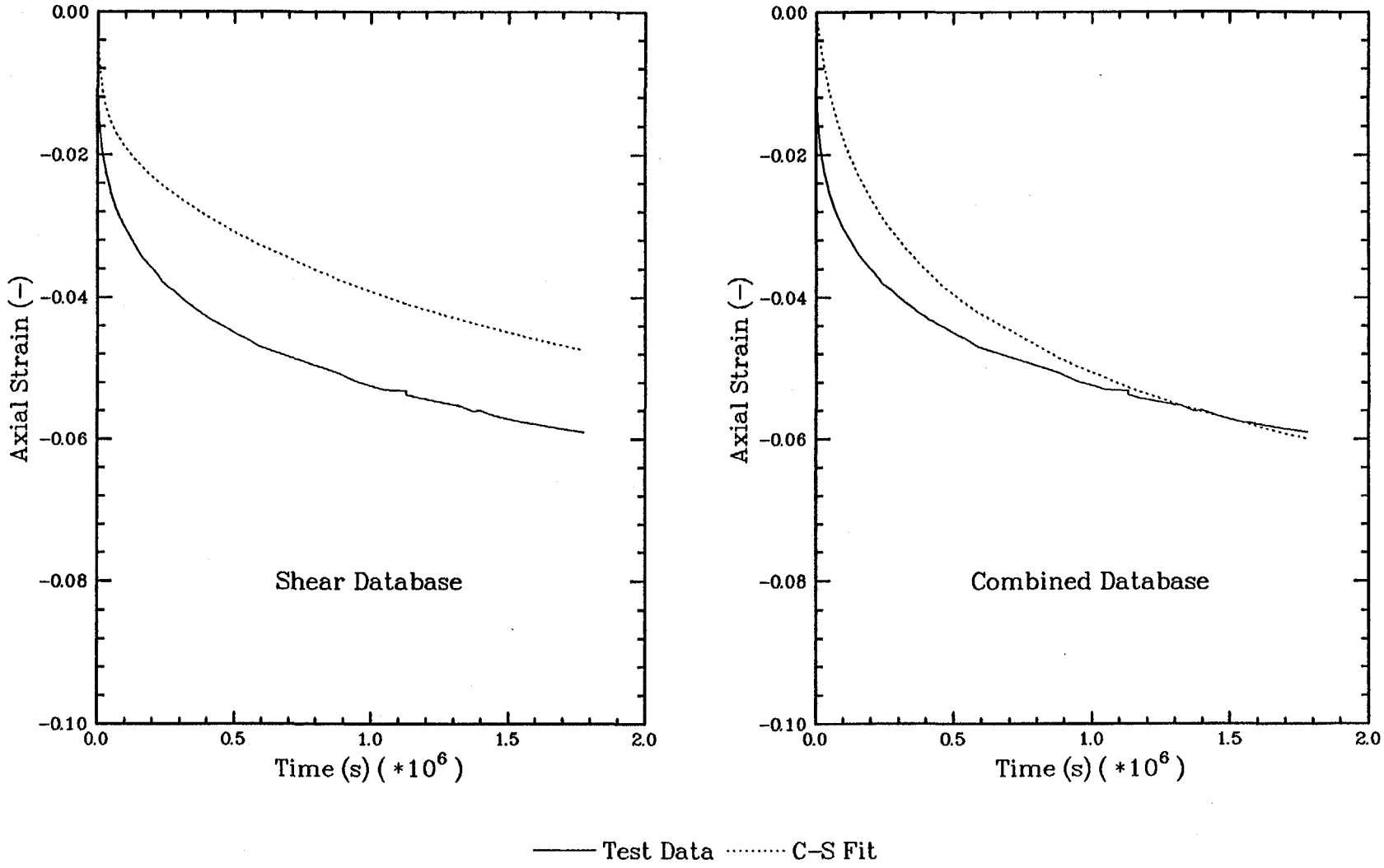

Figure C-35. Hydrostatic Consolidation Test 16JL51

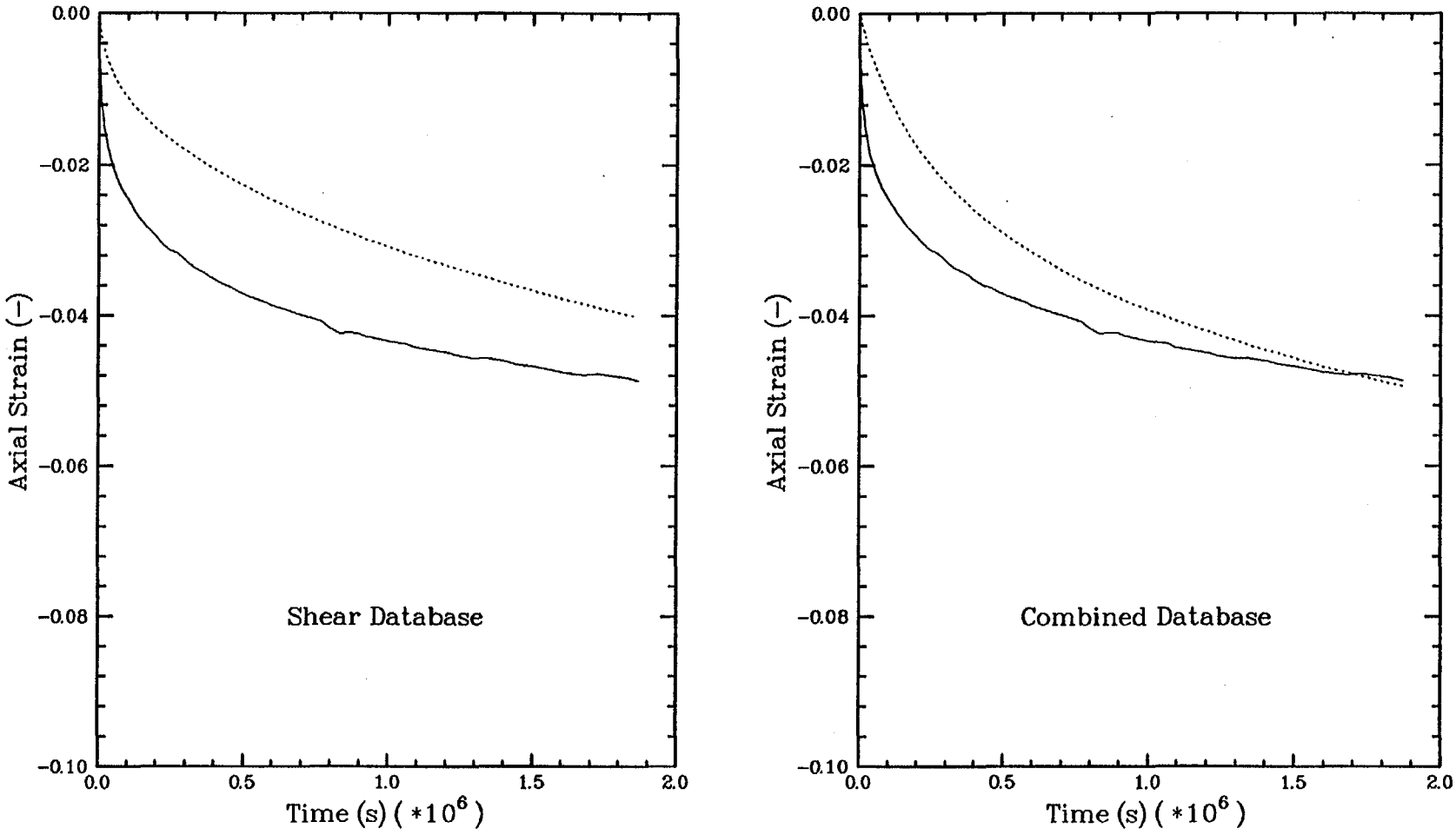

Figure C-36. Hydrostatic Consolidation Test 18JU51

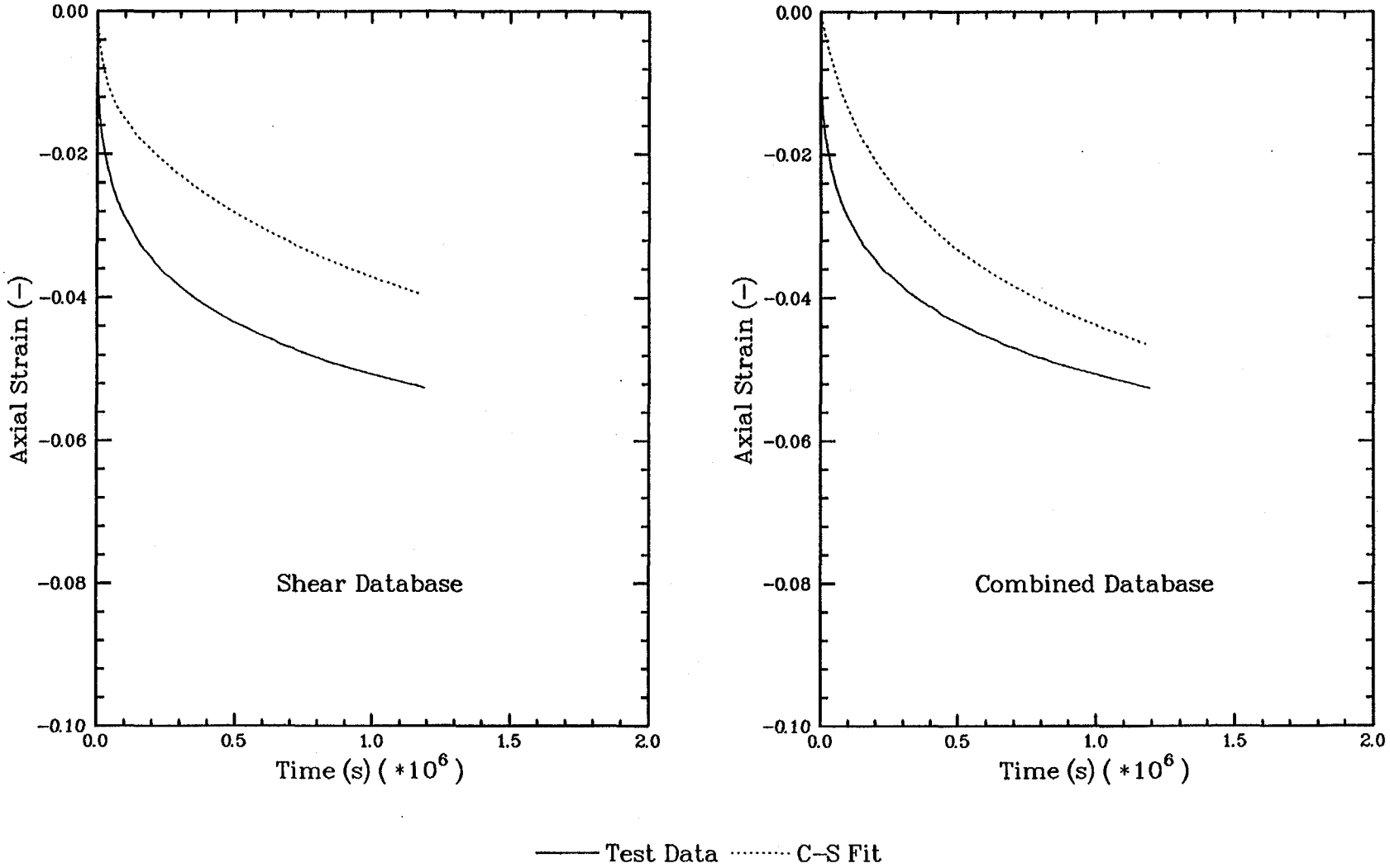

Figure C-37. Hydrostatic Consolidation Test 300C51

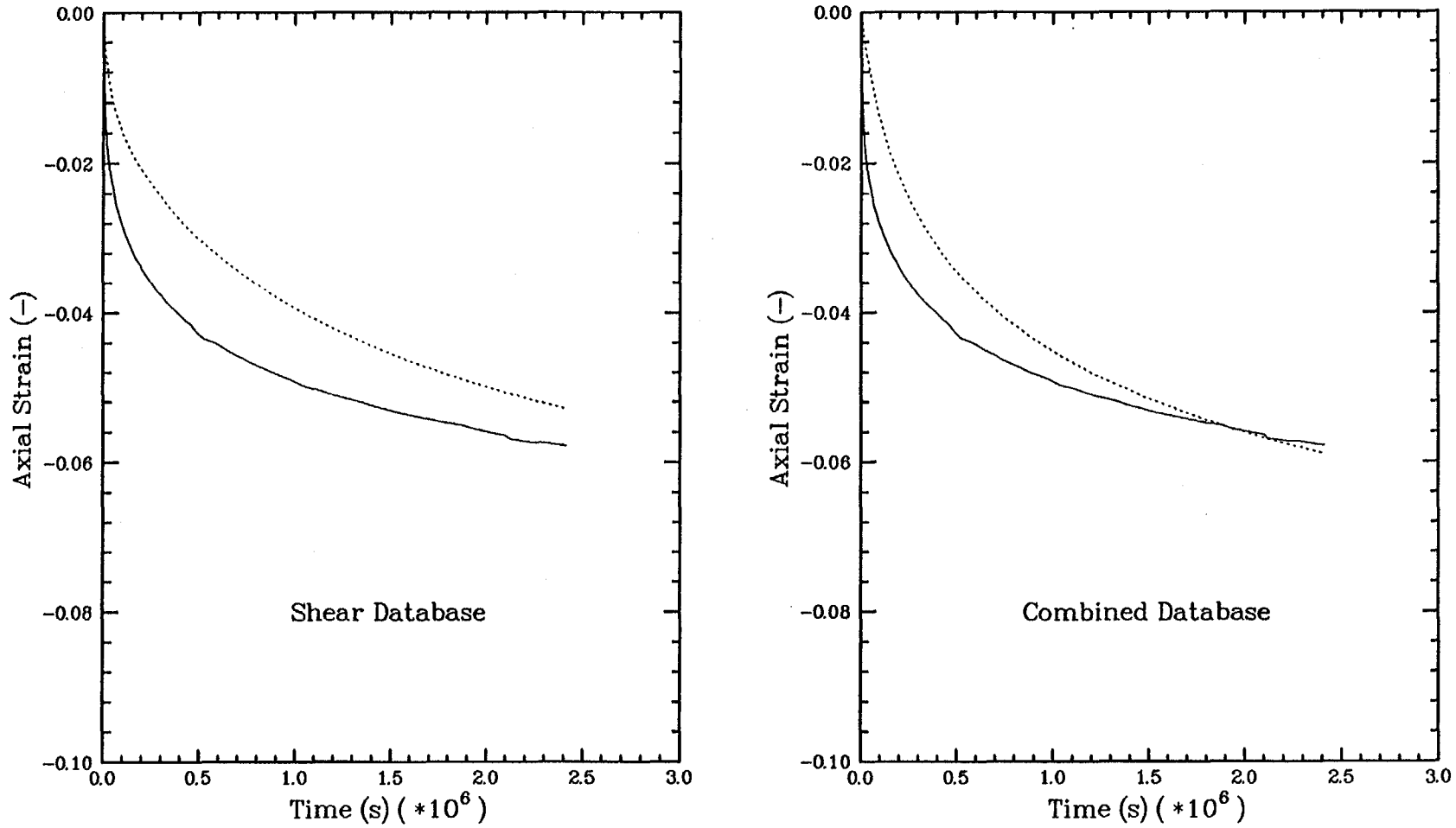

Figure C-38. Hydrostatic Consolidation Test 16JA61

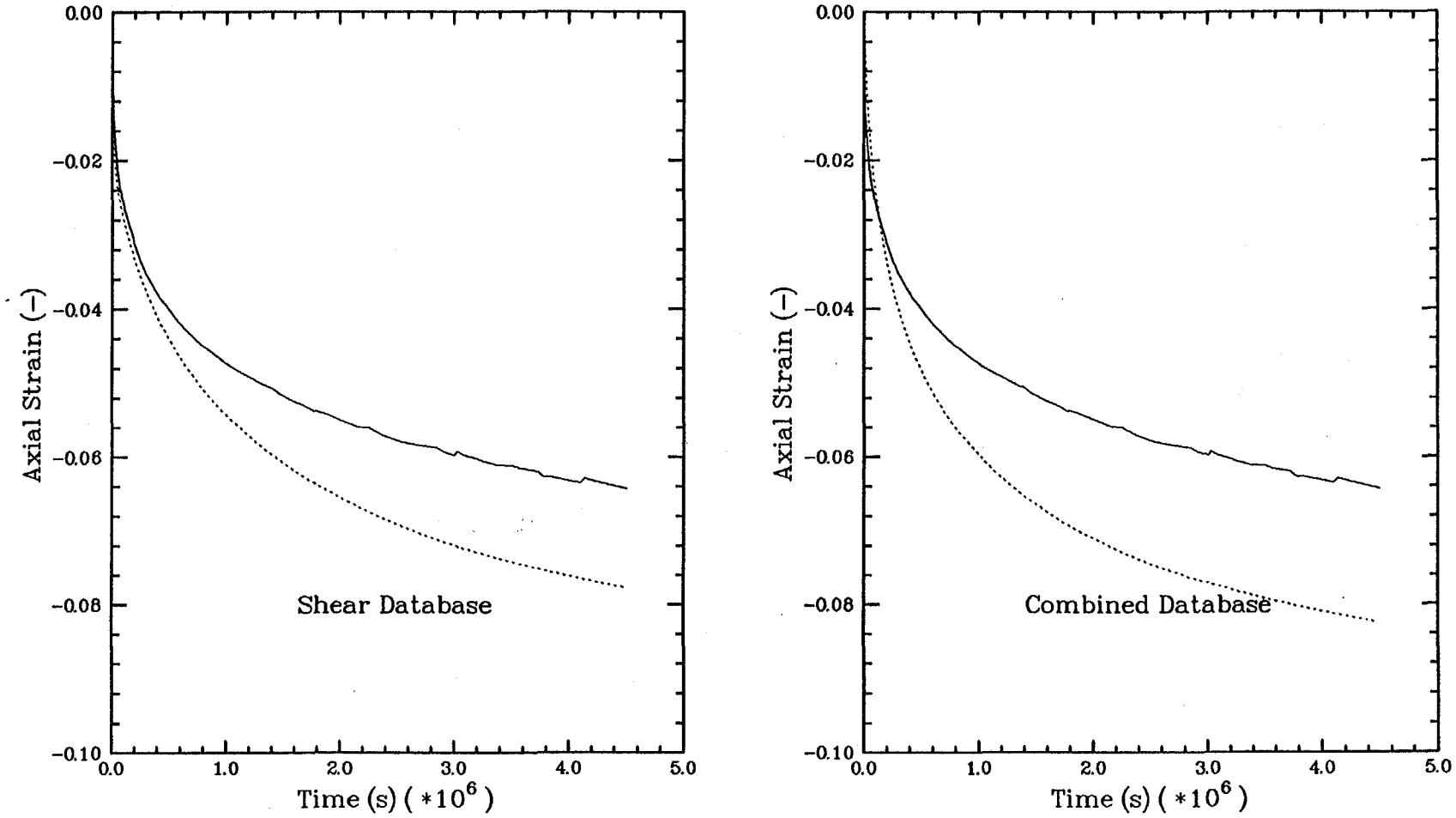

Figure C-39. Hydrostatic Consolidation Test 19DC44

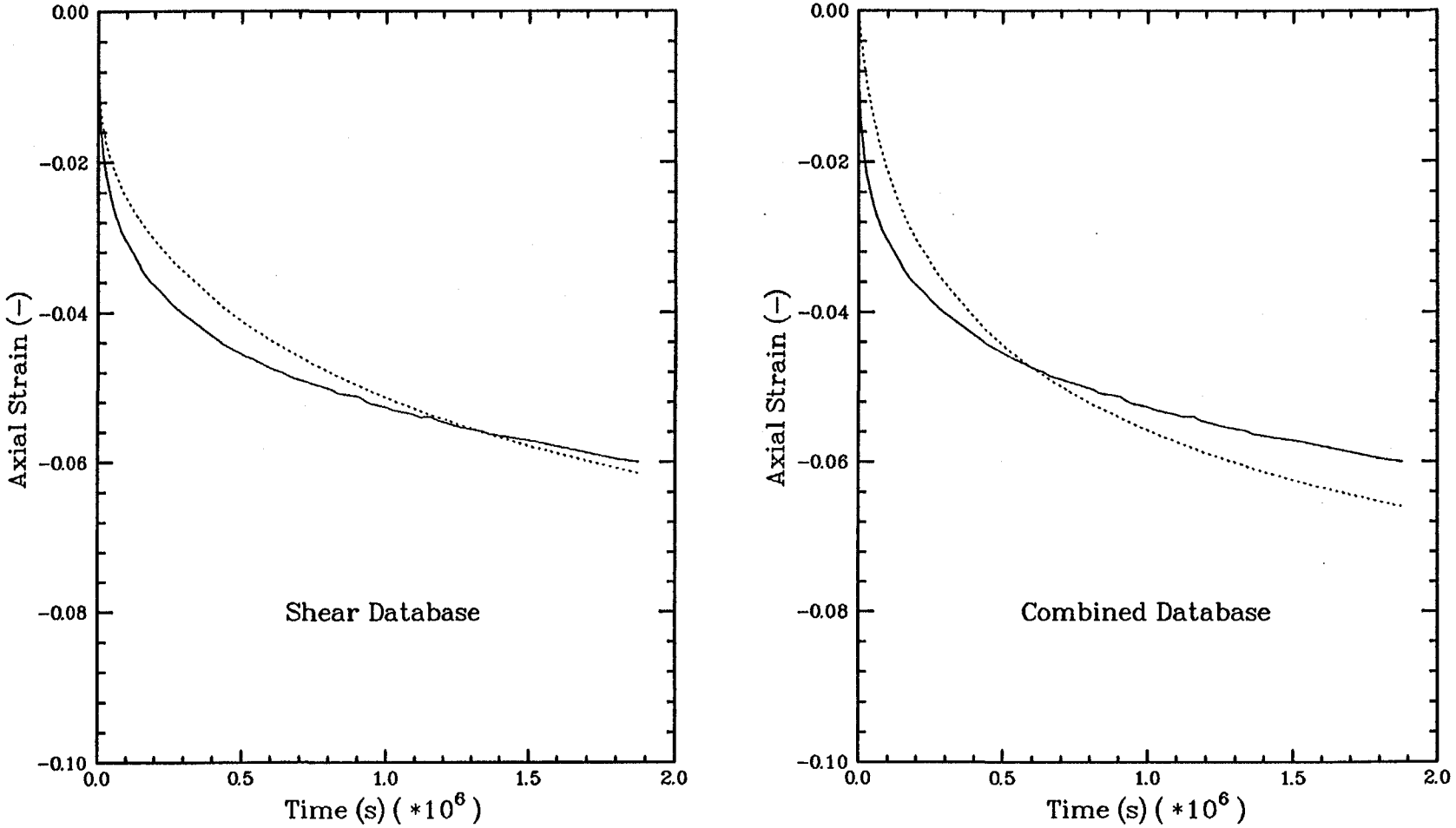

Figure C-40. Hydrostatic Consolidation Test 13AU51

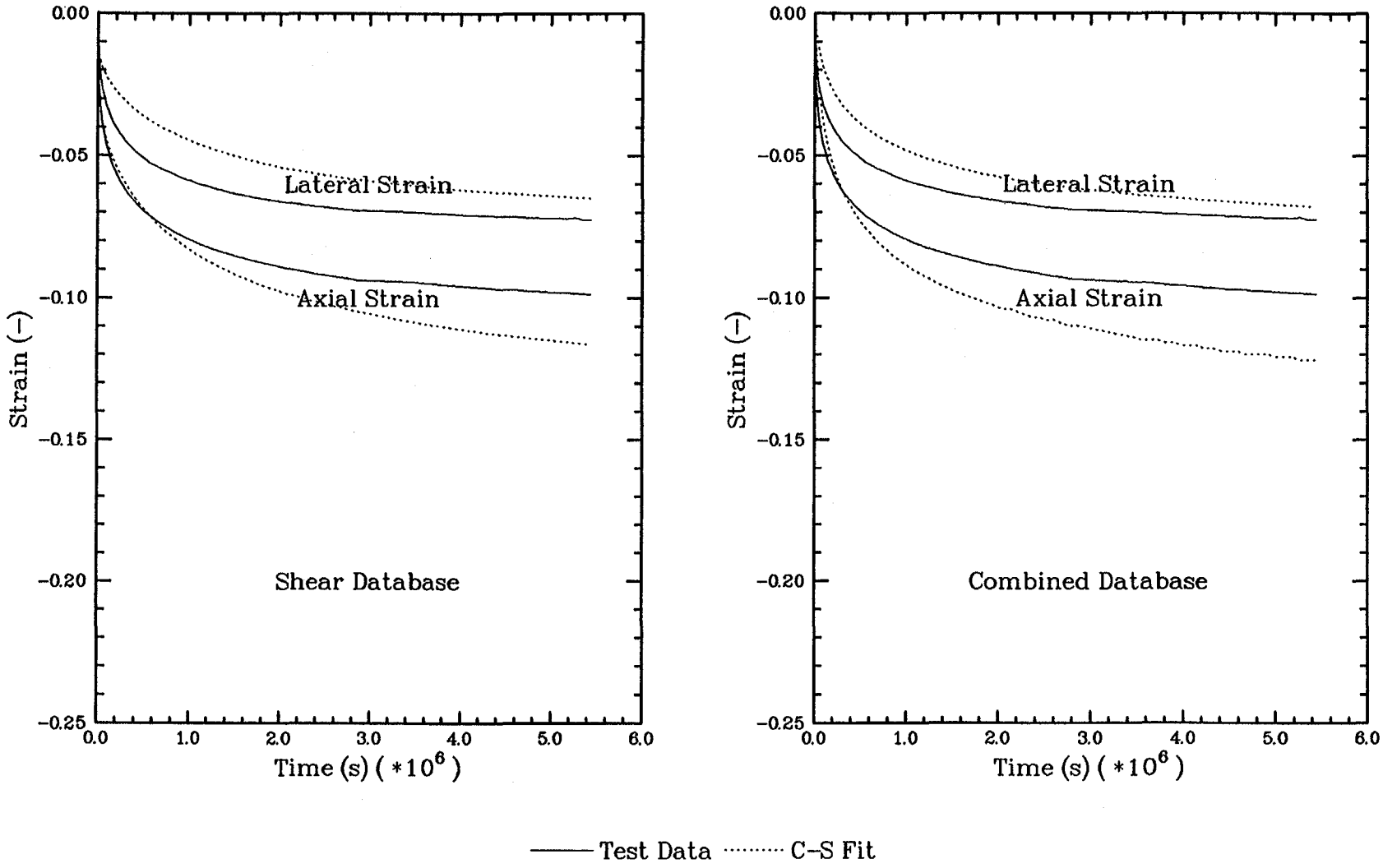

Figure C-41. Shear Consolidation Test SC1B

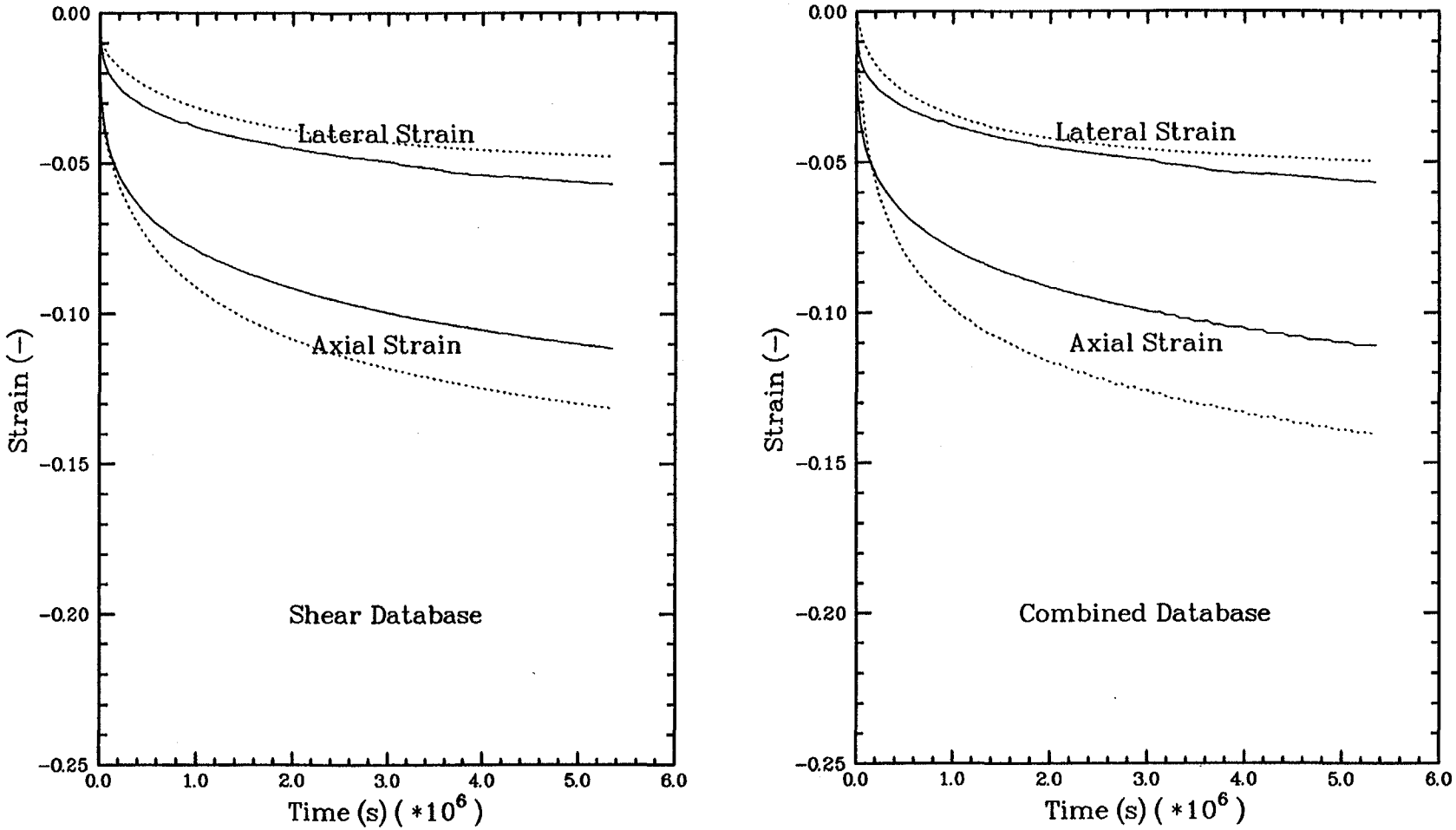

Figure C-42. Shear Consolidation Test SC2A

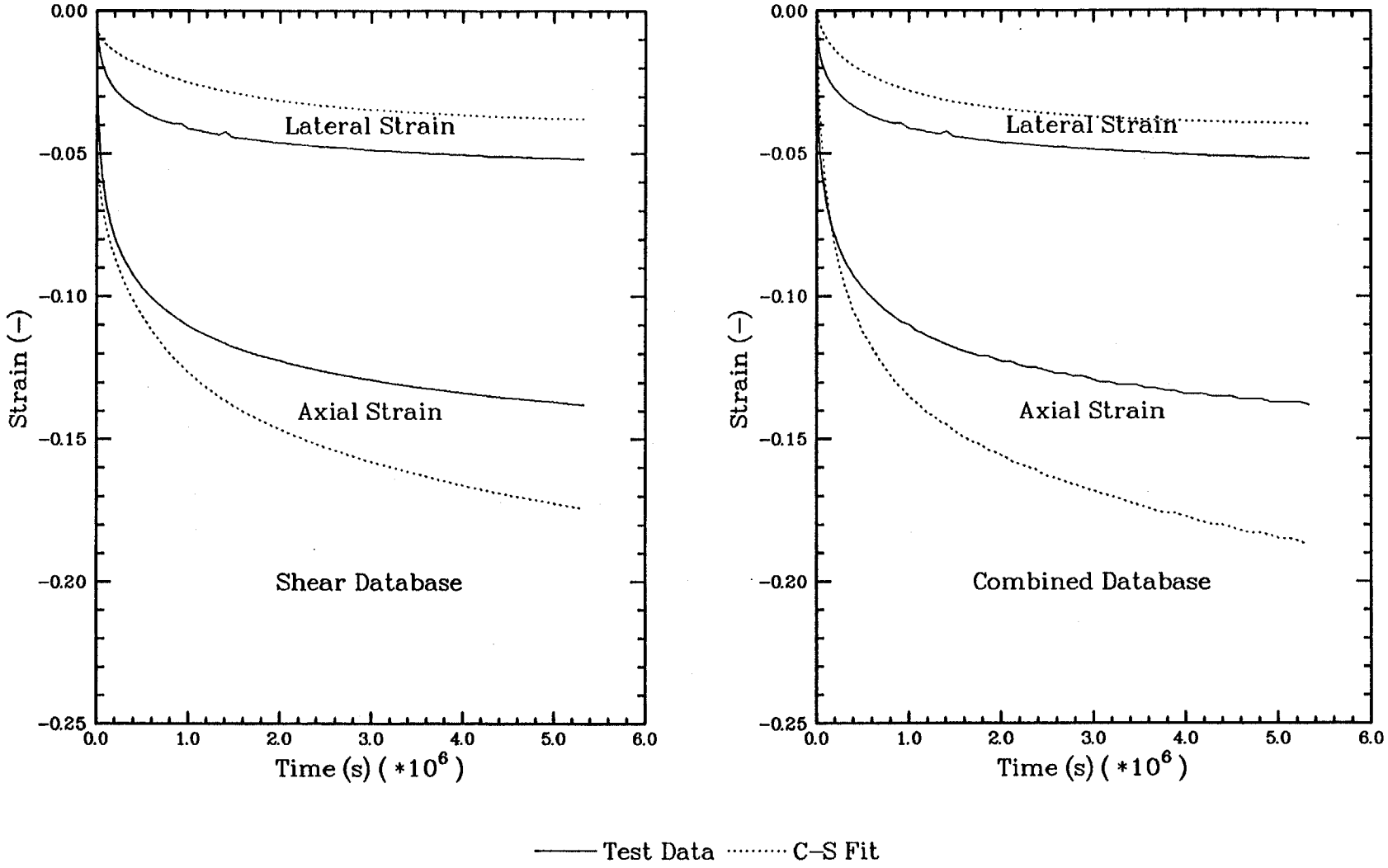

Figure C-43. Shear Consolidation Test SC3A

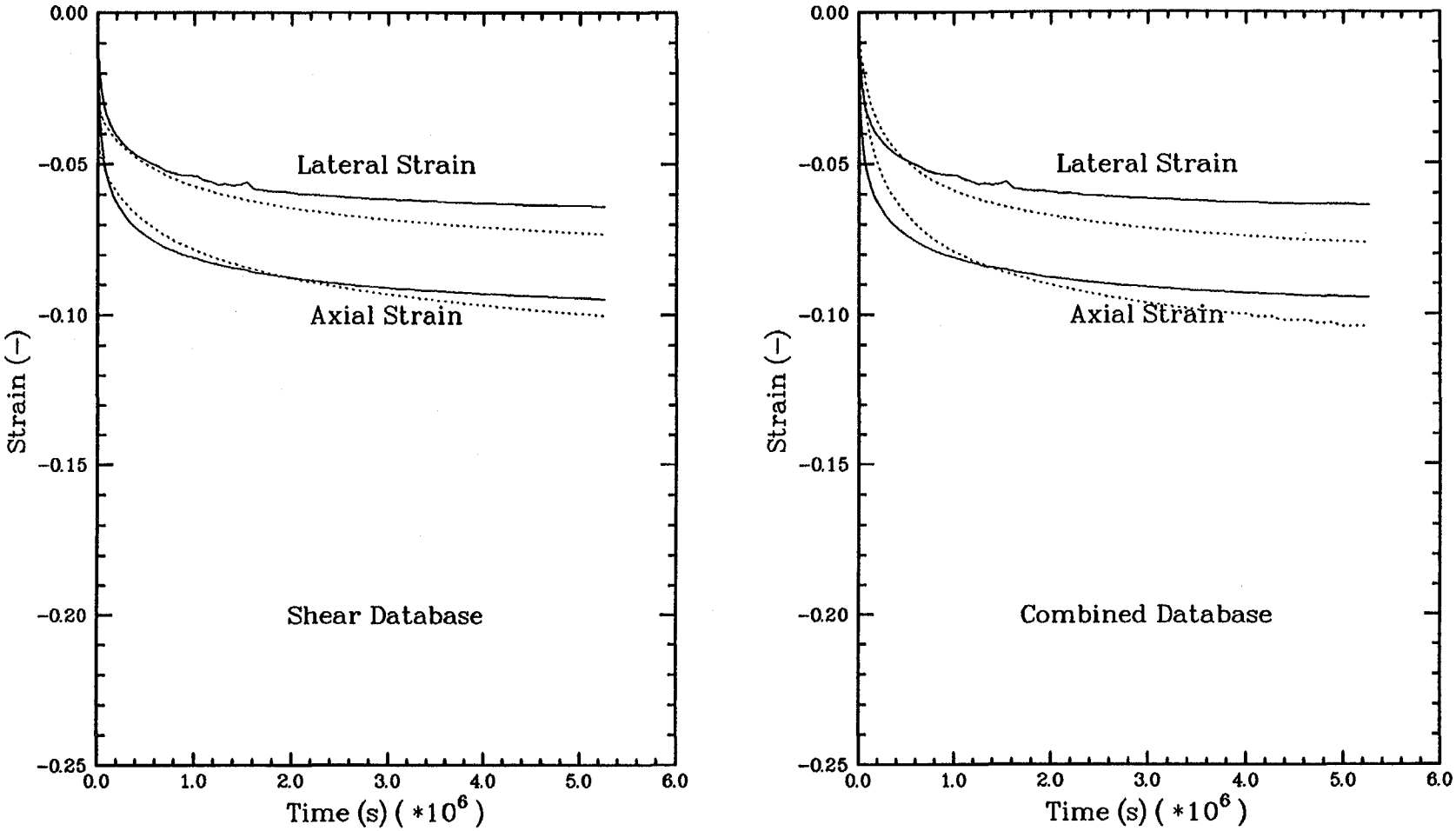

Figure C-44. Shear Consolidation Test SC4A

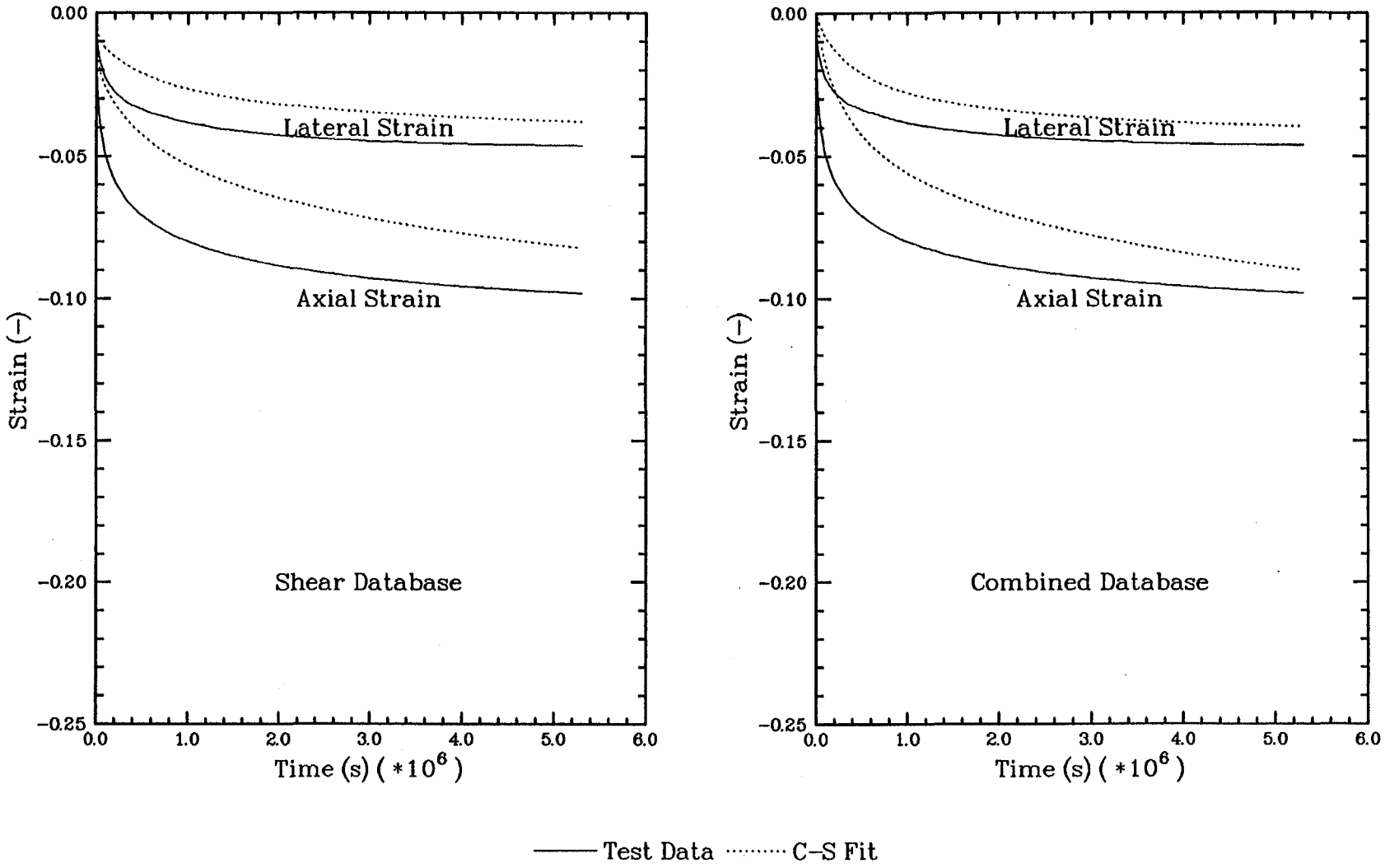

Figure C-45. Shear Consolidation Test SC5A

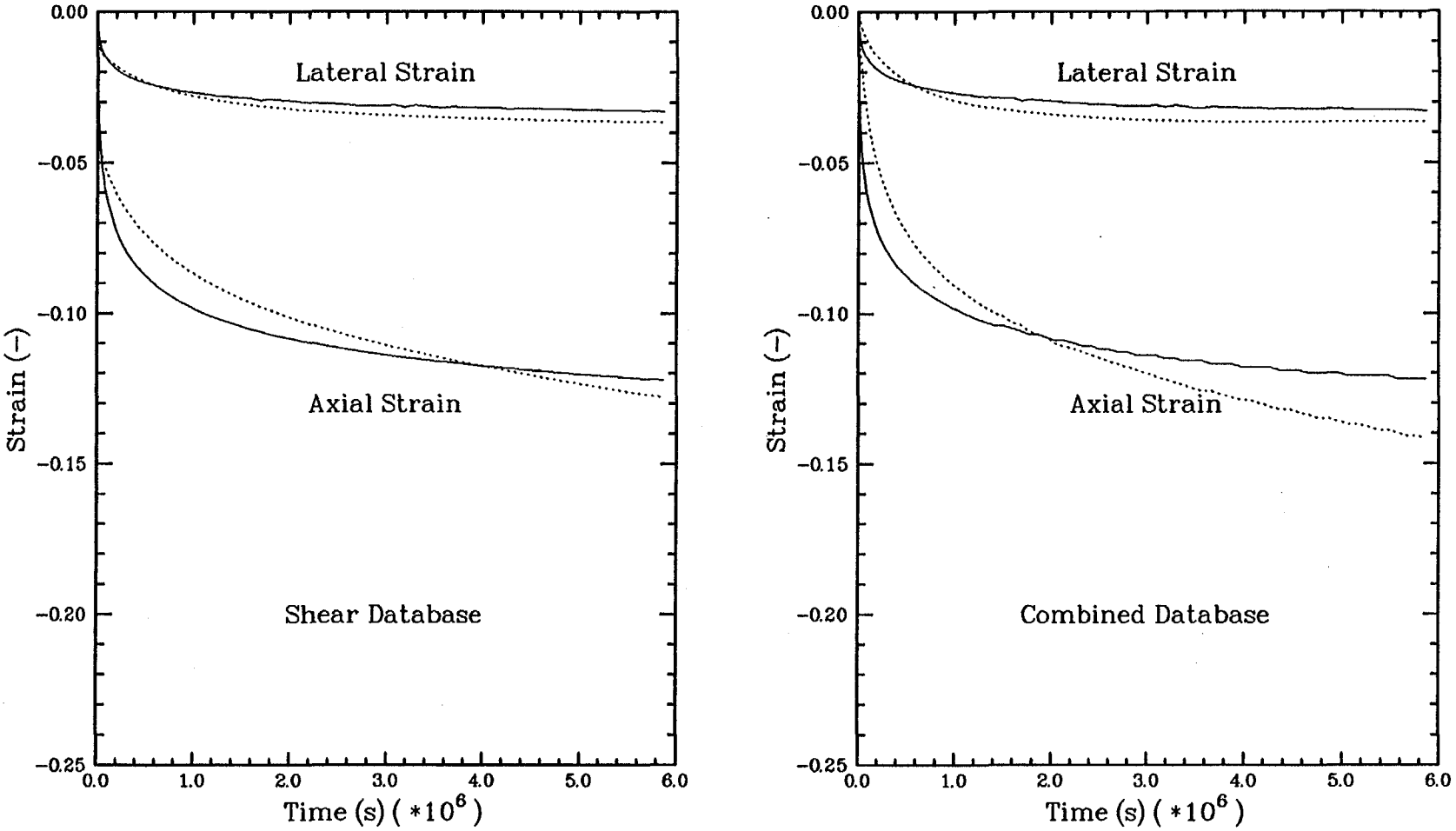

Figure C-46. Shear Consolidation Test SC6A

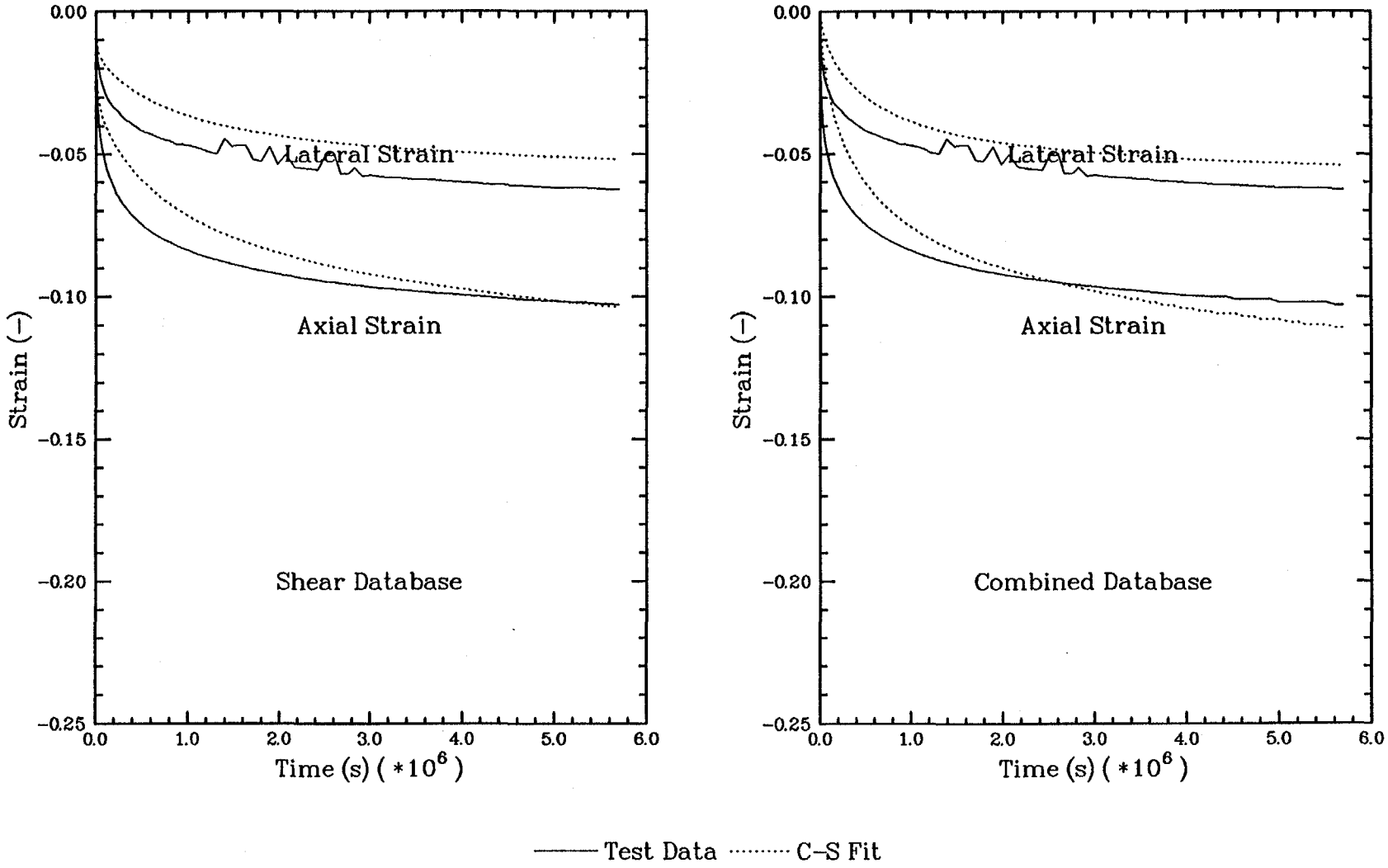

Figure C-47. Shear Consolidation Test SC7A

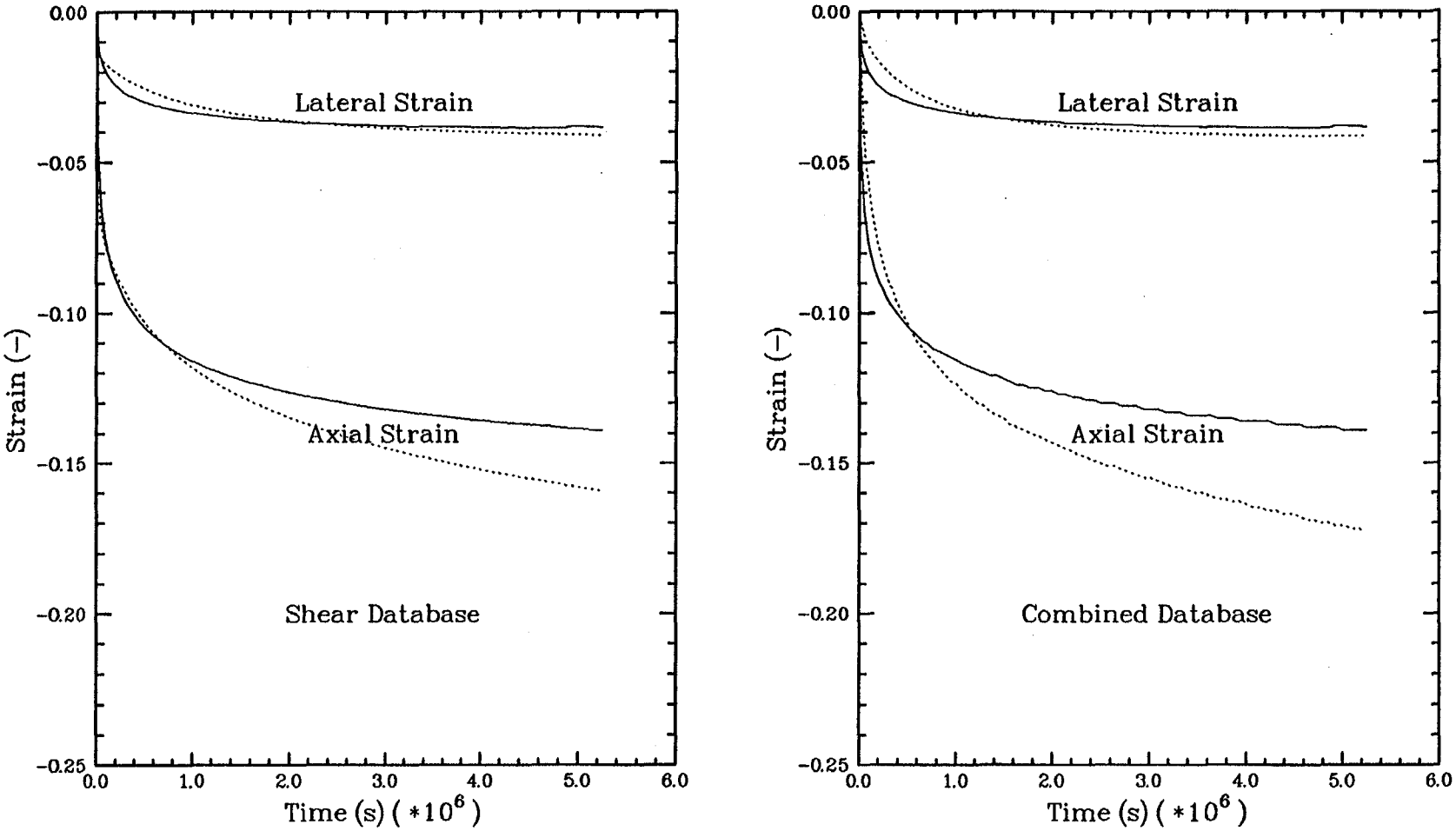

Figure C–48. Shear Consolidation Test SC8A

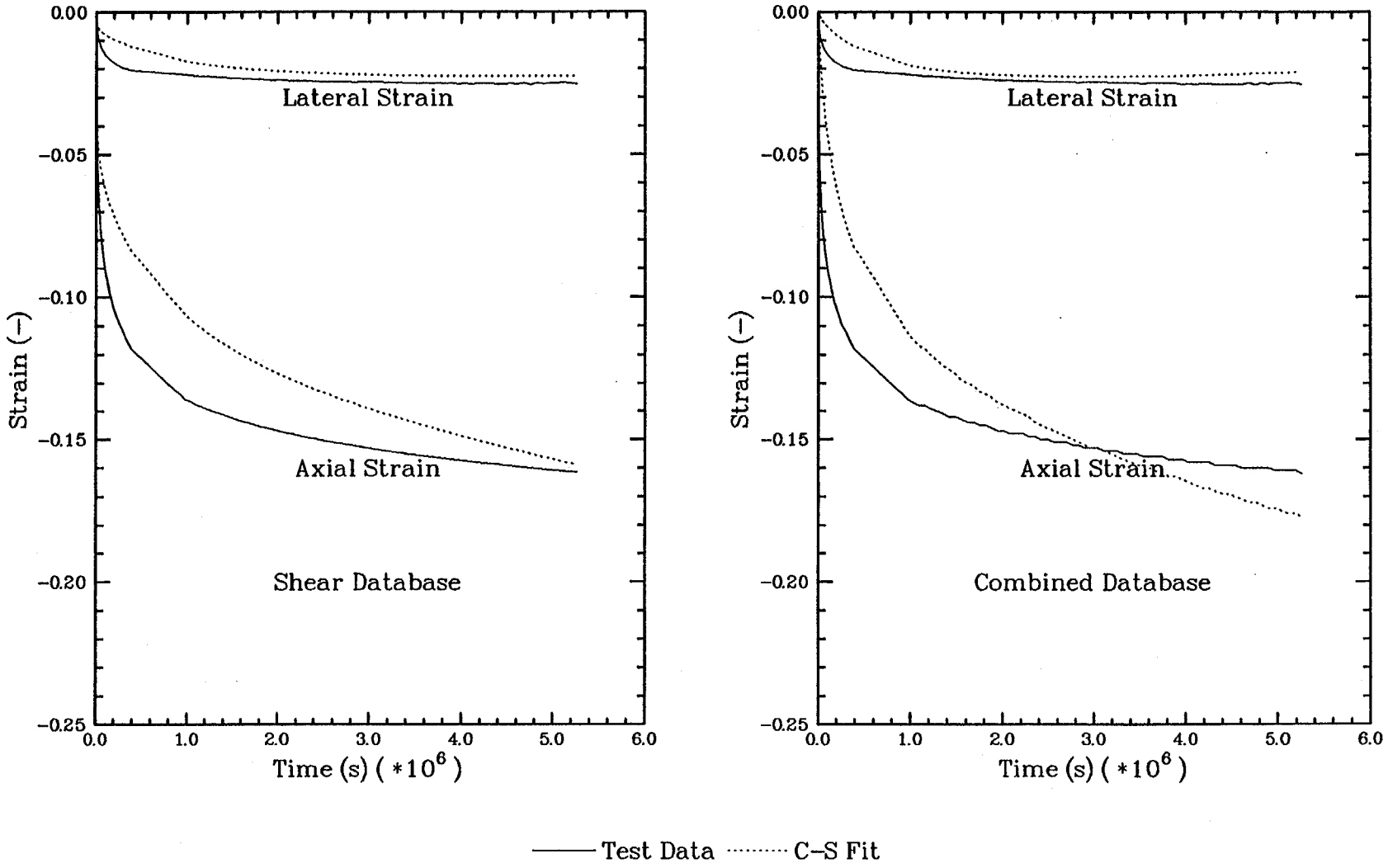

Figure C-49. Shear Consolidation Test SC9B

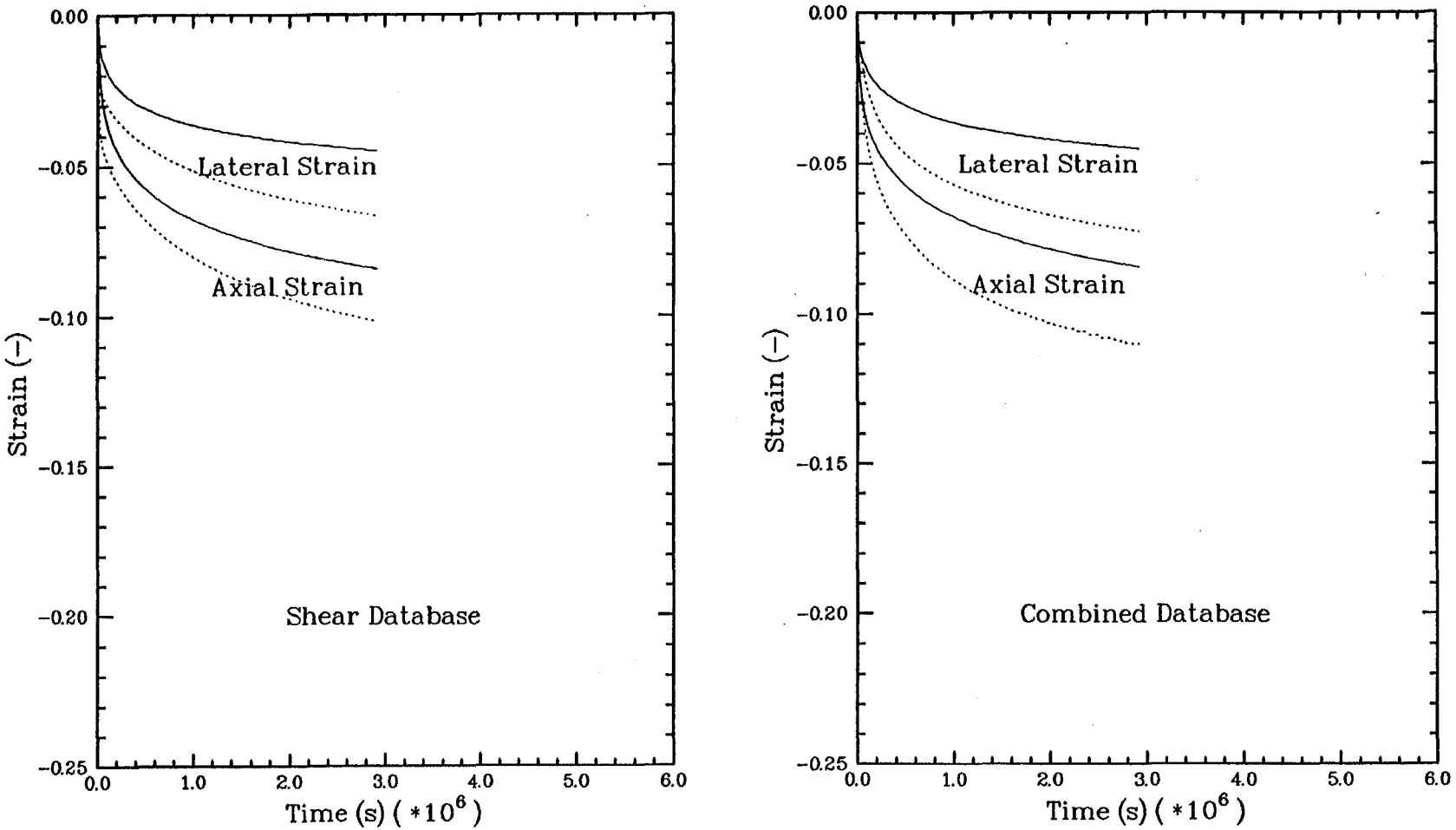

Figure C-50. Shear Consolidation Test 120C891

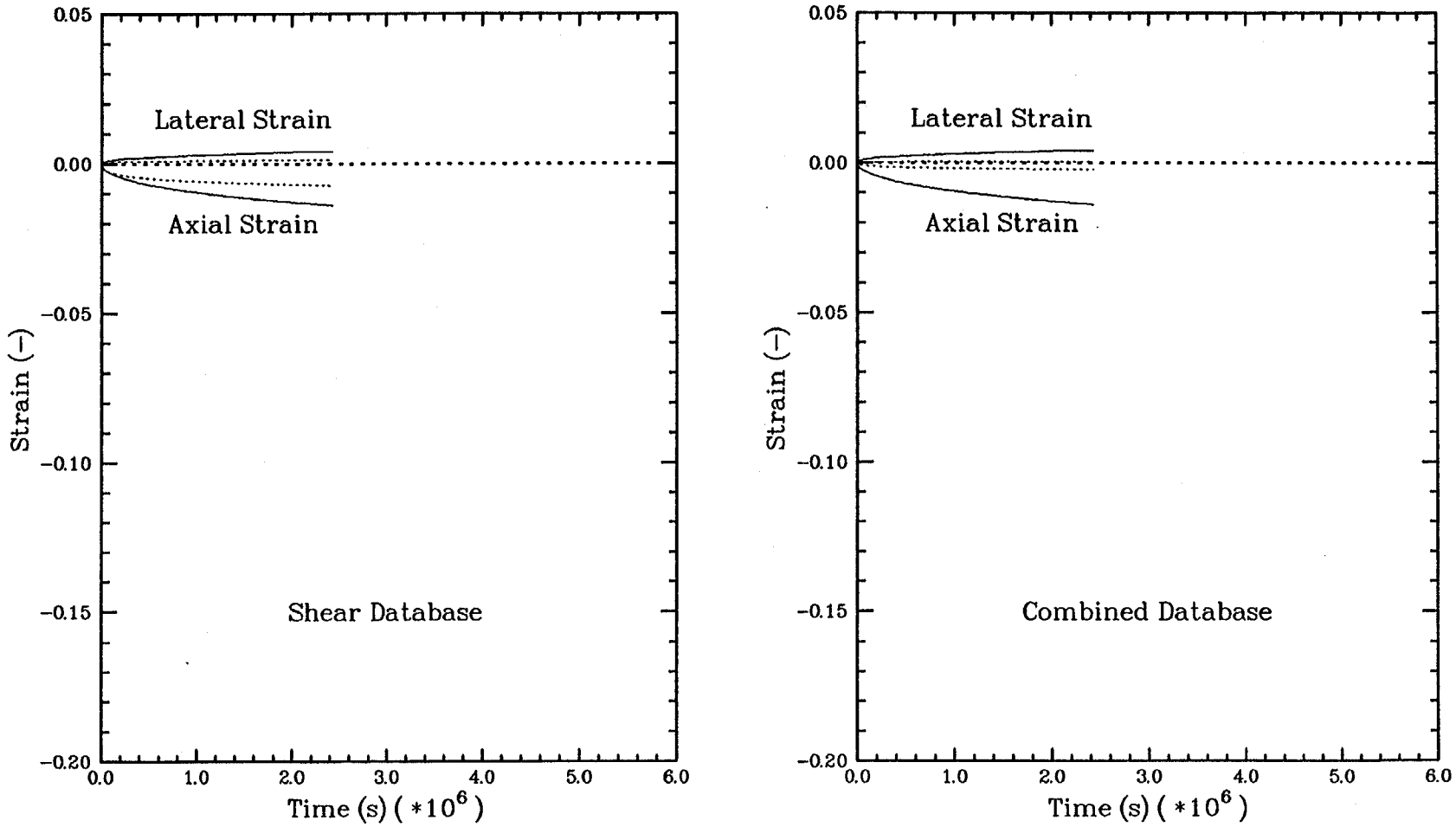

Figure C–51. Shear Consolidation Test SC10

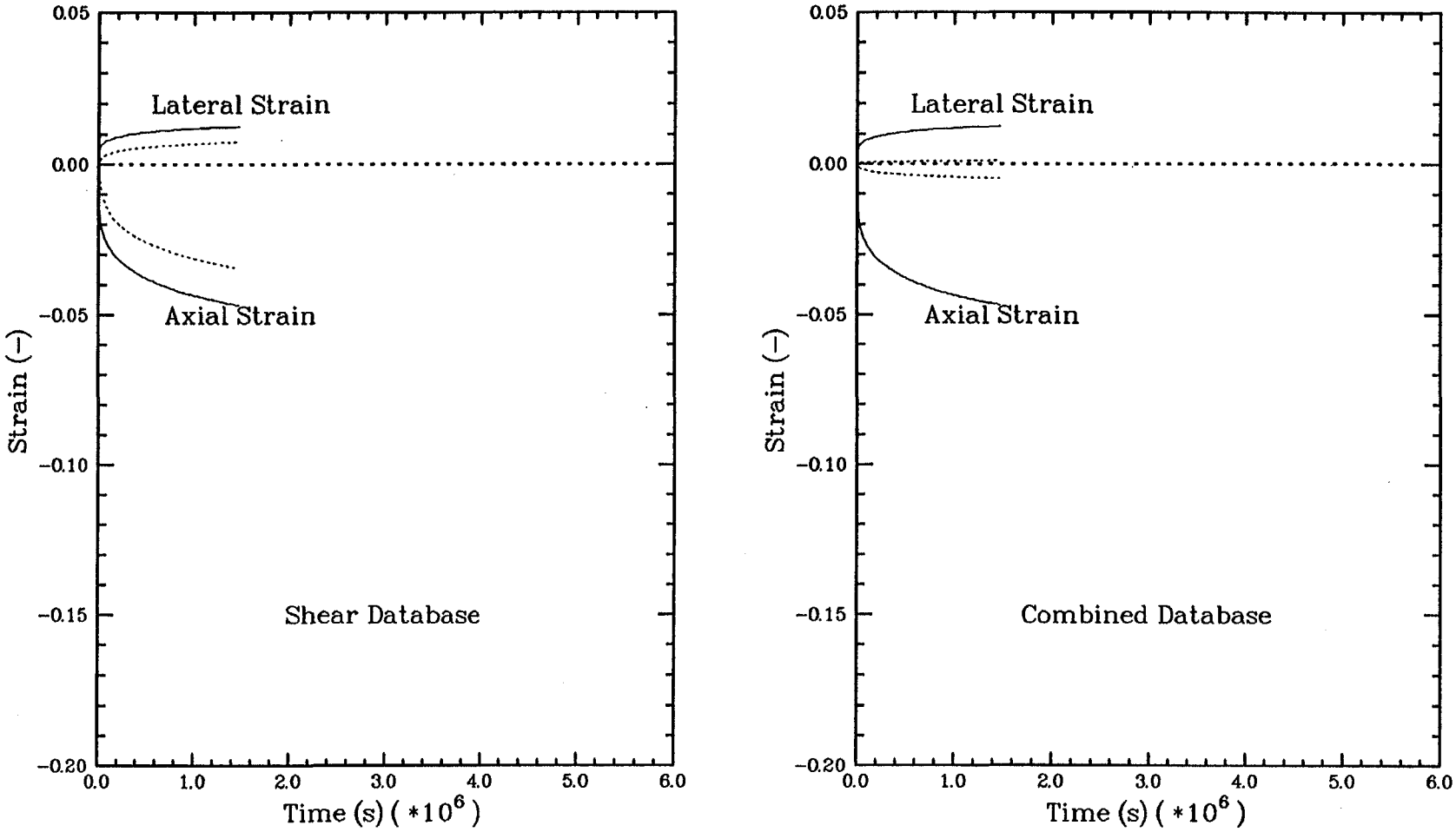

Figure C−52. Shear Consolidation Test SC11

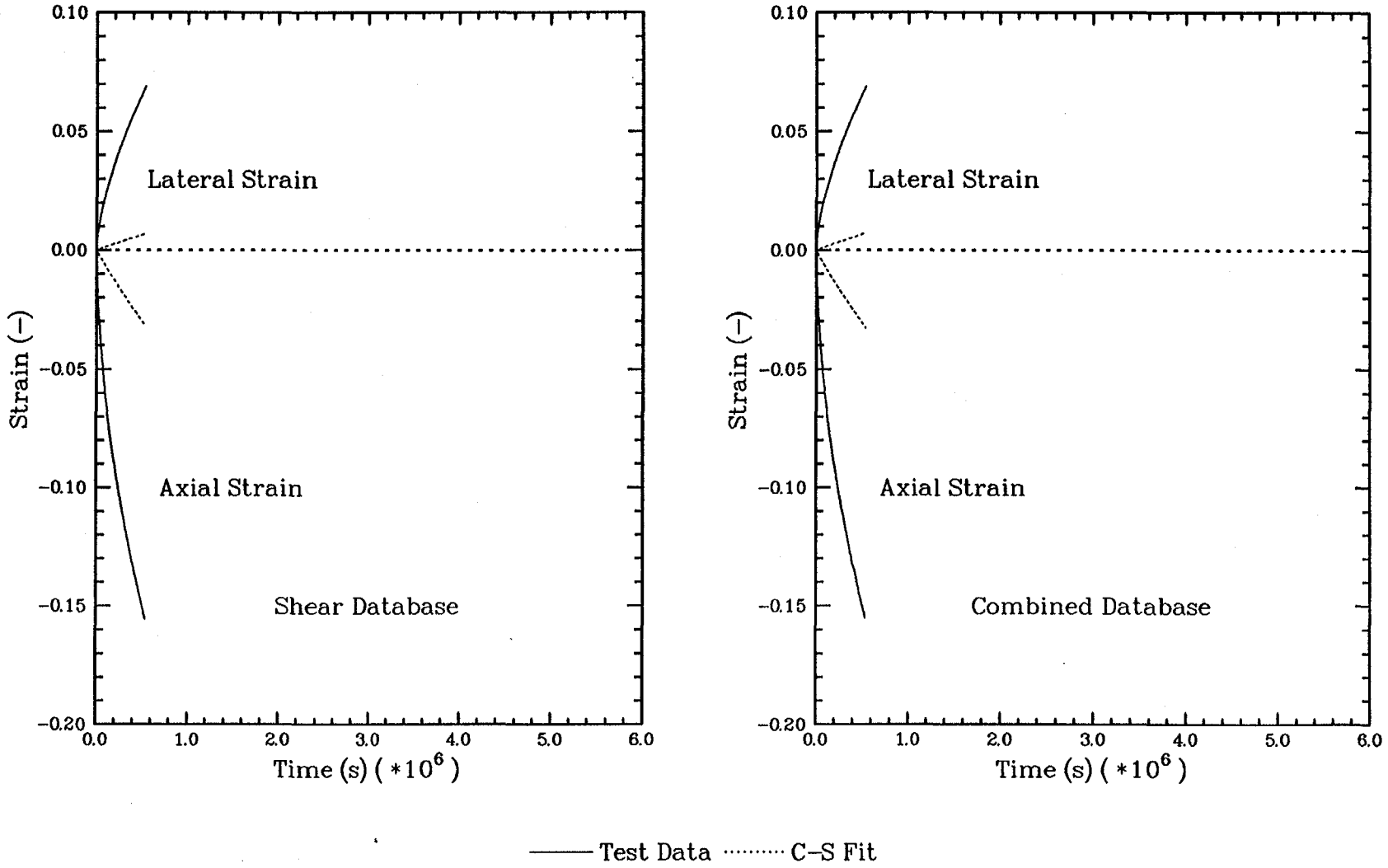

Figure C-53. Shear Consolidation Test RS/DCCS/1

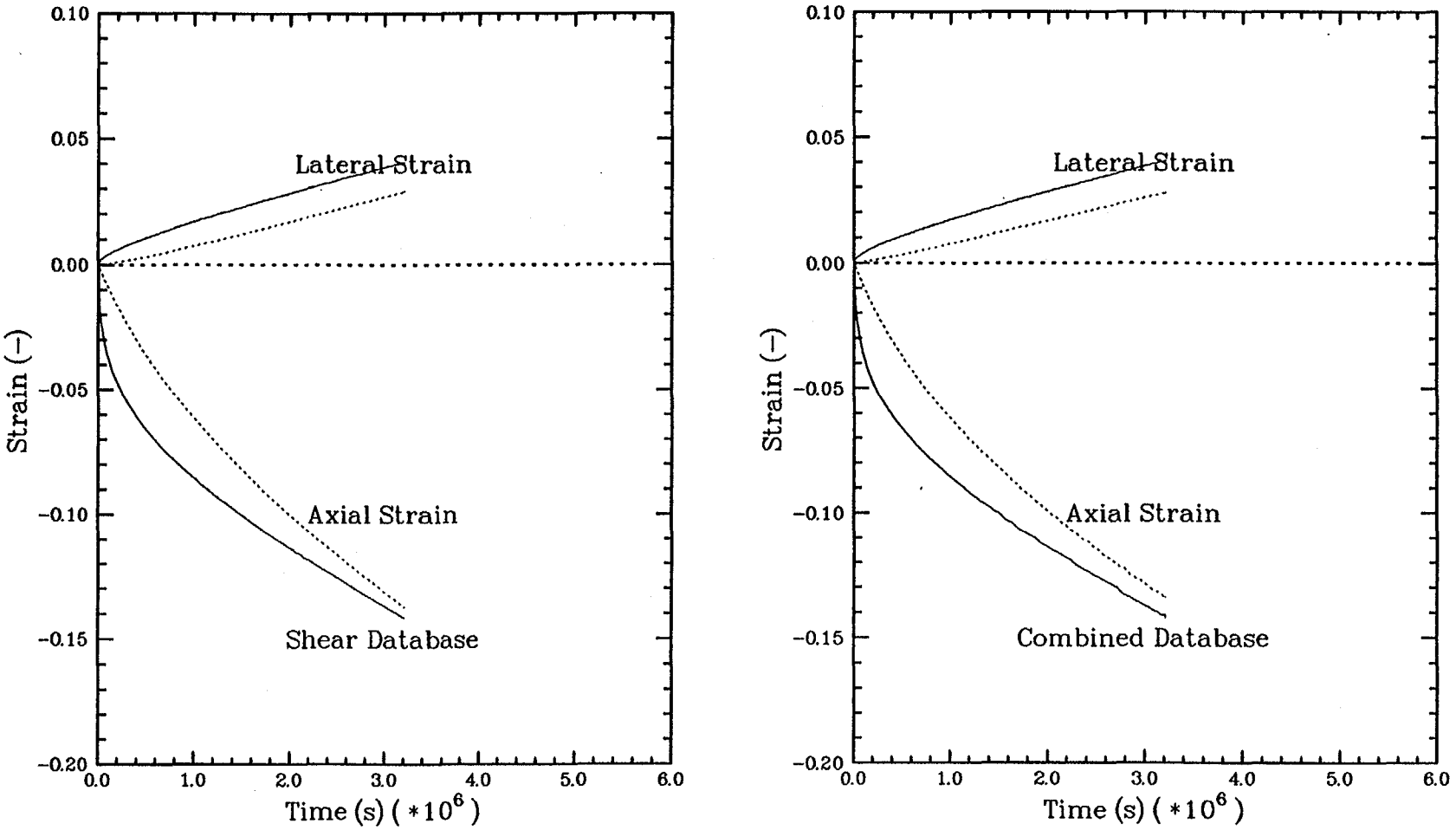

Figure C-54. Shear Consolidation Test RS/DCCS/3

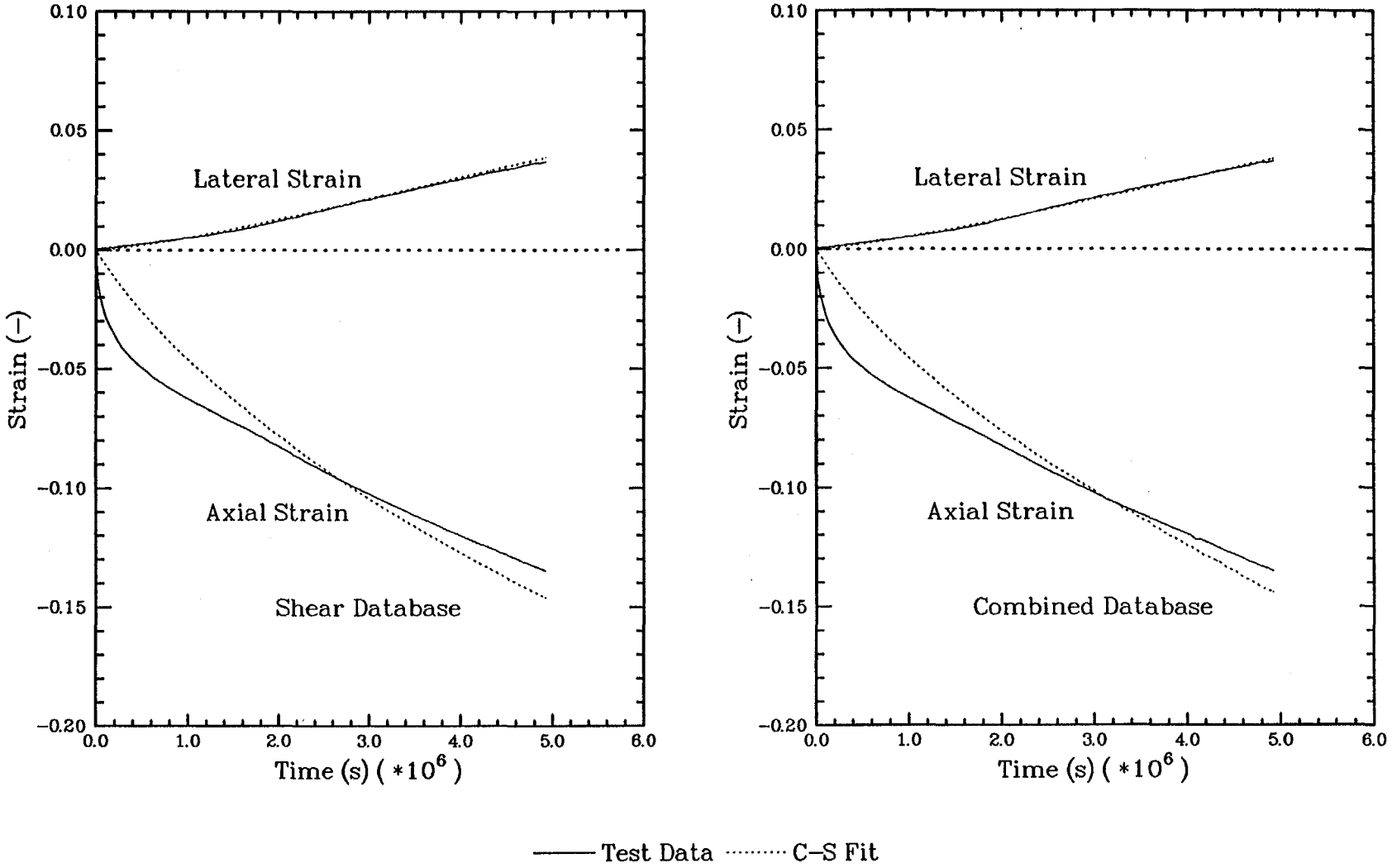

Figure C–55. Shear Consolidation Test RS/DCCS/4

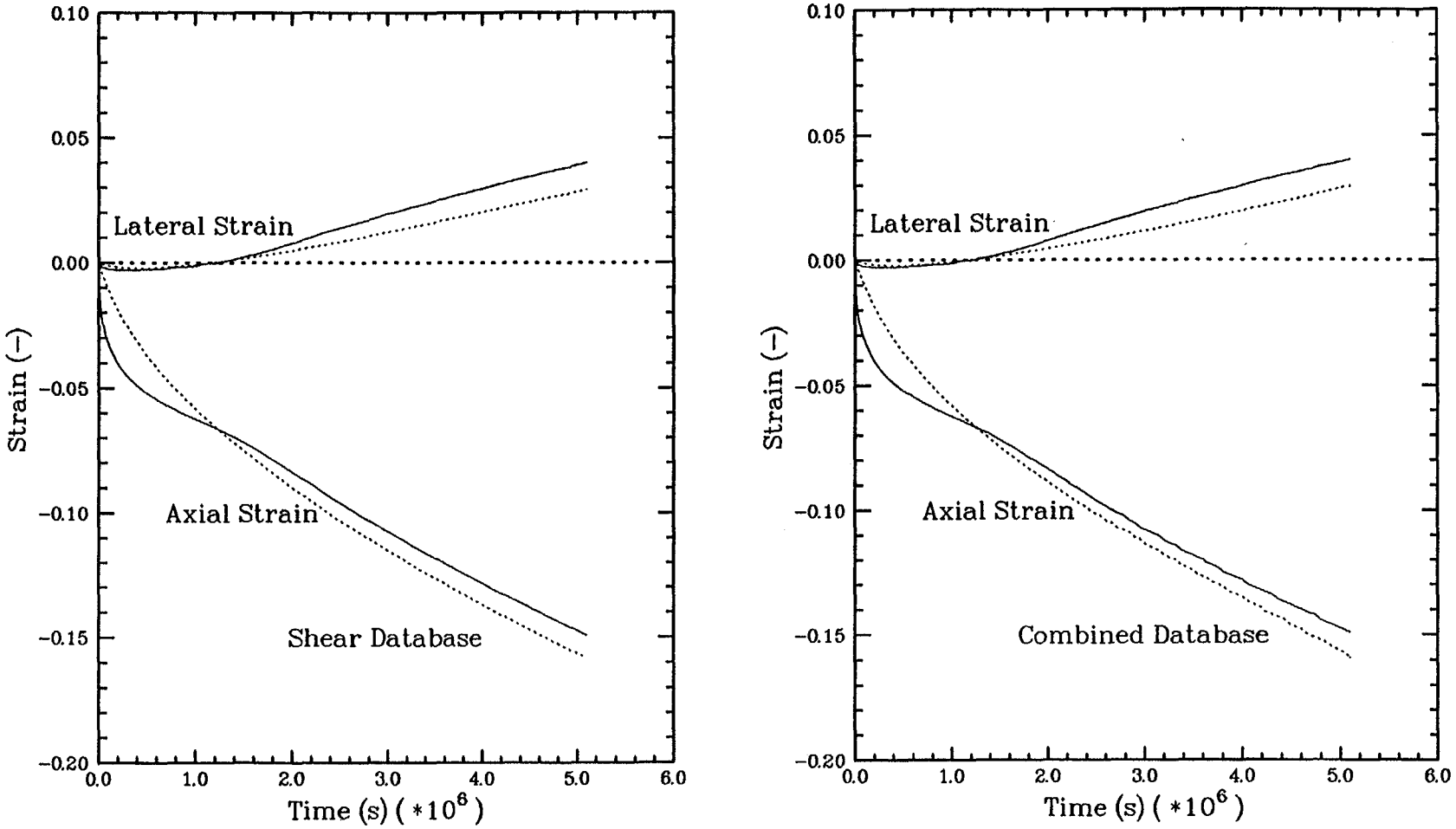

Figure C–56. Shear Consolidation Test RS/DCCS/5

WIPP
UC721 - DISTRIBUTION LIST
SAND97-2601

Federal Agencies

US Department of Energy (4)
Office of Civilian Radioactive Waste Mgmt.
Attn: Deputy Director, RW-2
Acting Director, RW-10
Office of Human Resources & Admin.
Director, RW-30
Office of Program Mgmt. & Integ.
Director, RW-40
Office of Waste Accept., Stor., & Tran.
Forrestal Building
Washington, DC 20585

Attn: Project Director
Yucca Mountain Site Characterization Office
Director, RW-3
Office of Quality Assurance
P.O. Box 30307
Las Vegas, NV 89036-0307

US Department of Energy
Albuquerque Operations Office
Attn: National Atomic Museum Library
P.O. Box 5400
Albuquerque, NM 87185-5400

US Department of Energy
Research & Waste Management Division
Attn: Director
P.O. Box E
Oak Ridge, TN 37831

US Department of Energy (5)
Carlsbad Area Office
Attn: G. Dials
D. Galbraith
M. McFadden
R. Lark
J. A. Mewhinney
P.O. Box 3090
Carlsbad, NM 88221-3090

US Department of Energy
Office of Environmental Restoration and
Waste Management
Attn: M Frei, EM-30
Forrestal Building
Washington, DC 20585-0002

US Department of Energy (3)
Office of Environmental Restoration and
Waste Management
Attn: J. Juri, EM-34, Trevion II
Washington, DC 20585-0002

US Department of Energy
Office of Environmental Restoration and
Waste Management
Attn: S. Schneider, EM-342, Trevion II
Washington, DC 20585-0002

US Department of Energy (2)
Office of Environment, Safety & Health
Attn: C. Borgstrom, EH-25
R. Pelletier, EH-231
Washington, DC 20585

US Department of Energy (2)
Idaho Operations Office
Fuel Processing & Waste Mgmt. Division
785 DOE Place
Idaho Falls, ID 83402

US Environmental Protection Agency (2)
Radiation Protection Programs
Attn: M. Oge
ANR-460
Washington, DC 20460

Boards

Defense Nuclear Facilities Safety Board
Attn: D. Winters
625 Indiana Ave. NW, Suite 700
Washington, DC 20004

Nuclear Waste Technical Review Board (2)
Attn: Chairman
J. L. Cohon
1100 Wilson Blvd., Suite 910
Arlington, VA 22209-2297

State Agencies

Attorney General of New Mexico
P.O. Drawer 1508
Santa Fe, NM 87504-1508

Environmental Evaluation Group (3)
Attn: Library
7007 Wyoming NE
Suite F-2
Albuquerque, NM 87109

NM Environment Department (3)
Secretary of the Environment
Attn: Mark Weidler
1190 St. Francis Drive
Santa Fe, NM 87503-0968

NM Bureau of Mines & Mineral Resources
Socorro, NM 87801

Laboratories/Corporations

Battelle Pacific Northwest Laboratories
Battelle Blvd.
Richland, WA 99352

Los Alamos National Laboratory
Attn: B. Erdal, INC-12
P.O. Box 1663
Los Alamos, NM 87544

Tech Reps, Inc. (3)
Attn: J. Chapman (1)
Loretta Robledo (2)
5000 Marble NE, Suite 222
Albuquerque, NM 87110

Westinghouse Electric Corporation (5)
Attn: Library
J. Epstein
J. Lee
B. A. Howard
R. Kehrman
P.O. Box 2078
Carlsbad, NM 88221

S. Cohen & Associates
Attn: Bill Thurber
1355 Beverly Road
McLean, VA 22101

RE/SPEC Inc. (6)
Attn: G. D. Callahan (2)
M. C. Loken (2)
K. D. Mellegard (2)
P. O. Box 725
Rapid City, SD 57709-0725

National Academy of Sciences, WIPP Panel

Howard Adler
Oxyrase, Incorporated
7327 Oak Ridge Highway
Knoxville, TN 37931

Tom Kiess
Board of Radioactive Waste Management
GF456
2101 Constitution Ave.
Washington, DC 20418

Rodney C. Ewing
Department of Geology
University of New Mexico
Albuquerque, NM 87131

Charles Fairhurst
Department of Civil and Mineral Engineering
University of Minnesota
500 Pillsbury Dr. SE
Minneapolis, MN 55455-0220

B. John Garrick
PLG Incorporated
4590 MacArthur Blvd., Suite 400
Newport Beach, CA 92660-2027

Leonard F. Konikow
US Geological Survey
431 National Center
Reston, VA 22092

Carl A. Anderson, Director
Board of Radioactive Waste Management
National Research Council
HA 456
2101 Constitution Ave. NW
Washington, DC 20418

Christopher G. Whipple
ICF Kaiser Engineers
1800 Harrison St., 7th Floor
Oakland, CA 94612-3430

John O. Blomeke
720 Clubhouse Way
Knoxville, TN 37909

Sue B. Clark
University of Georgia
Savannah River Ecology Lab
P.O. Drawer E
Aiken, SC 29802

Konrad B. Krauskopf
Department of Geology
Stanford University
Stanford, CA 94305-2115

Della Roy
Pennsylvania State University
217 Materials Research Lab
Hastings Road
University Park, PA 16802

David A. Waite
CH_2 M Hill
P.O. Box 91500
Bellevue, WA 98009-2050

Thomas A. Zordon
Zordan Associates, Inc.
3807 Edinburg Drive
Murrysville, PA 15668

Universities

University of New Mexico
Geology Department
Attn: Library
141 Northrop Hall
Albuquerque, NM 87131

University of Washington
College of Ocean & Fishery Sciences
Attn: G. R. Heath
583 Henderson Hall, HN-15
Seattle, WA 98195

University of Florida
Mechanics and Engineering
Attn: N. D. Cristescu
Gainseville, FL 32611

Libraries

Thomas Brannigan Library
Attn: D. Dresp
106 W. Hadley St.
Las Cruces, NM 88001

Government Publications Department
Zimmerman Library
University of New Mexico
Albuquerque, NM 87131

New Mexico Junior College
Pannell Library
Attn: R. Hill
Lovington Highway
Hobbs, NM 88240

New Mexico State Library
Attn: N. McCallan
325 Don Gaspar
Santa Fe, NM 87503

New Mexico Tech
Martin Speere Memorial Library
Campus Street
Socorro, NM 87810

WIPP Public Reading Room
Carlsbad Public Library
101 S. Halagueno St.
Carlsbad, NM 88220

Foreign Addresses

Atomic Energy of Canada, Ltd.
Whiteshell Laboratories
Attn: B. Goodwin
Pinawa, Manitoba, CANADA R0E 1L0

Ecole Polytechnique
Attn: M. Aubertin
C. P. 6079 Centre-ville
Montreal, QC CANADA H3C 3A7

Francois Chenevier (2)
ANDRA
Route de Panorama Robert Schumann
B. P. 38
92266 Fontenay-aux-Roses, Cedex
FRANCE

Claude Sombret
Centre d'Etudes Nucleaires de la Vallee Rhone
CEN/VALRHO
S.D.H.A. B.P. 171
30205 Bagnols-Sur-Ceze
FRANCE

Commissariat a L'Energie Atomique
Attn: D. Alexandre
Centre d'Etudes de Cadarache
13108 Saint Paul Lez Durance Cedex
FRANCE

Bundesanstalt fur Geowissenschaften und Rohstoffe
Attn: M. Langer
Postfach 510 153
D-30631 Hannover
GERMANY

Bundesministerium fur Forschung und Technologie
Postfach 200 706
5300 Bonn 2
GERMANY

Institut fur Tieflagerung
Attn: K. Kuhn
Theodor-Heuss-Strasse 4
D-3300 Braunschweig
GERMANY

Gesellschaft fur Anlagen und Reaktorsicherheit (GRS)
Attn: B. Baltes
Schwertnergasse 1
D-50667 Cologne
GERMANY

Shingo Tashiro
Japan Atomic Energy Research Institute
Tokai-Mura, Ibaraki-Ken, 319-11
JAPAN

Netherlands Energy Research Foundation ECN
Attn: J. Prij
3 Westerduinweg
P.O. Box 1
1755 ZG Petten
THE NETHERLANDS

Svensk Karnbransleforsorjning AB
Attn: F. Karlsson
Project KBS (Karnbranslesakerhet)
Box 5864
S-102 48 Stockholm
SWEDEN

Nationale Genossenschaft fur die Lagerung Radioaktiver Abfalle (2)
Attn: S. Vomvoris
P. Zuidema
Hardstrasse 73
CH-5430 Wettingen
SWITZERLAND

AEA Technology
Attn: J. H. Rees
D5W/29 Culham Laboratory
Abington, Oxfordshire OX14 3DB
UNITED KINGDOM

AEA Technology
Attn: W. R. Rodwell
044/A31 Winfrith Technical Centre
Dorchester, Dorset DT2 8DH
UNITED KINGDOM

AEA Technology
Attn: J. E. Tinson
B4244 Harwell Laboratory
Didcot, Oxfordshire OX11 ORA
UNITED KINGDOM

Internal

MS	Org.	
1324	6115	P. B. Davies
1320	6831	E. J. Nowak
1322	6121	J. R. Tillerson
1328	6849	D. R. Anderson
1328	6848	H. N. Jow
1335	6801	M. Chu
1341	6832	J. T. Holmes
1395	6800	L. Shephard
1395	6821	M. Marietta
1395	6801	F. D. Hansen (2)

1322	6121	L. D. Hurtado
1330	6811	K. Hart (2)
1330	4415	NWM Library (20)
9018	8940-2	Central Technical Files
0899	4916	Technical Library (5)
0619	12690	Review and Approval Desk (2), For DOE/OSTI